Déformation de la lithosphère continentale en convergence : de la tectonique paléozoïque à la réactivation cénozoïque intra-plaque dans le Tien Shan (Asie Centrale)

Anthony Jourdon

To cite this version:

Anthony Jourdon. Déformation de la lithosphère continentale en convergence : de la tectonique paléozoïque à la réactivation cénozoïque intra-plaque dans le Tien Shan (Asie Centrale). Sciences de la Terre. Université Côte d'Azur, 2017. Français. NNT : 2017AZUR4070 . tel-01662458

HAL Id: tel-01662458
https://theses.hal.science/tel-01662458
Submitted on 13 Dec 2017

École doctorale Sciences Fondamentales et Appliquées
Unité de recherche : Géoazur UMR 7329

Thèse de doctorat

Présentée en vue de l'obtention du
grade de docteur en Sciences de la Terre et de l'Univers
de
l'Université Côte d'Azur

par

Anthony Jourdon

Déformation de la lithosphère continentale en convergence :

de la tectonique paléozoïque à la réactivation cénozoïque intra-plaque dans le Tien Shan (Asie Centrale)

Dirigée par *Carole Petit, Professeure, Université de Nice-Sophia Antipolis*
et codirigée par Yann Rolland, Maître de conférence, Université de Nice-Sophia Antipolis

Soutenue le 08 Septembre 2017
Devant le jury composé de :

Marc	Jolivet	Chercheur CNRS (HDR), Géosciences Rennes	Rapporteur
Philippe	Yamato	Professeur, Géosciences Rennes	Rapporteur
Frédéric	Mouthereau	Professeur, Géosciences Environnement Toulouse	Examinateur
Laurent	Jolivet	Professeur, ISTO	Examinateur
Riad	Hassani	Professeur, Géoazur	Examinateur
Stefan	Schmalholz	Professeur, Université de Lausanne	Examinateur
Carole	Petit	Professeure, Géoazur	Directrice de thèse
Yann	Rolland	Maître de conférence (HDR), Géoazur	Co-directeur de thèse
Laëtitia	Le Pourhiet	Maître de conférence (HDR), ISTeP	Invitée

Thèse de doctorat

Présentée en vue de l'obtention du
grade de docteur en Sciences de la Terre et de l'Univers
de
l'Université Côte d'Azur

par

Anthony Jourdon

Déformation de la lithosphère continentale en convergence :

de la tectonique paléozoïque à la réactivation cénozoïque intra-plaque dans le Tien Shan (Asie Centrale)

Photo du Khan Tengri – Roi des cieux. Point triple Kirghizstan-Kazakhstan-Chine (Photo par Chloé Loury, Juillet 2014, lors de ma première mission de terrain dans le Tien Shan)

à ma sœur Céline Jourdon…

Table des matières

Remerciements 9

Résumé 11

Abstract 11

Introduction 13

I. Contexte géologique de la chaîne du Tien Shan 17

1. Tectonique paléozoïque 17

1.1. Structure générale du Tien Shan 19

1.2. Modèles d'accrétion du Tien Shan 24

1.3. Evolution post-orogénique du Tien Shan 26

2. Tectonique Cénozoïque 27

2.1. Déformation active 30

2.2. Structure crustale du Tien Shan 32

3. Problématique 34

II. Déformation et structure paléozoïque du Tien Shan 35

Résumé 36

Abstract 37

1. Introduction 38

2. Geological Setting of the Tien Shan Belt 39

2.1. General structure of the Kyrgyz Tien Shan 39

2.2. Previously proposed models of TS accretion 42

2.3. Post orogenic evolution of the Tien Shan 43

2.4. Cenozoic reactivation 43

3. Structural analysis 44

3.1. Structural geology of the Song-Kul zone 44

3.2. Structural geology of the At-Bashi region 55

3.3. The South Tien Shan in Khan-Tengri region 59

4. Discussion and structural interpretation of the Tien Shan accretionary belt during the Paleozoic. 63

4.1. Paleozoic structures of the Kyrgyz Tien Shan 63

4.2. Middle Carboniferous NTS/MTS/STS kinematics 66

Conclusion 68
Acknowledgments 68
III. Rôle et influence de l'héritage structural sur la localisation de la déformation 69
1. Modélisation numérique 70
1.1. Equations de Conservation 70
1.2. Loi de fluage en milieu continu 72
1.3. La méthode des éléments finis et le code pTatin2D 73
2. Structure profonde et réactivation de la chaîne du Tien Shan : modéliser le passé pour mieux contraindre le présent 75
Résumé 75
Abstract 77
Introduction 77
1. Tectonic units of the Tien Shan belt 80
1.1. The North and Middle Tien Shan 80
1.2. The Tarim block and the South Tien Shan 81
2. Active deformation in the Tien Shan belt 82
3. Modelling 85
3.1. Constraints on the lithospheric structure from geological and geophysical data 85
3.2. Initial model geometry 86
3.3. Model size and boundary conditions 88
3.4. Rheologies 88
4. Model results 90
4.1. Crustal weak zones 90
4.2. Initial weak zones in the mantle 93
4.3. Mantle and crust weak zones 95
5. Validation of the models and crustal structure 98
5.1. Validation of the models 98
5.2. Deep structures and crustal cross-section 102
6. Discussion 104
6.1. Influence of mantle versus crustal weak zones 104
Conclusions 107

Appendix A 108

1. Impact of the lithospheric resistance 111

1.1. Impact of thermal age of the lithosphere 111

1.2. Impact of the lithospheric resistance heterogeneity 111

1.3. Impact of the crustal rheology 112

IV. Influence des processus de surface sur la tectonique et l'exhumation basse température. 121

1. Trajets Température-temps. 121

2. Impact des processus d'éroion-sédimentation sur l'exhumation de roches de basse température dans les chaînes de montagnes : l'exemple du Tien Shan 123

Résumé 123

Abstract 125

Introduction 125

1. General overview on the Tien Shan and thermo-chronological constraints 127

2. Modelling setup 128

3. Impact of erosion rate 129

4. Quantification of out of plane drainage 130

5. Comparison with the Tien Shan belt 132

6. Discussion 134

V. Discussion 135

1. Tectonique paléozoïque du Tien Shan 135

1.1. La Nikolaev Line, zone de suture d'une subduction ou faille transformante ? 135

1.2. Tectonique hercynienne, de la subduction à la collision 137

1.3. Synthèse 144

2. Déformation intracontinentale, réactivation et rhéologie de la lithosphère : l'exemple de la déformation cénozoïque de l'Asie 145

Perspectives 149

Annexes 151

Minutes de terrain 151

Routines Matlab pour les trajets P-T-t d'après pTatin2D 157

Introduction 157

Functions 157
Scripts pour trajets P-T-t 162
Références 173

Remerciements

Avant tout je souhaite remercier Laëtitia Le Pourhiet qui m'a initié à la modélisation numérique au détour d'une conversation dans un appartement d'un arrondissement parisien dont j'ai oublié le numéro. Je voulais tester des hypothèses te semblant farfelues sur la tectonique paléozoïque du Tien Shan et au final je me suis retrouvé à faire des modèles d'héritage tectonique sur le Cénozoïque. Tu m'as appris de nombreuses choses sur la modélisation numérique, son utilité et comment on doit s'en servir même si je fais des erreurs… Merci en tout cas pour la patience et le temps que tu m'as consacré, merci de m'avoir hébergé dans la petite ville de province qu'est Paris et dans cette grande capitale qu'est Juvisy.

Bien que tu ne sois pas officiellement co-directrice de ma thèse tu as largement contribué au travail qui est présenté dans ce mémoire et ton nom en deuxième auteure sur les articles en est la preuve. Merci pour tout et que notre collaboration et amitié continue !

Je souhaiterai ensuite remercier Carole Petit, ma directrice de thèse. Tu as toujours été disponible lorsque j'avais besoin d'un conseil, de te faire lire un brouillon de manuscrit ou de discuter sur les résultats et interprétations des différents travaux menés au cours de cette thèse. Merci pour avoir été à l'écoute et patiente, car je sais que parfois je peux être un peu têtu. Merci également pour le co-voiturage sans quoi mon quotidien aurait été bien plus compliqué logistiquement !

Je souhaite bien évidemment remercier Yann Rolland mon co-directeur de thèse sans qui toute la partie terrain de cette thèse n'aurait pas été possible. Merci de m'avoir emmené découvrir cette formidable région qu'est le Tien Shan. Merci pour les discussions que nous avons pu mener au cours de cette thèse. Tu m'as fait découvrir et aimer la géologie de terrain en licence et depuis je ne l'ai plus quitté… Merci pour ce cadeau !

Merci également à Riad Hassani, tu m'as grandement aidé dans ma formation à la mécanique et au fonctionnement d'un code numérique en éléments finis. J'ai débarqué plusieurs fois dans ton bureau avec mes questions pas toujours bien claires ou bien formulées mais tu as toujours pris le temps d'y répondre ! Merci pour ces heures passées devant ce tableau blanc au fond du couloir dans le rez-de-chaussée sombre de l'annexe.

Enfin je souhaite remercier mon réalisateur, metteur en scène, les maquilleuses et costumières sans qui ce film n'aurait pas été réalisable… Snif… Snif… pardon c'est l'émotion, c'est pas tous les jours qu'on a un ... *Fouille dans sa poche...* Ah non pardon excusez-moi, je me suis trompé de texte, j'avais préparé celui-là pour le festival de Cannes.

Non en réalité je remercie le reste des personnes du laboratoire avec qui j'ai pu passer d'agréables moments et qui rendent le quotidien plus gai, merci à Maëlle, Alex, Jean-Xav, Marc Renier mon presque voisin de palier qui m'a bien fait rire (1D forever), Kévin, Sarah, Zoé, Manu, Laurent, Luc… Désolé si j'ai oublié quelqu'un.

Merci aussi à Caroline qui m'a souvent aidé face des problèmes informatiques insurmontables, et également à Véronique qui s'est toujours volontiers occupée des tâches administratives concernant nos dépenses et missions et sans qui je serai perdu quelque part entre Bishkek, Vienne et Nice.

Résumé

Le Tien Shan est une chaîne de montagne active située à plus de 1000 km de la limite de plaque la plus proche, le front Himalayen. Elle possède une histoire ancienne qui va de la fin du Protérozoïque à la fin du Paléozoïque dans un contexte d'accrétions successives formant la plus grande chaîne d'accrétion du monde, la CAOB. Afin de comprendre comment l'histoire paléozoïque du Tien Shan influence la localisation de la déformation cénozoïque, nous avons dans un premier temps étudié la structuration de la chaîne pour en identifier les principales structures héritées. Nous avons mis en avant le partitionnement de la déformation entre les zones de sutures Sud et Nord au cours de la collision entre le Tarim et le Tien Shan au Carbonifère supérieur. Le front de collision est caractérisé par des chevauchements et des détachements au sein d'unités métamorphiques. Au Nord, se trouve une zone en décrochement caractérisée par une structure en fleur positive. Ensuite, ces résultats sont utilisés comme les conditions initiales de modèles numériques thermo-mécaniques 2D dont le but est de tester l'influence de ces zones héritées sur la localisation de la déformation cénozoïque. Ces modèles montrent que la déformation cénozoïque dans le Tien Shan se localise à la faveur de zones de faiblesses crustales et non mantelliques. De plus, nous avons pu établir que la bordure nord du Tarim avait une rhéologie proche de celle du Tien Shan. Finalement, à l'aide des modèles numériques une étude systématique a permis de mettre en évidence que le couplage entre l'érosion et le réseau de drainage jouait un rôle important dans la répartition et l'âge des roches de basse température exhumées.

Abstract

The Tien Shan is an active mountain belt located at more than thousand kilometres of the closest plate boundary, the Himalayan front. Its Late Proterozoic to Late Paleozoic history takes place during the CAOB accretion which represents the largest accretionary belt in the world. In order to understand how the Paleozoic tectonics of the Tien Shan influences the Cenozoic strain localization, we aim at identifying the main inherited structures of the belt. We highlighted the strain partitioning between the North and South suture zones during the Tarim-Tien Shan Late Carboniferous collision. The collisional front is characterized by thrusts and detachments in metamorphic units while northward, a strike-slip zone is evidenced by a positive flower structure. Then, these results are used as variable inputs in 2D numerical thermo-mechanical models in order to assess the role of these inherited structures on the Cenozoic strain localization. These models show that the Cenozoic deformation in the Tien Shan is localized in favour of crustal weak zones instead of mantellic ones. Moreover, we are able to show that the northern border of the Tarim has a Tien Shan like rheology. Finally, we performed a systematic numerical modelling analyse in order to show that the coupling between erosion and drainage network plays an important role on low temperature rocks exhumation ages and repartition.

Introduction

La principale hypothèse sur laquelle est fondée la tectonique des plaques repose sur le fait que celles-ci soient rigides et résistantes dans leur ensemble et que l'essentiel de la déformation se concentre sur leurs limites, étroites et très localisées.

Grâce aux études géophysiques et au développement des moyens d'imager la Terre nous savons aujourd'hui, notamment par le biais des méthodes GPS et de la sismicité, identifier les zones localisant la déformation (Figure 1).

Il apparaît, conformément à la théorie, que la déformation de la lithosphère se concentre principalement le long de zones bien localisées représentant les frontières entre les différentes lithosphères. Ces frontières sont différenciées en trois types ; les limites convergentes (subductions et chaînes de montagnes), les limites divergentes (dorsales océaniques et rifts) et les limites transformantes (le long de grandes structures décrochantes qui accommodent des déplacements de type coulissage entre deux lithosphères, e.g. faille Nord Anatolienne, faille de San Andreas).

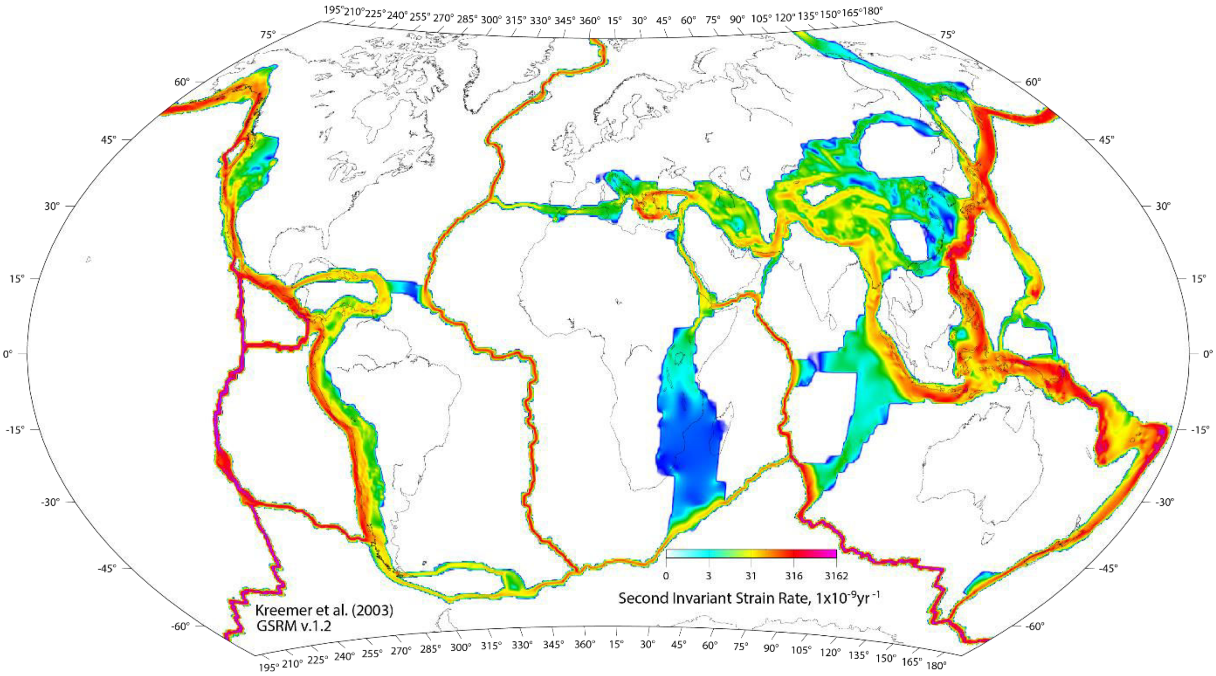

Figure 1 : Carte des vitesses de déformation à la surface de la Terre (Kreemer et al., 2003)

Cependant, cette carte d'intensité de la déformation à la surface de la Terre (Figure 1) (Kreemer et al., 2003) met en évidence des zones très larges (plusieurs centaines de kilomètres) dans lesquelles la déformation est diffuse, comme par exemple en Asie où l'on observe une déformation active à plusieurs milliers de kilomètres de toute limite de plaque, mais également dans la partie sud du Rift Est Africain et dans le sud-est de l'Océan Indien. Ces domaines particuliers sont appelés zones de déformation intra-plaque. En Asie Centrale, la déformation y est suffisamment importante pour générer des séismes de magnitude 7. Toutefois, cette carte représente un cliché qu'on pourrait qualifier d'instantané par rapport aux temps géologiques. Quels sont les facteurs (vitesses aux limites, variations rhéologiques, forces de volumes) qui influencent la localisation de la déformation intra-plaque ? Comment évolue-t-elle à l'échelle de plusieurs millions d'années ? Peut-elle aboutir à la formation de nouvelles limites de plaques ?

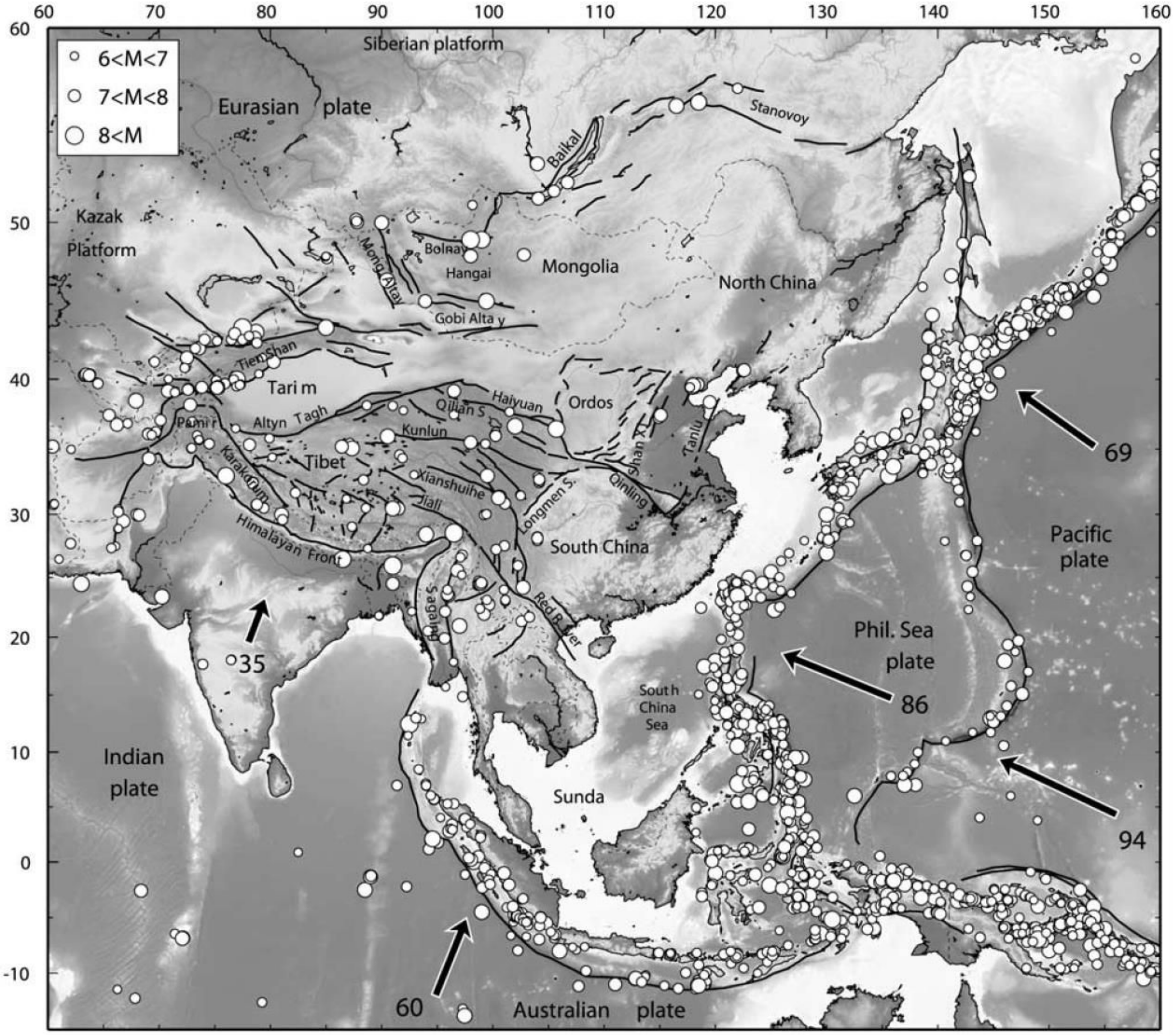

Figure 2 : *Vitesses relatives des plaques dans la région d'Asie de l'Est et du Sud-Est en mm/an, dans un référentiel Eurasie fixe. Les flèches indiquent les directions de convergence. Les séismes de magnitudes supérieures à 6 sont indiqués ainsi que les grandes structures tectoniques (traits noirs gras), (Vergnolle et al., 2007)*

En Asie, la déformation s'étend depuis les limites de plaques convergentes au Sud et à l'Est jusqu'au craton sibérien (Figure 2). Vergnolle et al. (2007) ont montré que les forces responsables de la déformation intra-plaque en Asie sont multiples et variables à l'intérieur du continent. La déformation des bordures Est et Sud-Est de l'Asie est principalement contrôlée par la dynamique de subduction (e.g. Kong and Bird, 1996; Sternai et al., 2016). En limite de plaque, les effets de la convergence relative dominent puis vers l'intérieur de la plaque on observe une cinématique dominée par un phénomène d'échappement vers l'Est. Dans cette partie de l'Asie plusieurs auteurs proposent que les forces de volumes principalement liées à l'énergie potentielle de pesanteur (England and Molnar, 2005, 1997; Flesch et al., 2001; Vergnolle et al., 2007) soient le facteur dominant de la déformation. D'autres proposent un rôle important des flux mantelliques liés à la dynamique de la subduction (e.g. Sternai et al., 2016). En revanche, dans la partie ouest-nord-ouest de l'Asie (Himalaya, Pamir, Tien Shan) le raccourcissement orienté nord-sud est contrôlé par les forces aux limites convergentes liées à la collision Inde-Asie (Avouac et al., 1993; Tapponnier et al., 1986; Vergnolle et al., 2007).

A l'échelle du Cénozoïque (depuis la collision Inde-Asie il y a ~57 Ma, e.g. de Sigoyer et al., 2000), la déformation propagée dans le continent asiatique met en évidence des zones très peu déformées comme les bassins du Tarim et du Junggar, et à l'inverse des zones fortement déformées comme le plateau du Tibet, le Tien Shan ou encore l'Altaï (Figure 3). Il est donc clair que la plaque eurasienne ne se comporte pas comme un milieu homogène et peu déformable mais bien comme une zone hétérogène localisant suffisamment de déformation pour former des chaînes de montagnes au cours du Cénozoïque.

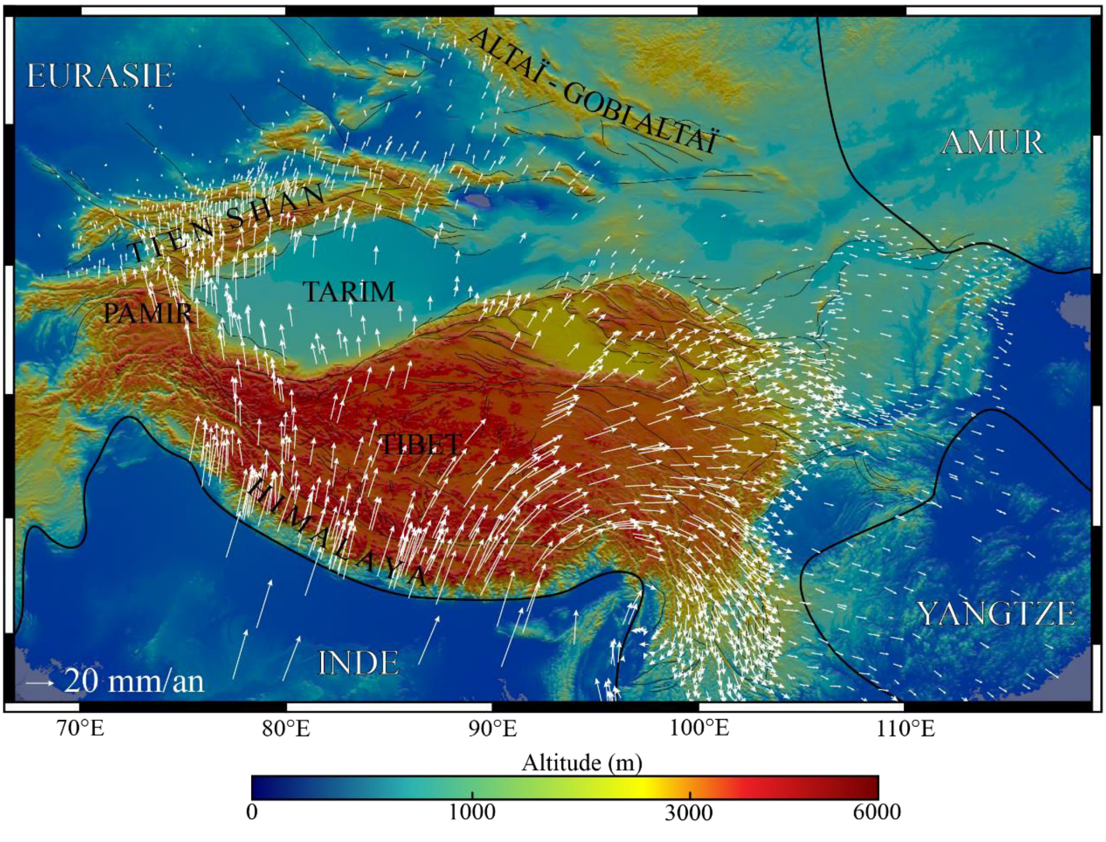

Figure 3 : Carte topographique de l'Asie Centrale. Les flèches blanches indiquent les vitesses GPS en mm/an par rapport à l'Eurasie fixe (Wang et al., 2016). Les traits noirs épais indiquent les limites de plaques (Bird, 2003). Les traits noirs fin indiquent les structures actives majeures (Vergnolle et al., 2007)

Les divers processus moteurs de la déformation étant relativement bien identifiés (e.g. Avouac et al., 1993; England and Molnar, 2005, 1997; Tapponnier et al., 1986; Vergnolle et al., 2007), il reste à comprendre pourquoi et comment la déformation se localise dans certaines zones comme le Tien Shan alors que d'autres comme le bassin du Tarim restent très peu déformées.

Un premier élément de réponse réside dans la pré-structuration du continent asiatique qui s'étend du Protérozoïque à l'actuel (e.g. Kröner et al., 2014; Şengör et al., 1993; Wilhem et al., 2012), période au cours de laquelle de nombreux blocs continentaux entrent en collision formant un gigantesque ensemble : le continent asiatique tel que nous le connaissons aujourd'hui. Cet ensemble est donc parsemé de zones de sutures, témoins des collisions passées entre deux masses continentales, de structures tectoniques : failles et zones de cisaillements, de lithologies variées et bien évidemment d'une histoire thermique de la lithosphère contrastée selon l'âge des précédents évènements tectoniques. Autant de paramètres qui vont contribuer à l'hétérogénéité de la lithosphère continentale introduisant en son sein des zones « faibles » et des zones « résistantes » qui joueront un rôle sur la localisation de la déformation, rôle que nous allons tenter de définir à travers cette thèse.

Le but de cette thèse est donc d'apporter des éléments de réponses à la compréhension de la localisation de la déformation de la lithosphère continentale. Ce mémoire s'articule en quatre grands chapitres clôturés par une discussion à l'échelle du Tien Shan et de l'Asie Centrale. La chaîne du Tien Shan représente en effet un parfait exemple de ce type de déformation intra-plaque long-terme de la lithosphère continentale. Bien que plus diffuse et moins intense qu'au front Himalayen, la déformation Cénozoïque a permis d'ériger cette chaîne de montagnes qui n'a pas à pâlir face à ses voisines avec une topographie atteignant jusqu'à 7 km d'altitude et un raccourcissement total d'environ 150 à 200 km.

Tout d'abord le contexte géologique et géodynamique dans lequel la chaîne du Tien Shan est formée est détaillé du Paléozoïque à l'actuel. Ensuite, le second chapitre se focalise sur l'étude de la déformation paléozoïque dans la partie kirghize du Tien Shan et les grandes structures qui lui sont associées dans le but d'intégrer et d'utiliser ces données comme contraintes pour les modèles thermomécaniques présentés dans les chapitres trois et quatre. Le troisième chapitre se concentre sur l'influence de la géométrie et de la rhéologie des zones hérités et de la lithosphère continentale alors que le quatrième chapitre se concentre sur la modélisation de l'exhumation basse température dans le Tien Shan. L'influence de la déformation et de l'érosion sur l'exhumation basse température y est abordée ainsi que l'importance des flux sédimentaires et du système de drainage sur la formation des bassins dans une chaîne intra-plaque.

I. Contexte géologique de la chaîne du Tien Shan

1. Tectonique paléozoïque

La chaîne du Tien Shan s'étend sur plus de 2000 km de l'Ouzbékistan au Nord-ouest de la Chine. Cependant, le Tien Shan s'inclut dans un domaine orogénique bien plus large appelé « Ceinture Orogénique d'Asie Centrale » ou encore « *Central Asian Orogenic Belt* » (CAOB) qui contribue, du Néo-protérozoïque (1 Ga) au Permien (250 Ma), à la construction du continent nord asiatique par le biais de l'accrétion de nombreux blocs continentaux et arcs volcaniques (Figure I-1) (e.g. Kröner et al., 2014; Şengör et al., 1993; Wilhem et al., 2012).

La CAOB représente la plus grande chaîne d'accrétion à travers le monde couvrant une étendue supérieure à 9 millions de kilomètres carrés depuis l'Oural à l'ouest, jusqu'au Pacifique à l'est, et de la bordure sud du craton sibérien au nord jusqu'à la suture Solonker au nord de Beijing (Pékin) se prolongeant ensuite le long de la suture Sud Tien Shan en Chine, au Kirghizstan, et en Ouzbékistan pour finalement rejoindre l'Oural (Figure I-1).

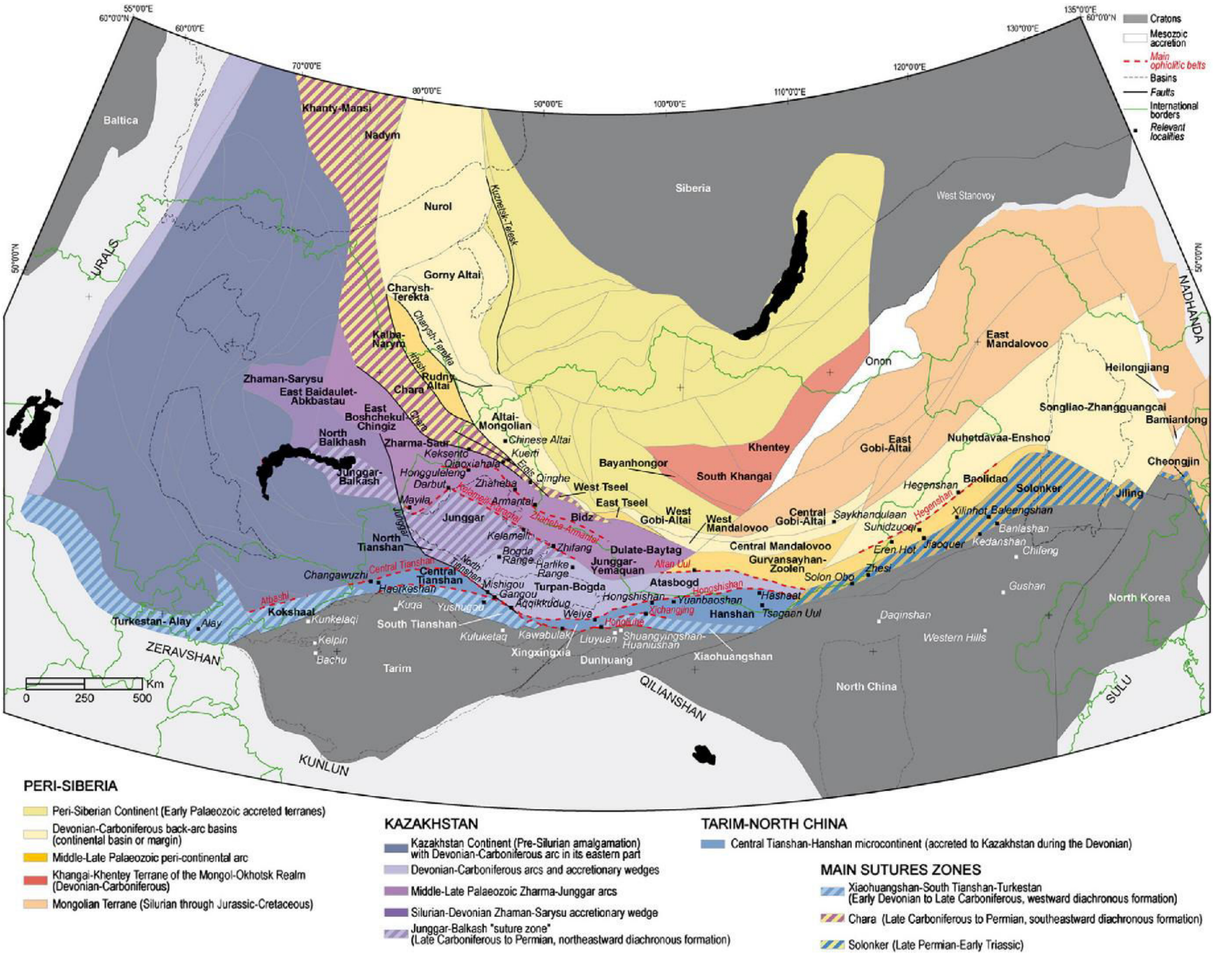

Figure I-1 : Carte des domaines principaux impliqués dans la formation de la CAOB au Paléozoïque supérieur (Wilhem et al., 2012)

La construction de cette chaîne s’effectue au détriment de paléo-domaines océaniques se refermant du Paléozoïque au Mésozoïque. Au début du Paléozoïque, trois domaines représentent les principaux continents impliqués dans l’histoire de la CAOB : le continent Siberia, le continent Baltica et le continent Gondwana (Figure I-2) (e.g. Wilhem et al., 2012). Ceux-ci sont séparés par des domaines océaniques :

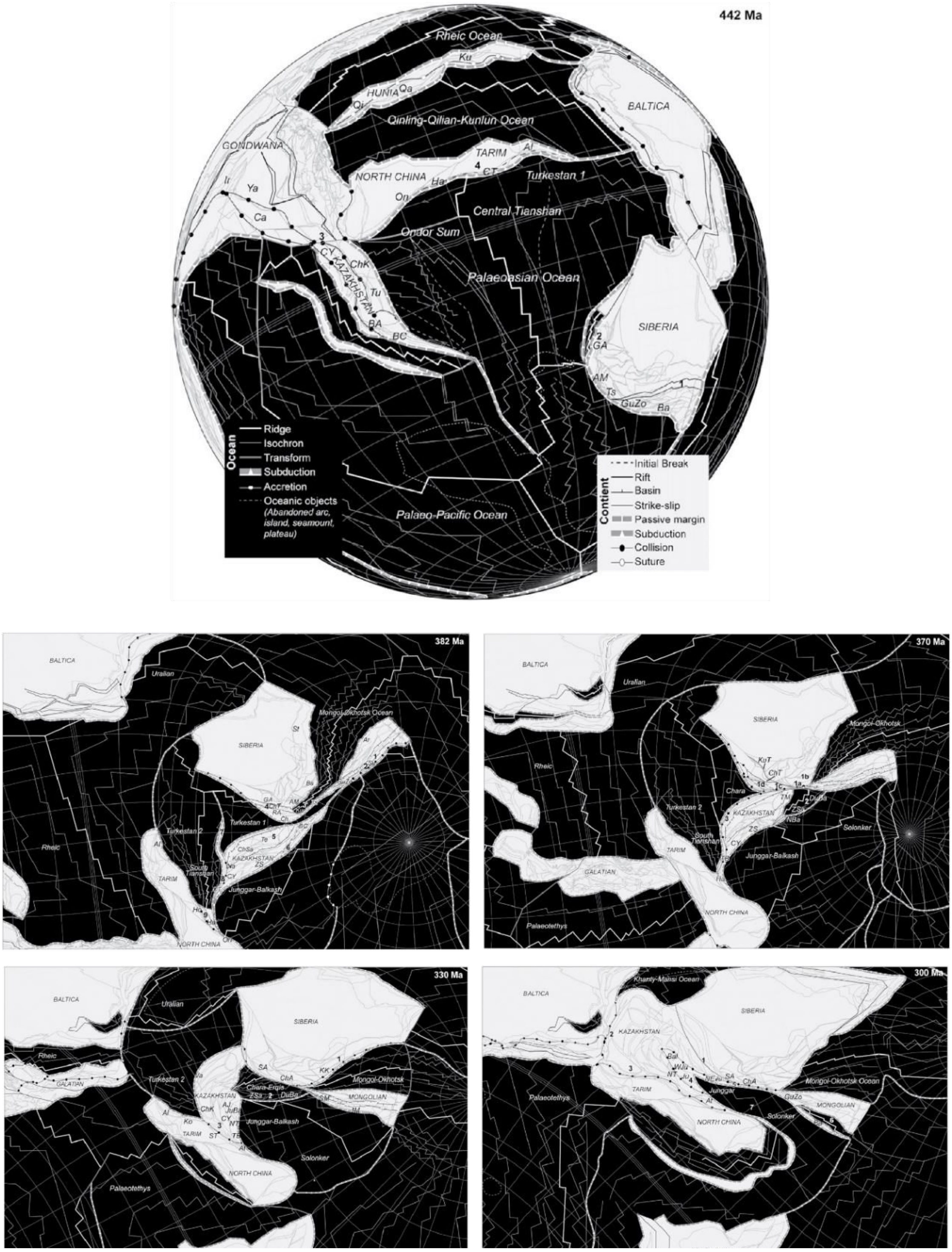

Figure I-2 : Reconstruction des mouvements des plaques tectoniques qui constituent aujourd’hui la CAOB du Silurien au Carbonifère supérieur (Wilhem et al., 2012)

- Le domaine ouralien sépare Siberia et Baltica
- L'Océan Rhéique sépare Baltica et Gondwana
- L'Océan Paléo-asiatique sépare Siberia et Gondwana

Tout au long du Paléozoïque, des blocs continentaux sont détachés du continent Gondwana donnant naissance à de nombreux domaines océaniques qui vont participer lors de leur fermeture aux différentes phases de collisions et d'accrétions qui érigent la CAOB. Le but ici n'est pas de décrire dans le détail l'histoire de cette chaîne mais de donner un aperçu du contexte général dans lequel la chaîne du Tien Shan se situe.

La CAOB est constituée par trois domaines qui résultent des collisions et accrétions de blocs continentaux et d'arc volcaniques séparés par des zones de sutures (Figure I-1). Le domaine Péri-sibérien composé à l'ouest d'arcs volcaniques et de blocs continentaux accrétés au craton sibérien au début du Paléozoïque, ainsi que d'un domaine arrière-arc suivi d'un arc d'âge Dévono-Carbonifère. En revanche à l'est le domaine Péri-sibérien est représenté par l'ancien domaine océanique du Mongol-Okhotsk bordé de part et d'autre par les différents blocs qui constituent la Mongolie et qui se sont accrétés au craton sibérien au cours du Paléozoïque puis du Mésozoïque lors de la fermeture de l'Océan Mongol-Okhotsk. La limite sud-est de cette zone est représentée par la présence d'une grande zone de suture, la suture Solonker (Figure I-1), qui marque la collision au Permo-Trias entre le bloc de Chine du Nord et les terrains mongols.

Le domaine Kazakh (Figure I-1) représente la partie occidentale de la CAOB. Il s'étend de l'Oural à l'ouest jusqu'au domaine Péri-sibérien à l'est du quel il est séparé par la zone de suture de Chiara. La partie ouest est composée de bloc accrétés au cours du Silurien dont la zone nord du Tien Shan (Figure I-2). La partie à l'est de ce domaine est en revanche constituée de blocs accrétés entre le Dévonien et le Carbonifère supérieur et notamment le bloc du Junggar qui correspond à la limite nord du Tien Shan.

Enfin le domaine du Central et Sud Tien Shan constitué d'un bloc continental et d'un arc volcanique mais surtout d'une zone de suture importante qui marque la terminaison sud de la CAOB avec la collision du Tarim au Carbonifère supérieur-Permien inférieur (Figure I-1).

La chaîne du Tien Shan représente donc la partie située actuellement la plus au Sud de la CAOB. Elle est orientée Nord-Est-Sud-Ouest entre les blocs Junggar-Balkash au Nord et le bassin du Tarim au Sud.

1.1.Structure générale du Tien Shan

Au Kirghizstan, le Tien Shan est caractérisé par trois domaines tectoniques : le « *North Tien Shan* » (NTS), le « *Middle Tien Shan* » (MTS) et le « *South Tien Shan* » (STS) séparés par deux zones de sutures (Figure I-3). Le NTS et le MTS sont situés de chaque côté d'une zone de suture d'âge Ordovicien orientée Est-Ouest : la « *Nikolaev Line* » (NL, Nikolaev, 1933), connue pour avoir fonctionné comme une faille décrochante majeure au cours du Permien (e.g. Mikolaichuk et al., 1997; Windley et al., 2007). Le MTS et le STS sont séparés par une zone de suture connue sous le nom de At-Bashi-Kokshaal, et qui s'étend du Kirghizstan au Nord-ouest de la Chine selon une orientation actuelle globalement Est-Ouest (Figure I-3) (e.g. Burtman, 2008; Glorie et al., 2011; Simonov et al., 2008).

Vers l'est, le bloc du MTS devient progressivement plus étroit et disparaît finalement aux abords de la frontière entre la Chine et le Kirghizstan. En Chine, des unités tectoniques différentes de celle présentes au Kirghizstan sont décrites et par conséquent une nomenclature différente est utilisée. Le TS chinois est donc composé, du Nord vers le Sud, du bassin du Junggar, du bloc Yili-NTS, du « *Central* » TS et du STS (Figure I-3) (e.g. Gao et al., 1998).

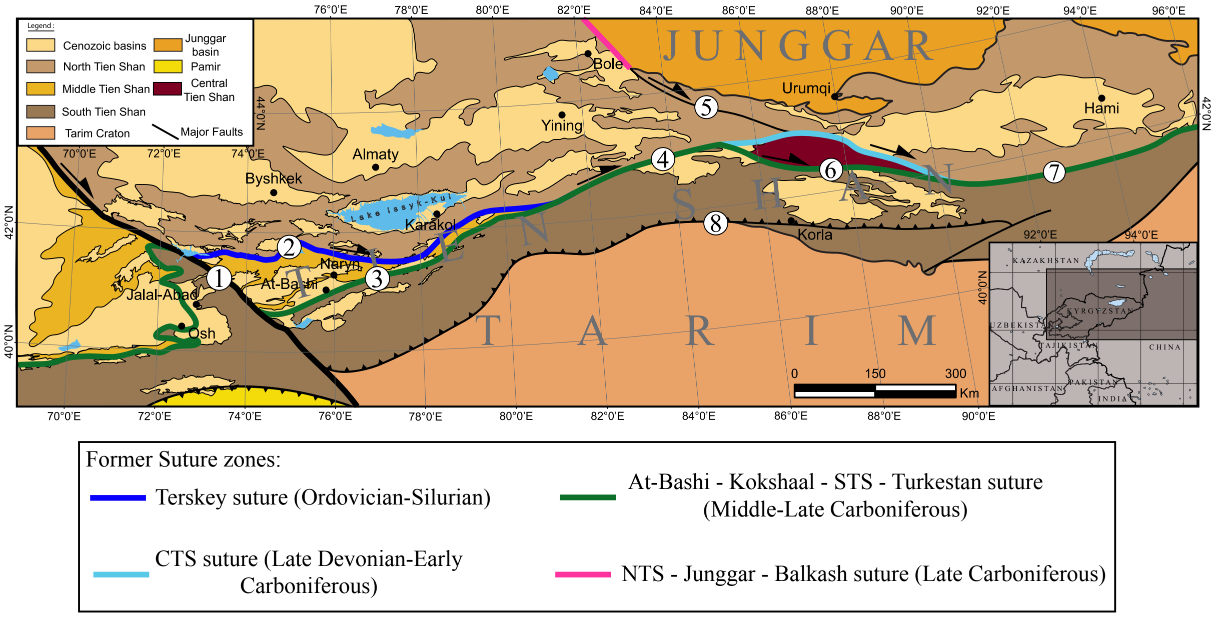

Figure I-3 : Schéma structural du Tien Shan. Les traits de couleurs représentent les différentes zones de sutures paléozoïques du Tien Shan. Les principales failles actives sont 1 : Faille de Talas Ferghana, 2 : Nikolaev Line, 3 : Faille d'At-Bashi-Inylshek, 4 : Faille de Narat, 5 :Faille du Nord Tien Shan, 6 :Faille de Baluntai, 7 : « Main Tien Shan Shear Zone », 8 : Faille Nord Tarim.

La suture At-Bashi Kokshaal marque, en Chine, la jonction entre le Yili-NTS et les blocs CTS et STS. La plupart des zones de sutures rejouent au Permien dans un régime décrochant, en particulier la NL qui se prolonge en Chine le long de la suture entre le NTS et le CTS (Faille de Naralt).

1.1.1. North Tien Shan

Le NTS est principalement composé d'intrusions plutoniques d'affinité calco-alcaline (Figure I-4) marquant la présence d'une marge active (Bakirov and Maksumova, 2001). Cependant la répartition des âges des plutons met en lumière deux phases magmatiques liées au fonctionnement de deux subductions différentes :

- La première phase, d'âge Ordovicien, est reliée à la subduction de l'Océan Terskey vers le Nord. Au Kirghizstan, la fermeture de cet océan plongeant sous le NTS entraîne l'accrétion du MTS et du NTS. En Chine, les marqueurs de cette subduction sont constitués par un arc magmatique à l'intérieur du bloc Yili-NTS (Bakirov and Maksumova, 2001; Glorie et al., 2010; Konopelko et al., 2008; Kröner et al., 2014, 2012a; Wang et al., 2007a).

- La seconde phase magmatique, d'âge Carbonifère, ne se retrouve qu'en Chine et résulte de la fermeture du domaine océanique NTS-Junggar-Balkash, situé entre le bloc du Junggar et le NTS, plongeant sous le NTS (Charvet et al., 2011; Wang et al., 2009, 2008, 2007b; Zhu et al., 2005).

La couverture sédimentaire du NTS est représentée par :

1- Des flyschs ordoviciens composés de tuffs volcaniques, de grès et d'argiles.
2- Des sédiments détritiques carbonifères composés de grès et d'argiles contenant des lentilles de gypse caractérisant un environnement de dépôt sous une faible tranche d'eau (Mikolaichuk et al., 1997).

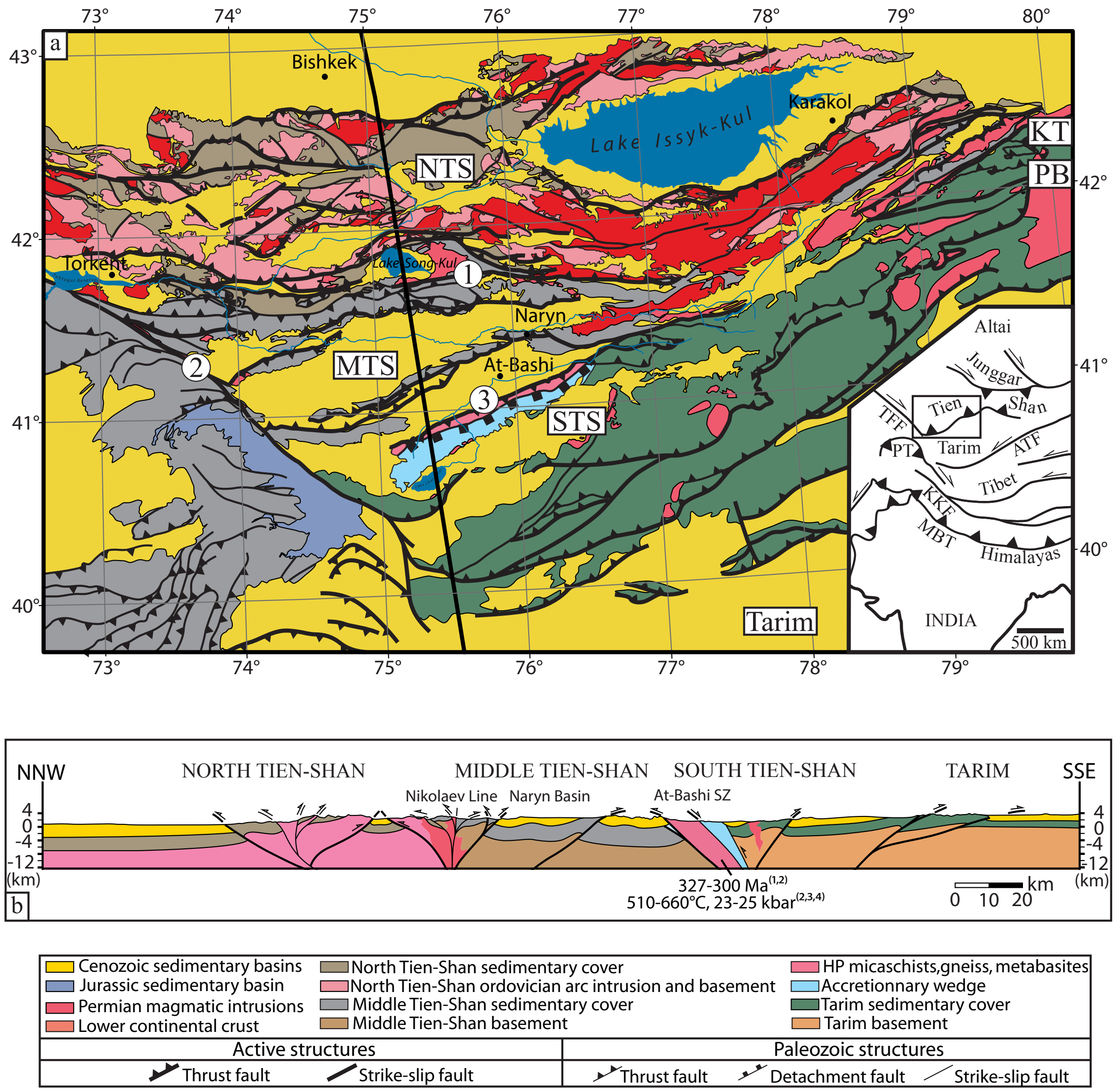

Figure I-4 : Carte géologique du Tien Shan (modifiée d'après Jukov et al., 2008). Le trait noir épais indique la localisation de la coupe. NTS : North Tien Shan. MTS: Middle Tien Shan. STS: South Tien Shan. KT: Khan Tengri. PB: Pobeda. 1: Nikolaev Line, 2: Faille de Talas Ferghana, 3: Zone de suture d'At-Bashi.

1.1.2. Middle Tien Shan

Le MTS est un domaine continental composé d'un socle Protérozoïque dont les datations (U/Pb sur zircon) ont donnés des âges compris entre 2.3 Ga et 1.7 Ga (Glorie et al., 2011; Keselev et al., 1982; Kiselev et al., 1993; Kröner et al., 2012a). La couverture sédimentaire reposant directement sur le socle est caractérisée par des tillites et des diamectites du Néo-protérozoïque. La couverture Paléozoïque représente une épaisseur d'environ 5 km caractérisée par des dépôts marno-calcaires du Cambrien au Carbonifère. Un hiatus régional est observé entre l'Ordovicien supérieur (450 Ma) et le Dévonien moyen (380 Ma). Les calcaires carbonifères de cette couverture représentent des séquences de plateforme carbonatée (Jukov et al., 2008; Karpovitch et al., 1964; Mikolaichuk et al., 1997). Une discordance angulaire est également observée entre le Carbonifère inférieur et supérieur (Osmonbetov et al., 1982).

1.1.3. South Tien Shan et Central Tien Shan

Le STS représente la partie la plus au Sud de la chaîne du Tien Shan mais également de la CAOB. En Chine, le STS est séparé du NTS par la suture d'At-Bashi-Kokshaal prolongée par la faille de Naralt (Figure I-3). Le CTS est actuellement séparé du STS par une faille décrochante récente (la Faille de Baluntai).

Le STS est caractérisé par un système de nappes et des roches de haute pression (HP)-basse température (BT) (e.g.Alekseev et al., 2009; Gao and Klemd, 2003; Klemd et al., 2014; Loury et al., 2015a; Su et al., 2010) alors que le CTS est interprété comme un arc magmatique continental Siluro-Dévonien (Charvet et al., 2011; Gao et al., 2009; Liu et al., 2014; Wang et al., 2011; Xiao et al., 2013).

En Chine, la zone de suture d'At-Bashi-Kokshaal séparant le South/Central TS et le NTS est composée d'unités métamorphiques dont les estimations pression-température (P-T) sont de l'ordre de 28-30 kbar et 520-540°C pour le pic de pression, et 22-27 kbar et 540-590°C pour le pic de température (Tian and Wei, 2013). L'âge du pic de pression est estimé entre 319 Ma et 308 Ma à partir de la méthode U-Pb sur zircon et rutile (Q. L. Li et al., 2011; Liu et al., 2014; Su et al., 2010; Zhang et al., 2009).

Au Kirghizstan, cette zone de suture sépare le STS et le MTS (Figure I-4). Elle est caractérisée par un assemblage tectonique d'unités métamorphiques chevauchant vers le Nord (Alekseev et al., 2007; Biske, 1996; Biske et al., 1985; Loury et al., 2015a). Nous les décrivons du bas vers le haut dans leur position structurale actuelle :

- En certains endroits, une écaille de socle continental métamorphique affleure à la base. Il est constitué de granitoïdes et de gneiss possédant une forte empreinte schiste vert (Loury et al., 2015a) et est interprété comme étant une partie du socle du MTS (Alekseev et al., 2009).

- Une ophiolite non métamorphique démembrée a été observée dans la région d'At-Bashi le long de la suture (Alekseev et al., 2009). Elle est représentée par une association de serpentinites, gabbros et radiolarites.
- Une unité de micaschistes et de gneiss à grenat, phengite et quartz ayant subi un métamorphisme de haute pression basse température (19-25 kbar et 500-550°C, Hegner et al., 2010; Loury et al., 2015a; Simonov et al., 2008; Tagiri et al., 1995). Cette unité est parfois surmontée par une unité métasédimentaire contenant des boudins d'éclogites basiques ayant subi des conditions P-T similaires. Des datations Ar^{40}/Ar^{39} ont permis d'estimer l'exhumation de cette unité continentale entre 328 Ma et 319 Ma (Hegner et al., 2010; Loury, 2016).
- Un prisme d'accrétion composé de calcschistes et de grès du Silurien au Carbonifère ainsi que de boudins de roche basiques. Ces lithologies ont enduré des conditions métamorphiques de l'ordre de 10-12 kbar et 300-350°C (Loury et al., 2015a) dans le faciès des schistes bleus et ont été rétromorphosées dans le faciès des schistes verts.
- Une épaisse formation de marbres dont l'âge du protolithe est interprété entre le Silurien et le Dévonien est généralement observée au sommet du prisme d'accrétion (Burtman, 2008; Karpovitch et al., 1964).
- Enfin, un conglomérat du Carbonifère supérieur-Permien inférieur repose sur les unités précédentes (Baslakunov et al., 2007). Celui-ci est composé de galets d'éclogites et de serpentinites.

1.2.*Modèles d'accrétion du Tien Shan*

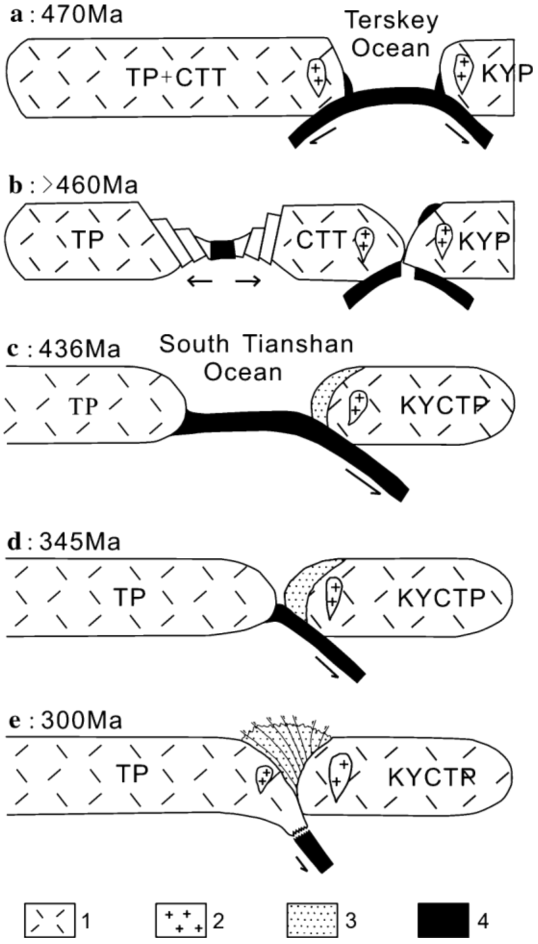

Figure I-5 : Modèle conceptuel de l'Ordovicien au Carbonifère supérieur de la formation du Tien Shan (Gao et al., 2009) TP :Tarim plate, CTT : Central Tien Terrane, KYCTP : Kazakhstan-Yili-Central Tien Shan plate

Plusieurs modèles ont été proposés pour interpréter et reconstituer l'histoire géologique et tectonique du Tien Shan. Cependant, malgré le nombre de modèles disponibles dans la littérature, la question du nombre et de la polarité des subductions ayant conduit à la formation de la chaîne au Paléozoïque reste débattue.

Au Kirghizstan, la plupart des études s'accordent sur la présence d'une subduction, dirigée vers le Nord, de l'Océan Terskey sous le NTS au cours de l'Ordovicien et responsable du magmatisme calco-alcalin (Bakirov and Maksumova, 2001; Glorie et al., 2010; Kröner et al., 2013, 2012a). La fermeture de ce domaine océanique semble se terminer avec l'accrétion du MTS au NTS (Lomize et al., 1997; Mikolaichuk et al., 1997). En Chine, ce magmatisme paléozoïque inférieur se retrouve le long de la bordure Sud du bloc Yili qui est considéré comme une partie du NTS (B. Wang et al., 2010; Wang et al., 2011).

Certains auteurs considèrent que la subduction vers le Nord de l'Océan Terskey s'effectue simultanément avec une subduction vers le Sud du même domaine océanique sous le bloc du Tarim (Figure I-5) (Bazhenov et al., 2003; Gao et al., 2009; Lomize et al., 1997). Cette seconde subduction entraînerait un amincissement crustal du Tarim et l'ouverture d'un bassin océanique d'arrière arc, l'Océan Sud Tien Shan. La taille de ce domaine arrière arc reste débattue, certains auteurs proposent un grand domaine océanique continu (e.g. Gao et al., 2009) alors que d'autres (Wang et al., 2016) proposent la possibilité de plusieurs petits bassins plutôt qu'un domaine océanique à proprement parler. Quoi qu'il en soit, le bloc détaché du Tarim est interprété comme étant le CTS caractérisé par la présence d'un arc magmatique d'âge Siluro-Dévonien lié à la subduction de l'Océan Terskey vers le sud (Lin et al., 2009; Wang et al., 2011, 2008). Le CTS serait donc originaire du Tarim avant de s'en détacher suite à régime extensif en domaine arrière-arc. Cette hypothèse semble être validée par plusieurs arguments structuraux et magmatiques (Charvet et al., 2011, 2007, Dong et al., 2011, 2006, 2005; Guo et al., 2002; Laurent-Charvet, 2001; Ma et al., 1993; Zhong et al., 2014).

La fermeture de l’Océan STS au Sud du CTS est en revanche sujette à d’âpres débats. En effet, certains auteurs (Chen et al., 1999; Gao et al., 2009; Liu et al., 2014; Xiao et al., 2013) considèrent que ce domaine océanique se referme à la faveur d’une subduction vers le Nord sous le NTS et le CTS, entrés en collision suite à la fermeture de l’Océan Terskey (Figure I-5). Cette hypothèse se base sur l’observation d’une succession du Nord vers le Sud, d’un arc magmatique (CTS), d’une zone d’accrétion (STS) et d’unités de marge passive sur la bordure Nord du Tarim. D’autres auteurs (Charvet et al., 2011, 2007, Ge et al., 2014, 2012; Lei et al., 2011; Lin et al., 2013; Loury et al., 2015a; Wang et al., 2007a) suggèrent quant à eux une subduction vers le Sud du domaine océanique du Sud Tien Shan sous le Tarim basé sur plusieurs évidences de déformations asymétriques vers le Nord au sein du complexe d’accrétion du STS (Figure I-6). Quel que soit le modèle proposé, la majeure partie des auteurs s’accordent à dire

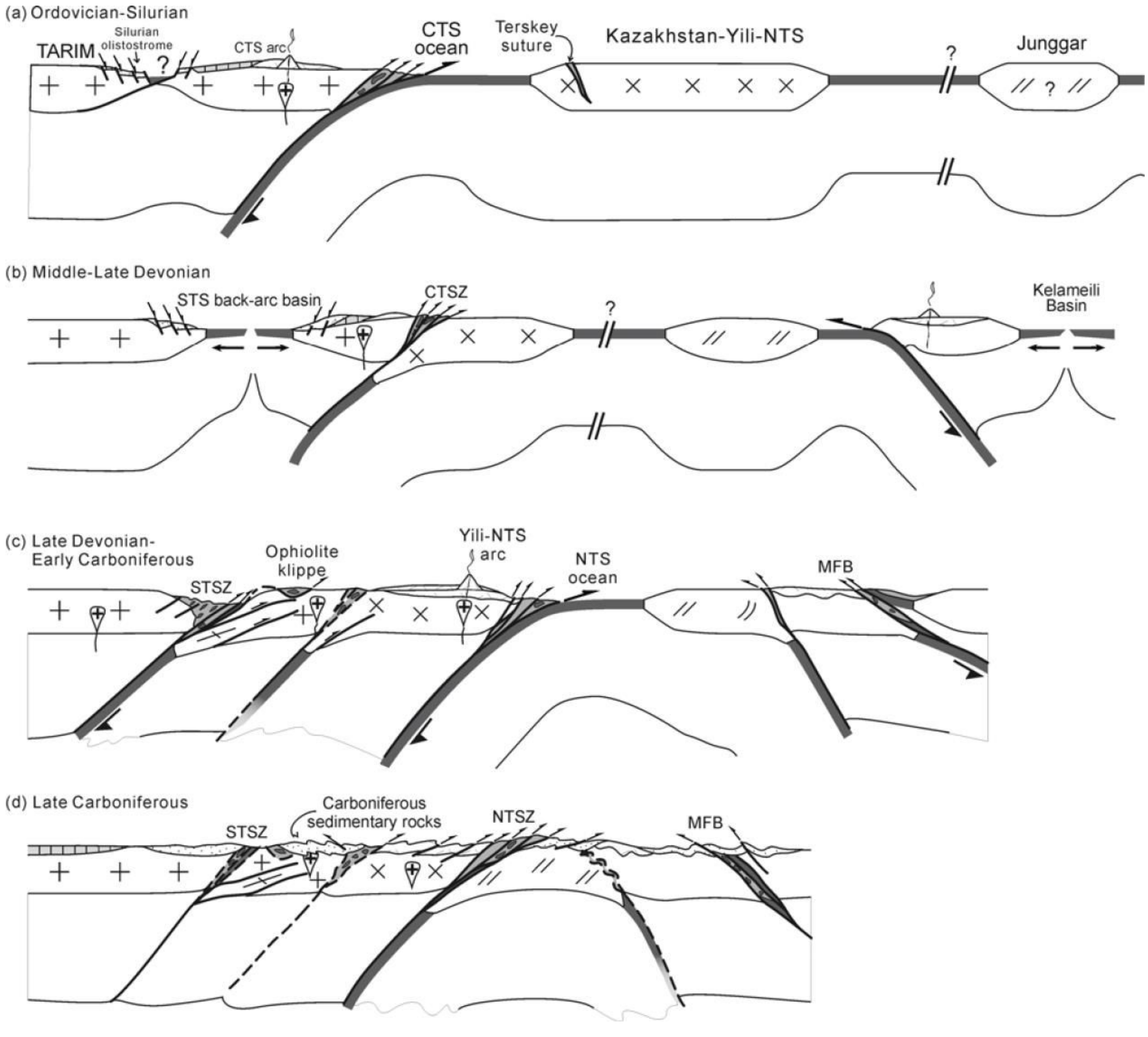

Figure I-6 : Modèle conceptuel de l’évolution tectonique du Tien Shan et du bloc du Junggar de l’Ordovicien au Carbonifère supérieur (Charvet et al., 2011). CTS : Central Tien Shan, NTS : North Tien Shan, CTSZ : Central Tien Shan Suture Zone, NTSZ : North Tien Shan Suture Zone, STSZ : South Tien Shan Suture Zone, MFB : Mongolian Fold Belt que le domaine océanique du STS est complètement refermé autour de 340 Ma en Chine et 320 Ma au Kirghizstan.

Finalement, en Chine, une dernière phase de collision paléozoïque se déroule au Nord du NTS entre le Junggar et les blocs précédemment assemblés du CTS/NTS et Tarim à la suite de la fermeture de l'Océan du NTS-Junggar-Balkash responsable du magmatisme calco-alcalin d'âge Carbonifère retrouvé dans le NTS chinois (Allen et al., 1993; Charvet et al., 2011; Chen et al., 1999; Gao et al., 2009, 1998; Qian et al., 2009; Wang et al., 2009; Windley et al., 1990; Xiao et al., 2004).

1.3.Evolution post-orogénique du Tien Shan

1.3.1. Tectonique décrochante

Suite au dernier évènement collisionel entre le TS et le Tarim un changement s'effectue dans le régime de déformation passant de compressif à décrochant entre le Carbonifère supérieur et le Permien. Cette tectonique décrochante entraîne la formation et le jeu de failles d'orientation Nord-Ouest-Sud-Est et Est-Ouest dont certaines sont directement liées à la réactivation des zones de sutures présentées précédemment (Alekseev et al., 2007; Konopelko et al., 2013; Mikolaichuk et al., 1997; Rolland et al., 2013; Wang et al., 2007a). La Faille de Talas-Ferghana (TFF) est un exemple de grande structure résultant de ce régime décrochant. En effet l'activité la plus ancienne ayant pu être datée sur la TFF par la méthode Ar^{40}/Ar^{39} montre une initiation à 312 ± 4 Ma alors que la phase principale correspondant aux grands déplacements le long de la faille se situerai au minimum entre 290 Ma et 260 Ma (Rolland et al., 2013).

Le Mésozoïque en revanche est marqué par une forte chute de l'activité tectonique dans la chaîne du Tien Shan. En effet, une longue période d'érosion est soulignée par la présence d'une surface pénéplanée sur laquelle se déposeront plus tard les sédiments cénozoïques (Abdrakhmatov et al., 2001; Jolivet et al., 2013, 2010; Macaulay et al., 2014). Des dépôts de gypse Jurassique de faible épaisseur se retrouvent épisodiquement à l'intérieur de la chaîne. Cependant, un large bassin Jurassique se forme le long de la TFF, lié à une activité tectonique modérée de la faille au cours du Trias supérieur-Jurassique inférieur. Cette phase est bien contrainte dans le temps grâce à la présence du bassin sédimentaire mais également à la datation de filon de pegmatites syn-cinématiques (195 ± 3 Ma avec la méthode Ar^{40}/Ar^{39} sur muscovite; Rolland et al., 2013).

1.3.2. Evénement magmatique et haute température

Au cours du Permien, un évènement magmatique alcalin de grande ampleur affecte toute la chaîne du Tien Shan. Celui-ci est caractérisé par de nombreuses intrusions granitiques recoupant les structures paléozoïques liées aux phases orogéniques présentées précédemment (Alekseev et al., 2009; Biske et al., 2013; Chen et al., 2009; Seltmann et al., 2011; Wang et al., 2009). Cette phase magmatique a mené à plusieurs interprétations quant à son origine et les processus de sa mise en place.

Certains auteurs favorisent l'activité d'un panache mantellique (Wei et al., 2014; Xu et al., 2014; Yang et al., 2013) en se basant sur la présence à travers une grande partie de l'Asie de provinces magmatiques d'âge Permien telles que la province magmatique du Tarim (280-290 Ma, e.g. Xu et al., 2014), les trapps d'Emeishan au Sud-ouest de la Chine (295 Ma, e.g. Ali et al., 2005 et références incluses) ou encore les trapps de Sibérie (248 Ma, e.g. Renne and Basu, 1991; Saunders et al., 2005).

D'autres auteurs attribuent le magmatisme du Tien Shan à une cause d'origine tectonique (Konopelko et al., 2009, 2007, Wang et al., 2014, 2009). En effet les plutons se mettent en place de manière quasi-systématique le long de failles décrochantes permiennes et ont une étendue plus faible que dans les grandes provinces magmatiques.

Enfin, un modèle intermédiaire propose que la source du magmatisme soit liée à l'activité d'un panache mantellique alors que les plutons se mettent en place le long des grandes structures crustales guidée par le régime de déformation décrochant.

Une étude récente (Loury, 2016), focalisée sur le massif granulitique du Pobeda montre qu'il existe une interaction entre les magmas d'origine mantellique (panache mantellique mélangé au manteau lithosphérique métasomatisé) et la croûte continentale (Loury, 2016). En effet, des niveaux de gneiss migmatitique sont mélangés à des niveaux de charnockites, où la mise en place de matériel mantellique provoque la fusion partielle de niveaux de croûte intermédiaire séparant la partie fondue (migmatites) du résidu de fusion (charnockite). Cet événement s'effectue dans des contions P-T estimées à 6 kbar et une température supérieure à 1000°C. Les datations du processus de fusion partielle par méthode U-Pb sur zircon et Ar^{40}/Ar^{39} sur amphibole révèlent potentiellement trois épisodes distincts à 287 Ma, 275 Ma et 265 Ma. Les datations Ar^{40}/Ar^{39} sur biotites permettent en revanche de dater le refroidissement et l'exhumation de cette unité de haute température entre 256 Ma et 265 Ma.

Cette dernière étude penche également pour un modèle dans lequel la source des magmas proviendrait d'un panache mantellique mélangé au manteau lithosphérique métasomatisé en interaction avec les zones dans lesquelles la déformation est localisée. Ainsi, les structures décrochantes du STS localisent les remontées magmatiques, et permettent l'exhumation d'unités de haute température et de plutons.

2. Tectonique Cénozoïque

La déformation cénozoïque du Tien Shan est à l'origine de la formation d'une chaîne intracontinentale qui se développe en réponse à la convergence Inde-Asie. Les données géodésiques montrent que le Tien Shan accommode actuellement entre 40% et 50% de cette convergence. En incluant le raccourcissement de la marge nord du bassin du Tarim cela représente 200 ± 50 km depuis 30 Ma maximum (Abdrakhmatov et al., 1996; Avouac et al., 1993; DeMets et al., 1994).

Cette phase de déformation aboutit au développement de cinq chaînons topographiques délimitant et séparant des bassins intra-montagneux dans lesquels se déposent les sédiments tertiaires. Les sédiments cénozoïques reposent sur une surface d'érosion mésozoïque (e.g. Jolivet et al., 2013). Une discordance angulaire à l'échelle régionale marque donc le début des dépôts sédimentaires du Tertiaire. Les études de thermo-chronologie basse température (traces de fissions sur apatite et zircon) montrent un soulèvement qui s'initie autour de 25 Ma mais la mise en place d'un relief significatif et le dépôt de sédiments dans les bassins intra-montagneux commencent réellement vers 11-12 Ma et s'accélèrent entre 3 Ma et 5 Ma (Figure I-7) (Abdrakhmatov et al., 2001; Bullen et al., 2001; Burbank et al., 1999a; De Grave et al., 2004; Macaulay et al., 2014, 2013; Sobel et al., 2006; Thompson et al., 2002).

L'activité tectonique récente est caractérisée par une tectonique de socle impliquant des failles raides, visibles entre les chaînons et les bassins (e.g. Goode et al., 2011; Macaulay et al., 2014; Thompson et al., 2002). En revanche, l'évolution de la déformation au sein des bassins est contrôlée par des chevauchements enracinés à faible profondeur, à l'interface entre les formations du Paléozoïque et du Cénozoïque qui peut agir comme un niveau de décollement (Goode et al., 2011; 2014).

(a) **Late Oligocene–early Miocene (~25–15 Ma)**

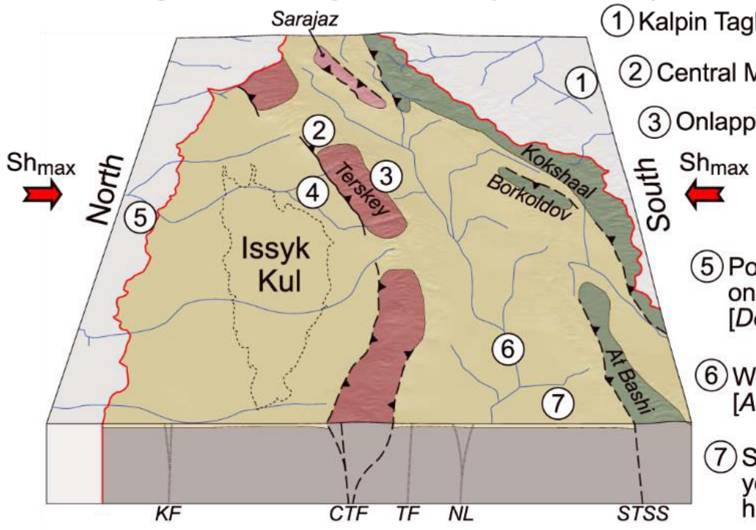

① Kalpin Tagh onset at 22-20 Ma [*Chang et al.*, 2012]

② Central MTF segment propagating eastward

③ Onlapping sediment

④ Low sedimentation rate (<0.1 km/Myr) for Shamsi unit in Issyk Kul [*Wack et al.*, 2012]

⑤ Possible Late Oligocene-Early Miocene onset for Zailiy Range – based on AFT data [*De Grave et al.*, 2013]

⑥ W-directed paleocurrent directions [*Abdrakhmatov et al.*, 2001]

⑦ Syn-tectonic sediments (Shamsi unit) younger in Naryn than Issyk Kul – highly time-transgressive deposition.

(b) **Mid–late Miocene (~15–5 Ma)**

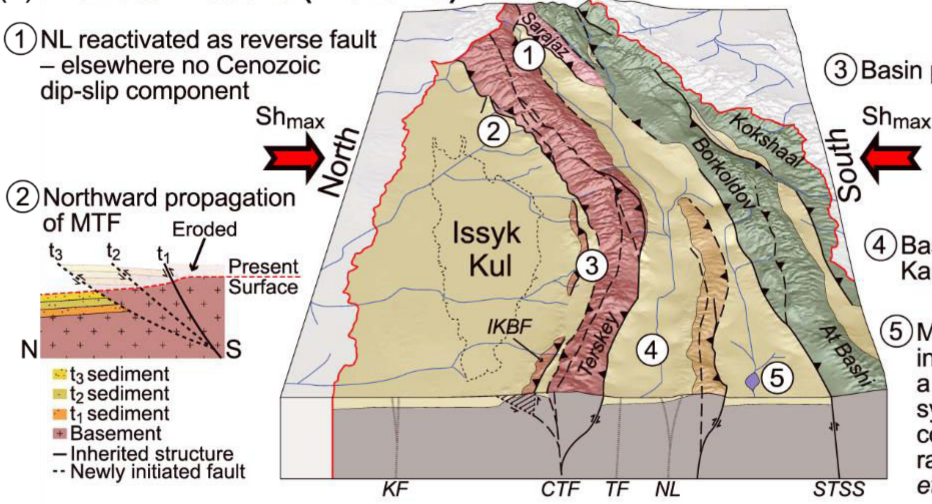

① NL reactivated as reverse fault – elsewhere no Cenozoic dip-slip component

② Northward propagation of MTF

③ Basin progressively overthrust

④ Basin later partitioned by Karakudjur Ranges

⑤ More lacustrine sediment in Chu, possibly indicating a less connected fluvial system after the construction of new ranges [*Abdrakhmatov et al.*, 2001].

(c) **~5 Ma to present**

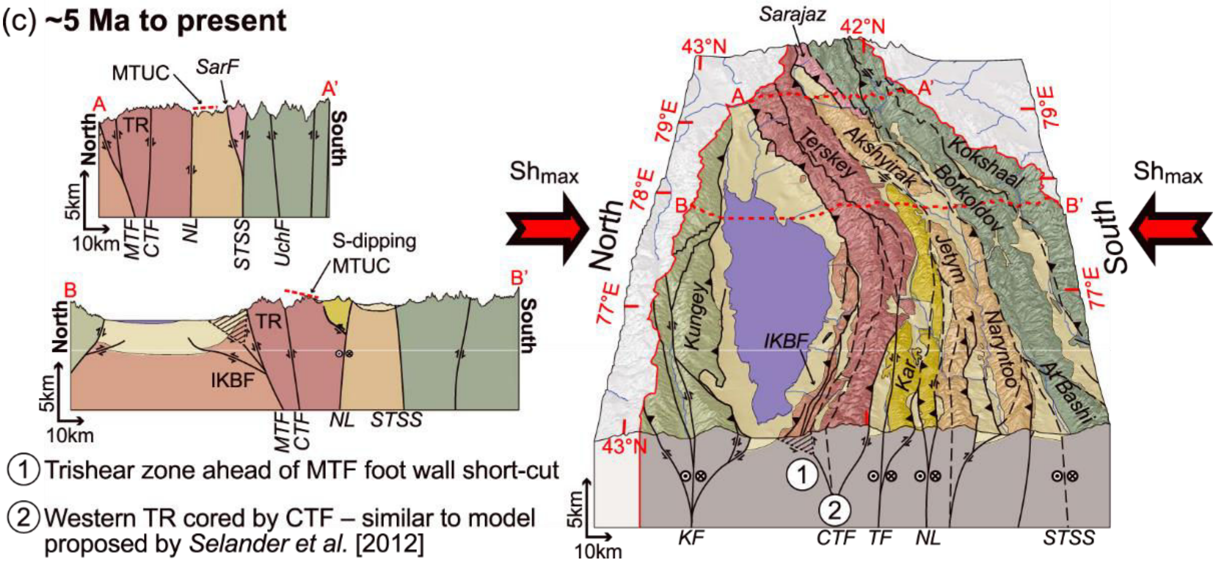

① Trishear zone ahead of MTF foot wall short-cut

② Western TR cored by CTF – similar to model proposed by *Selander et al.* [2012]

Figure I-7 : Modèle conceptuel de l'évolution de la déformation cénozoïque du Tien Shan (Macaulay et al., 2014). KF : Kungey Fault, MTF : Main Terskey Fault, CTF : Central Terskey Fault, TF : Tyulek Fault, NL: Nikolaev Line, STSS: South Tien Shan Suture.

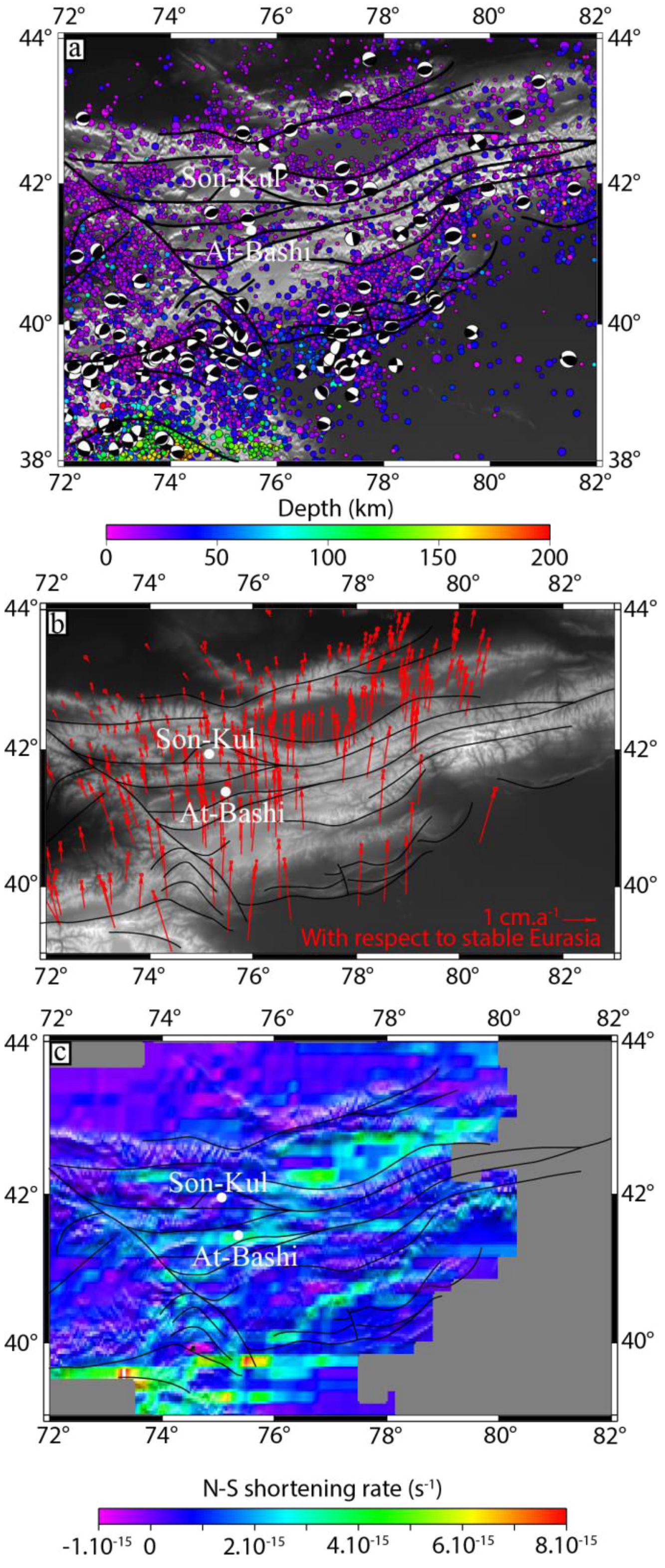

Figure I-8 : a) Carte de la sismicité (magnitude > 3) dans le Tien Shan d'après le catalogue EMCA (Mikhailova et al., 2015a, 2015b) b) Vitesses GPS dans le Tien Shan en référence à l'Eurasie stable (Zubovich et al., 2008) c) Taux de raccourcissement Nord-Sud calculé d'après les vitesses GPS

2.1. Déformation active

L'activité sismique dans le Tien Shan (Figure I-8a) est relativement importante avec de nombreux séismes de magnitudes entre 3 et 5 et certains événements beaucoup plus importants pouvant atteindre des magnitudes supérieures à 7. Les mécanismes au foyer de la base CMT (Centroid Moment Tensor, Ekström et al., 2012) montrent un régime de déformation dominé par des failles inverses. Certains mécanismes au foyer indiquent la présence de failles décrochantes le long de structures bien connues telles que la faille dextre de Talas Ferghana. La base de données EMCA (Earthquake Model of Central Asia, Mikhailova et al., 2015a, 2015b) montre que la majeure partie des séismes situés à l'Est de la TFF sont localisés à des profondeurs crustales entre la surface et 45-50 km. En revanche, à l'Ouest de la TFF certains séismes localisés à des profondeurs supérieures à 100 km correspondent à la zone d'indentation du Pamir. La faille de Talas Ferghana est considérée comme une structure lithosphérique majeure permettant le découplage de la déformation des régions situées de chaque côté de la faille (Bande et al., 2015).

Alors que certains séismes s'alignent le long de structures formées avant la tectonique cénozoïque, d'autres correspondent à des structures néoformées. L'activité sismique autour du lac Song-Kul et au Nord du massif d'At-Bashi est localisée le long de deux massifs majeurs correspondants aux anciennes zones de sutures entre le NTS et le MTS et entre le MTS et le STS. Cependant, sur la bordure Nord du Tarim, où les unités du Tien Shan chevauchent le bassin du Tarim, un grand nombre d'événements sismiques sont répartis selon un alignement Est-Ouest loin de la zone de suture d'At-Bashi-Kokshaal et suggèrent la présence d'une structure néoformée.

Les données GPS (Figure I-8b) montrent un déplacement vers le Nord du Tien Shan et du Tarim par rapport à l'Eurasie stable (Zubovich et al., 2010). Les vitesses de déplacements vers le Nord diminuent progressivement depuis le Sud vers le Nord indiquant un raccourcissement Nord-Sud important et actif à l'intérieur de la chaîne du Tien Shan. Nous avons ici calculé le raccourcissement Nord-Sud à partir des vitesses GPS sur une grille régulière de 10' avec une interpolation de proche en proche à l'aide de GMT (Figure I-8c) (General Mapping Tools, Wessel et al., 2013). En dépit des incertitudes relatives à la distribution disparate des stations GPS, les taux de raccourcissement varient entre 3.10^{-15} et 5.10^{-15} s^{-1}. A l'Est de la TFF, les taux de raccourcissement les plus importants se situent le long d'un alignement Nord-est-Sud-ouest correspondant à la bordure nord du Tarim actuellement chevauché par les unités du STS. Au Nord, le long de la NL et du lac Issyk-Kul, les taux de raccourcissement varient entre $2.5.10^{-15}$ et 5.10^{-15} s^{-1}.

A l'Ouest de la TFF, les taux de raccourcissement sont supérieurs au contact entre le Tien Shan et le Pamir où ils s'échelonnent entre 4.10^{-15} et 8.10^{-15} s^{-1}. Cette zone de déformation accommode la majeure partie du raccourcissement Nord-Sud étant donné que très peu de déformation est décelable plus au Nord. Les données GPS, de même que les données sismiques, montrent que la TFF représente une structure permettant le partitionnement de la déformation entre les compartiments Est et Ouest de la faille (Figure I-8).

2.2.Structure crustale du Tien Shan

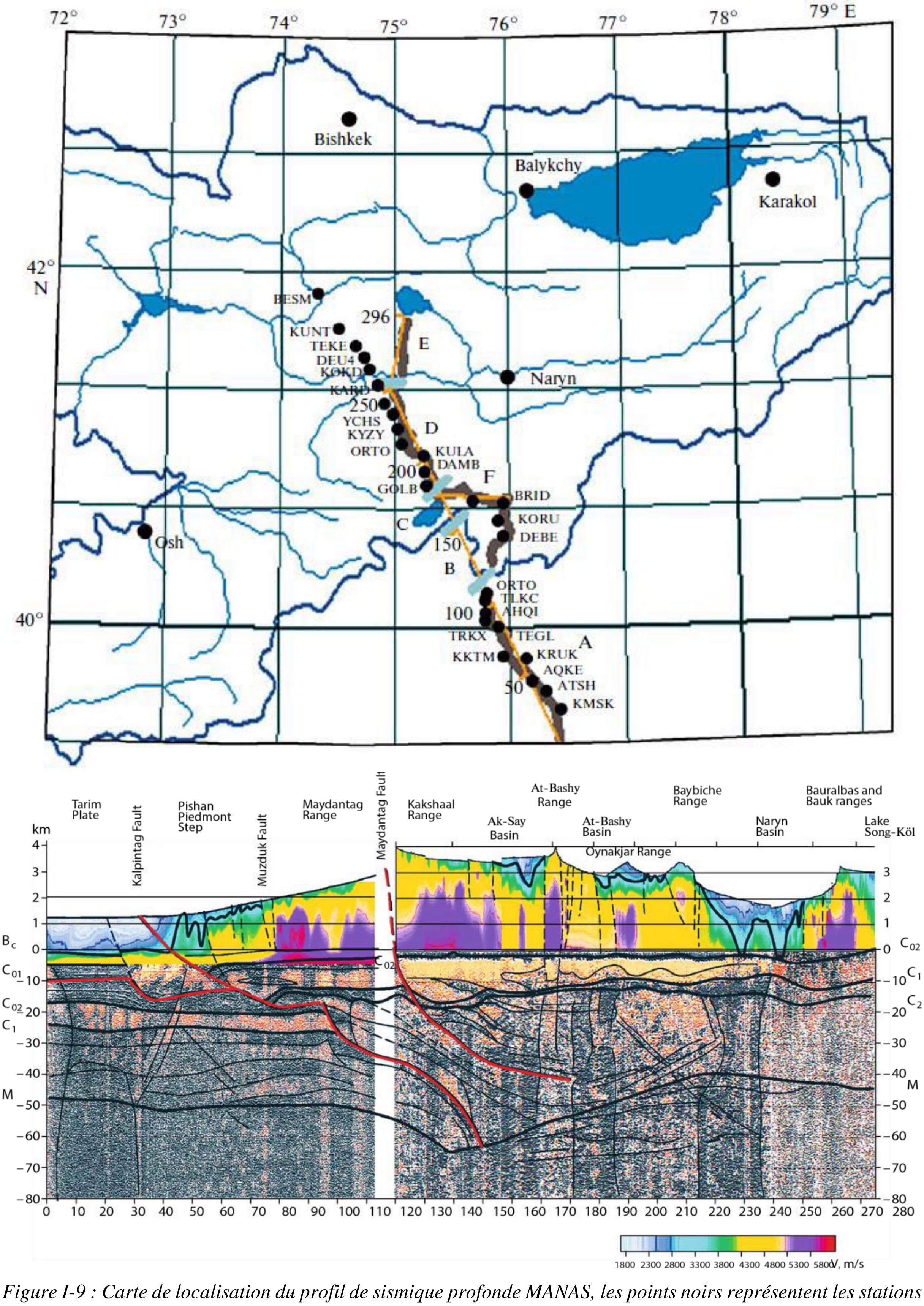

Figure I-9 : Carte de localisation du profil de sismique profonde MANAS, les points noirs représentent les stations sismiques et le trait gris les points de tirs. Sur le profil sismique, les couleurs indiquent la vitesse de propagation des ondes P dans la partie superficielle de la croûte. Les traits noirs indiquent les principaux réflecteurs. (Makarov et al., 2010)

Plusieurs études, notamment basées sur des données géophysiques ont tenté d'imager la structure crustale du Tien Shan. Les travaux les plus importants ayant permis d'imager les structures les plus profondes de la chaîne au Kirghizstan sont issues du profil de sismique profonde MANAS (Makarov et al., 2010) qui s'étend du lac Song-Kul au bassin du Tarim (Figure I-9).

Cette expérience de sismique a livré deux résultats majeurs. Premièrement, une image bien contrainte du Moho a pu être établie, montrant une croûte dont l'épaisseur est comprise entre 40 km et 45 km sous les zones les plus basses topographiquement (NTS, bordure Nord du Tarim) et qui s'épaissit sous le STS pour atteindre plus de 60 km. Deuxièmement, la flexure du Tarim sous le Tien Shan ainsi que la présence d'une structure à pendage Nord délimitant la croûte du Tarim de celle du Tien Shan montrent qu'actuellement le Tarim est sous-charrié vers le Nord sous le TS. Une seconde étude basée sur la méthode des fonctions récepteurs a été réalisée en 2004, et propose également une géométrie de Moho (Vinnik et al., 2004). Celle-ci montre une racine crustale d'une épaisseur supérieure à 60 km entre le MTS et le NTS mais, à l'inverse du Moho proposé par Makarov et al. (2010), il n'y aurait pas d'épaississement crustal sous le STS (Figure I-10). Cependant, d'après les auteurs, la station sismique située dans la zone du STS présente des données de mauvaise qualité ce qui empêche d'imager précisément la forme du Moho à cet endroit.

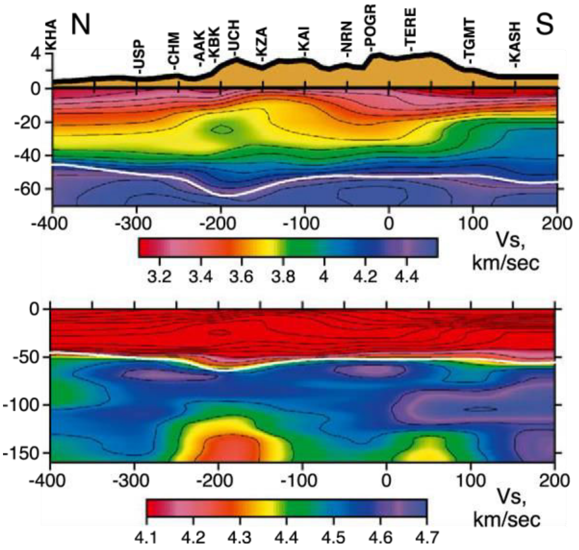

Figure I-10 : Coupes de vitesse de propagation des ondes S dans la croûte et dans le manteau. Le trait blanc représente le Moho estimé par fonctions récepteurs (Vinnik et al., 2004)

Enfin, d'autres études géophysiques ont également permis de caractériser les grandes

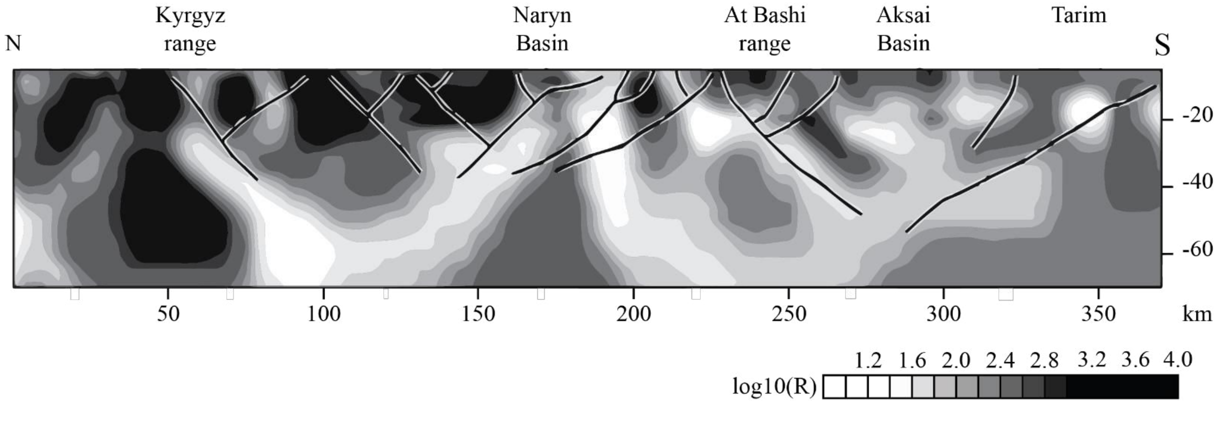

Figure I-11 : Profil magnéto-tellurique acquis le long du méridien 76°E dans le Tien Shan kirghize. L'échelle de gris indique la résistivité dans la croûte. Les traits noirs représentent les traces interprétées des failles principales (Batalev et al., 2011) structures sous le Tien Shan, notamment à l'aide de profil magnétotelluriques (Figure I-11) le long du même transect que celui du profil MANAS (Batalev et al., 2011; Bielinski et al., 2003). Ceux-ci montrent une corrélation très forte entre les grandes structures connues à l'aide des données géologiques et sismiques et la résistivité électrique de la croûte. En effet, les zones de la croûte où la résistivité est la plus faible correspondent au prolongement en profondeur des grandes structures tectoniques connues en surface dans le Tien Shan.

3. Problématique

La chaîne du Tien Shan constitue un objet géologique aux caractéristiques multiples :

1- Le Tien Shan fait partie d'une ancienne chaîne d'accrétion paléozoïque dont l'histoire tectonique reste débattue.
2- La présence d'une zone de déformation active aussi intense située à plusieurs milliers de kilomètres de toute frontière de plaque en fait un cas d'étude caractéristique pour la déformation intra-plaque.
3- La déformation et la pré-structuration de la chaîne au cours du Paléozoïque représente un enjeu important dans la localisation de la déformation cénozoïque. En effet, l'héritage structural et rhéologique issu des orogenèses paléozoïques semble contrôler en grande partie la structuration actuelle de la chaîne et donc son activité tectonique.

L'histoire tectonique polyphasée et la situation géographique du Tien Shan soulèvent donc plusieurs questions auxquelles cette étude est consacrée :

1- Quelles sont les structures majeures de la chaîne, acquises au cours du Paléozoïque ?
2- Quelle est la géométrie de ces structures et quel régime de déformation leur est associé au cours du Paléozoïque ?
3- Dans quelle mesure les structures héritées du Paléozoïque contribuent à la localisation de la déformation cénozoïque ?
4- Quelle est la structure actuelle de la chaîne, du terrain à l'échelle crustale ?

Pour apporter des réponses à ces questions un travail de terrain a tout d'abord été effectué dans la partie Kirghize du Tien Shan. Les données et interprétations issues de cette étude et combinées avec celles disponibles dans la littérature nous ont ensuite permis de proposer plusieurs modèles thermo-mécaniques visant à tester et déterminer comment la déformation et les structures héritées du Paléozoïque influencent la localisation de la déformation cénozoïque.

II. Déformation et structure paléozoïque du Tien Shan

Comme exprimé précédemment, le but de cette étude est de comprendre quel rôle l'héritage structural et tectonique joue sur la localisation de la déformation dans la lithosphère continentale en domaine intra-plaque. Pour ce faire, la première étape a été d'identifier quelles étaient les structures majeures du Tien Shan héritées des phases tectoniques précédentes susceptibles d'influencer la localisation de la déformation cénozoïque. Ce travail est basé sur des données acquises au cours de deux missions de terrain en été 2014 et 2015 (Figure de localisation).

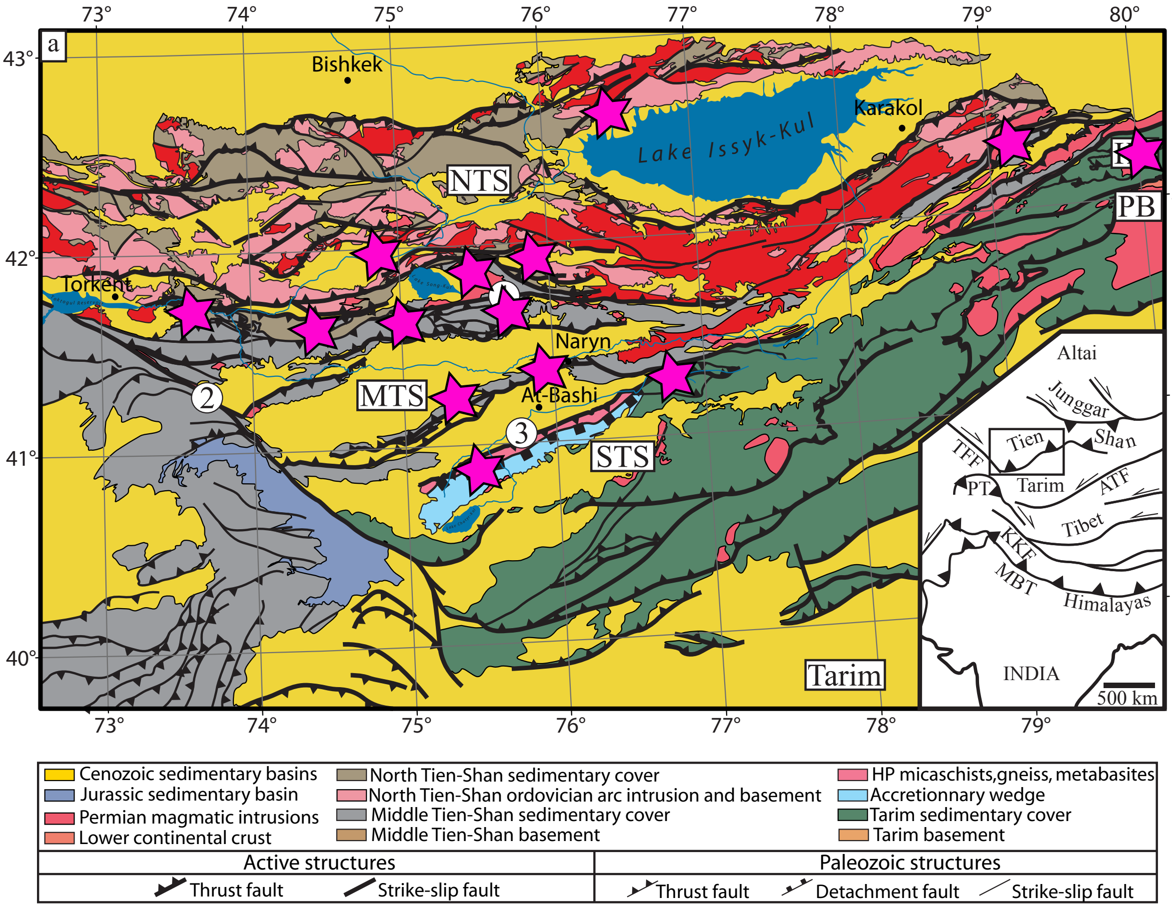

La figure ci-dessus montre les différents lieux explorés sur le terrain au cours des deux missions (étoiles violettes). NTS : North Tien Shan, MTS : Middle Tien Shan, STS : South Tien Shan

Le travail présenté dans cette section a fait l'objet d'une publication dans Gondwana Research : Jourdon, A., Petit, C., Rolland, Y., Loury, C., Bellahsen, N., Guillot, S., Le Pourhiet, L., Ganino, C., 2017. New structural data on Late Paleozoic tectonics in the Kyrgyz Tien Shan (Central Asian Orogenic Belt). Gondwana Research 46, 57-78. doi: 10.1016/j.gr.2017.03.004.

Résumé

L’évolution tectonique de la Ceinture orogénique d’Asie Centrale (CAOB) est caractérisée par l’accrétion successive de blocs lithosphériques. Les interprétations à propos de la polarité des subductions au Paléozoïque, le nombre de microplaques et de bassins océaniques ainsi que la durée des différents événements tectoniques sont nombreuses, particulièrement dans le cas du Tien Shan. Dans cette publication, nous proposons de nouvelles cartes et coupes structurales dans le MTS et le STS. Ces coupes mettent en lumière une zone de décrochement crustale dextre dans le MTS ainsi qu’une structure chevauchante à vergence Nord dans le STS. Ces structures sont carbonifères et sont scellées par un conglomérat du Carbonifère supérieur puis surmontée par les formations du Mésozoïque et du Cénozoïque. Le STS est marqué par deux phases de déformation : (1) une déformation cisaillante normale à vergence Sud qui peut être associée à la dynamique de subduction et exhumation ainsi que (2) une mise en nappe à vergence Nord que nous relions à la phase de collision entre le MTS et Tarim au Paléozoïque supérieur. Une nouvelle interprétation est proposée à propos de l’évolution tectonique du Tien Shan kirghize au cours de la collision au Paléozoïque supérieur. Ce modèle implique un partitionnement de la déformation, avec au Sud, une collision orthogonale entre le Tarim et le MTS et au Nord, un régime de déformation décrochant entre le MTS et le NTS le long de la Nikolaev Line. L’accrétion du Tarim à la CAOB correspond à une phase de collision qui met fin à la longue histoire paléozoïque de construction de la chaîne et est directement suivi au cours du Permien par une phase de déformation décrochante associée à un magmatisme intense à travers toute la chaîne du Tien Shan.

New structural data on Late Paleozoic tectonics in the Kyrgyz Tien Shan (Central Asian Orogenic Belt)

Anthony Jourdon[a,*], Carole Petit[a], Yann Rolland[a], Chloé Loury[a], Nicolas Bellahsen[b], Stéphane Guillot[c], Laëtitia Le Pourhiet[b] and Clément Ganino[a]

a- Université de Nice-Sophia Antipolis, CNRS, IRD, Observatoire de la Côte d'Azur, Géoazur UMR 7329, 250 rue Albert Einstein, Sophia Antipolis 06560 Valbonne, France.
b- ISTeP, Université Pierre et Marie Curie, Paris, France.
c- ISTerre, CNRS, Université Grenoble Alpes, 38041 Grenoble, France.

Abstract

The tectonic evolution of the Central Asian Orogenic Belt (CAOB) is characterized by the successive accretion of lithospheric blocks, leading to different interpretations about the polarity of subductions during the Paleozoic, the number of microplates and oceanic basins and the timing of tectonic events. This is especially the case in the Tien Shan area.

In this paper, we propose new structural maps and cross-sections of Middle and South Kyrgyz Tien Shan (MTS and STS respectively). These cross-sections highlight an overall dextral strike-slip shear zone in the MTS at the crustal scale and a North verging structure in the STS. These structures are Carboniferous in age and sealed by a late Carboniferous conglomerate, later overlain by Mesozoic and Cenozoic deposits. The STS exhibits two deformation phases: (1) a top-to-the-South normal shearing that can be related to subduction or exhumation dynamics and (2) a top to the North nappe stacking that we link to the late Paleozoic collisional events between the MTS and the Tarim block.

We propose a new interpretation of the tectonic evolution of the Kyrgyz Tien Shan during the Late Paleozoic collision. This model involves a partitioned collisional deformation in Late Carboniferous times, with an orthogonal collision to the south, between the Tarim and MTS, and a strike-slip regime to the north along a dextral E-W zone located between the MTS and the North Tien-Shan/ Kazakh platform, the so-called Nikolaev Line. The docking of the large Tarim Craton against the CAOB corresponds to a collision phase, which ended the long-lived Paleozoic subduction history in the CAOB and was followed in the TS region by intense strike-slip deformation during the Permian.

Keywords: Tien Shan, Paleozoic, tectonics, structural geology.

1. Introduction

Orogens are classically divided into collisional orogens and accretionary orogens (e.g., Cawood et al., 2009; Kusky, 2011). The Alpine-Himalayan and Andean orogens are considered as typical examples of these two end-members, respectively (Demets et al., 1990; Guillot et al., 2003; Isaks, 1988; Le Fort, 1975). Collisional orogens commonly involve large cumulated strains both on the plate interface and within the colliding plates (e.g., Vanderhaeghe, 2012). They are the result of continental subduction and/or continental underthrusting and shortening, following the closure of an oceanic domain (Chen et al., 1999; Faccenda et al., 2008). In contrast, accretionary orogens develop on long-lasting oceanic subduction zones. As a result, they are composed of an amalgamation of material from the upper and lower plates associated with magmatic and metamorphic rocks (e.g., Cawood et al., 2009), and references therein). Accretion itself corresponds to a short-lived collisional phase (10-20 Ma) followed by a subduction jump, which favors the transfer of the plate interface to the opposite block boundary (e.g., Rolland et al., 2012). In such long-lived subduction systems, the subduction of oceanic ridges and transforms might induce large strike-slip motions in the upper plate with the detachment and oblique accretion of continental slices like in the NW American coast (Atwater, 1970; Furlong et al., 1989). Accretion can therefore be characterized by different kinematics from frontal collision to strike-slip motion.

The Central Asian Orogenic Belt (CAOB, e.g., (Windley et al., 2007; Xiao et al., 2014), also named “Altaids” (Şengör et al., 1993), results of the docking of numerous continental blocks and volcanic arcs against the Archean Siberian craton since the late Proterozoic and until the late Paleozoic (e.g., De Boisgrollier et al., 2009; Windley et al., 2007; Yarmolyuk et al., 2014). Although it has long been recognized as a typical example of an accretionary orogen, the collisional or accretionary nature of the CAOB is still a matter of debate. Indeed, it involves

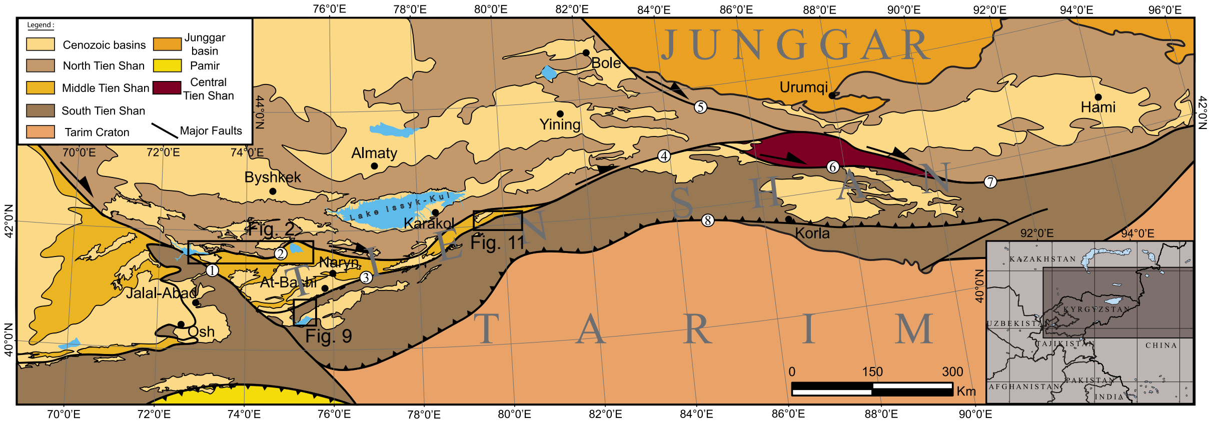

Figure 1: Synthetic structural map of the CAOB and surrounding areas fromKyrgyzstan to North China. (Modified after (Charvet et al., 2011; Xiao et al., 2013) and official 1:500,000 geological map of Kyrgyz Republic). 1. Talas Fergana Fault; 2.Nikolaev Line (reworking the Terskey suture); 3. At-Bashi-Inylshek Fault (reworking the Turkestan Ocean suture); 4.Narat Fault; 5.North Tien Shan Fault; 6. Baluntai Fault; 7. Main Tien Shan Shear Zone; 8. North Tarim Fault. Insets show the location of Figs. 2, 9 and 11.

several large-scale collisions between important cratonic blocks, like the cratonized Kazakh platform and the Tarim craton (e.g., Xiao et al., 2014, 2013).The Paleozoic CAOB accretion history ended in Late Carboniferous with the collision of the large and rigid Tarim block with the Kazakh continent (e.g. Charvet et al., 2011; Windley et al., 2007).

The Tien Shan (TS) belt (Figure 1) is a part of the CAOB and runs in a ~SW-NE direction over more than 2000 km from Uzbekistan to western China; it is located between the Kazakh and Junggar blocks to the North, and the Tarim craton to the South. Since about 30 Ma (Macaulay et al., 2014; Sobel et al., 2006), this area has been a typical intracontinental collision zone undergoing a ~North-South shortening rate of ~1.3 cm/yr in response to the India-Asia convergence (Abdrakhmatov et al., 1996; Avouac et al., 1993). The present-day morphology and structural pattern of the TS belt largely result from this still on-going compression. Although it is widely admitted that most Cenozoic structures reactivate ancient thrusts and suture zones inherited from previous deformation stages (e.g., Buslov et al., 2007; Glorie et al., 2011), the amount of Paleozoic shortening is still largely unconstrained. In the following sections, we will only consider the part of the Paleozoic TS belt located east of the major dextral Talas Fergana Fault (TFF).

Lateral correlation of the different units constitutive of the TS belt remains difficult because of its complex geometry because it spreads over different countries. Another point of debate is the vergence of subduction zones that led to the final Paleozoic collage. There have been some attempts to synthesize the tectonic history of the TS belt based on unit correlation and available geochronological constraints (e.g., Loury et al., 2015; Wilhem et al., 2012; Windley et al., 2007; Xiao et al., 2013), but their interpretations differ in terms of timing and vergence of subduction zones.

In this paper, we present new field data in the Kyrgyz TS combined with published structural and geochronological results, which allow us to shed light on the style of deformation and unravel the Late Paleozoic tectonic history of the TS.

2. Geological Setting of the Tien Shan Belt

2.1. General structure of the Kyrgyz Tien Shan

In Kyrgyzstan, the TS is characterized by three tectonic domains: the North, Middle and South TS (NTS, MTS and STS, respectively), squeezed between the more rigid lithospheres of the Kazakh platform and Tarim craton (Figure 1). Suture zones of different ages and kinematics separate all these domains. The NTS and MTS are located on both sides of a ~E-W suture zone of middle Ordovician age, which worked as a broad strike-slip crustal zone during Permian times (e.g., Choulet et al., 2011). This broad wrench zone as well as the succession of individual strike-slip fault segments (when observed) are given the name “Nikolaev line” (e.g., Mikolaichuk et al., 1997; Windley et al., 2007). Further south, the MTS and STS are separated by a suture zone and an accretionary complex known as the At-Bashi-Kokshaal suture zone, running E-W from Kyrgyzstan to NW China (e.g., Burtman, 2008; Glorie et al., 2011; Simonov et al., 2008).

The MTS progressively narrows eastward and disappears near the Kyrgyzstan/China border. Likewise, other blocks are only present in China and consequently, the tectonic units of the Chinese Tien Shan have a different nomenclature. There, the TS belt encompasses from North to South the Junggar, Yili-NTS, Central TS and South TS blocks (e.g., Gao et al., 1998).

From China to Kyrgyzstan, the At-Bashi-Kokshaal suture zone therefore marks there the junction between the Yili-NTS, and the CTS and STS blocks (Figure 1). Most of the sutures are reworked by Permian strike-slip faults (e.g., Laurent-Charvet et al., 2003, 2002; Wang et al., 2007a). In particular, the prolongation of the strike-slip Nikolaev line in China runs along the NTS-CTS suture (Narat Fault, Figure 1).

2.1.1. North Tien Shan

The NTS is essentially composed of deformed Proterozoic to Cambrian sediments and volcanics highly intruded by magmatic bodies with calc-alkaline affinities, suggesting the presence of an active margin which lasted from the Ordovician in Kyrgyzstan (Bakirov and Maksumova, 2001; Bazhenov et al., 2003; Glorie et al., 2010; Konopelko et al., 2008; Kröner et al., 2014, 2012a) to the Carboniferous in China (Wang et al., 2007b; Zhu et al., 2005).

In Kyrgyzstan, the active margin setting of the NTS is interpreted as the result of the northward subduction and closure of the Terskey Ocean during the Ordovician, eventually leading to the accretion of the MTS against the NTS in the Middle-Late Ordovician (Bakirov and Maksumova, 2001; Glorie et al., 2010; Lomize et al., 1997).

In China, observations on this margin two magmatic events are observed and correspond to the closure of two different oceanic domains: (i) the northward subduction of an oceanic domain located between the Tarim craton and the Yili-NTS block during the Ordovician (Allen et al., 1993; Chen et al., 1999; Gao et al., 2009, 1998; Qian et al., 2009; Windley et al., 1990; Xiao et al., 2014, 2004) ; (ii) the southward subduction of an oceanic domain located between the NTS and the Junggar block during the Carboniferous (Allen et al., 1993; Charvet et al., 2011; Wang et al., 2009, 2008; Windley et al., 1990).

The rest of the Paleozoic sedimentary cover of the NTS consists of Ordovician flyschs composed of volcanic tuffs, siltstones and sandstones sometimes overlain by Devonian volcanics (Bazhenov et al., 2003). Carboniferous (Late Tournaisian to Bashkirian) deposits in the NTS are clastic sediments composed of sandstones and siltstones with gypsum lenses characteristic of a shallow water to continental sedimentary environment (Mikolaichuk et al., 1997).

2.1.2. Middle Tien Shan

The MTS is a continental domain composed of a Neoproterozoic basement where the oldest observable rocks are characterized by an assemblage of metamorphosed sediments, amphibolites and orthogneisses. These rocks have been dated between 2.3 Ga and 1.7 Ga (Glorie et al., 2011; Keselev et al., 1982; Kiselev et al., 1993; Kröner et al., 2012a). The basement of the MTS is overlain by Late Proterozoic tillites and diamectites and by a thick Paleozoic sedimentary cover principally composed of slates and carbonates from Cambrian to Carboniferous age. A regional-scale sedimentation hiatus is observed between the Late Ordovician and the Middle Devonian. The Carboniferous limestones of this sedimentary cover represent a carbonate platform sequence. An angular unconformity is also observed between the Early and Late Carboniferous (Osmonbetov et al., 1982). The Carboniferous carbonate platform of the MTS is thrusted towards the North over the clastic sequences of the NTS, and the thrusts are sealed by a conglomerate of Late Carboniferous age, which indicates a middle Bashkirian age for the thrust activity (Bazhenov et al., 2003).

2.1.3. South and Central Tien Shan

The STS represents the southernmost part of the TS and CAOB. In China, the STS is separated from the NTS by the At-Bashi-Kokshaal suture zone along which runs the Permian Narat strike-slip Fault (Yin et al., 1998). The CTS is separated from the STS by a strike-slip fault which may also be related to the Permian strike slip events (the Baluntai fault, Laurent-Charvet et al., 2003; Wang et al., 2009; Yang et al., 2007, Figure 1). The STS is characterized by an accretionary complex and tectonic nappes, while the CTS is interpreted as a continental magmatic arc (Charvet et al., 2011; Gao et al., 2009; Liu et al., 2014; Wang et al., 2011; Xiao et al., 2014, 2013).

In China, the At-Bashi-Kokshaal suture zone is composed of metamorphic units with Pressure-Temperature (P-T) estimates of 28-30 kbar and 520-540°C for the pressure peak, and 22-27 kbar and 540-590°C for the temperature peak (Tian and Wei, 2013). The pressure peak has been dated with U-Pb method on zircon and rutile from 319 Ma to 308 Ma (Li et al., 2011; Liu et al., 2014; Su et al., 2010; Zhang et al., 2009).

In Kyrgyzstan, the At-Bashi-Kokshaal suture is characterized by an accretionary complex composed of several metamorphosed units associated with a non-metamorphic ophiolite cropping out South of the At-Bashi city (Alekseev et al., 2007; Biske, 1996a; Biske et al., 1985; Loury et al., 2015b). Recent geological mapping of the At-Bashi range evidenced a South-dipping top-to-the-North tectonic stack, with from bottom to top: (1) a low-grade unmetamorphosed ophiolite thrusted by (2) a greenschist to blueschist accretionary prism and (3) eclogite-facies continental and oceanic units (Loury et al., 2015b). A Gzhelian to Asselian conglomerate seals the deformation phase related to the exhumation of these high-pressure rocks (Baslakunov et al., 2007).

To the East, near the Chinese boundary, Loury et al., (2015a) described in the STS a granulitic unit composed of an assemblage of pyroxene, feldspar, quartz and garnet overthrusting towards the North a low grade (greenschist facies) metamorphic sediments unit.

*2.2.**Previously proposed models of TS accretion***

Different models were proposed to interpret and reconstitute the geological and tectonic history of the TS and CAOB (Kröner et al., 2014; Windley et al., 2007; Xiao et al., 2014). The formation of this kind of orogenic belt is closely associated to one or several oceanic subductions. However, for the TS, the number, polarity and duration of these subductions are still debated.

In Kyrgyzstan, most studies agree on the presence of a northward subduction of the Terskey ocean (Figure 1) during the Ordovician, responsible for the widespread calc-alkaline magmatism encountered in the NTS (Bakirov and Maksumova, 2001; Glorie et al., 2010; Kröner et al., 2013, 2012a). Closure of the Terksey Ocean at ~ 480 Ma resulted in the collision between the MTS and the NTS (Lomize et al., 1997; Mikolaichuk et al., 1997). In China, this Early Paleozoic magmatism is found at the southern boundary of the Yili block which was then already a part of the NTS block (B. Wang et al., 2010; Wang et al., 2011). Because of the disappearance of the MTS block in China, the Ordovician active margin and suture are probably at least partially reworked there by the late Paleozoic CTS and STS/Tarim collision. Indeed, Gao et al. [2009] evidenced a long-lasting calc-alkaline magmatism from Early Ordovician to Permian times east of the MTS block, associated with HP metamorphism (Bazhenov et al., 2003; Lomize et al., 1997). They interpreted this magmatism as due to the simultaneous northward and southward closure of the Terskey Ocean between the CTS and NTS, and to the northward closure of the STS Ocean between the CTS and the Tarim (Figure 1). According to Gao et al. (2009), the CTS would be a continental block rifted away from the Tarim in a back-arc setting, due to the southward subduction of the Terskey Ocean. This hypothesis of a Tarim affinity for CTS is supported by other authors (Lin et al., 2009; Wang et al., 2011, 2008) based on structural and magmatic arguments (Charvet et al., 2011, 2007, Dong et al., 2011, 2006, 2005; Guo et al., 2002; Laurent-Charvet, 2001; Ma et al., 1993; Zhong et al., 2014). However, Charvet et al. (2011) considered that the CTS rifted away from the Tarim margin during the Devonian following the South-dipping subduction of another ocean ("the South Tien Shan Ocean") beneath the Tarim.

The closure of the STS Ocean south of the CTS is another matter of debate. Some authors consider that it subducted towards the North under the NTS/CTS collided blocks, based on the observed N-S succession of magmatic arc (in the CTS block), accretionary complex (STS), and passive margin (Tarim) units (e.g., Chen et al., 1999; Gao et al., 2009; Liu et al., 2014; Xiao et al., 2014, 2013). Other authors rather propose a subduction towards the South, beneath the Tarim, based on the presence of subduction-related magmatic rocks on the North Tarim margin, and on numerous evidences of top-to-the-North deformations inside the STS accretionary complex (Charvet et al., 2011, 2007, Ge et al., 2014, 2012; Lei et al., 2011; Lin et al., 2013; B.

Wang et al., 2016; Wang et al., 2007a). Most authors finally agree on a closure of the STS Ocean achieved at ~ 310-340 Ma in China and ~ 320 Ma in Kyrgyzstan.

Finally, in China, a last Paleozoic collision was related to the closure of the North Tien Shan ocean between the previously assembled CTS/STS/Tarim blocks and the Junggar block to the North (Allen et al., 1993; Charvet et al., 2011; Chen et al., 1999; Gao et al., 2009, 1998; Qian et al., 2009; Wang et al., 2009; Windley et al., 1990; Xiao et al., 2004).

2.3.<u>Post orogenic evolution of the Tien Shan</u>

After the last collisional event between the Tarim and the TS during the Carboniferous, the compressional regime was followed during the Permian by a strike-slip regime accommodated by large NW-SE and ENE-WSW wrench faults (e.g., the Talas Fergana Fault), which reactivated the suture zones of the TS belt (Alekseev et al., 2007; Jong et al., 2009; Konopelko et al., 2013; Rolland et al., 2013; Wang et al., 2007a). The Nikolaev Line as well as other large ~EW trending faults in the Chinese TS accommodated several hundreds of km of right-lateral shear (e.g. Choulet et al., 2011; Laurent-Charvet et al., 2003, 2002). A pervasive magmatic event occurred in all the TS and was characterized by granitic intrusions cross-cutting the Paleozoic structures and following the trace of the strike-slip faults (Alekseev et al., 2009; Biske et al., 2013; Chen et al., 2009; Seltmann et al., 2011; Wang et al., 2009). Mesozoic times are characterized by a long-lived erosion phase marked by a peneplain surface on which the Cenozoic formations were deposited (Abdrakhmatov et al., 2001; Jolivet et al., 2010; Macaulay et al., 2014). Despite this apparent tectonic quiescence, the dating of syn-kinematic pegmatites evidences a moderate tectonic activity of the TFF during the Late Triassic-Early Jurassic (195 ± 3 Ma, ^{40}Ar/^{39}Ar on muscovite; (Rolland et al., 2013).

2.4.<u>Cenozoic reactivation</u>

With respect to the Cenozoic deformation, the TS is a typical example of an intracontinental mountain range, which undergoes active compression in response to the India-Asia convergence (e.g. Avouac et al., 1993; Patriat and Achache, 1984; Sobel and Dumitru, 1997; Tapponnier et al., 1986). Geodetic data show that the TS currently accommodates of about 40% to 50% of the India-Asia convergence rate (i.e., ~20 mm/yr) in the western part of the collided zone, including the shortening across the northern margin of the Tarim basin, for a total amount of crustal shortening of 200 ± 50 km since max. 30 Ma (Abdrakhmatov et al., 1996; Avouac et al., 1993; DeMets et al., 1994).

Cenozoic deformation has resulted in the development of five major mountain ranges delineating intra-mountainous molassic basins accumulating fluvial deposits. Cenozoic sediments overlie the late Mesozoic peneplain surface. A regional-scale angular unconformity can be traced in the landscape due to the higher erodibility of recent sediments compared to that of the Paleozoic bedrock. Low-temperature thermochronological data and sedimentary deposits suggest that uplift initiated ~25 Ma ago, but most of sediment deposition and relief exhumation started 11-12 Ma ago with a possible acceleration at 3-5 Ma (Abdrakhmatov et al., 2001; Bullen et al., 2001; Burbank et al., 1999a; De Grave et al., 2004; Macaulay et al., 2014, 2013; Sobel et al., 2006; Thompson et al., 2002).

Tertiary tectonics is characterized by a dominant thick-skin tectonic with steep crustal ramps emerging between the ranges and the basins and accommodating basement exhumation on high-angle thrust faults (e.g. Macaulay et al., 2013). Moderate and more recent shallow ramp-flat faulting and a thin-skin tectonic propagating within the basins occurred in the late Quaternary (Thompson et al., 2002 and references therein, Goode et al., 2011).

As exposed in the next sections, our field data confirm that Cenozoic deformation is localized principally along basins border faults and within the Cenozoic basins, whereas the inner parts of mountain ranges show uplifted remnants of flat-lying Cenozoic sediments.

3. Structural analysis

We present here a structural study of different stratigraphic and metamorphic units of the NTS, MTS and STS and their suture zones. Ages and lithological descriptions of sedimentary units in the MTS are after Karpovitch et al., (1964) and Lasovski and Mozolev, (1960).

3.1. Structural geology of the Song-Kul zone

The Song-Kul zone (Figure 2) spreads over a 20 x 150 km area and is characterized by a general northward thrusting of the MTS Carboniferous carbonate platform over the NTS detrital Carboniferous formations.

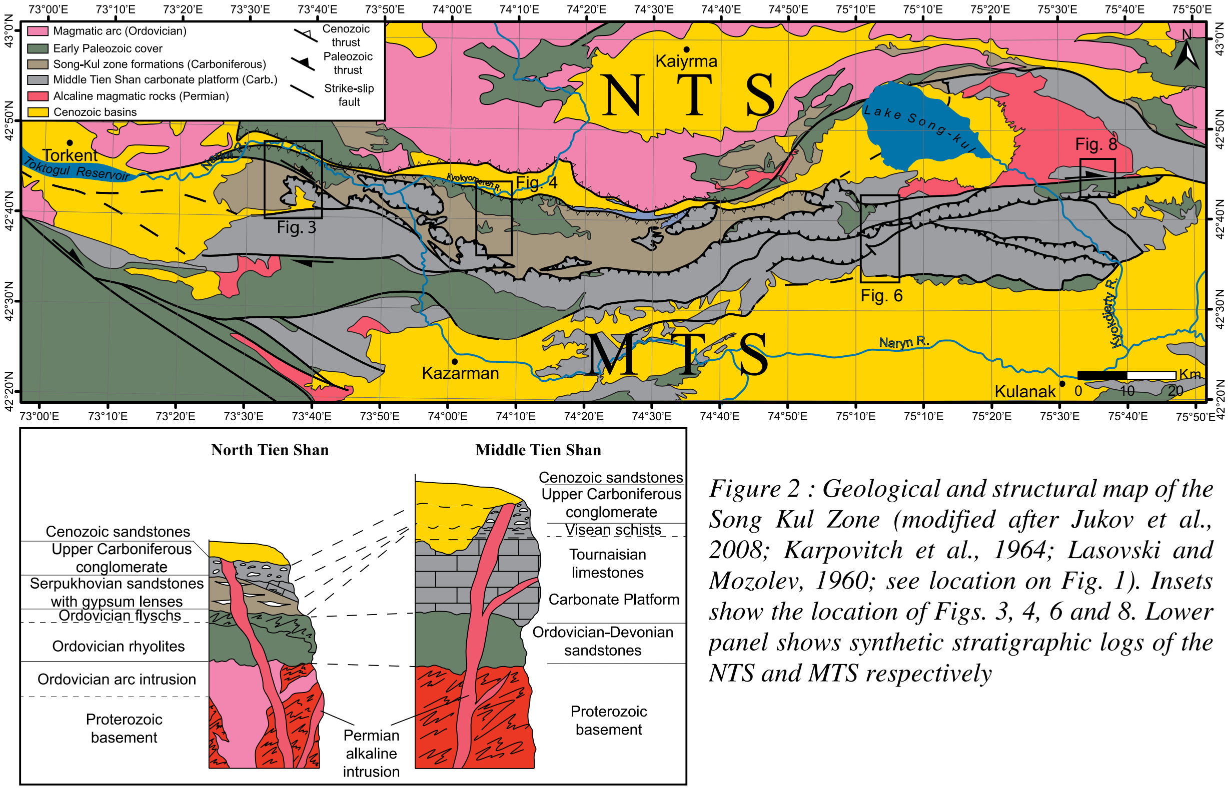

Figure 2 : Geological and structural map of the Song Kul Zone (modified after Jukov et al., 2008; Karpovitch et al., 1964; Lasovski and Mozolev, 1960; see location on Fig. 1). Insets show the location of Figs. 3, 4, 6 and 8. Lower panel shows synthetic stratigraphic logs of the NTS and MTS respectively

In the NTS, the Early Paleozoic is represented by Ordovician rhyolites, sandstones and siltstones related to an active margin setting (Bakirov and Maksumova, 2001; Glorie et al., 2010; Konopelko et al., 2008; Kröner et al., 2014, 2012a). A regional unconformity separates these Early Paleozoic formations from Serpukhovian sandstones with gypsum lenses, characteristic of the NTS deposition environment. Outcropping formations of the MTS are characterized by Upper Devonian sandstones overlain by a Tournaisian to Visean carbonate platform sequence, which thickness increases towards the south. Early Paleozoic sediments of the MTS do not crop out.

We discuss here in detail the nature and geometry of the contact between the MTS and the NTS. Three cross-sections through the Song-Kul zone are presented in the following section.

3.1.1. Toktogul area

The Toktogul area (Figure 3) is characterized by a northward thrusting of the MTS Tournaisian carbonate formation upon the Serpukhovian NTS clastic deposits. This NE-SW thrust is associated on the field and on geological maps with evidences of dextral strike-slip faulting on NW-SE vertical planes (Figure 3). It is sealed by flat-lying Cenozoic continental sandstones (Figure 3) overlying the Tournaisian limestones with an angular unconformity. It is difficult to precisely give an age to these Cenozoic sediments. Clearly, their deposition pre-

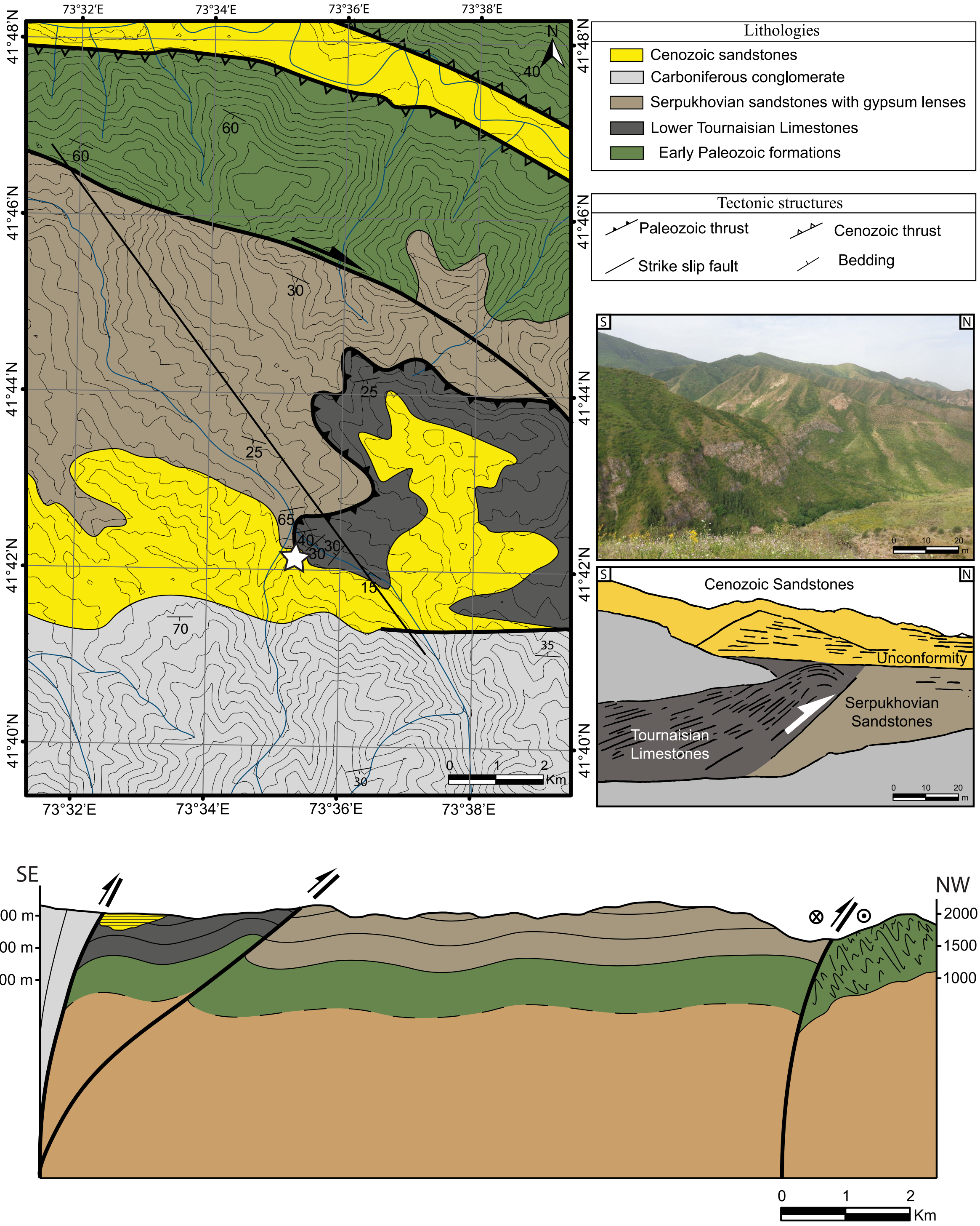

Figure 3 : Geological map and cross-section of the Toktogul reservoir area (see Fig. 2 for location). The cross-section is indicated on the map by the thick black line. Star indicates the location of the picture.

dated the formation of this mountain range, since they are now uplifted and deeply incised. By comparison with the onset of uplift of the Kyrgyz range north of the Toktogul area ~11 Ma ago (Sobel et al., 2006), they may be of Late Oligocene to Miocene age.

South of this thrust, a large rhombohedral basin is slightly thrusted upon Tournaisian formations along high angle reverse faults that look like inverted normal faults (Figure 3). The age of this basin is poorly constrained, but Jukov et al. (2008) consider its age as Devonian to Early Carboniferous, or as Late Carboniferous, on the basis of pollen assemblages. Its geometric shape on map suggests it could have been emplaced in a strike-slip context (i.e., as a pull-apart basin), but at present we can only speculate on its origin.

To the North, Serpukhovian sandstones of the NTS are also slightly thrusted along a dextral strike-slip fault over the Ordovician flysch, which is intensely folded.

On map, the geometry and kinematics of thrusts and normal faults is consistent with an E-W dextral strike-slip deformation regime that prevailed during the end of the Early Carboniferous (Figure 2). This suggests that both the thrusting of Tournaisian formations of the MTS over the Serpukhovian formations of the NTS, and the possible opening of a pull-apart basin can be roughly contemporaneous. Bazhenov et al. (2003) indicate that a Late Carboniferous conglomerate seals the northward thrusting of the MTS over the NTS and ascribes it a Bashkirian age, which is consistent with this interpretation.

3.1.2. Central Song-Kul area

In this area (Figure 4), Early Paleozoic formations crop out and are thrusted over a narrow E-W Cenozoic basin (Figure 5a). The border of this basin is strongly folded and reveals an anticline core composed of Jurassic gypsum formations (Figure 5b). Early Paleozoic rocks are represented by a thick rhyolitic series on which Serpukhovian sandstones with gypsum lenses are unconformably lying (Figure 5c). Deformation of the rhyolites and overlying sequences is characterized by long-wavelength upright folds (Figures 4 and 5) and top-to-the-North thrusts with moderate throw.

Gypsum layers interbedded in Serpukhovian sandstones allow the development of small-scale thrusts (Figure 5d), which may root at depth beneath the rhyolite series.

Hence, in this area, the only major visible deformation is the Cenozoic thrusting of the Ordovician rhyolites upon the Cenozoic basin (Figures 4 and 5a); there is no clear evidence of pre-Cenozoic deformation, although it is possible that a part of the moderate shortening observed in the Ordovician-Serpukhovian sequence is Paleozoic.

More to the South, the Tournaisian carbonate platform of the MTS is thrusted towards the North over these Ordovician and Serpukhovian formations of the NTS (Figure 4). Based on the interpretation of Bazhenov et al. (2003) and on the similarity of this area with the Toktogul section, we assume that this northward thrust is of middle Carboniferous age (Figure 3).

However, we did not observe any post-tectonic unconformity that can definitely confirm this age in this area.

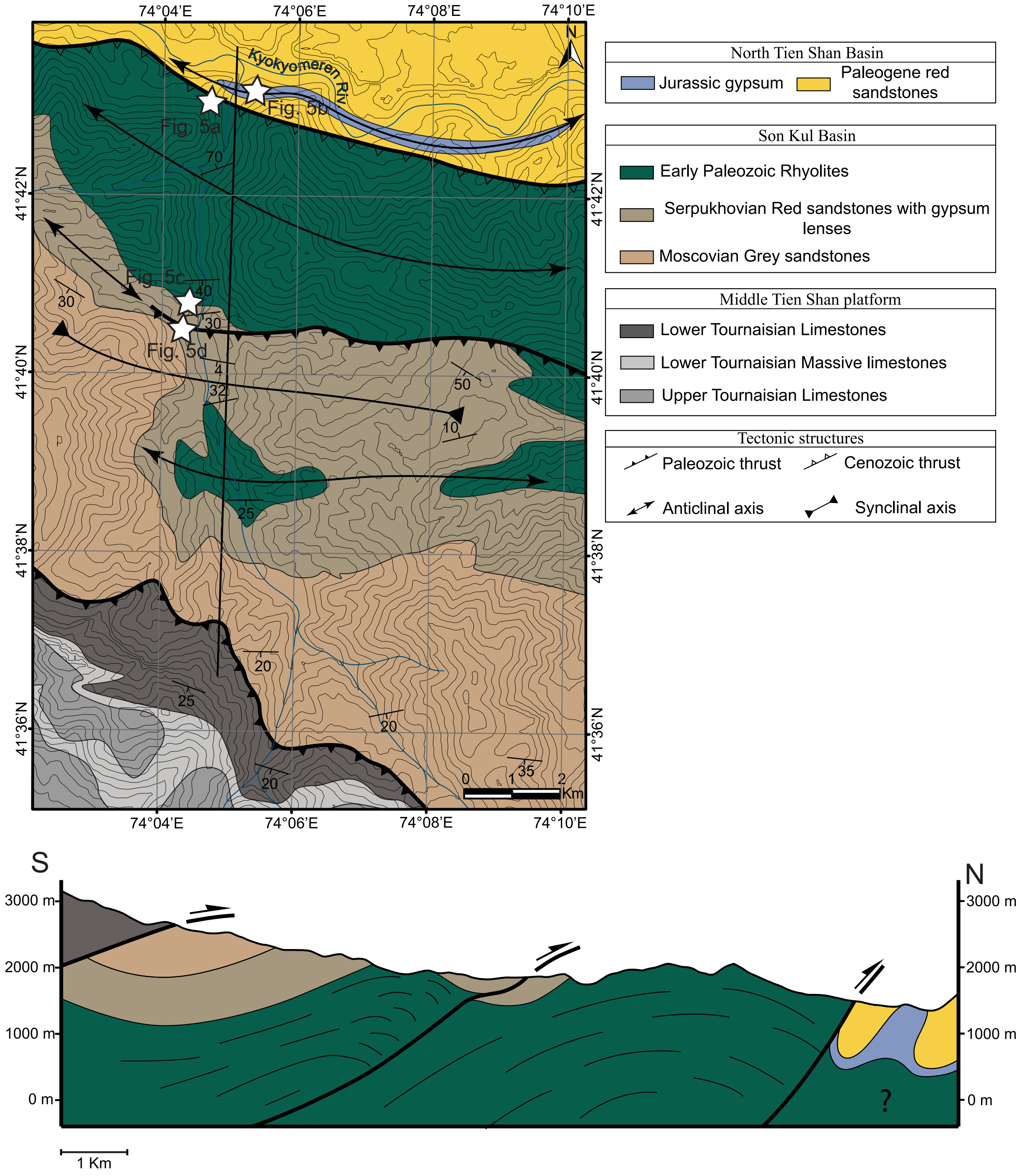

Figure 4 : Geological map and cross-section of the Central Song-Kul area (see Fig. 2 for location). The cross-section is indicated on the map by the thick black line. The stars indicate the locations of field pictures on Fig. 5.

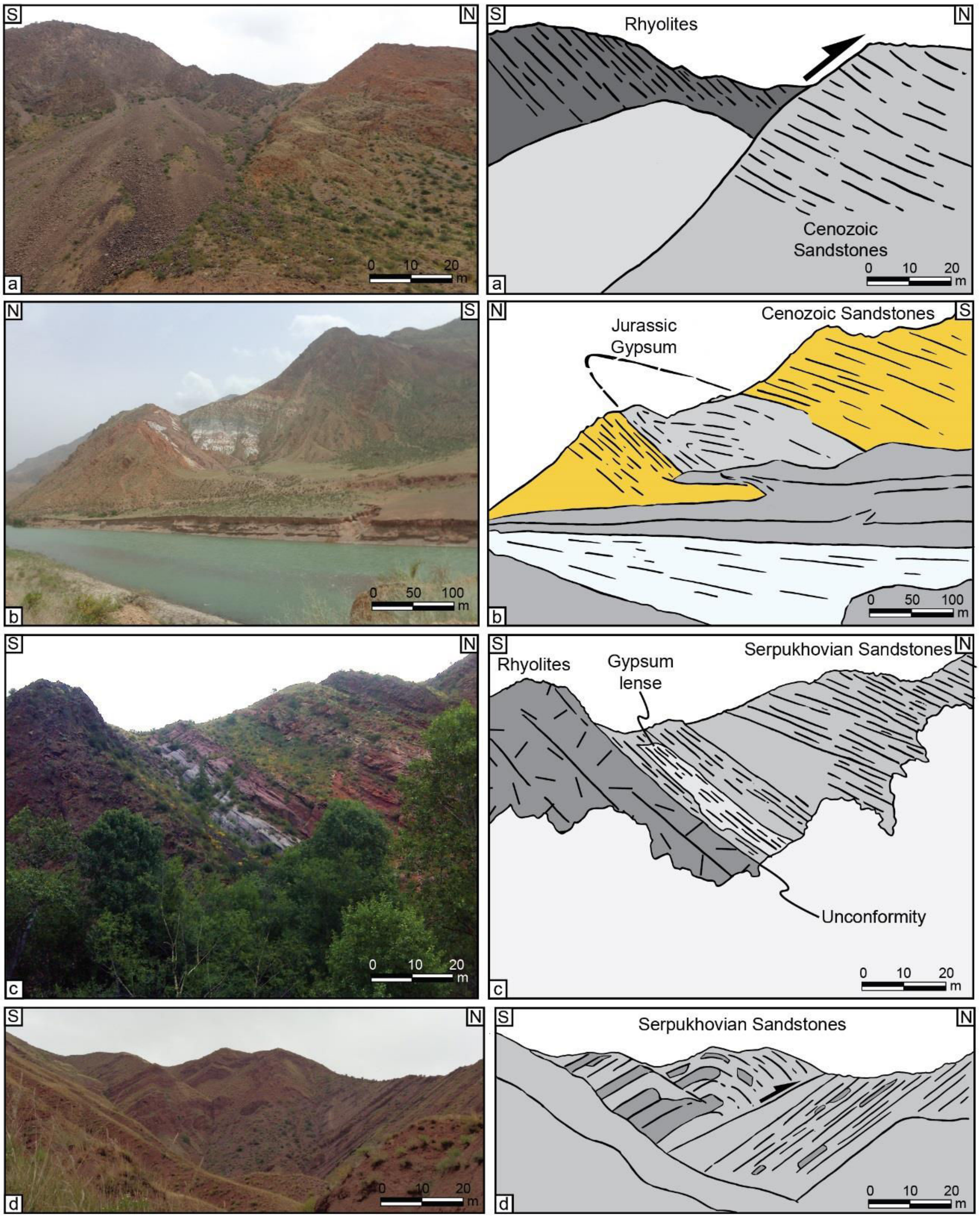

Figure 5 : Field pictures and their interpretations of the Central Song Kul area. a. Northward thrusting of Ordovician Rhyolites on Cenozoic sediments; b. Northward overturned anticline with Cenozoic sediments overlying Jurassic gypsum-bearing deposits; c. Unconformity between Ordovician rhyolites and Carboniferous (Serpukhovian) gypsum-bearing sandstones typical of the NTS domain; d. Small-scale internal thrust in Carboniferous (Serpukhovian) gypsum-bearing sandstones. See Fig. 4 for location.

3.1.3. Song-Kul cross-section

This cross-section (Figure 6) is located entirely in the Carboniferous carbonate platform of the MTS. Devonian deposits are characterized by sandstones while the Carboniferous is represented by Tournaisian limestones overlain by siltstones and sandstones of Visean age.

To the South, Cenozoic sediments of the Naryn basin overlay an anticline limb of Tournaisian limestones, and are slightly folded. North of this anticline, Visean deposits crop out in a syncline in which top-to-the-South-East overturned folds are visible (Figure 6). North of this structure, Tournaisian limestones are thrusted over the Visean syncline and also display southward overturned folds. Beyond this thrusted and folded unit, a normal fault slightly offsets Tournaisian deposits (Figure 7a). Bedding measurements indicate that fold axes consistently trend NE-SW (Figure 6).

A marble slice delimited by two highly dipping tectonic contacts crops out north of this fold-and-thrust structure. It presents a well-developed N60°E foliation with a 50° to 60° southward dip (Figure 7b). The stretching lineation associated with this foliation has a pitch of 38°W, which gives a ~N220°E direction i.e., parallel to the fold axes in the Tournaisian-Visean cover. Asymmetric markers (boudins) show a top to the south-west normal sense of shear (Figure 7b). This oblique normal deformation can be associated with the exhumation of this marble unit in a strike-slip context with a NW-SE shortening and NE-SW stretching. To the North, this unit is thrusted northwards upon Lower Tournaisian limestones (Figure 7c). These limestones in turn overlay Devonian sandstones, where we could observe a minor shear zone probably associated with a decollement between both series.

Both large-scale fold axes in the Tournaisian-Visean sequences and ductile deformation of the marble units are thus compatible with a NW-SE shortening and a NE-SW stretching. We interpret this deformation as related to a ~E-W dextral strike slip deformational regime. The presence of the marble unit leads to several interpretations: (i) metamorphism and ductile deformation can be due to shear heating, so that the marbles could be highly deformed and metamorphosed Tournaisian limestones. (ii) alternatively, this unit can correspond to an older part of the Paleozoic cover, which was exhumed in the favor of the strike-slip fault zone. Unfortunately, there is no possibility to better constrain the depth at which these carbonates were deformed and metamorphosed.

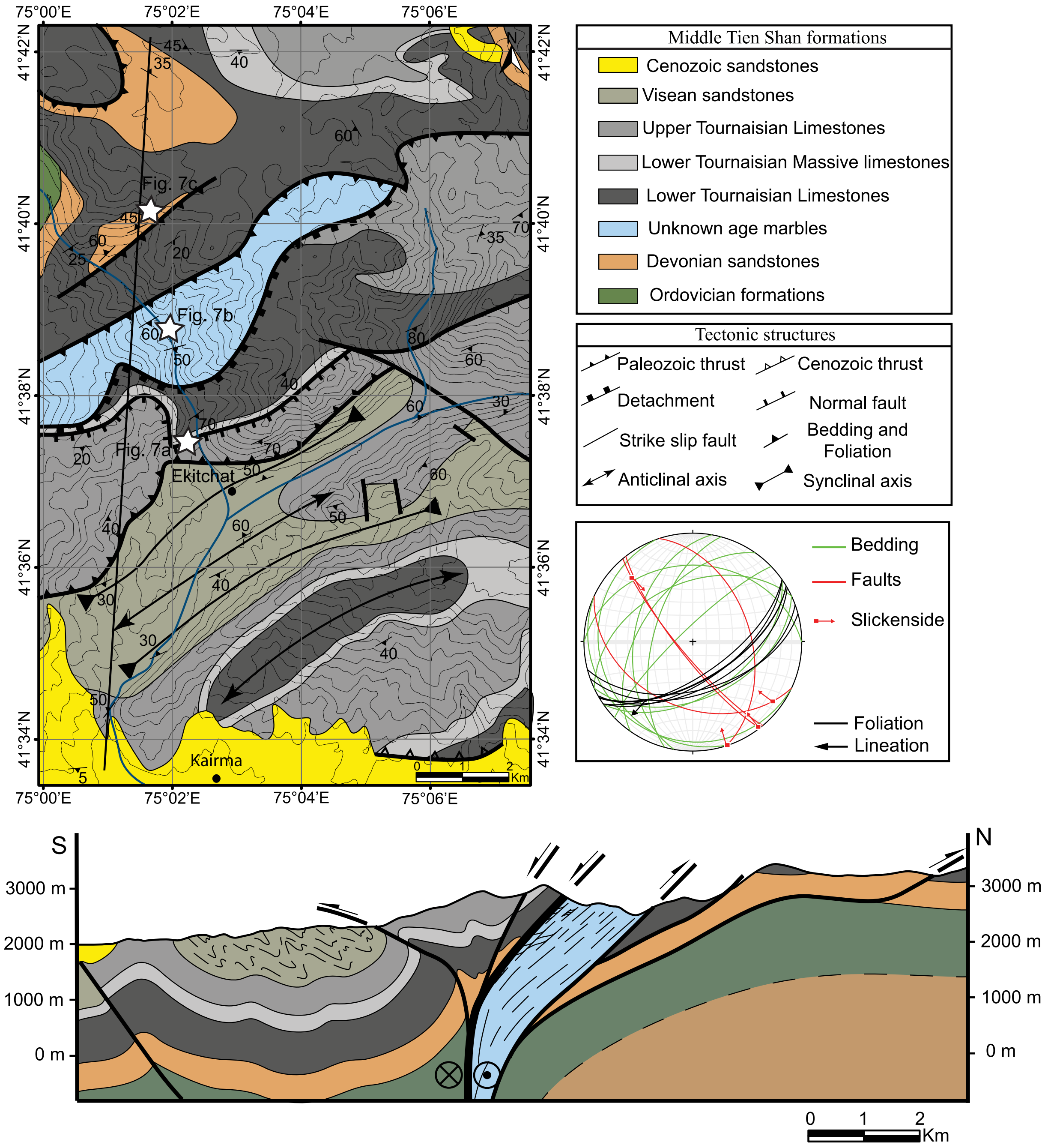

Figure 6 : Geological map and cross-section south of the Song Kul Lake. The thick black line indicates the cross-section location. The stars indicate the location of field pictures shown on Fig. 7. The stereoplot shows the projection, in the Schmidt diagram lower hemisphere, of the bedding, schistosity, lineation and faults measured in this zone. The thicker black line on the cross-section indicates a ductile detachment.

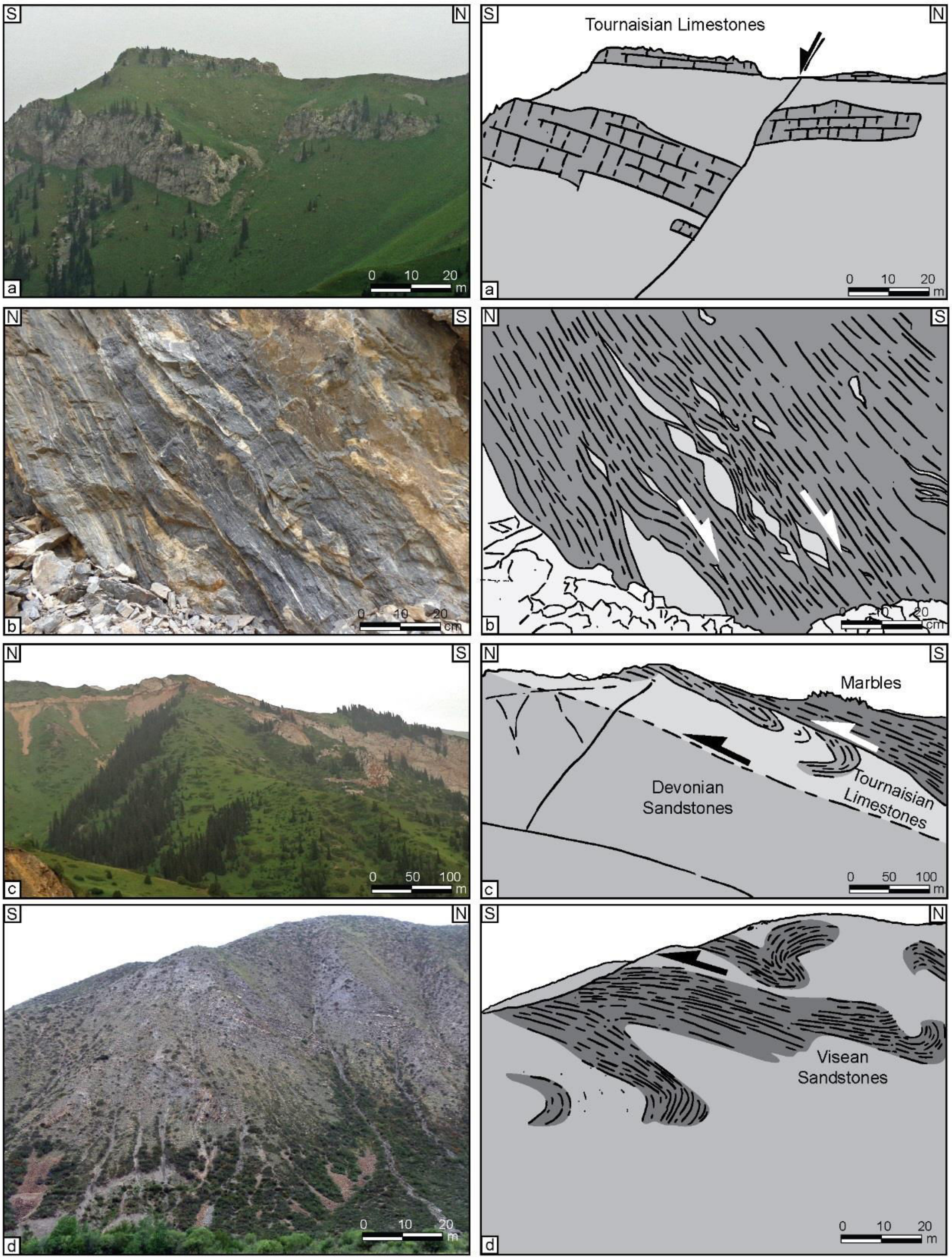

Figure 7 : Field pictures and their interpretations of the Lake Song Kul area. a. Normal fault in Carboniferous platform carbonates (Tournaisian) of the MTS; b. Deformed marbles with asymmetric top to the SW ductile shearing; c. Top to the North thrusting of the marbles on Tournaisian MTS carbonate platform and Devonian sediments; d. Southward overturned folds in Visean pelites and sandstones. Fig. 6 displays the location of pictures.

3.1.4. East Song-Kul area

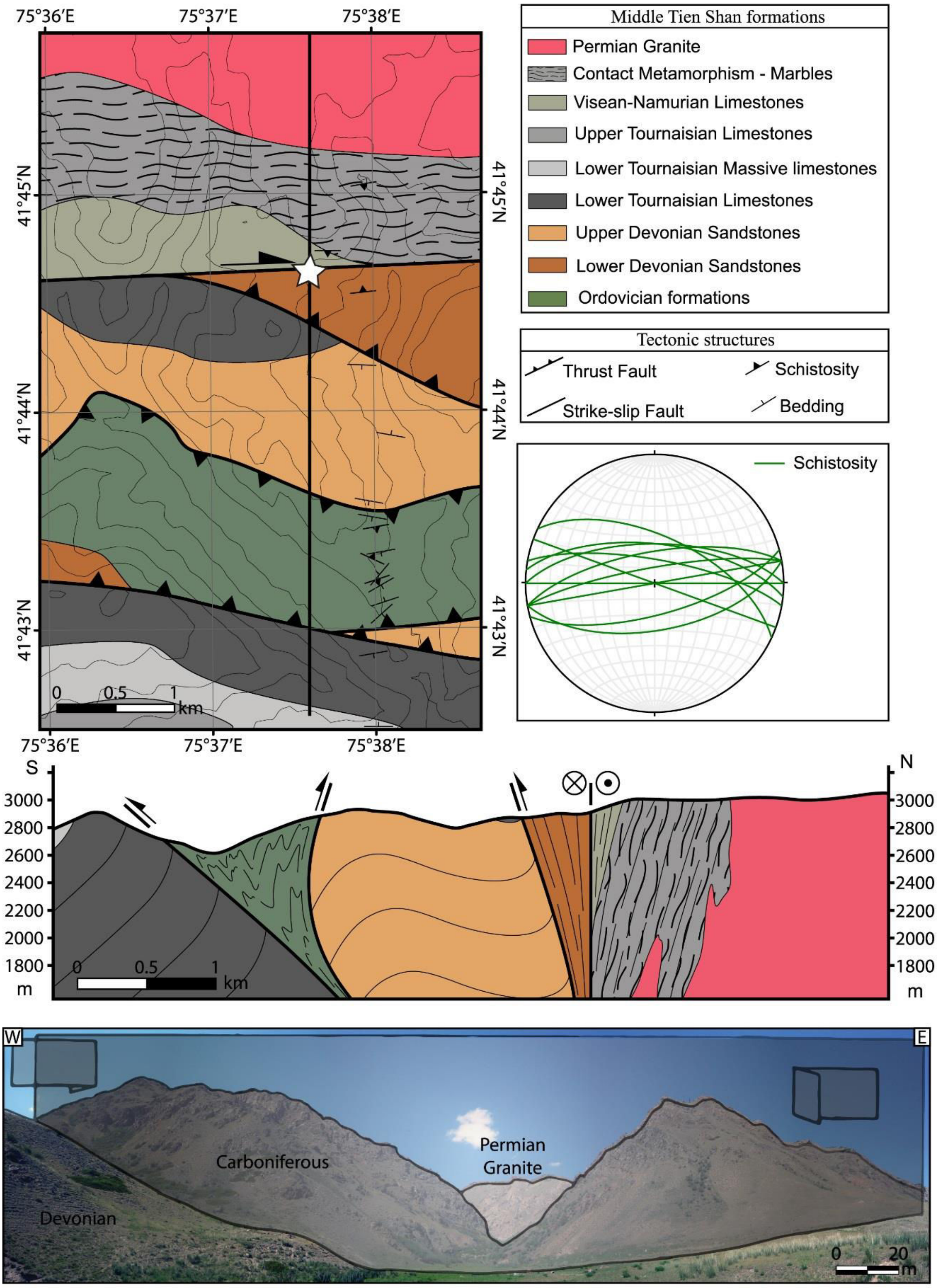

Figure 8 : Geological map and cross-section of the East Son-Kul area. The thick black line indicates the cross-section location. Star indicates the picture location. The stereoplot shows the projection, in Schmidt diagram lower hemisphere, of the schistosity measured in this zone. The picture shows the vertical dextral fault considered as the trace of the Nikolaev Line at the surface.

SE of Lake Song-Kul, a short NS valley crosses the Song-Kul zone and ends towards the North on the trace of a major strike-slip fault (often referred to as the Nikolaev Line, although, as explained above, this term has a more regional meaning). Basically, sediments of Ordovician to Carboniferous age are deformed by steep top-to-the-south thrusts and tight upright folds trending ~N80, sometimes accompanied by an almost vertical EW schistosity. More recent (Permian) intrusions following the trace of the fault caused high-temperature metamorphism in host (Carboniferous) sediments resulting in marbles formation.

Microtectonic measurements (bedding, schistosity, slickenslides, stretching lineations) on all these areas of the Song-Kul zone point out towards shortening and stretching directions oriented ~N135°E and ~N45°E, respectively (Figure 6). Schistosity follows the general NE-SW axis direction of main folds, except close to the strike-slip fault where it trends more E-W, i.e., parallel to the fault (Figure 8). Overall, the Song-Kul zone shows deformations compatible with a broad EW dextral strike-slip zone forming a positive flower structure, with fold and thrust axes trending between perpendicular to the shortening direction and parallel to the strike-slip fault.

3.2. Structural geology of the At-Bashi region

3.2.1. Lithology

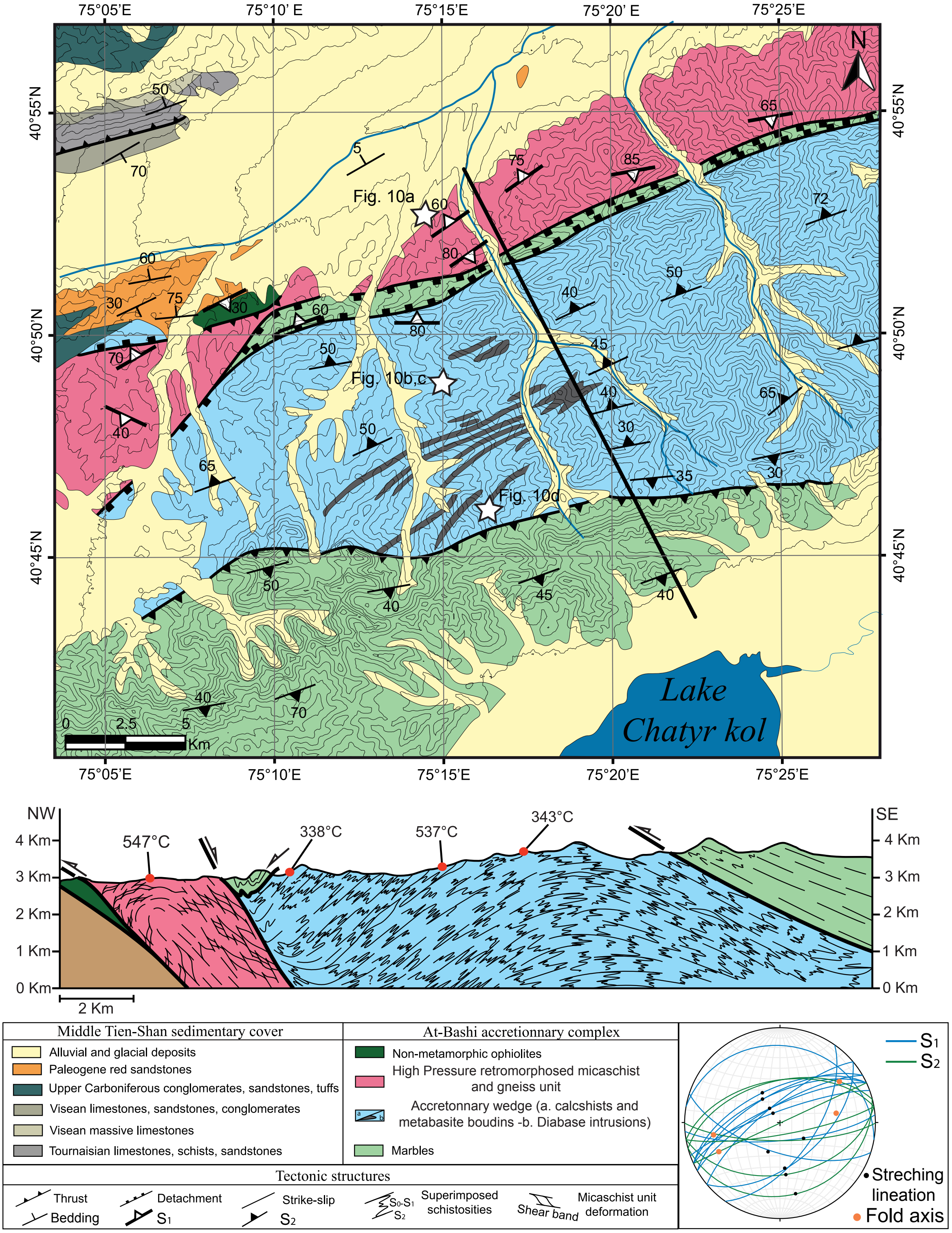

Figure 9 : Geological map and cross-section of the At-Bashi area modified after (Karpovitch et al., 1964). The thick black line indicates the cross-section location. The stars indicate the location of Fig. 10 pictures. Red dots on the cross-section indicate the location of the samples KG-14-58, KG-14-64 and KG-14-67 (from North to South). The stereoplot shows the projection, in the Schmidt diagram lower hemisphere, of the S1 (blue lines), S2 (green lines) schistosity, lineations (solid dots) and fold axis (orange dots) measured in this zone.

The At-Bashi accretionary complex (Figure 9) crops out south of the Cenozoic At-Bashi basin and is characterized by a tectonic stack of metamorphic units thrusted towards the North. We describe them below, from bottom to top in their present structural position:

- In some places, a slice of metamorphic continental basement crops out at the foot of the At-Bashi ridge. It is composed of granitoids and gneisses presenting a greenschist facies imprint (Loury et al., 2015b) and interpreted as a part of the MTS basement (Alekseev et al., 2007).
- A dismembered non-metamorphic ophiolite unit has been observed in several places of the At-Bashi range (Alekseev et al., 2009), with serpentinites, gabbros and radiolarites.
- A micaschist and gneiss unit bearing garnet, phengite and quartz underwent High-Pressure (HP) metamorphic conditions (500-660°C– 20-25 kbar) and is interpreted as a retrogressed eclogitic continental unit (Loury et al., 2015b). In some places, this HP continental unit overlays a metasedimentary unit containing lenses of mafic eclogites with similar metamorphic conditions (Loury et al., 2015b; Simonov et al., 2008; Tagiri et al., 1995).
- An accretionary wedge unit made of calcshists and sandstones of Silurian to Carboniferous age (Alekseev et al., 2007) and metabasite boudins, which recorded blueschist and greenschist facies metamorphism, constitutes the largest part of the At-Bashi range (Figure 10b and 10c).
- A thick pile of marbles of possible Silurian to Devonian protolith age (Burtman, 2008; Karpovitch et al., 1964) is generally observed on top of the accretionary wedge (Figure 10d).
- A Late Carboniferous to Early Permian conglomerate with serpentines and eclogites pebbles unconformably overlies the former units (Alekseev et al., 2007).

Simonov et al. (2008) dated the At-Bashi HP units with the $^{40}Ar/^{39}Ar$ method on phengite at 327 ± 4 Ma, and more recently Hegner et al., (2010) obtained Sm/Nd isochron age of 319 ± 4 Ma and a $^{40}Ar/^{39}Ar$ on phengite age of 316 ± 3 Ma interpreted as a crystallization age at the pressure peak and a cooling age, respectively.

Cenozoic deposits of the Naryn and At-Bashi basins rest with an angular unconformity upon Paleozoic formations.

3.2.2. New structural observations of the MTS and STS in the At-Bashi region

Between the Cenozoic Naryn and At-Bashi basins (Figure 2), Paleozoic sediments of the MTS crop out along an elongated discontinuous range made of en-echelon segments, which are uplifted and tilted by Cenozoic E-W South verging thrusts.

The At-Bashi and Naryn basins themselves are characterized by a moderate deformation with long-wavelength folds and South-verging thrusts, which are rooted probably at the interface between Paleogene and Paleozoic formations (Figure 4). The MTS South of the Song-

Kul zone and North of At-Bashi is largely covered by Cenozoic basins, which complicates the precise characterization of Paleozoic deformations.

The At-Bashi accretionary complex (Figure 9) is uplifted by a Cenozoic North-verging thrust over the At-Bashi basin. In the accretionary complex, the micaschist and gneiss unit is thrusted northward onto the ophiolitic unit, the latter being also thrusted northward over the metamorphic basement. The micaschist unit displays top-to-the-North ductile shear criteria (Figure 10a) associated with a top-to-the-South ductile shearing on a South-dipping normal shear zone separating this unit from the accretionary wedge (Figure 9). These deformations have been interpreted as resulting from the exhumation of this high grade metamorphic unit as further East in the Tash-Rabat area (Loury et al., 2015a).

In the accretionary wedge itself, the deformation is characterized by a pervasive S_1 schistosity that may develop on former bedding (S_0) planes. These S_0-S_1 planes are intensely folded and associated with the development of an axial planar schistosity S_2 globally trending NE-SW and dipping toward the North (Figure 9). The S_2 schistosity is moderately folded by a late deformation stage (Figure 9), which age is unconstrained. Shortening direction inferred from schistosity fold axes and lineations is approximately N165°E, i.e., rotated clockwise by 20° with respect to the Song-Kul zone (Figure 9). Both schistosities S_1 and S_2 display similar kinematics, which suggest that they correspond to a continuous deformation.

In order to better constrain the internal structure of the accretionary wedge and the temperature difference between the micaschist HP unit and the wedge unit, three samples collected in the wedge unit (KG-14-58, KG-14-64 and KG-14-67) and one sample in the HP unit (KG-11-43) (Figure 9) have been analyzed with Raman spectroscopy of Carbonaceous Material (RSCM). This method is based on the estimation of the degree of organization of the carbonaceous matter (CM) by Raman microspectroscopy (Beyssac et al., 2003, 2002). As this organization is temperature-dependent and persists during retrogression, this method allows determination of the maximum temperature (Tmax) reached by the samples (e.g. Beyssac et al., 2004; Cottle et al., 2011; Rahl et al., 2005). Spectra obtained on samples from the At-Bashi complex provide temperatures of 338 ± 3°C, 537 ± 7°C and 343 ± 2°C for KG-14-58, KG-14-64 and KG-14-67 respectively, and 547 ± 4°C for KG-11-43 (Table 1 and Figure 9). Tmax for the central sample (KG-14-64) of the wedge unit can be explained either by: (i) an antiform structure in the accretionary wedge with deeper, higher grade rocks in the core than on the flanks; (ii) a tectonic mélange within the accretionary wedge where high grade metamorphic slices are mixed with low-grade metamorphic sediments during subduction and subsequent exhumation. In any case, the structure has then been re-folded during the exhumation and collision events.

Finally, the marbles unit overlays the accretionary wedge and micaschist units with a northward kinematics (Figure 9). This allochtonous unit was therefore probably emplaced at the final stage of the collision.

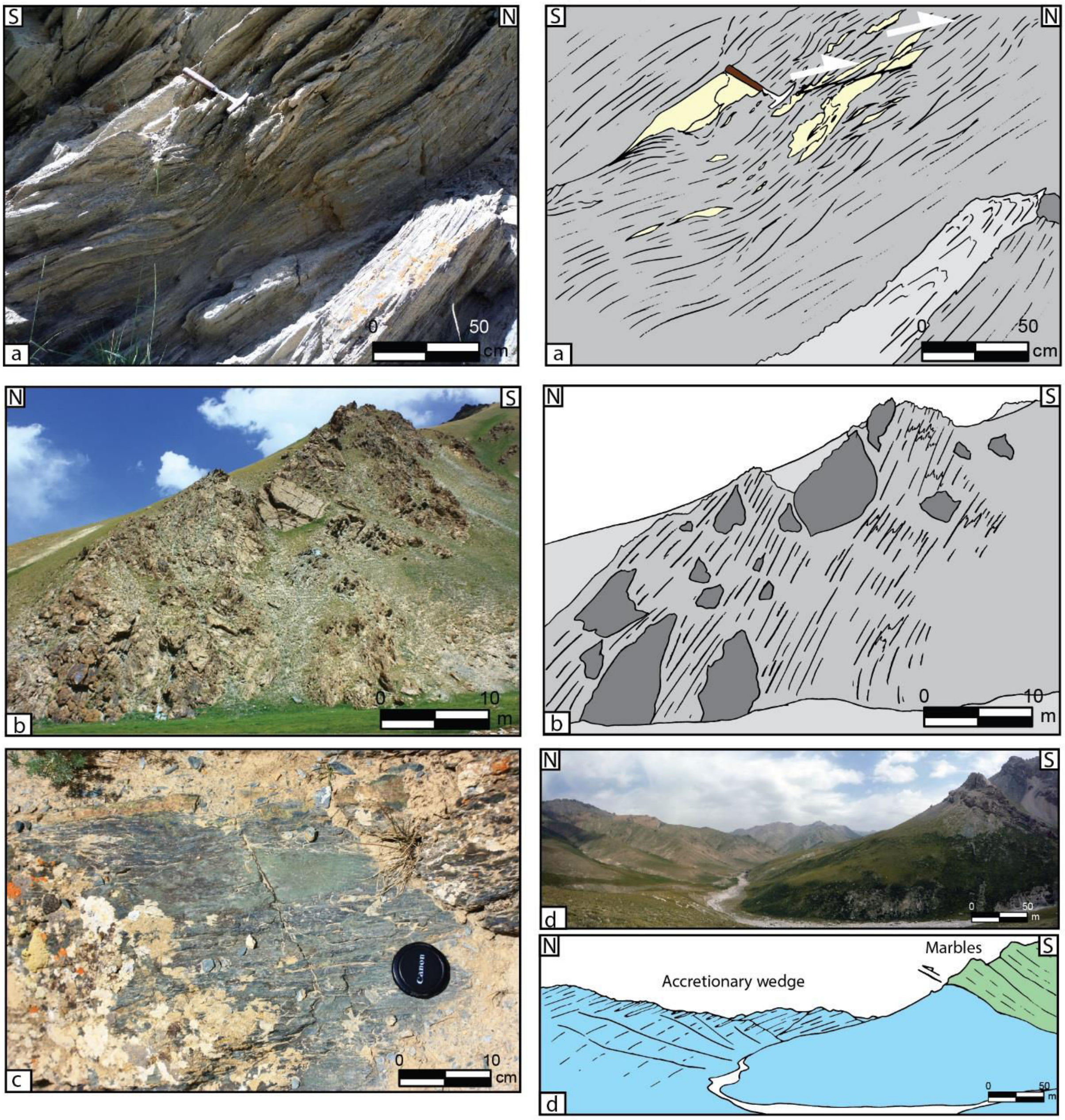

Figure 10 : Field pictures and their interpretations of the At-Bashi accretionary complex. a. Top-to-the north asymmetric shearing in the micaschist unit. b. Accretionary wedge with metabasite boudins. The S0–S1 is folded and a S2 schistosity is developed in the axial fold planes. c. Metabasite boudin metamorphosed in the blueschists facies. d. Northward thrusting of marble units onto the accretionary wedge. See Fig. 9 for the location of pictures.

3.3. The South Tien Shan in Khan-Tengri region

In the Khan-Tengri area (Figure 11), the STS is mainly composed of Paleozoic metamorphic sedimentary rocks. The oldest formations are of Silurian-Early Devonian age (Zubovich et al., 2008) and consist of light-grey marbles and schists. The Devonian is characterized by metamorphosed sandstones and limestones. The Carboniferous is represented by a succession of thin limestones and dark marls beds. In the Pobeda Massif, a granulitic unit is thrusted over the latter (Loury et al., 2015b).

3.3.1. New structural observations and cross-section in the Khan-Tengri massif (STS)

Unlike the At-Bashi massif, the STS in the Khan-Tengri massif does not display typical features of an accretionary complex, but rather corresponds to a nappe stack of several sedimentary units affected by a long wavelength (several km) folding possibly of Cenozoic age. The vertical structure of the Khan-Tengri massif can be observed in tectonic windows where Carboniferous and Devonian formations appear overthrusted by Silurian marbles and schists (Figure 11). In the tectonic window of the Khan-Tengri massif, a polyphase ductile deformation with two deformation stages is clearly visible in Carboniferous sediments:

1- A top-to-the-South shearing creates large-scale tight ductile folding of the bedding S_0 and leads to the development of a north-dipping S_1 schistosity in the axial plane of the folds (Figures 11, 12a, 12b and 12c).

2- A top-to-the-North shearing reworks the S_1 schistosity in some places via small-scale folds and creates a south-dipping S_2 schistosity in the axial planes of S_1 folds. This S_2 is in turn deformed by an asymmetric top-to-the-North shearing (Figures 11, 13a, 13b and 13c). Lineations indicate a ~NNW-SSW transport direction, i.e. slightly oblique to the normal to schistosity planes.

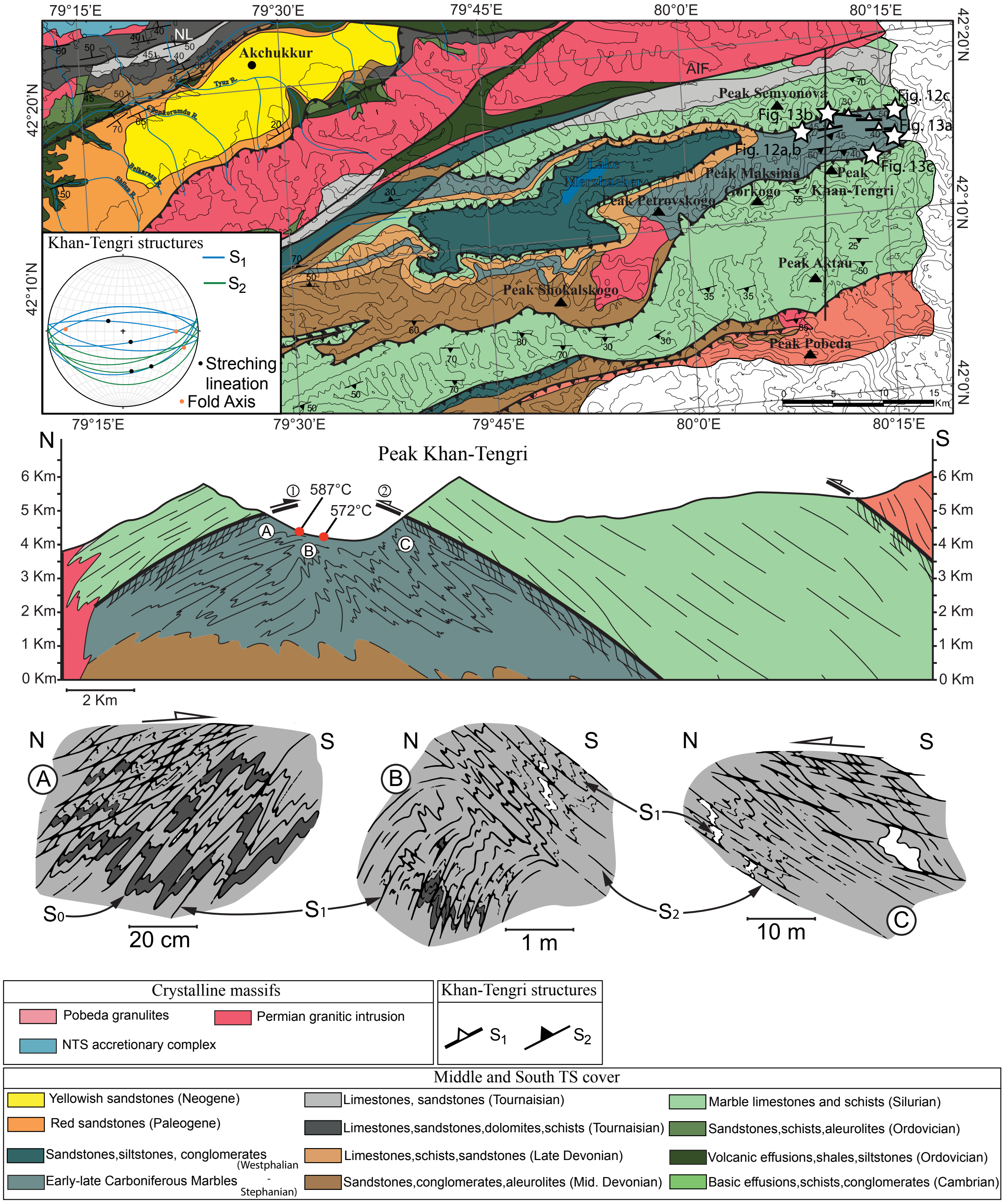

Figure 11: Geological and structuralmap (Modified after (Zubovich et al., 2008)) and cross-section of eastern KyrgyzMiddle and South Tien Shan in the Khan-Tengri region. NL:Nikolaev Line. AIF: At-Bashi-Inylchek Fault. The thick black line indicates the cross-section location. The stars indicate the location of field pictures shown on Figs. 12 and 13. The red dots on the crosssection indicate the location of the samples KG-14-18 and KG-14-20 (fromNorth to South). 1. Top-to-the south deformation. 2. Top-to-the north deformation. A, B and C represent detailed structures visible along the N-S cross-section (See pictures on Figs. 12 and 13). The stereoplot shows the projection, in the Schmidt diagram lower hemisphere, of the S1 (blue lines), S2 (green lines) schistosity, lineations (solid dots) and fold axis (orange dots) measured in this zone.

A non-ambiguous relative chronology can be established due to the overprint of phase (1) by phase (2) as evidenced by the deformation of the top-to-the-South structures by the top-to-the-North deformation phase (Figures 11, 13a, 13b and 13c). Moreover, whereas the S_1-related ductile folding is widely distributed and affects the whole sedimentary pile in the Khan Tengri window, the S_2 deformation is mostly visible near its southern limit where it completely overprints the S_1. On the contrary, near the northern limit of the window, S_2 is barely visible

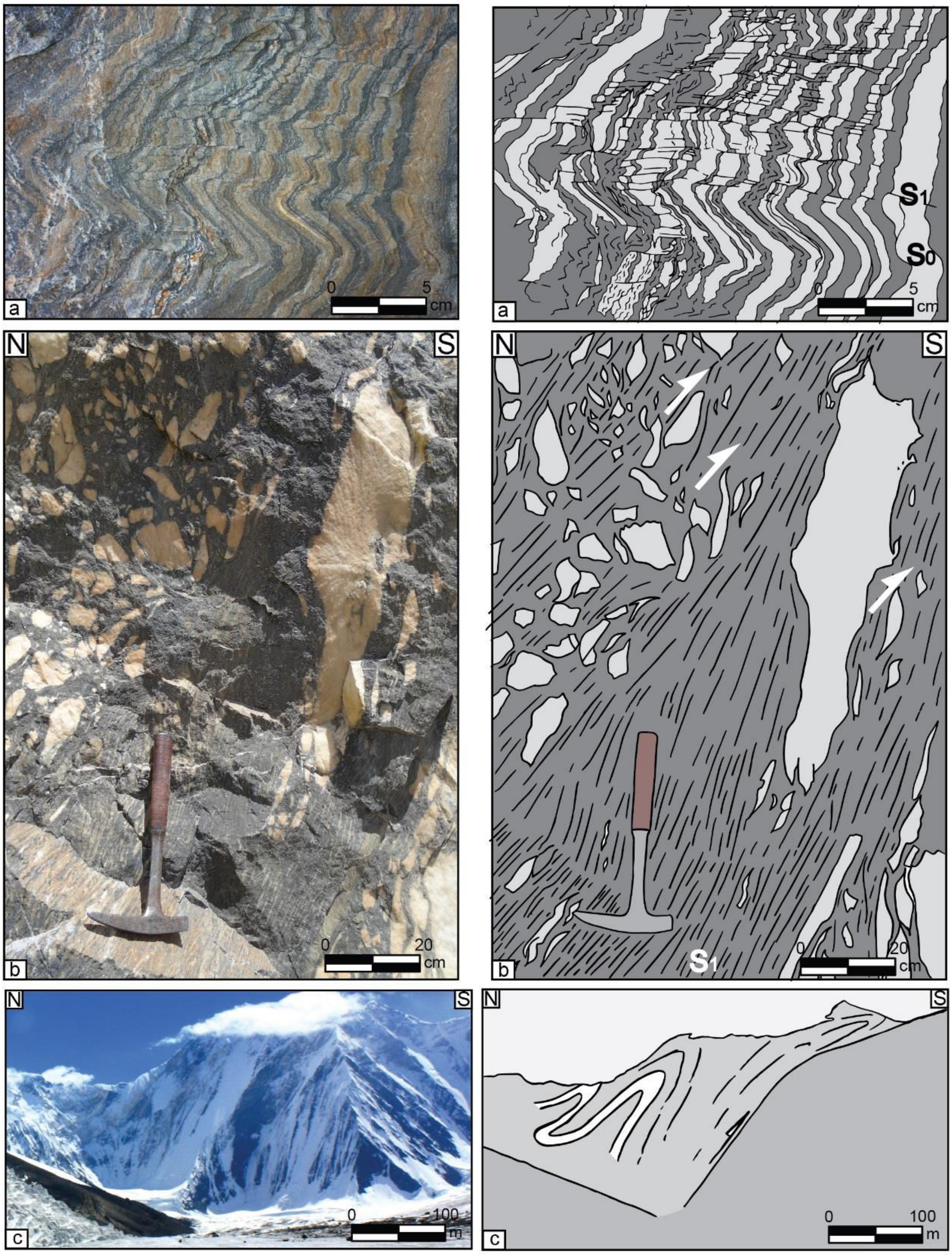

Figure 12 : Field pictures and their interpretations in the Khan-Tengri tectonic window. a. Development of the S1 schistosity in the axial fold planes of the S0. b. Top-to-the-South shearing of the S1 schistosity. c. Large-scale southward overturned ductile folds in the STS meta-sediments. See Fig. 11 for the location of pictures

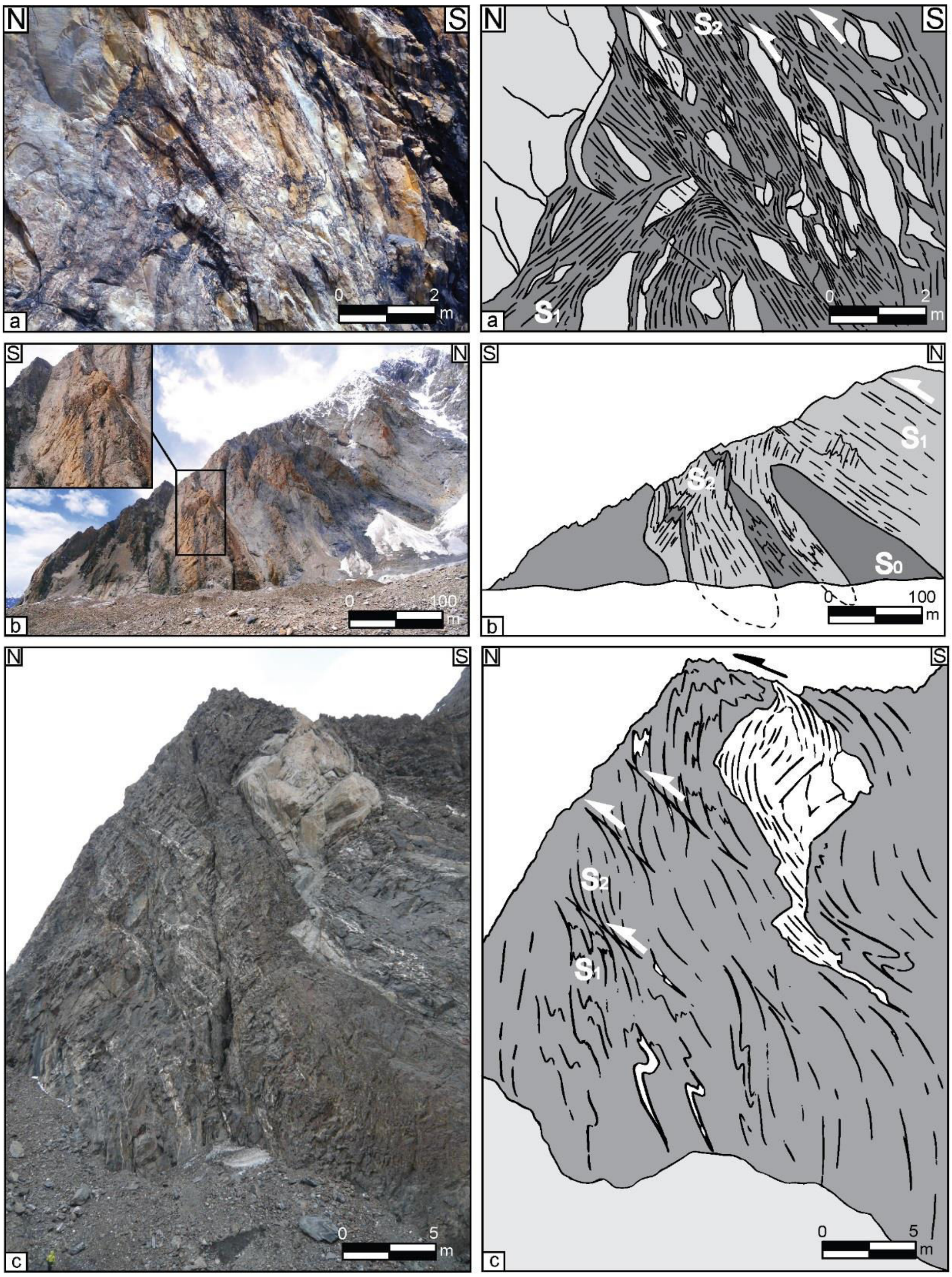

Figure 13 : Field pictures and their interpretations in the Khan-Tengri tectonic window. a. Development of the S2 schistosity in the axial folds planes of the S1 schistosity and its top-to-the- North shearing. b. Large scale southward overturned folds of the S0 associatedwith the development of the S1 schistosity in the axial fold planes of the S0 and top to the south shearing. The S1 schistosity is then folded and associated with the development of the S2 schistosity in the axial fold planes of S1 and top to the North shearing. The blow-up shows the development of the S2 in the axial fold planes of the S1. c. Top to the North shearing of the S2 schistosity. See Fig. 11 for the location of pictures.

(Figure 11, 12c and 13b). Hence, it looks like that the S_2 schistosity is more localized than S_1 and is associated with a major top-to-the-North thrust in the southern part of the Khan-Tengri window.

Two samples (KG-14-18 and KG-14-20) collected in the tectonic window of the Khan-Tengri massif (Figure 11) have been analyzed with RSCM (Beyssac et al., 2003, 2002). Spectra obtained on these two samples provide temperatures of 587 ± 9°C and 572 ± 5°C for the samples KG-14-18 and KG-14-20 respectively (Table 1) evidencing a peak temperature slightly warmer than that of At-Bashi continental HP metamorphic unit.

Finally, South of the Khan Tengri massif, the granulitic unit of the Pobeda Massif is thrusted along a top-to-the-North shear zone upon Paleozoic formations (South of the Figure 11 frame) (Loury et al., 2015b) but the age (Paleozoic or Cenozoic) of this thrust remains unknown.

4. Discussion and structural interpretation of the Tien Shan accretionary belt during the Paleozoic.

4.1. *Paleozoic structures of the Kyrgyz Tien Shan*

4.1.1. The Song-Kul Zone and the Carboniferous deformation of the North Middle Tien Shan

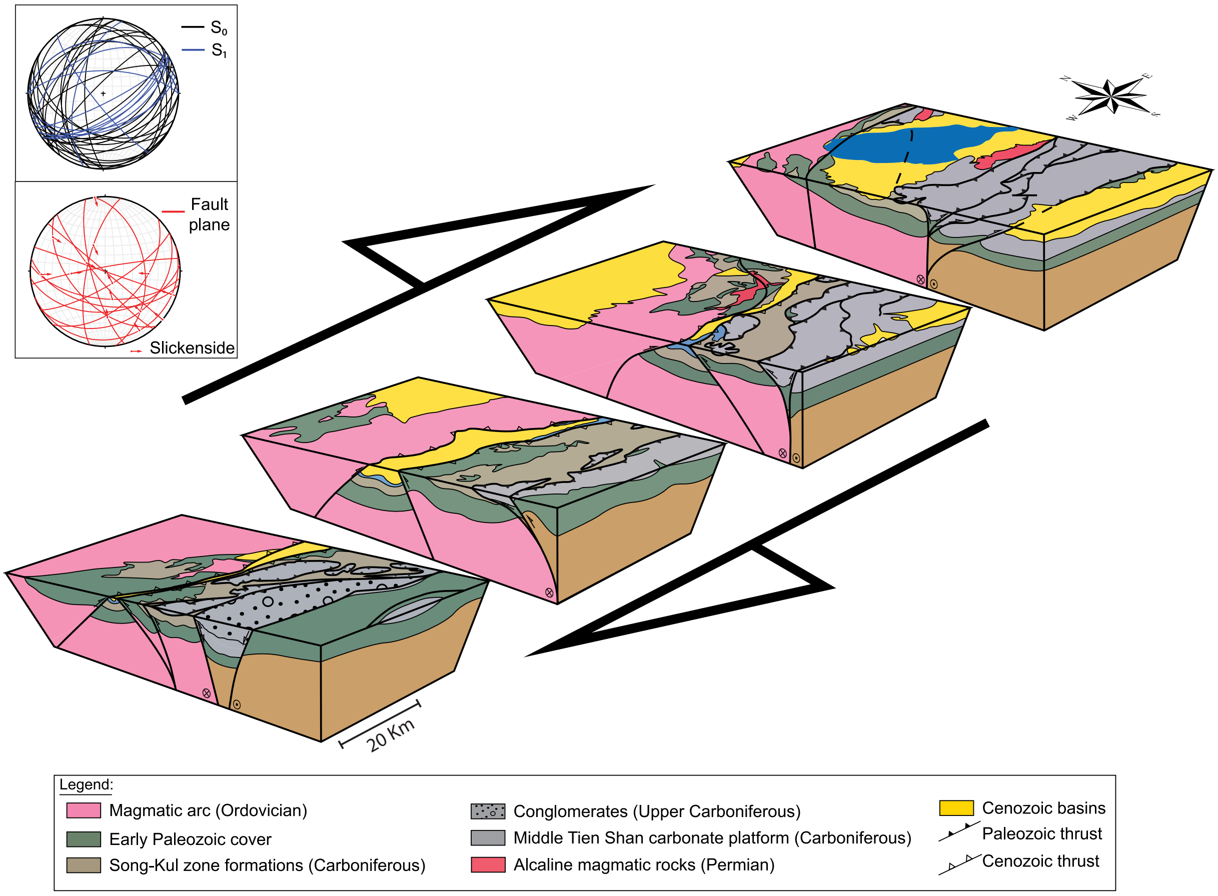

Figure 14 : 3D interpretative structural diagram of the dextral shear zone of the Song-Kul Zone showing the lateral (from West to East) correlation of the structures associated with the strike-slip shear zone during Late Carboniferous times. Stereoplots represent stratigraphic (black lines), schistosity (blue lines) and faults (red lines) planes measured in the Song Kul Zone and projected in the Schmidt projection lower hemisphere.

Field observations and compilation of bibliographic data in the Song-Kul zone highlighted the presence of both South and North verging thrusts and folds oriented ~NE-SW. Tectonic and structural analyses provide consistent NW-SE shortening direction and NE-SW stretching direction in both ductile and brittle deformation fields over the whole Song-Kul area. Some NW-SE strike-slip faults appear to act as lateral ramps for the NE-SW thrusts and folds systems. Although its age is poorly constrained, the presence of a NW-SE rhomboidal conglomeratic basin bounded by rectilinear faults in the Toktogul area is compatible with the NE-SW stretching direction. The latter is also visible in a deformed marble unit with a clear stretching lineation. Close to a major EW fault, fold axes and schistosity trend parallel to the direction of the fault. According to the fold and thrust orientations, the orientation of ductile stretching lineation and foliations, we propose that this system worked as a large-scale broad dextral shear zone oriented East-West (Figure 14). This shear zone controlled the regional-scale northward thrusting of the MTS cover over the NTS, but also the southward thrusts and folds in the MTS cover and the local development of NW-SE strike-slip faults and/or pull-apart basins in a large flower structure. Along the Song-Kul zone (Figure 2), the most striking feature is the northward thrusting of the MTS Carbonate platform over the NTS detrital and volcanic sequences. Beneath this main thrust, the deformation of the NTS is moderate both in the Ordovician substratum and its Carboniferous cover, represented by large wavelength folds and minor thrusts of unknown age (Figure 4).

Chronological relationships between the different units lead us to interpret the thrust and fold structures described above as of Late Carboniferous in age. Indeed, in the Toktogul area, Cenozoic deposits seal a northward thrust in Carboniferous formations (Figure 3). Moreover, Cenozoic formations cropping out inside the mountain range are flat-lying, although uplifted with respect to their basin counterparts. This suggests that Cenozoic shortening is mostly localized on the basin bounding thrusts and that mountain areas have undergone mostly block uplift with only minor internal shortening. The presence of a Late Carboniferous to Early Permian conglomerate sealing the thrusts provides an upper bound for the age of this deformation (i.e., Bashkirian, Bazhenov et al., 2003). The transpressional deformation observed along the northern suture is thus synchronous with the continental collision in the At-Bashi and Khan-Tengri areas; it can therefore be related to the accretion of the Tarim continent against the Kazakh-Yili continental block southward. We thus propose that deformation propagated northward inside the MTS-NTS block up to the Nikolaev line, which was reactivated as a large dextral shear zone. This suggests that the convergence between the Tarim and Kazakh-Yili continents was oblique.

This transpressional deformation developed on the former Ordovician suture between the NTS and the MTS. Although the NTS and the MTS were already accreted during the Carboniferous, they were characterized by different sedimentary conditions, with gypsum and sandstones in the NTS and platform carbonates in the MTS. The Song-Kul zone in the Early Carboniferous was therefore an old continent-shelf transitional domain of the NTS-MTS continent. This broad EW wrench zone that separates the NTS from the MTS, which is the original definition of the Nikolaev line (Nikolaev, 1933), was therefore a crustal-scale structure until at least the middle Carboniferous.

During the Permian, this area was characterized by a dominant strike-slip deformation regime associated with ~E-W strike-slip faults and by the intrusion of granitic plutons (Alekseev et al., 2009; Biske et al., 2013; Chen et al., 2009; Choulet et al., 2012, 2011; Mikolaichuk et al., 1997; Seltmann et al., 2011; Wang et al., 2009). Whether Permian wrench tectonics took place in the continuity of Carboniferous deformations, or in a completely different setting is difficult to assess. A possible interpretation for the NTS-MTS boundary is that it was activated as a wide strike-slip to transpressional area in the late Carboniferous (with North- and South-verging thrusts) and became a more localized strike-slip zone in the Permian.

4.1.2. The STS deformation

In the STS, a major top-to-the-North ductile thrust structure is well marked in the accretionary complex of At-Bashi (Figure 9), particularly in the micaschists unit. To the South, the accretionary complex is uplifted and exhumed along a conjugate south-verging thrust, which separates this unit from the less deformed Devonian-Carboniferous series of the STS-Tarim. In China, similar units and kinematics are found in the same structural position, along the north boundary of the STS (Charvet et al., 2011, 2007). A similar HP accretionary complex is observed north of the Khan-Tengri nappes stack on the Chinese side (e.g. Tian and Wei, 2013).

The tectonic nappes observed in the Khan-Tengri massif (Figure 11) present temperature range comparable to (or slightly higher than) the highest metamorphic grade units of the STS (Loury et al., 2015b; Simonov et al., 2008; Tagiri et al., 1995; Tian and Wei, 2013). However, the structural position of the Khan-Tengri massif is still unclear and we cannot affirm that these metamorphic sediments are equivalent to the high-grade metamorphic micaschist and gneiss units of At-Bashi. These nappes of Paleozoic sediments are characterized by two superimposed deformation phases where a first top-to-the-South deformation phase is reworked by a second top-to-the-North deformation phase (Figures 11, 12 and 13).

Comparison betwen the Khan-Tengri and At-Bashi regions allow us to propose that the ductile deformation stage characterized by top-to-the-North thrusts corresponds to the same tectonic episode, i.e. to the collision between the Tarim and the Kazakh block. This episode corresponds to the development of the S_2 schistosity in both massifs. Oppositely, the origin of the older S_1 schistosity associated with a top-to-the-South kinematics in the Khan-Tengri area is more difficult to interpret. It can be associated with the exhumation of metamorphic units in the At-Bashi area (evidenced by a top-to-the-South ductile detachment) and correspond to the exhumation of MTS-derived sedimentary units underthrusted beneath the Tarim. The detachment must have then be refolded in the Khan-Tengri area, since it is now a north-dipping reverse structure.

Otherwise, the top-to-the-South deformation in the Khan-Tengri massif could be related to the northward burial of this unit beneath the MTS while the already buried At-Bashi HP unit was exhuming (see Beaumont et al., 2009 for details about exhumation processes in collision zones). In this second hypothesis, the top-to-the-South deformation is associated with the underthrusting of the Tarim beneath the MTS. In this case, the At-Bashi and Khan-Tengri units need to be back-thrusted over the MTS in later stage of deformation to reach their final structural position.

This typical collisional deformation sequence has been described similarly in the Chinese TS (Lin et al., 2009; B. Wang et al., 2010). Numerous thermo-mechanical models of collision zones show continental units that are firstly exhumed along detachment structures and then folded, shortened and thickened during the collision (e.g. Beaumont et al., 2009; Duretz and Gerya, 2013; Z. H. Li et al., 2011; Warren et al., 2008).

Considering the age of sedimentary and magmatic rocks affected or not by this deformation (e.g., Alekseev et al., 2007), we bracket this collisional tectonic event between the Late Carboniferous and the Permian.

Our field data therefore allow us to constrain the collisional event that shaped the STS area at the end of the Paleozoic. However, we cannot bring here decisive arguments in the controversy concerning the vergence of the Carboniferous subduction that preceded collision, because the upper crustal structure is compatible with both senses of subduction. Oppositely, the deep crustal and lithospheric structure should be different depending on the subduction vergence and should influence the Cenozoic deformation in a way that has to be quantified, possibly by thermo-mechanical modelling.

4.2.Middle Carboniferous NTS/MTS/STS kinematics

Based on these new field observations we propose a synthetic 3D diagram and kinematic interpretation of the NTS-MTS and MTS-STS sutures during Late Paleozoic (Figure 15).

During the middle/late Carboniferous collision between the Tarim block and the NTS/MTS continents, the southern suture (At-Bashi) between STS and MTS developed as a rather classical frontal collisional complex, where previously subducted metamorphic rocks were exhumed as different tectonic slices trending parallel to the direction of the range (Figure 15). Oppositely, the MTS/NTS suture was an E-W strike-slip dextral structure with all classically associated deformations (negative and positive flower structures, Figures 14 and 15). These observations suggest that: 1) the collision between the Tarim continent and the Kazakh platform was at least slightly oblique and was accommodated by strain partitioning, with a dip-slip deformation at the colliding plate boundary and a strike-slip deformation further north in the continental plate; 2) the reactivation of the Nikolaev line as a strike-slip zone was favored by a preexisting E-W vertical structuration, otherwise such a strain partitioning would be unlikely. It is therefore possible that the Ordovician accretion of the MTS against the NTS had already occurred in a context of strike-slip setting, similar to today's accretion along the San Andreas

Fault (SAF) in the NW America (e.g. Atwater, 1970; Furlong et al., 1989). In this area, oblique convergence between North America and Pacific plates is accommodated by strike-slip faulting along the SAF, which led to the detachment and shortening of a continental block (the Salinian block) against the western North American margin (e.g.Tavarnelli, 1998). This could be a good modern analogue to the MTS/NTS Early Paleozoic tectonics.

Considering very simple plate geometries and kinematics during the Late Carboniferous collisional episode, we can schematically draw the following relative plate kinematics (Figure 15):

- The MTS/STS convergence vector was approximately NNW-SSE (in present coordinates), i.e., perpendicular to the At-Bashi suture, which at the time of the collision belonged to the upper plate (i.e., to the STS-Tarim) according to the north-verging thrusts kinematics. Indeed, whether it was initially a south-dipping or a north-dipping subduction, the STS-Tarim always ends up overthrusting the MTS during the collision stage.

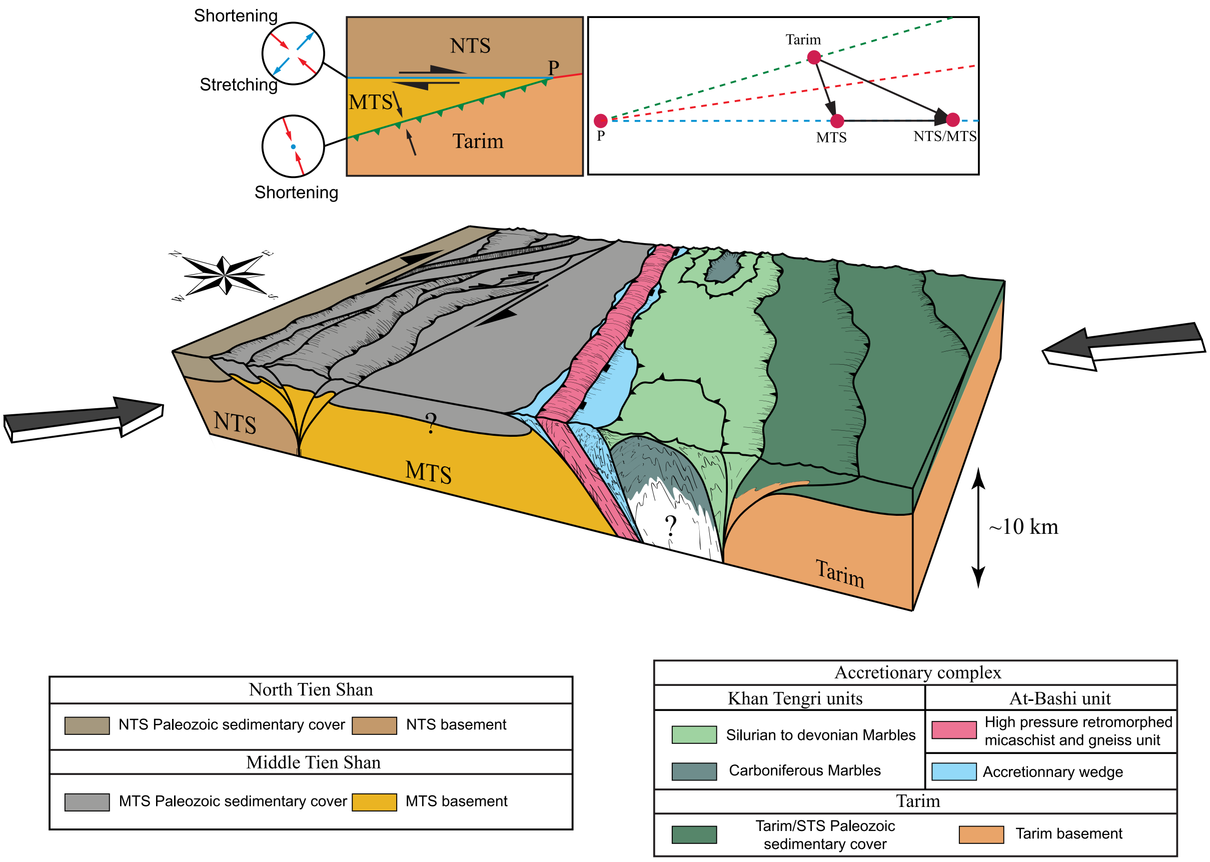

Figure 15 : Structural and kinematic scheme of the Middle-Late Carboniferous oblique collision between the Tarim and the Kazakh platform, with a strain partitioning between a frontal collision to the south and a strike-slip motion to the North. Inset shows possible schematic block boundaries geometry (left) with mean strain directions compatible with field observations, and velocity triangle (right, no scale); plate boundaries are delineated with different colors. P is the Tarim-NTS-MTS triple junction.

- Meanwhile, the MTS/NTS vector was approximately EW, i.e., parallel to the Nikolaev line. Depending on the relative lengths of both vectors, the relative NTS/STS convergence could have trend approximately NW-SE or WNW-ESE.
- During the collision, this construction can give a stable triple junction located west of the MTS point in the velocity triangle if we assume that the NTS/STS block boundary east of the triple junction was an intraplate oblique convergence zone oriented NE-SW to ENE-WSW. In this case, the NTS/MTS/STS triple junction was migrating fast towards the west, which is consistent with other kinematic reconstructions (Wilhem et al., 2012).

Conclusion

This study brings new structural data and insights on the timing, nature and extent of Late Paleozoic deformations based on field observations undertaken in the Kyrgyz Middle and South TS. The main phases of deformation are:

- (1) A Middle to Late Carboniferous top-to-the-south deformation phase in the Khan-Tengri region, possibly coincidental with top-to-the-south detachment on the top of the At-Bashi continental unit. This deformation phase can be interpreted as the exhumation of continental-derived units that were previously underthrusted beneath the Tarim.
- (2) A Late Carboniferous top-to-the-North deformation phase, which postdates the top-to-the-south structures in the Khan-Tengri massif. We ascribe this deformation stage to a nappe stack related to the collision between the MTS and the Tarim craton during the Late Carboniferous, based on the age of the pressure peak in At-Bashi HP units and on the age of overlying conglomerates.
- (3) A Late Carboniferous deformation stage characterized by the deformation of the MTS and its thrusting over the NTS. This deformation occurred on a large dextral shear zone between the NTS and the MTS known as Song-Kul Zone or Nikolaev Line and was a “far-field effect” of the Tarim/MTS collision.

Acknowledgments

This work is part of the first author’s PhD thesis granted by the French Ministry of Research. Field studies were supported by the project DSP-Tibet funded by the Agence Nationale de la Recherche (ANR-13-BS06-012-01). Additional support was provided by the Darius programme. Many thanks to Olivier Beyssac and Alberto Vitale-Brovarone (IMPMC, Paris, France) who trained A.J. on the RSCM method. Thanks to Alexander Mikolaichuk (Institute of Geology, National Academy of Science, Bishkek, Kyrgyzstan) for being our guide during this field work. We also thank Editor in chief M. Santosh and Associate Editor Y. Dong for their help, and Michel Faure and three other anonymous reviewers for their constructive remarks. Data presented in this paper are in the figures, tables and the supplement and are available on request at jourdon@geoazur.unice.fr.

III. Rôle et influence de l’héritage structural sur la localisation de la déformation

Le rôle de l’héritage structural est une question clé concernant les processus de déformation continentale. Dans de nombreux contextes (extensif, compressif ou décrochant) la pré-structuration de la lithosphère est invoquée pour expliquer la localisation de la déformation au cours d’une phase tectonique. La structure de la chaîne pyrénéenne est par exemple fortement contrôlée par les failles héritées du rift continental ayant précédé la collision entre l’Ibérie et l’Europe (e.g Calignano et al., 2015a; Desegaulx et al., 1990; Jammes et al., 2014; Velasque et al., 1989). De la même manière, certaines structures compressives de la chaîne des Alpes sont liées à la structuration des bassins et du socle par d’anciennes failles normales téthysiennes (e.g. Bellahsen et al., 2014, 2012; Gillcrist et al., 1987; Jourdon et al., 2014; Lemoine et al., 1986). Cependant, les paramètres exerçant un contrôle sur la déformation de la lithosphère continentale sont nombreux et difficiles à quantifier. En effet, grâce à la modélisation numérique nous savons désormais que l’héritage structural ne représente pas simplement d’anciennes failles susceptibles d’être réactivée mais plutôt:

1- Des variations de lithologies latérales et/ou verticales liées à l’activité d’anciennes failles (ou zones de cisaillement) normales ou aux processus de mise en nappe (e.g. Buiter and Pfiffner, 2003; Lafosse et al., 2016; Le Pourhiet et al., 2004).

2- Les variations de l’état thermique de la lithosphère : une lithosphère plus froide est plus résistante et inversement, une lithosphère plus chaude l’est moins (Figure III-1) (e.g. Burov, 2011; Burov and Diament, 1995; Toussaint et al., 2005).

3- Les variations de rhéologie du manteau lithosphérique lié à sa composition (e.g. Calignano et al., 2015a, 2015b, Heron et al., 2016a, 2016b; Heron and Pysklywec, 2016).

4- La présence de fluides et leur circulation au sein des roches (Mezri et al., 2015; Ranalli, 2000)

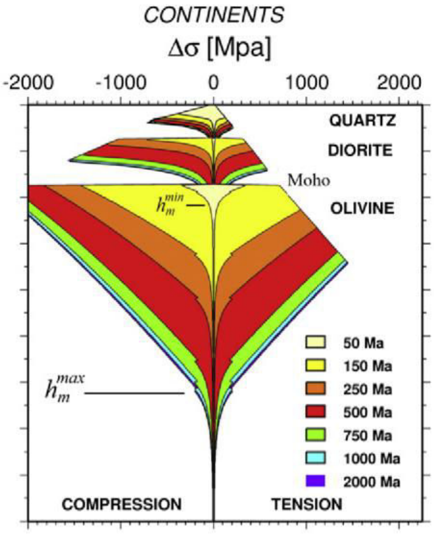

Figure III-1 : Enveloppes rhéologiques d’une lithosphère continentale à 3 couches (quartz, diorite et olivine) pour un âge thermique variant de 50 Ma à 2 Ga. La résistance de la lithosphère augmente avec l’âge thermique (Burov, 2011)

Les différents paramètres qui contrôlent la déformation de la lithosphère continentale forment donc une longue liste incluant notamment la taille de grain, le comportement frictionnel des failles, l’état thermique du milieu, et la composition chimique de la croûte et du manteau (Ranalli, 2000).

Cette étude se concentre sur l’exemple de la chaîne du Tien Shan pour tenter d’apporter des éléments de réponse quant aux processus à l'origine de la localisation de la déformation dans le cadre d'une chaîne intra-plaque.

L'approche utilisée et présentée ici repose sur l'élaboration de modèles thermomécaniques dont le but est de tester l'influence de zone de suture héritées du Paléozoïque sur la déformation tertiaire.

1. Modélisation numérique

Pour ce faire, le code pTatin2D (May et al., 2015, 2014) est utilisé ici. Celui-ci est basé sur la méthode des éléments finis et utilise une discrétisation lagrangienne et eulérienne.

1.1. Equations de Conservation

L'évolution au cours des temps géologiques d'un objet tel qu'une chaîne de montagne fait appel à des processus de déformation multi-échelles allant du domaine cassant au domaine ductile. Chacun de ces régimes de déformation à priori fondamentalement différents répondent, en mécanique, à deux théories que sont la mécanique des milieux fracturés et la mécanique des milieux continus.

A l'échelle lithosphérique, la déformation des roches sur de courtes périodes de temps (de la seconde à plusieurs siècles) est dominée par un comportement élastique. En revanche au cours des temps géologiques (plusieurs millions d'années) la lithosphère est principalement contrôlée par des processus de déformation ductile. De ce fait, le comportement des roches, sur de longues périodes de temps, est décrit par les équations de Stokes comme un fluide incompressible à forte viscosité (non-newtonienne). La dynamique de la lithosphère est donc décrite, comme dans de nombreux problèmes physiques, en termes d'équations de conservation.

1.1.1. Conservation de la masse

L'idée présente derrière la conservation de la masse se traduit par l'hypothèse qu'il n'y a ni destruction ni production de masse dans le système. Dans le cas d'un fluide incompressible cela se traduit par :

$$\nabla . \mathbf{v} = 0 \qquad (1)$$

Où $\mathbf{v}$ représente la vitesse en m.s^{-1}. Autrement dit, les variations de pression n'entraînent pas de variations de volume, le flux de matière entrant dans un volume équivaut au flux de matière sortant de celui-ci. La densité ρ est donc considérée constante en fonction du matériel.

Cependant, l'approximation de Boussinesq (Rayleigh, 1916) permet tout de même de considérer de faibles variations de densité liées à la température et à la pression pour tenir compte des forces de flottabilité telles que :

$$\rho_{eff} = \rho_0[1 - \alpha(T - T_0) + \beta(P - P_0)] \qquad (2)$$

Où α et β représentent, respectivement, les coefficients d'expansion thermique et de compressibilité adiabatique. ρ_{eff} représente la masse volumique effective, en kg.m^{-3}, prenant en compte les variations de volume liées aux conditions de pression et de température.

1.1.2. Conservation du moment pour un fluide visqueux

La conservation du moment peut se traduire par l'équation de Stokes décrivant les mouvements d'un fluide visqueux incompressible et sans inertie tel que

$$\nabla.\boldsymbol{\sigma} + \rho_{eff}\mathbf{g} = 0 \tag{3}$$

Pour un matériau de densité ρ_{eff}, tel que le tenseur des contraintes

$$\boldsymbol{\sigma} = \boldsymbol{\sigma}^{\mathrm{d}} - \mathbf{I}P \tag{4}$$

représente la somme entre contraintes déviatoriques $\boldsymbol{\sigma}^{\mathrm{d}}$ (Pa) pour un matériau de viscosité effective η_{eff} et un terme de pression isotrope P (Pa) où

$$\boldsymbol{\sigma}^{\mathrm{d}} = 2\eta_{eff}\dot{\boldsymbol{\varepsilon}} \tag{5}$$

Ce qui revient à la forme

$$\nabla.\left(2\eta_{eff}\dot{\boldsymbol{\varepsilon}}\right) - \nabla\mathbf{P} + \rho_{eff}\mathbf{g} = 0 \tag{6}$$

Dans laquelle $\dot{\boldsymbol{\varepsilon}}$ (s^{-1}) est le tenseur des vitesses de déformation donné par

$$\dot{\boldsymbol{\varepsilon}} = \frac{1}{2}(\nabla\mathbf{v} + \nabla\mathbf{v}^{\mathrm{T}}) \tag{7}$$

Le tenseur des vitesses de déformation contient toutes les déformations géométriques qui affectent la forme (angle et taille) d'un objet. De plus, dans le cadre d'un régime incompressible (cf. équation 1) le tenseur des vitesses de déformation peut être séparé en une partie scalaire ($\dot{\boldsymbol{\varepsilon}}^0$) et une partie déviatorique ($\dot{\boldsymbol{\varepsilon}}^{\mathrm{d}}$)

$$\dot{\boldsymbol{\varepsilon}} = \dot{\boldsymbol{\varepsilon}}^0 + \dot{\boldsymbol{\varepsilon}}^{\mathrm{d}} \tag{8}$$

Où d'après l'équation (1) la partie scalaire est nulle

$$\dot{\boldsymbol{\varepsilon}}^0 = \frac{1}{3}\mathrm{tr}(\dot{\boldsymbol{\varepsilon}}) = \frac{1}{3}(\nabla.\mathbf{v}) = 0 \tag{9}$$

Donc le tenseur des vitesses de déformation équivaut à son déviateur

$$\dot{\boldsymbol{\varepsilon}} = \dot{\boldsymbol{\varepsilon}}^{\mathrm{d}} \tag{10}$$

Etant donné sa qualité de tenseur il en a également les propriétés, notamment la possibilité de calculer ces invariants. Le second invariant du tenseur des vitesses de déformation

$$\dot{\varepsilon}^{II} = \sqrt{\frac{1}{2}\dot{\varepsilon}_{ij}\dot{\varepsilon}_{ij}} \tag{11}$$

représente le taux de déformation cisaillante maximal.

1.1.3. Conservation de l'énergie

Dans les processus de déformation la température représente un paramètre d'une importance capitale étant donné qu'il contrôle en partie le régime de déformation auquel sont soumises les roches. De plus, toutes les formes de déformation (élastique, plastique et ductile) dissipent de l'énergie. Il est donc nécessaire de considérer l'équation de la chaleur :

$$\rho Cp\frac{\partial T}{\partial t} = \nabla.(\mathrm{k}\nabla \mathrm{T}) - \mathbf{v}.\nabla \mathrm{T} + \rho \mathrm{H} \tag{12}$$

Pour une température T (K) et une diffusivité thermique constante κ ($m^2.s^{-1}$). H ($W.kg^{-1}$) représente le terme source, c'est-à-dire toute production de chaleur par désintégration radioactive, frottement, chaleur latente. Dans le cas de notre étude, la production de chaleur par désintégration radioactive est prise en compte. En revanche, les frottements et la chaleur latente sont négligés.

1.1.4. Modélisation des processus de surface

Dans le but de modéliser au premier ordre les processus d'érosion-sédimentation, c'est-à-dire le transport de matière des zones de haute altitude (sommets) vers les basses altitudes (bassins) il est possible d'utiliser la loi de diffusion de Culling (1964)

$$\frac{\partial h}{\partial t} = -\nabla.(k\nabla h) \tag{13}$$

Où h représente l'altitude (m), t le temps (s) et k ($m^2.s^{-1}$) un coefficient de diffusion permettant de considérer l'érodabilité des matériaux et pouvant varier selon la roche à éroder. Physiquement cela revient à dire que le flux de sédiment est proportionnel à la pente définie par le gradient de l'altitude.

1.2.Loi de fluage en milieu continu

1.2.1. Loi de puissance, fluage dislocation

Le comportement des roches soumises au régime de déformation ductile peut être assimilé à un fluide dit non-newtonien, c'est-à-dire que la relation entre déformation, contraintes et viscosité est non linéaire. La viscosité effective η_{effd} dans le cadre du fluage dislocation est évaluée en utilisant la loi de puissance suivante :

$$\eta_{effd} = \frac{1}{4}(\dot{\varepsilon})^{\frac{1}{n}}\left(\frac{3}{4}A\right)^{-\frac{1}{n}} e^{\frac{Q+PV^*}{nRT}} \tag{14}$$

Où A, n et Q sont des coefficients définis expérimentalement pour une loi de fluage dislocation. V* représente le volume d'activation qui permet d'augmenter l'énergie d'activation (Q) avec la pression (P).

1.2.2. Comportement cassant en milieu continu

Les modèles numériques décrivant le comportement à long terme de la lithosphère utilisent la mécanique des milieux continus qui semble incompatible avec l'idée d'interfaces discontinues (failles ou fractures) dominées par un comportement frictionnel. Cependant, pour décrire la partie « cassante » de la lithosphère, il est possible d'appliquer des équations constitutives non-linéaires qui représentent le fluage plastique ou pseudo-plasticité.

La viscosité η_{effp} dans le cadre du fluage plastique peut être évaluée par le critère de plasticité de Drucker-Prager en fonction de l'angle de friction Φ et de la cohésion Co :

$$\eta_{effp} = \frac{P\sin\Phi + Co\cos\Phi}{\dot{\varepsilon}^{II}} \qquad (15)$$

pour définir le régime de déformation « cassant ». Si les contraintes déviatorique calculées pour le fluage dislocation dépassent le critère de Drucker-Prager la viscosité effective est évaluée suivant :

$$\eta_{eff} = \min(\eta_{effp}, \eta_{effd}) \qquad (16)$$

L'endommagement sur une faille, qui en l'occurrence est considérée comme une zone de cisaillement plus qu'un plan à proprement parler, est implémenté par la décroissance linéaire du coefficient de cohésion et/ou de l'angle de friction avec l'accumulation de la déformation plastique (Lavier et al., 1999) (Figure III-2) tel que :

$$Co = \max\left(Co_\infty, Co - \frac{\epsilon(Co_0 - Co_\infty)}{\epsilon_\infty}\right) \qquad (17)$$

$$\phi = \max\left(\phi_\infty, \phi - \frac{\epsilon(\phi_0 - \phi_\infty)}{\epsilon_\infty}\right) \qquad (18)$$

Où Co_0/ϕ_0, Co_∞/ϕ_∞ et ϵ_∞ sont respectivement la cohésion/friction initiale (non endommagée), la cohésion/friction à la fin de l'adoucissement et la déformation plastique caractéristique après que l'adoucissement soit achevé.

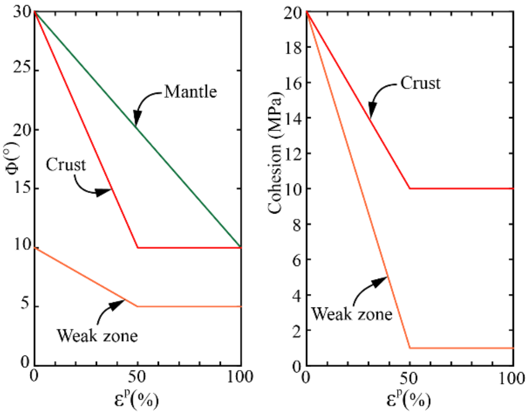

Figure III-2 : Diminution de la friction (à gauche) et de la cohésion (à droite) en fonction de la déformation plastique ϵ jusqu'à un maximum de déformation plastique accumulée ϵ_∞ pour différentes phases

1.3. La méthode des éléments finis et le code pTatin2D

Le recours à la modélisation numérique est généralement lié au fait que le problème physique posé n'admet pas de solutions simples (analytiques). Dans le cadre du comportement long terme de la lithosphère, la non-linéarité des équations gouvernant la déformation des roches ainsi que la complexité des conditions initiales représente un défi de taille et c'est ici que la modélisation numérique prend tout son sens.

Le code pTatin2D (May et al., 2015, 2014) résout l'équation de Stokes pour un fluide incompressible (équation 6) par la méthode des éléments finis. Cette dernière est une méthode de discrétisation des équations différentielles de même que les méthodes des différences finies et des volumes finis. Discrétiser une équation différentielle signifie l'approximer par un système d'équations algébriques valides sur un domaine fini. Les éléments finis minimisent l'intégrale de l'erreur d'approximation (le résidu) sur ce domaine. Cette intégrale est évaluée en deux temps. Le domaine est d'abord discrétisé en sous domaines simples appelés éléments dans lesquels il est possible d'utiliser une quadrature de gauss. Ces intégrales élémentaires sont ensuite sommées algébriquement pour obtenir l'intégrale sur le domaine complet. Cette méthode fonctionne donc très bien pour prendre en compte des géométries complexes, et notamment pour s'adapter à la surface topographique de la Terre, la véritable difficulté étant de s'assurer que les éléments ne sont pas superposés (sinon l'intégrale serait comptée deux fois !).

Dans le cas de l'équation de Stokes pour un fluide incompressible (équation 6), le système algébrique est mal posé car il contient des pivots nuls dans l'équation de la pression. Pour résoudre ce système on peut soit utiliser une méthode de pénalité qui consiste à remplacer les pivots nuls par une valeur petite soit utiliser une méthode itérative. pTatin2D utilise la seconde solution. Pour assurer la convergence de ces itérations dans un écoulement à surface libre, il est nécessaire de discrétiser la pression et la vitesse à l'aide d'éléments mixtes qui sont reconnus pour stabiliser les itérations. pTatin2D utilise des éléments Q_2-P_1 dans lesquels la vitesse est interpolée avec des fonctions quadratiques dans des éléments à 9 nœuds, alors que la pression est interpolée par un polynôme de degré 1. La pression est donc discontinue entre les éléments alors que la vitesse est continue.

La dernière spécificité de pTatin tient à la prise en compte des grands déplacements. Pour un domaine qui se déforme, il est possible d'utiliser deux méthodes :

- une méthode eulérienne, qui permet de considérer un ensemble d'éléments qui ne se déplacent pas avec la matière qui est advectée passivement à l'aide de marqueurs.
- une méthode lagrangienne, qui permet de déplacer et déformer les éléments avec la matière.

pTatin possède une formulation mixte, appelée « *arbitrary lagrangian eulerian* », les limites du domaine se déforment avec la matière mais l'intérieur du domaine se déforme seulement en réponse au changement de forme aux limites. Les propriétés de la matière sont donc advectées par des marqueurs comme pour les méthodes eulériennes, mais la surface topographique est restituée avec précision.

2. Structure profonde et réactivation de la chaîne du Tien Shan : modéliser le passé pour mieux contraindre le présent

Le travail présenté dans cette section a été soumis dans la revue Tectonophysics. La version présentée dans ce mémoire est une version corrigée après un premier processus d'évaluations par des pairs.

Résumé

La déformation active et cénozoïque dans le Tien Shan est guidée par des structures tectoniques et des contrastes rhéologiques partiellement hérités de la phase orogénique varisque au cours du Paléozoïque et réactivés par la collision Inde-Asie. Les estimations de la quantité de déformation acquise au cours du Cénozoïque sont actuellement contraintes d'après des coupes lithosphériques s'appuyant sur les reconstructions paléozoïques de la CAOB. Cependant, plusieurs scenarii ont été proposé (impliquant une subduction à vergence Nord ou Sud) et sont toujours débattus en raison du manque de contraintes sur l'évolution tectonique de la chaîne au cours du Paléozoïque. Dans cette étude, nous proposons de tester différentes hypothèses à propos de la vergence initiale et la rhéologie des zones de sutures héritées et plus particulièrement en ce qui concerne la suture Sud entre le Tien Shan et le bassin du Tarim. Les différentes géométries paléozoïques sont considérées ici comme un paramètre variable visant à être étudié par le biais de modèles thermo-mécaniques évoluant dans le temps. Après une certaine quantité de raccourcissement, les structures auto-générées (i.e. hors des zones de faiblesses initialement introduites), sont analysées et comparées à la déformation cénozoïque finie et active. Cette étude montre qu'une zone de suture crustale plongeant initialement vers le Sud et reposant sur un manteau lithosphérique relativement résistant explique le mieux la localisation de la déformation, la géométrie actuelle des structures et du Moho. En se basant sur ces résultats nous proposons une coupe crustale du Tien Shan Kirghize mécaniquement consistante qui incorpore à la fois les données géologiques et géophysiques.

The deep structure and reactivation of the Kyrgyz Tien Shan: modelling the past to better constrain the present

Anthony Jourdon[1], Laetitia Le Pourhiet[2], Carole Petit[1], Yann Rolland[1]

1- Université Côte d'Azur, CNRS, IRD, Observatoire de la Côte d'Azur, Géoazur, Valbonne, France
2- ISTeP, Université Pierre et Marie Curie, Paris, France

Abstract

Cenozoic and active deformation in the Tien Shan is guided by structures and rheological contrasts partly inherited from the Paleozoic Variscan orogeny, reactivated by the India-Asia collision. The net estimates of Cenozoic deformation are constrained by lithospheric scale geological cross-sections, which rely on reconstructions of the Paleozoic Central Asian Orogenic Belt (CAOB). However, several geodynamic scenarii have been proposed for its formation (which include a south or a north dipping subduction), and are still debated due to the lack of constraints. Here, we designed numerical experiments to test different hypotheses about the initial vergence and the effective rheology of the paleo-sutures and especially the one located between the Tien Shan and the Tarim basin, where most Cenozoic deformation localizes. The different geometries of Paleozoic structures are used as input variables in the thermo-mechanical models, which are then run forward in time. After a finite amount of shortening, the structures that develop self-consistently out of the proposed heterogeneities are then compared to the current Cenozoic finite and active deformations. We find that a crustal south-dipping suture zone lying on a resistant lithospheric mantle best explains the localization of the deformation, the current geometry of the structures and the Moho depth variations. Using the model results, we propose a mechanically consistent depth-interpolated crustal cross-section of the Kyrgyz Tien Shan, which incorporates both geological and geophysical data.

Keywords: *Intraplate deformation, Structural inheritance, Tien Shan, Thermomechanical modelling, Cenozoic*

Introduction

The Cenozoic and active deformation of the Eurasian continent in response to the India-Asia collision extends over several thousand kilometres away from the Himalayan belt (Avouac et al., 1993; Patriat and Achache, 1984; Sobel and Dumitru, 1997; Tapponnier et al., 1986). However, deformation is heterogeneously distributed in Central Asia. Some areas like the Tarim basin are less deformed, whereas the Tibetan plateau suffers significant uplift and lower crust ductile deformation and the Tien Shan belt is uplifted and deformed (Abdrakhmatov et al., 2001, 1996; Avouac et al., 1993; Jourdon et al., 2017; Loury et al., 2015b). Similar observations also pertain for the current rates of deformation (Avouac et al., 1993; DeMets et al., 1994). Strain localization partly follows the limits of terranes of different ages, which were accreted to the Eurasian continent since the Proterozoic. These terranes and their boundaries are believed to have left significant rheological anisotropies in the lithosphere (e.g. Kröner et al., 2014; Molnar and Tapponnier, 1975; Sengör, 1984; Windley et al., 2007).

Structural inheritance is a key factor for continental deformation dynamics. For example, the compressional structuration of the Pyrenean belt is strongly controlled by former structures inherited from the continental rifting phase (Buiter and Pfiffner, 2003; Calignano et al., 2015a; Desegaulx et al., 1990; Jammes et al., 2014; Velasque et al., 1989). Similarly, some Alpine collisional structures are known to rework former Tethyan rift faults (Bellahsen et al., 2012; Butler et al., 2006; Gillcrist et al., 1987; Jourdon et al., 2014; Lemoine et al., 1986).

Thanks to combined modelling and structural analysis of mountain belts, it is now well understood how structural inheritance can take many other forms than just a single 'fault reactivation process'. Structural inheritance mostly emerges from (i) lateral variations in lithologies due to past normal fault activity and/or to nappe stacking (Buiter and Pfiffner, 2003; Lafosse et al., 2016; Le Pourhiet et al., 2004; Ranalli, 2000; von Tscharner et al., 2016), (ii) variations in the mantle composition (Calignano et al., 2015b; Chenin et al., 2017; Heron et al., 2016a, 2016b), (iii) or variations of rock fluid content (e.g., Mezri et al., 2015; Ranalli, 2000). The different parameters that control the deformation of the continental lithosphere form a long list which includes the grain size, the faults frictional behaviour, the thermal state, and the chemical composition, of crust and mantle (Ranalli, 2000). The large spectrum of inherited geological features requires defining the geological setting and the model scaling in order to draw further conclusions.

This study focuses on the case of structural inheritance in the Kyrgyz part of the Tien Shan belt (Figure 1). We aim at integrating geological studies, geophysical data and thermo-mechanical modelling to build a new crustal cross-section of the Kyrgyz Tien Shan linking the deep crustal structures inferred by geophysical models with the shallow structure constrained by geological observations. In the Tien Shan case the localization of Cenozoic deformation is clearly established by former geological (e.g. Burbank et al., 1999; Goode et al., 2014, 2011; Thompson et al., 2002), geophysical (e.g. Batalev et al., 2011; Makarov et al., 2010; Vinnik et al., 2004) and thermo-chronological studies (e.g. De Grave et al., 2011; Glorie et al., 2010; Macaulay et al., 2014, 2013), which limits the panel of possible inherited structures, which have been reactivated. However, the main unknown remains their initial geometry.

Our approach relies on testing by the means of forward thermo-mechanical models how the hypothetic inherited Paleozoic suture zones, their geometry and depth extent could have

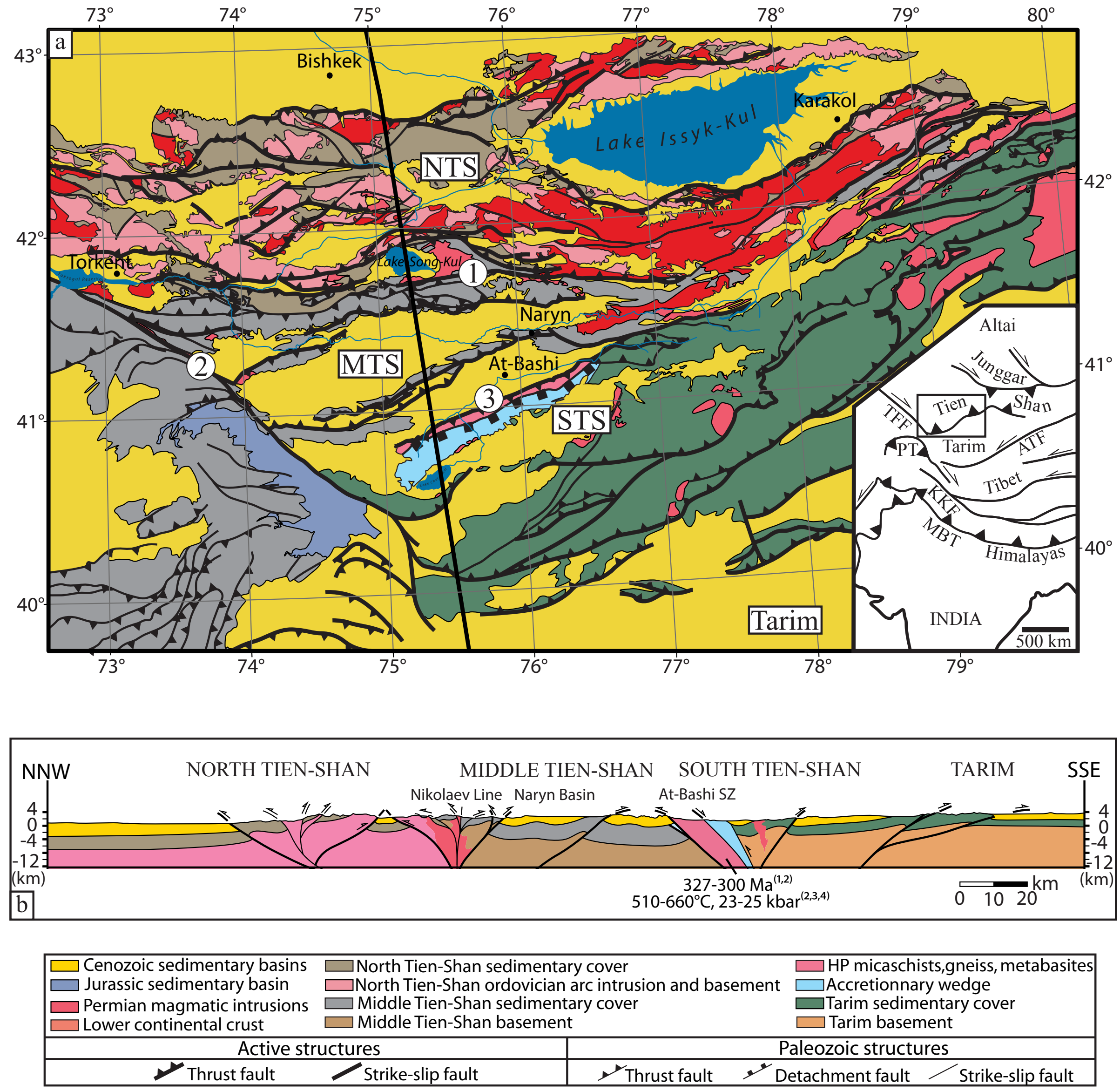

Figure 1: a) Geological map of the Kyrgyz Tien Shan (after Jukov et al., 2008; active structures are modified from Thompson et al., 2002). Insert represents the schematic tectonic context of Central Asia. b) Geological cross-section of the Kyrgyz Tien Shan along the thick solid line (after Goode et al., 2011; Jourdon et al., 2017), numbers are referred to (1) (Simonov et al., 2008) (2) (Hegner et al., 2010) (3) (Tagiri et al., 1995) (4) (Loury et al., 2015a).1: Nikolaev Line. 2: Talas Ferghana Fault. 3: At-Bashi suture zone. NTS: North Tien Shan. MTS: Middle Tien Shan. STS: South Tien Shan. KT: Khan Tengri Massif. PB: Pobeda massif.

influenced the mode and extent of Cenozoic shortening accommodation at the crustal scale. The different hypotheses are then (in)validated by comparing the results of the forward models to both the long term Cenozoic and active deformation patterns.

We first briefly synthesize the Paleozoic history of the Kyrgyz Tien-Shan in order to describe the possible pre-Cenozoic structuration of the lithosphere, which will be used as initial conditions for the thermo-mechanical models. We then describe the Cenozoic and active deformations of the Tien Shan belt. Further, we present the model setups and results, and finally we propose a re-interpretation of the belt structure based on the comparison of modelling results with geophysical and geological data.

1. Tectonic units of the Tien Shan belt

The Tien Shan belt extends over ~2000 km from Uzbekistan to western China and is an active intracontinental mountain belt, which develops on the remnants of the Central Asian Orogenic Belt (CAOB) built mainly during the Paleozoic by the accretion of several tectonic blocks (e.g. Bakirov and Maksumova, 2001; Biske and Seltmann, 2010; Kröner et al., 2014; Rojas-Agramonte et al., 2013). These accretion phases and subsequent post-collisional strike-slip tectonics resulted in compressional sutures and transcurrent shear zones (Alekseev et al., 2007; Biske, 1996a; Macaulay et al., 2014; Mikolaichuk et al., 2008; Nikolaev, 1933).

The initial structuration of Kyrgyz Tien Shan occurred in Neoproterozoic to Paleozoic times by the collision of three continental blocks: the North Tien Shan (NTS), the Middle Tien Shan (MTS) and the Tarim. These blocks are separated by two suture zones, the Nikolaev Line (NL) (Nikolaev, 1933) to the North (between the NTS and the MTS) and the South Tien Shan accretionary complex also named the At-Bashi-Kokshaal suture zone to the South (between the MTS and the Tarim) (e.g. Alekseev et al., 2007; Biske, 1996a; Burtman, 2008; Loury et al., 2015a, 2015b; Simonov et al., 2008 and Figure 1). These two suture zones formed after the closure of two oceanic domains located between the NTS/MTS and MTS/Tarim, during the Ordovician and the Carboniferous, respectively.

The Mesozoic was a period of tectonic quiescence (De Grave et al., 2012; Jolivet et al., 2013, 2010). Indeed, thermo-chronological data show that ages older than Cenozoic are split into two groups: Permian-Triassic and Jurassic-Cretaceous (e.g. Glorie and De Grave, 2016; Jolivet et al., 2010). The oldest group is interpreted as reflecting a cooling phase posterior to Permian magmatic events, while the Jurassic-Cretaceous ages are related to an erosional phase resulting in the formation of an erosional surface (Jolivet et al., 2013, 2010; Vassallo et al., 2007). Therefore, during the Mesozoic the Tien Shan was not affected by major tectonic events able to modify or rework Paleozoic crustal structures.

1.1. The North and Middle Tien Shan

The NTS is essentially represented by calc-alkaline magmatic intrusions (Figure 1) composing an Early Paleozoic active margin (Bakirov and Maksumova, 2001; Glorie et al., 2010; Konopelko et al., 2008; Kröner et al., 2014, 2012b). This active margin setting is interpreted as resulting from the northward (in present-day coordinates) subduction and closure of a Precambrian oceanic domain during the Ordovician-Silurian, which led to the accretion of the MTS with the NTS (Bakirov and Maksumova, 2001; Glorie et al., 2010).

The MTS (Figure 1) is a continental block composed of a Mesoproterozoic-Neoproterozoic basement characterized by metamorphosed sediments and orthogneisses (Glorie et al., 2010; Keselev et al., 1982; Kiselev et al., 1993; Kröner et al., 2012b) overlain by a ~5 km thick sedimentary cover principally represented by sandstones and limestones (Jukov et al., 2008; Karpovitch et al., 1964; Mikolaichuk et al., 1997).

The Nikolaev Line crops out as a 15 to 20 km wide right-lateral strike-slip system which was active from Late Carboniferous to Permian times (e.g. Jourdon et al., in press: Mikolaichuk et al., 1997; Windley et al., 2007 and Figure 1). It follows a former Ordovician suture zone separating the NTS from the MTS (Bakirov and Maksumova, 2001; Glorie et al., 2010).This E-W strike-slip shear zone forms a positive flower structure surrounded by North- and South-verging Paleozoic thrusts (Jourdon et al., 2017). It extends from the Talas Fergana Fault (TFF) to the west to the Naralt Fault to the east. The latest is the eastern continuity of the NL in China (e.g. Charvet et al., 2007; Gao et al., 1998; Xiao et al., 2013).

1.2. The Tarim block and the South Tien Shan

The Tarim block is made of Late Proterozoic ortho- and para-gneissic basement (Ye et al., 2016; Zhang et al., 2014) overlained by Phanerozoic sediments ranging from Late Neoproterozoic to Quaternary in age. The Paleozoic cover is about 5 km thick, while the Mesozoic rocks represent only 500 m to 1.5 km of sediments, whereas the thickness of Cenozoic sediments reaches up to 8- 10 km (Wang et al., 1992). The low sedimentation rates recorded between the Paleozoic and the Cenozoic times in the Tarim basin is ascribed to a period of tectonic quiescence in the Tien Shan area (Allen et al., 1999, 1993; Q. Wang et al., 2010).

The South Tien Shan is subdivided into two parts: (i) a Paleozoic fold and thrust belt thrusted over the Tarim Cenozoic sediments and (ii) an accretionary complex, the At-Bashi-Kokshaal complex, which represents a Late Carboniferous suture zone between the MTS and the Tarim in Kyrgyzstan (and the NTS and the Tarim in China) (Figure 1). It is represented by an assemblage of several metamorphic units and ophiolites (Alekseev et al., 2007; Biske, 1996a; 1985; Loury et al., 2015b) . Recent studies on this suture evidenced a top-to-the-North thrust stack (Figure 1) with from bottom to top: (1) a low-grade unmetamorphosed ophiolite thrusted by (2) eclogite-facies micaschists and oceanic units (500-660°C and 20-25 kbar, Hegner et al., 2010; Loury et al., 2015a; Simonov et al., 2008; Tagiri et al., 1995), and (3) a greenschist to blueschist facies accretionary prism (Biske, 1996b; Burtman, 2008; Karpovitch et al., 1964; Loury et al., 2015a).

The structure of the At-Bashi accretionary complex is interpreted as the result of the late Carboniferous collision between the Tarim and the Tien Shan (Charvet et al., 2011, 2007; Xiao et al., 2013). Deep crustal structures imaged on the northern border of the Tarim by the MANAS deep seismic experiment (Makarov et al., 2010) clearly indicate the presence of a deep crustal reflector in the Tarim crust, which progressively bends towards the North and suggests that today the Tarim is underthrusted beneath the Tien Shan. However, there are two opposite interpretations regarding the age of that thrust. Some authors (Alekseev et al., 2007; Biske, 1996b; Burtman, 2008; Chen et al., 1999; Gao et al., 2009; Liu et al., 2014; Xiao et al., 2013) consider that the Tarim was underthrusted beneath the Tien Shan (NTS-MTS) during the Late Carboniferous and that the whole structure was back-thrusted toward the North afterwards. Other authors (Charvet et al., 2007; Choulet et al., 2011; Loury et al., 2015b; Wang et al., 2011) rather propose that the MTS was underthrusted beneath the Tarim during the Late Paleozoic and that the underthrusting of the Tarim beneath the Tien Shan highlighted by the seismic profile would be of Cenozoic age and not related to the Paleozoic deformation.

The first interpretation is principally based on the vergence of thrusts (towards the South) observed in the Paleozoic sedimentary cover of the Tarim south of the At-Bashi massif. The second interpretation is based on the presence of subduction-related magmatic rocks on the northern Tarim margin (Ge et al., 2014, 2012; Lei et al., 2011; Lin et al., 2013) and on numerous evidences of top-to-the North thrusts associated with top-to-the South detachments in the ductile deformed units of this accretionary complex. The interpretation of this structure has therefore strong implications on the vergence of structures at the onset of cenozoic deformation as it affect both the orientation of mantle weak zones (i.e. the vergence of the subduction preceding the paleozoic collision) and on the vergence of thrust in the crust. In this study, we consider this interpretation as a varying parameter in our models.

2. Active deformation in the Tien Shan belt

Geodetic data show that the TS currently accommodates about 40% to 50% of the India-Asia convergence rate, including the shortening across the northern margin of the Tarim basin, for a total amount of crustal shortening of 200 ± 50 km since max. 30 Ma (Abdrakhmatov et al., 1996; Avouac et al., 1993; DeMets et al., 1994).

Focal mechanisms from the CMT database (Centroid Moment Tensor, Ekström et al., 2012) show predominant thrust faulting (Figure 2a). Some strike-slip mechanisms are located along well-identified strike-slip structures such as the right-lateral Talas Fergana Fault (TFF). The Earthquake Model of Central Asia database (EMCA, Mikhailova et al., 2015a, 2015b) shows that most seismic events occurring to the east of the TFF are located at crustal depths, i.e., between the near surface and 45-50 km. On the other hand, to the west of the TFF, deep foci are observed (>100 km), which correspond to the Pamir indentation zone. The TFF can therefore be considered as a major lithospheric structure that separates two different deforming regions (Bande et al., 2015) (Figure 2a): the Pamir area with deep (100 km) earthquakes, and our study area where earthquakes depth distribution is limited to crustal levels. Among them, some hypocentres closely follow inherited Paleozoic structures, while others correspond to newly formed (Cenozoic) faults. In the North, near Lake Song-Kul and on the northern side of the At-Bashi massif, the seismicity clusters along two major belts corresponding to the Kyrgyz Tien Shan Paleozoic suture zones. South of the Tien Shan Belt, where the Tien Shan is thrusted over the Tarim (Figure 2a), most seismic events are geographically spread out and located far away from the original At-Bashi suture zone. Finally, a few seismic events align along recent, short ~EW mountain ranges uprising between the Naryn and At-Bashi basins (Goode et al., 2014; Joseph K. Goode et al., 2011).

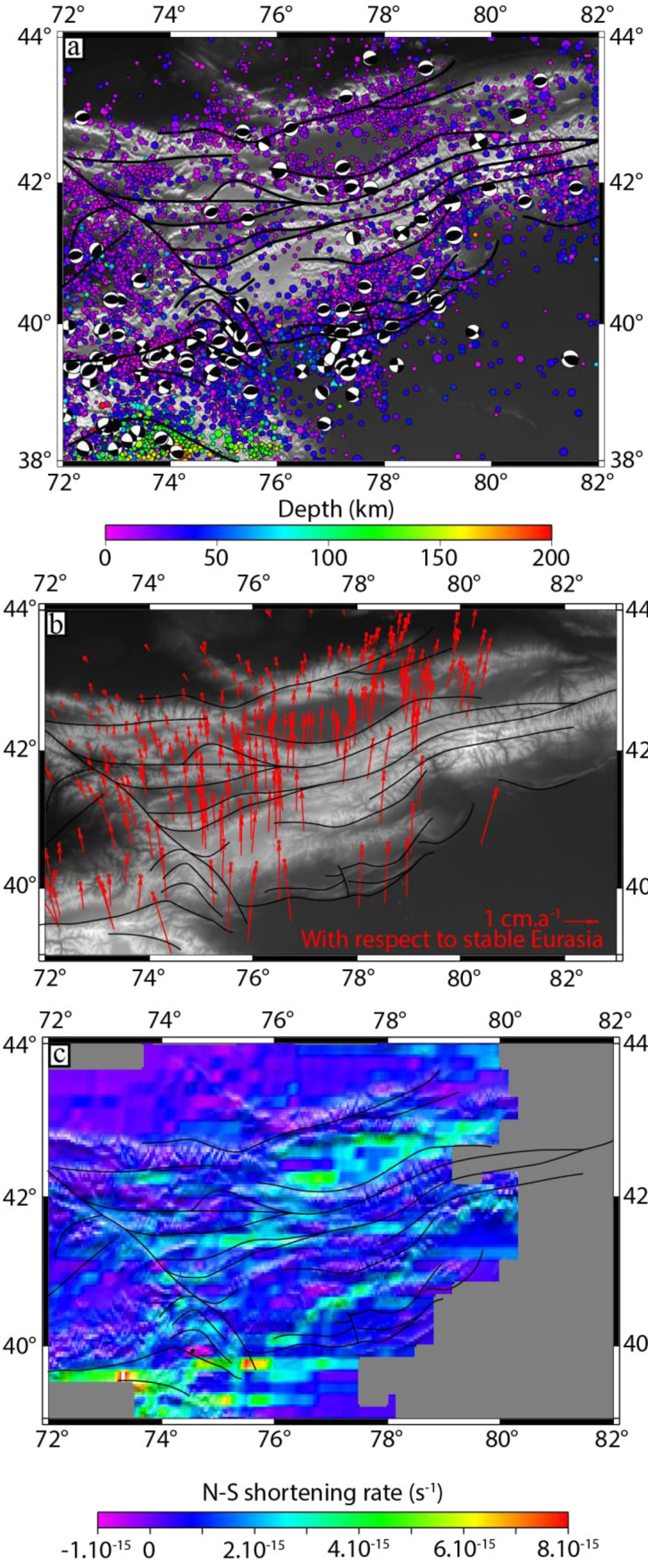

Figure 2: a) Map of seismic events and focal mechanisms in the Kyrgyz Tien Shan. Solid lines represent the main faults. Epicentres location are from the EMCA catalogue (Mikhailova et al., 2015a, 2015b) and focal mechanisms from the CMT database (Ekström et al., 2012). b) GPS velocities with respect to stable Eurasia (Zubovich et al., 2010). c) N-S shortening rate on a regular 10'grid where GPS vector components were interpolated using a nearest neighbour algorithm (Generic Mapping Tools, Wessel et al., 2013).

GPS data highlight a northward displacement of the Tien Shan and Tarim blocks with respect to stable Eurasia (Zubovich et al., 2010, and Figure 2b). Northward velocities decrease from South to North, indicating active N-S shortening within the Tien Shan (Figure 2b). In order to better describe this deformation, we computed the N-S shortening rate on a regular 10'grid where GPS vector components were interpolated using a nearest neighbour algorithm (Generic Mapping Tools, Wessel et al., 2013). Despite uncertainties linked to the uneven distribution of GPS data, two zones of localized deformations stand out from our analysis with shortening rates ranging between 2.5 10^{-15} and $5.10^{-15} s^{-1}$. The first one is located east of the TFF stretched along a NE-SW direction, which corresponds to the northern border of the Tarim and the southern limb of the At-Bashi massif (Figure 2c). The second one is located northward, along another NE-SW trending zone extending along the Nikolaev Line and in the Issyk-Kul area. Significantly larger rates of shortening (from 4.10^{-15} to 8.10^{-15} s^{-1}) are observed at the boundary between the Pamir and the Tien Shan, west of the TFF. This deformation zone accommodates most of the N-S shortening, since no significant deformation is visible further North (Figure 2c). Therefore, the GPS shortening rates and the seismicity vs. depth distribution evidence that the TFF separates two areas behaving in different ways with respect to active deformation. This 3D complexity cannot be capture by our 2D models. Hence, we focus our modelling approach and comparison with active deformation on the domain located east of the TFF, where our geological cross-section is located.

To summarize, GPS and earthquake data show that active deformation east of the TFF localizes on several major structures: i) the At-Bashi suture and its conjugate counterpart, i.e. the south-verging thrust of the STS over the Tarim basin; ii) the Nikolaev line area; iii) less importantly, in the middle of a large intra-mountainous Cenozoic basin located between these two suture zones (Figure 3a).

In the following sections, models will be considered as acceptable if they can capture these first order deformation patterns.

3. Modelling

3.1. Constraints on the lithospheric structure from geological and geophysical data

Extrapolating a geological cross section at depth requires incorporating geophysical constrains on the deep crustal and lithospheric structures. However, there are only few available data about the mantle structure below the Tien Shan belt (Deng et al., 2017; Huang and Zhao, 2006; Lei and Zhao, 2007; Zhiwei et al., 2009). Most of these studies are based on global tomography models and their resolution is not good enough to derive interpretations on the geometry of the lithospheric mantle beneath the Tarim and the Tien Shan. Yet, as the seismicity depth distribution reveals that the mantle is not affected by any significant brittle deformation (unlike in the Pamir region), we can posit that the deformation does not tend to be localized in the mantle.

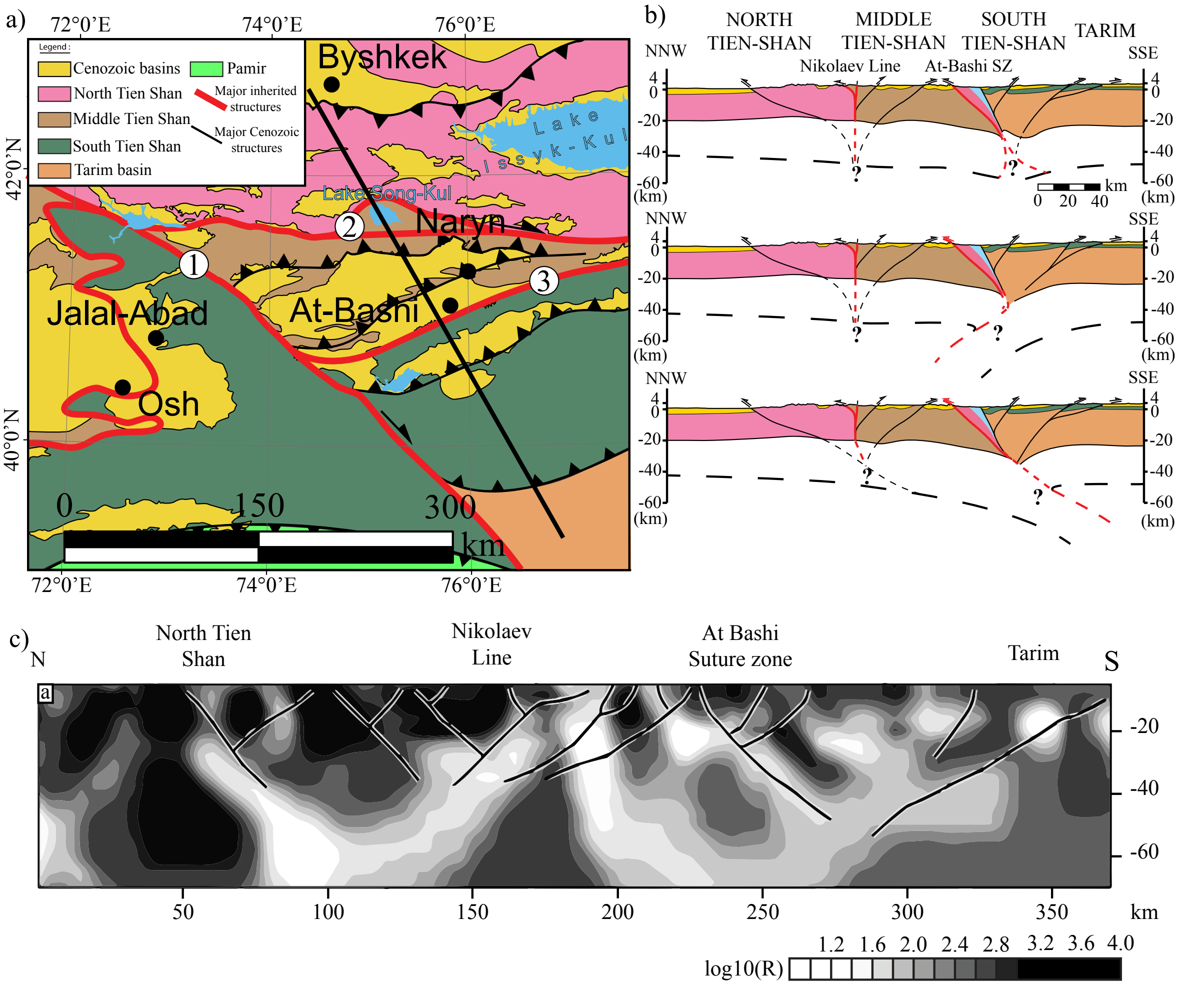

Figure 3: a) Simplified tectonic map of the Kyrgyz Tien Shan. The thick black line indicates the position of the cross-section. 1: Talas Ferghana Fault. 2: Nikolaev Line. 3: At-Bashi-Kokshaal suture zone. b) Simplified crustal cross-sections of the Kyrgyz Tien Shan highlighting several hypotheses about the deep crustal structure and the potential involvement of mantellic structures. c) Magneto-telluric profile after (Batalev et al., 2011). Grey shades represent the $\log_{10}$ of the resistivity in the crust and upper lithospheric mantle.

The geometry of the Moho in the Kyrgyz Tien Shan has been constrained using different methods: receiver functions (Vinnik et al., 2004) and seismic refraction (Makarov et al., 2010; Roecker, 2001). All studies agree on an overall crustal thickness in the TS of about 45 km. Nevertheless, the models are not fully consistent with each other, especially in the most deformed regions. For numerical models validation, we chose to consider the Moho geometry interpreted from the MANAS seismic refraction experiment (Makarov et al., 2010), because it presents the best resolution due to the wealth of seismic stations that were installed for that purpose.

A recently published deep magneto-telluric sounding (MT) profile acquired along the 76°E meridian in the Kyrgyz Tien Shan provides additional constraints on the deep crustal structure (Batalev et al., 2011). These authors compared this MT profile with the MANAS seismic experiment (Makarov et al., 2010) and with laboratory measurements and concluded that the lowest resistivities (Figure 3c) correspond to major recent faults visible on the field. Their study highlights localized deformation on the At-Bashi suture zone and on new structures that are located on the northern boundary of the Tarim and in the Naryn basin (Figure 3a), which is compatible with the map distribution of seismic events.

Although important, these data do not allow extrapolating the deep crustal and lithospheric structures of the TS without being biased by the preferred geodynamic scenario proposed for the Paleozoic evolution of the Kirgiz Tien Shan (Figure 3b). In order to add additional mechanical constrain on this extrapolation, we conduct a numerical study in which the Paleozoic scenario is treated as a variable. Our models aim at addressing first order questions about the structuration and the deformation of the TS:

(i) How does the geometry of inherited structures influence the ongoing deformation?
(ii) Is it possible to retrieve the actual structure of the belt from different starting (i.e., pre-Cenozoic) structural configurations?
(iii) Is the mantle still weak in the continuity of Paleozoic crustal suture zones? How does the mantle rheology influence crustal deformation?

3.2.Initial model geometry

We focus our study on the possible role of the two main suture zones of the region, namely the Nikolaev Line located between the NTS and the MTS north of the range and the At-Bashi suture zone located south of the range between the MTS and the Tarim (Figure 3a). The different initial geometric configurations of our models are designed to represent different hypotheses about the pre-Cenozoic structures (Figure 4a and 4b). Model results are displayed in Figures 5-7.

Runs 1, 3 and 5 (Figures 5-7) involve a right (south-) dipping inclined suture representing the At-Bashi suture, and a vertical one representing the Nikolaev Line in the crust and/or lithospheric mantle. Runs 2, 4 and 6 involve a folded suture zone to the right, corresponding to the hypothesis of an initially left (north-) dipping subduction that was back-tilted during the Paleozoic collision. As for other runs, those also contain a vertical weak zone on the left (north) that mimics the Nikolaev Line. Oppositely to Runs 3 and 5, the mantle part of the Nikolaev Line is not mechanically weakened.

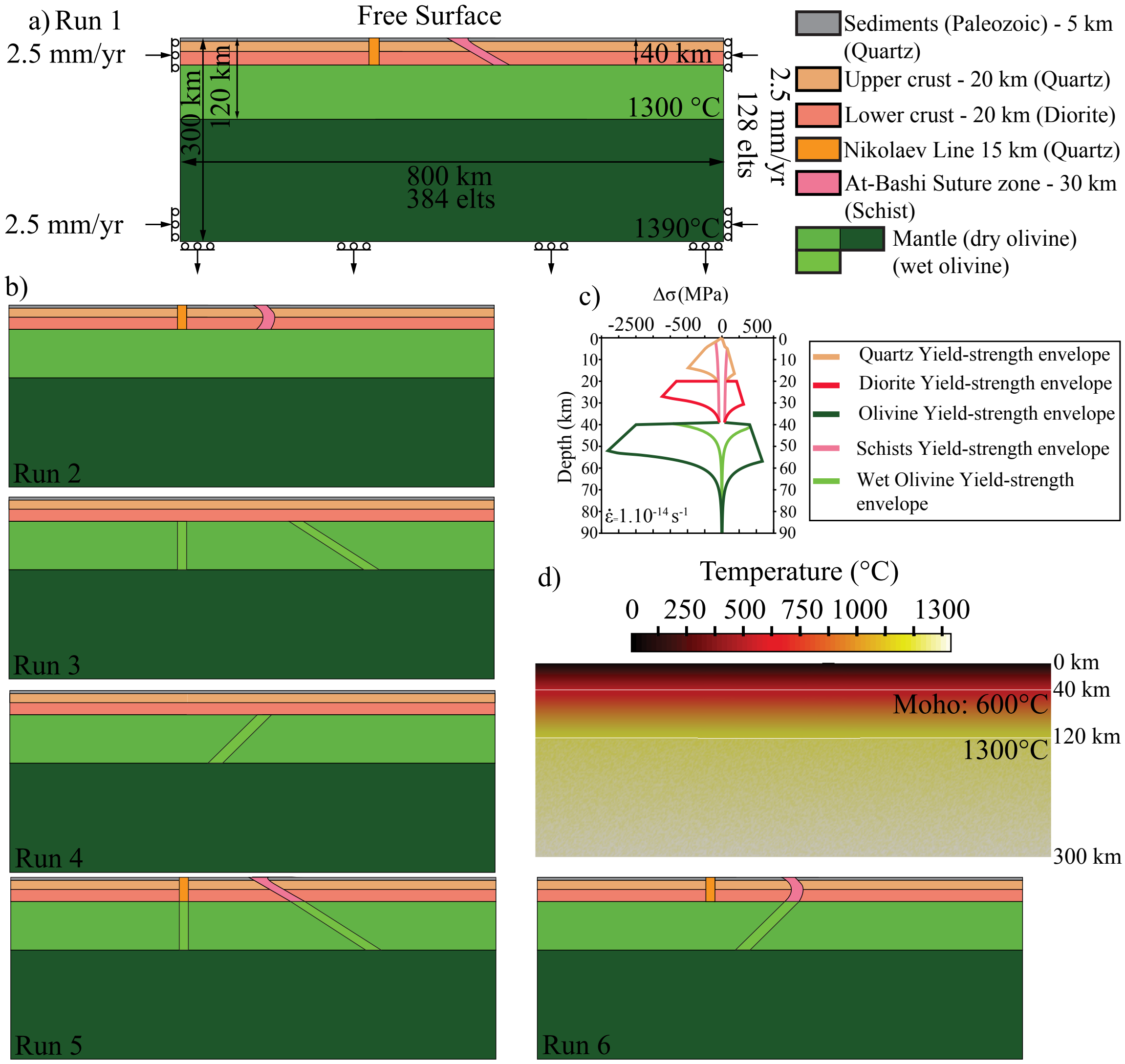

Figure 4: Modelling setup. a) Geometry of model 1, with dimensions and boundary conditions for all simulations (elts = elements). b) Geometries of models 2 to 6. c) Yield-strength envelopes of the simulated materials calculated for a strain rate of 1.10^{-14} *s*$^{-1}$*. Δσ represents the deviatoric stress, positive values under extension and negative values under compression. d) Initial temperature state of the lithosphere for all the simulations presented. The two white lines represent from top to bottom, the Moho and the lithosphere-asthenosphere boundary respectively.*

Our models were also designed to explore the effect of the locations and relative weaknesses of the suture zones in a more systematic manner. Runs 1 and 2 (Figure 5) aim at testing the influence of the initial geometry of inherited structures in the crust and do not contain any weak zone in the mantle. Runs 3 and 4 (Figure 6) address more specifically the influence of weak zones in the mantle and do not contain any weak zone in the crust. Finally, Runs 5 and 6 (Figure 7) are designed to test which part of the lithosphere (crust or mantle) has the largest influence on the crustal deformation pattern and contains both crustal and mantellic weak zones.

All the models evolve in time for the same far field shortening (150 km), which was chosen because it balances the observed crustal thickening as today. With this shortening, the rate of deformation across the model is similar to geodetic rates if the rates were constant during 30 Myr.

3.3.Model size and boundary conditions

We use a model box of 800 x 300 km with a spatial resolution of 2 x 2 km (Figure 4a). The thermal structure of the continental lithosphere is computed for a plate thickness of 120 km, a thermal age of 100 Myr, and a surface radiogenic heat production of 1.10^{-9} $W.kg^{-1}$ with an exponential decay characteristic depth of 10 km using the formula in Burov and Diament (1995). For the asthenosphere, an adiabatic gradient of 0.5°K/km is used (Figure 4a). Temperatures are fixed at the top and base of the model at 0°C and 1390°C respectively, and a null heat flux is assumed on the model lateral boundaries. Kinematic boundary conditions are defined as follows: the lateral sides of the models have a constant, in time and depth, convergent horizontal velocity of 0.25 $cm.yr^{-1}$ whereas vertical slip is left free. The lower boundary of the model is vertically fixed and horizontally free (Figure 4a). In our models, we use a free upper boundary surface, which allows development of a realistic topography, and is subject to erosion - sedimentation. These surface processes (erosion and sedimentation) are modelled using Culling's (1965) law with a diffusivity (κ_e) of 5.10^{-7} $m^2.s^{-1}$. Appendix A details the equations solved and the method.

3.4.Rheologies

Both lithospheric mantle and asthenosphere have been assigned ductile creep parameters corresponding to an olivine rheology (Goetze and Evans, 1979) (Figure 4c). In experiments 2 and 4 (Figures 5-6), the continuation of suture zones in the mantle have been given a wet mantle rheology (Hirth and Kohlstedt, 1996) in order to simulate the possible presence of inherited weak zones (Figure 4c). The other experiments have a homogeneous mantle rheology, which supposes that Paleozoic mantle heterogeneities were healed before the onset of Cenozoic reactivation. The upper continental crust and sediments are simulated using a quartz rheology, which is equivalent to granites or granitoids (Ranalli and Murphy, 1987). A diorite rheology (Carter and Tsenn, 1987) is used to simulate the behaviour of the lower crust. Several observations motivated this choice:

- The NTS is principally composed of subduction-related magmatic rocks with calc-alkaline affinities (Bakirov and Maksumova, 2001; Glorie et al., 2010; Konopelko et al., 2008; Kröner et al., 2014, 2012b). This kind of magmatism is generally characterized by granites in the upper crust and diorites in the lower crust (Albare, 1998; Hacker et al., 2011; Rudnick and Fountain, 1995; Taylor and Mclennan, 1995).

- The Tarim lower crust crops out in some places in Kyrgyzstan and China and is represented by a felsic garnet-free granulite composition, (Loury et al., 2015b; Zhang et al., 2015) which is consistent with a diorite rheology.
- The MTS is often considered as a part of the Tarim rifted away during the Paleozoic (Charvet et al., 2011, 2007, Dong et al., 2011, 2006, 2005; Ma et al., 1993; Zhong et al., 2014). Hence, the continental crust of the MTS should have the same composition as the Tarim.

Phase	**Unit**	**Sed.**	**U.C.**	**L.C.**	**ABS**	**NMTS**	**Mantle**	
Litho		Quartz	Quartz	Diorite	Schist	Quartz	Olivine	Wet Olivine
n		3	3	3.05	31	3	3	3.4
A	$MPa^{-n} s^{-1}$	$6.8.10^{-6}$	$6.8.10^{-6}$	$6.3.10^{-6}$	$1.3.10^{-67}$	$6.8.10^{-6}$	7.10^{3}	$1.9.10^{3}$
Q	$kJ.mol^{-1}$	156	156	275	98	156	510	420
Ref.		R and M	R and M	C and T	S and K	R and M	G and E	H and K
ρ_0	$kg.m^{-3}$	2700	2700	2850	2700	2700	3300	3300
ϕ_0	°	30	30	30	10	10	30	10
ϕ_∞	°	10	10	10	5	5	10	10
Co_0	MPa	20	20	20	20	20	20	20
Co_∞	MPa	1	1	10	1	1	20	10

Table 1: Rheological parameters used in all experiments. See Appendix A for details. References are from R and M (Ranalli and Murphy, 1987), C and T (Carter and Tsenn, 1987), S and K (Shea and Kronenberg, 1992), G and E (C. Goetze and Evans, 1979), H and K (Hirth and Kohlstedt, 1996). Other parameters described in appendix A, which have fixed values, are listed here: $\alpha = 3.10^{-5} K^{-1}$, $\beta = 1.10^{-11} Pa^{-1}$, $\kappa_e = 5.10^{-7} m^2.s^{-1}$, $\kappa = 1.10^{-6} m^2.s^{-1}$, $\varepsilon_{min} = 0$, $\varepsilon_{max} = 1$, $Cp = 1000 J.kg^{-1}.K^{-1}$, $H = 1.10^{-9} W.kg^{-1}$.

As the NTS/MTS suture zone is composed of granitoids and a sedimentary cover, the At-Bashi suture zone is formed by micaschists (see 1.2. and Hegner et al., 2010; Loury et al., 2015a; Simonov et al., 2008; Tagiri et al., 1995), we assigned these sutures quartz and mica rheological parameters, respectively. Mica flow parameters are found in Shea and Kronenberg (1992) and have been used by Yamato et al. (2007) and many others to model this type of rocks. With this rheology, creep is activated at very shallow depths (5 km), but their weak temperature dependence predicts that micas become more resistant than quartz (Ranalli and Murphy, 1987) between 20 and 40 km and more resistant than diorite (Carter and Tsenn, 1987) beneath that depth (Figure 4c). All the rheological parameters described in this part are listed in Table 1.

4. Model results

In order to better assess how variations in the lithospheric strength would influence the deformation pattern in the Tien Shan belt, we have completed our study with several models, in which the initial thermal age, the lower crustal strength vary. We also included models with lateral heterogeneities in the mantle lithosphere. The detailed representation of these models is reported as a supplementary material of this article and their results in terms of Moho geometry, of topography and deformation are summarized in Table 2 together with the results of the models that are presented in the main body of the paper. In order to simplify the reading, the principal structures formed during the simulations are numbered in sequence of their localization for each run (see Figures 5, 6 and 7).

4.1. Crustal weak zones

4.1.1. Model with a right dipping crustal weak zone (Run 1)

In this experiment, the inclined suture dips 30° towards the right (featuring a southward dip of the At-Bashi suture) in the crust, while the mantle is given a strong homogeneous olivine rheology (Figures 4 and 5a).

After ~ 5 Myr, deformation localizes in the crust along the two suture zones (structures 1 and 2 on Figure 5a), yet localization is more important along the inclined suture (structure 1 on Figure 5a) because it is more favourably orientated (Figure 5a). Sedimentary basins form on both sides of the sutures and in the central part of the model. After ~15 Myr, the base of the crust in the central block is visibly deflected under the weight of the material thrusted over the inclined suture. At this moment, the base of the crustal shear zone corresponding to the inherited right-dipping suture connects with a flat top-to-the-right newly formed shear zone to form a fishtail structure. At the same time, two top-to-the-left shear zones (structure 3 on Figure 5a) develop in the central block: one nucleates at the middle/upper crust interface and the other one at the Moho interface. As models continue to evolve in time (21 and 30 Myr), the right tip of the fishtail structure propagates within the lower crust of the right block and decouples the upper and middle/lower crust from the mantle lithosphere. As a result, the upper part of the right block crust is uplifted and exhumed, while the lower part is underthrusted beneath the central block. The downward flexure of the right block mantle increases while it is underthrusted to the left. The initially flat shear zone is also deflected and its dip angle progressively increases. After a 20 Myr, this deep shear zone connects upward to a newly formed top-to-the right thrust (structure 4 on Figure 5a) in the crust of the right block. This thrust accommodates more and more deformation and uplift with time at the expense of the original inclined suture. At the end of the simulation (~ 30 Ma), the strain rate of the newly formed shear zone (structure 3 on Figure 5a) developed in the right block ranges between $1.5.10^{-15}$ s^{-1} and $2.5.10^{-15}$ s^{-1}.

The vertical suture zone on the left side of the model is not reactivated but favours the localization of two conjugate thrusts (structures 2 and 5 on Figure 5a), which root at the base of the crust. The deformation pattern is rather complex, but after 20 Ma, the left-dipping thrust (structure 5 on Figure 5a) localizes more strain than the right-dipping one (structure 2 on Figure 5a), and deforms the central basin that emplaced between the two sutures.

The topography reaches about 7 km for the highest zones located above the inclined suture while the basement of the central basin lies between 2 and 7 km depth. Moho depth ranges from 40 km under the non-deformed crust to 70 km beneath the inclined suture.

4.1.2. *Model with a folded crustal weak zone (Run 2)*

In this model, the right suture zone is re-folded: it dips to the right from the surface to the middle crust and to the left from the middle crust to the Moho. The mantle part of the weak suture zones has the same strong olivine rheology as the rest of the mantle (Figures 4 and 5a and b).

At 5 Myr, deformation localizes equally on the two suture zones. Along the folded suture, a right-dipping shear zone (structure 1 on Figure 5b) develops throughout the crust, ignoring the initial folding of the weak zone. Along the vertical suture, two conjugate shear zones (structures 2 and 3 on Figure 5b) start localizing deformation. Between 15 and 20 Myr, the shear zone 2, rooted on the vertical suture, propagates into the central block, where a basin develops. At 20 Myr, a new right-dipping shear zone (structure 4 on Figure 5b) is formed in sequence from middle crustal depths to the surface. In the right block, a diffuse top-to-the-right shear zone (structure 5 on Figure 5b) develops between 20 and 30 Myr with strain rates never exceeding 7.10^{-16} to 1.10^{-15} s^{-1}. In contrast, shear zones associated with the folded and vertical sutures record larger strain rates ranging between $1.5.10^{-15}$ and 5.10^{-15} s^{-1}.

At the end of the simulation, as in Run 1, the central basin is affected by two large thrusts of opposite senses of shear (structures 1 and 2 on Figure 5b), and a large top-to-the-left shear zone (structure 3 on Figure 5b) has developed on the left part of the vertical suture.

The topography reaches 5 km for the highest zone above the vertical suture zone and 4 km above the inclined suture. The central basin reaches a thickness of 4 km. The crust is thickened from 40 km to 60 km beneath the two suture zones.

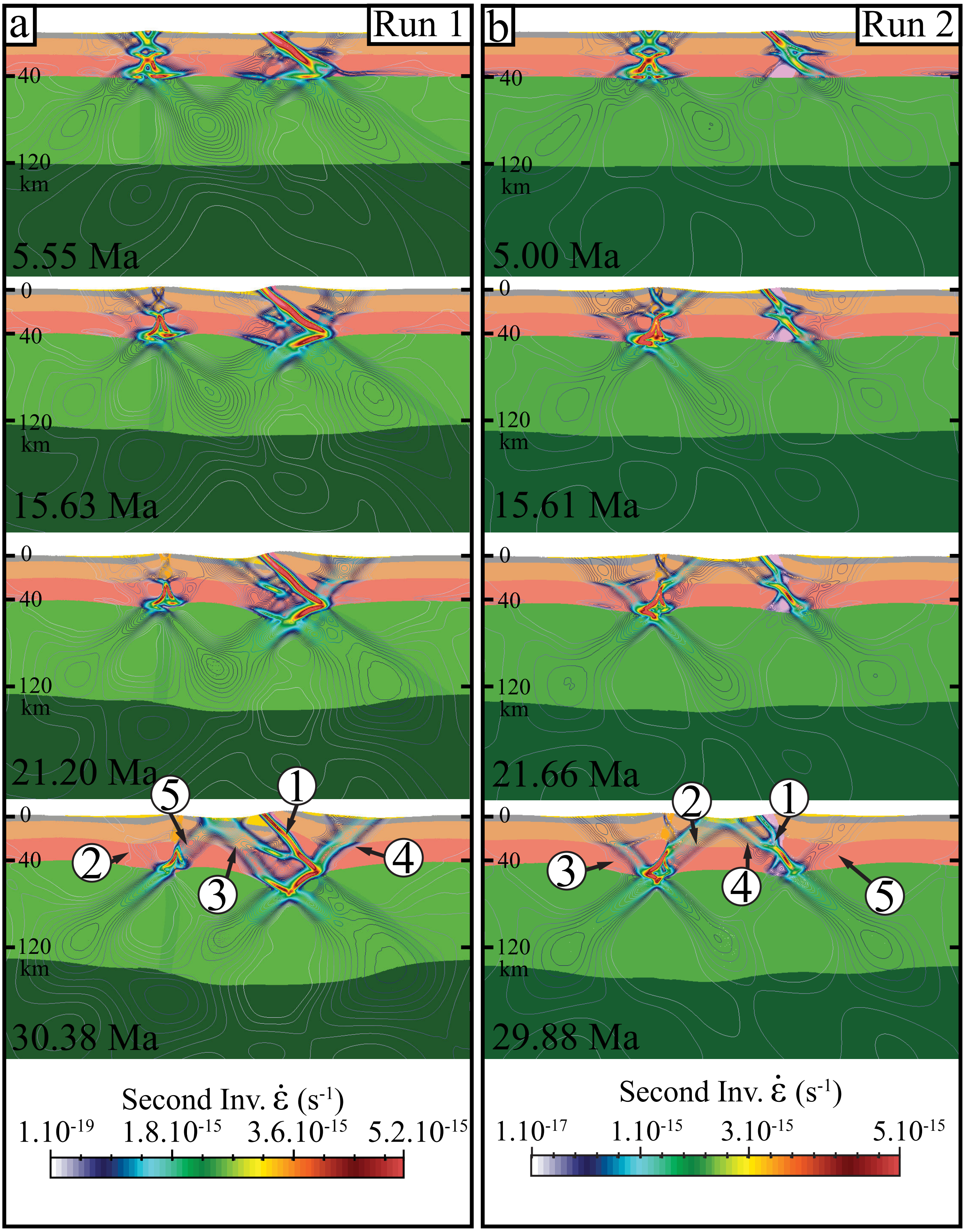

Figure 5: Simulations with crustal weak zones (Runs 1 and 2). Colours represent the different phases of the model (see figure 4 for legend) while coloured lines represent the isovalues of second invariant of the strain rate tensor. a) Simulation 1 with a 30° right-dipping crustal weak zone. b) Simulation 2 folded suture in the crust.

4.2. Initial weak zones in the mantle

4.2.1. *Model with a right dipping weak zone in the mantle (Run 3)*

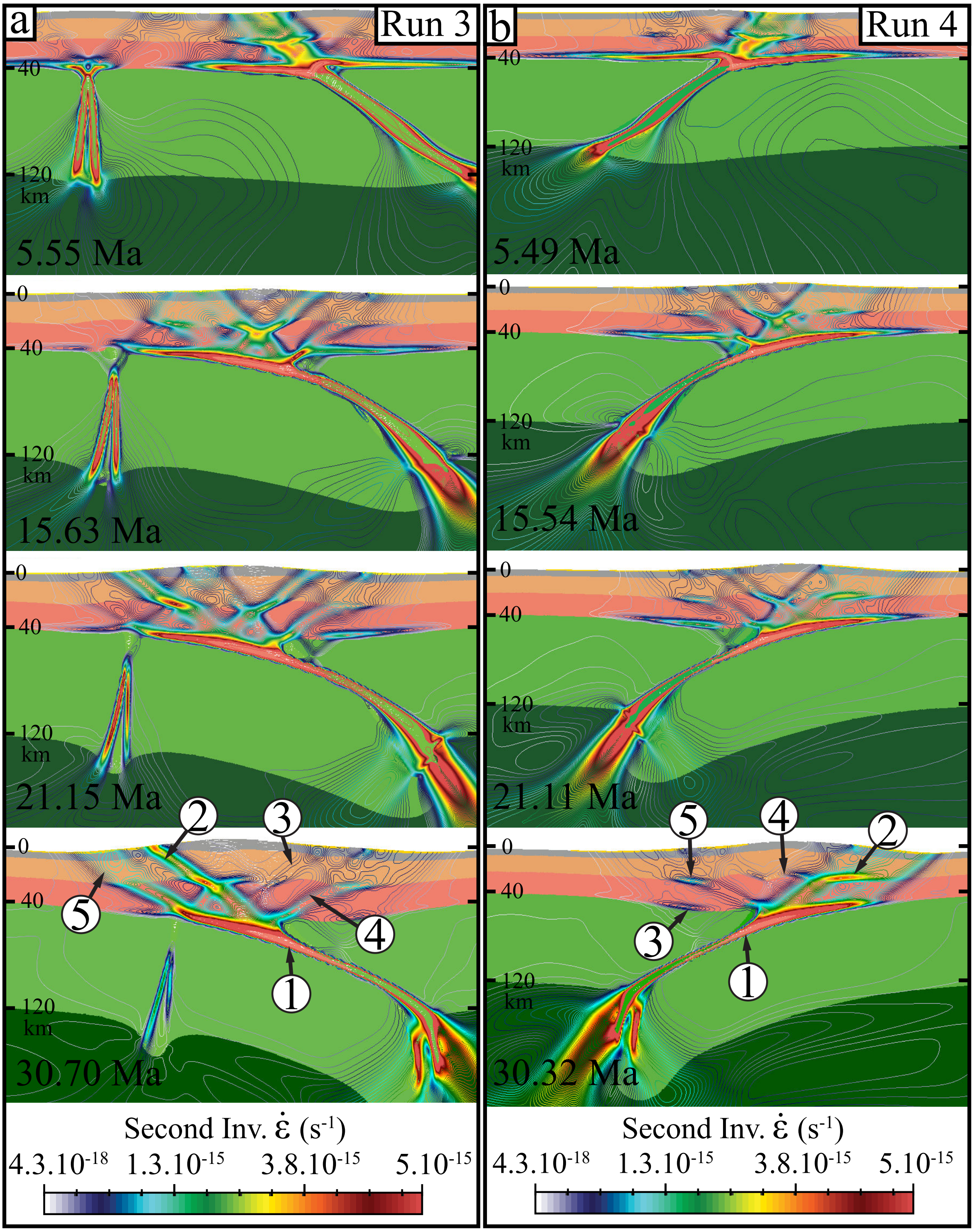

Figure 6: Simulations with mantle weak zones (Runs 3 and 4). Colours represent the different phases of the model (see figure 4 for legend) while coloured lines represent the isovalues of second invariant of the strain rate tensor. a) Simulation 3 with a vertical and 30° right dipping weak zones in the mantle. b) Simulation 4 with a 30° left dipping weak zone in the mantle.

In this experiment, the crust is laterally homogeneous, without any weak zone. The lithospheric mantle contains two weak zones with a wet olivine mantle rheology, following the location and geometry of the crustal weak zones in run 1.

After 5 Myr, deformation mostly localizes along the mantle weak zones and starts to propagate into the crust. Near the inclined weak zone (structure 1 on Figure 6a), the deformation is transferred upwards along the crust-mantle boundary, and in the lower and upper crust along a ~40° dipping shear zone (structure 2 on Figure 6a). The deformation related to the vertical mantle weak zone is transferred into the crust on two conjugate shear zones localizing a small amount of strain.

At 15 Myr, the main shear zone (structure 1 on Figure 6a) propagates into a shallow dipping shear zone along the Moho, which acts as a decollement level decoupling the crust and the lithospheric mantle. The latest starts sinking into the asthenosphere. Progressively, the shear zone associated with the inclined mantle weak zone (structure 1 on Figure 6a) separates into several crustal shear zones rooted at the crust-mantle boundary: a large distributed deformation zone dipping rightward in the central part of the model and two more localized shear zones (structures 3 and 4 on Figure 6a) dipping leftward.

As shortening goes on, the crustal deformation evolves into four localized shear zones: shear zones 2 and 5 (Figure 6a) develop with top-to-the left kinematics while shear zones 3 and 4 (Figure 6a) are characterized by top-to-the right kinematics. The lower crust is dragged into the lithospheric mantle along shear zone 1 (Figure 6a) and the initial vertical weak zone is progressively abandoned.

At 30 Myr, most of the crustal deformation is accommodated by two top-to-the left frontal thrusts (structures 2 and 5 on Figure 6a), while, in the mantle, strain is localized on the initial mantle weak zone. The topography is represented by a high relief zone (8 km) in the central part of the belt and two flexural basins on both sides. The lower crust reaches a depth of 90 km along the mantle shear zone.

4.2.2. *Model with a left dipping weak zone in the mantle (Run 4)*

This model is designed with the same setup as Run 3 but with a different dip direction for the inclined mantle weak zone.

After 5 Myr, the deformation is strongly localized along the initial mantle weak zone (structure 1 on Figure 6b), which accommodates the lithospheric mantle underthrusting on the left side of the shear zone. In response, the crust bends and a flat shear zone develops at the crust-mantle interface on both sides of the mantle shear zone. In the crust, the deformation propagates from the mantle to the surface along a ~40° left dipping shear zone (structure 2 on Figure 6b). With time, the deformation remains localized in the mantle and drags downward a part of the lower crust. In the crust, the deformation becomes more diffuse than in the early stages of the run. Starting from the initial wide shear zone 2 (Figure 6b), less localized deformation zones dipping rightward with top-to-the left kinematics develop and the strain rate progressively decreases in the shear zone 2.

At the end of the run, the crustal deformation is largely distributed through 5 shear zones with low strain rates (around 1.10^{-15} s^{-1} to $1.5.10^{-15}$ s^{-1} for shear zones 3 to 5 (Figure 6b) and around $3.8.10^{-15}$ s^{-1} for the maximal strain rate of the shear zone 2). Meanwhile, in the lithospheric mantle, shear zone 1 (Figure 6b) localizes a large amount of strain, leading the part of the mantle located in the footwall to sink into the asthenosphere.

At the end of the simulation, the crustal deformation mainly localizes in a wide (80 km width) top-to-the right shear zone (structure 2 on Figure 6b) connected to a more localized mantle shear zone (1). The topography reaches 10 km in the central part of the belt and is surrounded by two flexural basins on both sides. The lower crust is pulled downward along the mantle shear zone and attains a depth of 95 km.

4.3.Mantle and crust weak zones

4.3.1. *Model with a right dipping weak zone in the crust and mantle (Run 5)*

In this experiment, the propagation of crustal suture zones into mantle are simulated with a wet olivine rheology in order to induce weak and localizing zones in the mantle (Figures 4 and 7a). The rest of the model is the same as in Run 1.

After 5 Myr, deformation localizes along the inclined suture zone (structure 1 on Figure 7a) from the surface to the base of the Lithosphere along a lithospheric-scale thrust. At this stage, the vertical suture zone is reactivated to a lesser extent and solely in the mantle and the lower crust. A flat shear zone (structure 2 on Figure 7a) located at the base of the crust in the central block nucleates and connects with the vertical suture at ~15 Ma, forming a crustal-scale flat décollement. Another top-to-the-left thrust (structure 3 on Figure 7a) develops to the left of the inclined suture and roots at depth into this flat shear zone (structure 2 on Figure 7a). The Moho therefore acts as a décollement level where deformation localizes and propagates, decoupling the crust and mantle layers of the central block. The mantle lithosphere of the central block delaminates from the crust and starts sinking in the asthenosphere. The remaining crustal part is shortened against the right block, which acts as a backstop. Two top-to-the-left shear zones develop (structures 4 and 5 on Figure 7a) and root on the Moho décollement. At the same time, a top-to-the-right shear zone (structure 6 on Figure 7a) develops inside the right block, forming a back-thrust which delimits a newly formed 'Alpine' type orogenic wedge. Strain rates in the shear zones are significantly higher than in the previous simulation, with largest values in the crust ranging between 2.10^{-15} and 5.10^{-15} s^{-1}, and around 5.10^{-14} s^{-1} in the mantle weak zone.

After 30 Myr the deepest part of the crust, dragged downwards by the sinking of the lithospheric mantle, reaches a depth of 100 km while the average crustal thickness in the mountain range is around 70 km. The final topography is unrealistically high (10-11 km) and the central basin reaches a thickness of 10 km.

4.3.2. *Model with a folded weak zone in the crust and a left dipping weak zone in the mantle (Run 5)*

This model is similar to the previous one, except that a wet olivine rheology is used for the mantle part of the folded suture, allowing us to introduce a weak zone in the lithosphere corresponding to the fossil subduction zone (Figures 4 and 7b).

At the beginning of the model (5 Myr), strain localizes along the left-dipping mantle suture (structure 1 on Figure 7b) and along a flat décollement located at the base of the crust in the central and right blocks (structures 2 and 3 on Figure 7b). The crustal part of the folded suture helps localizing strain along two shear zones, a right-dipping one (structure 4 on Figure 7b) located on the suture and a left-dipping one (structure 5 on Figure 7b) located in the lower crust in the prolongation of the weak mantle shear zone. The top-to-the right shear zone (structure 5 on Figure 7b) with a low strain rate first develops (at 5 Myr) in the upper crust of the right block, in the prolongation of the mantle suture weak zone (structure 1 on Figure 7b). At the same time, conjugate thrusts in the upper and lower crust develop on both parts of the vertical suture.

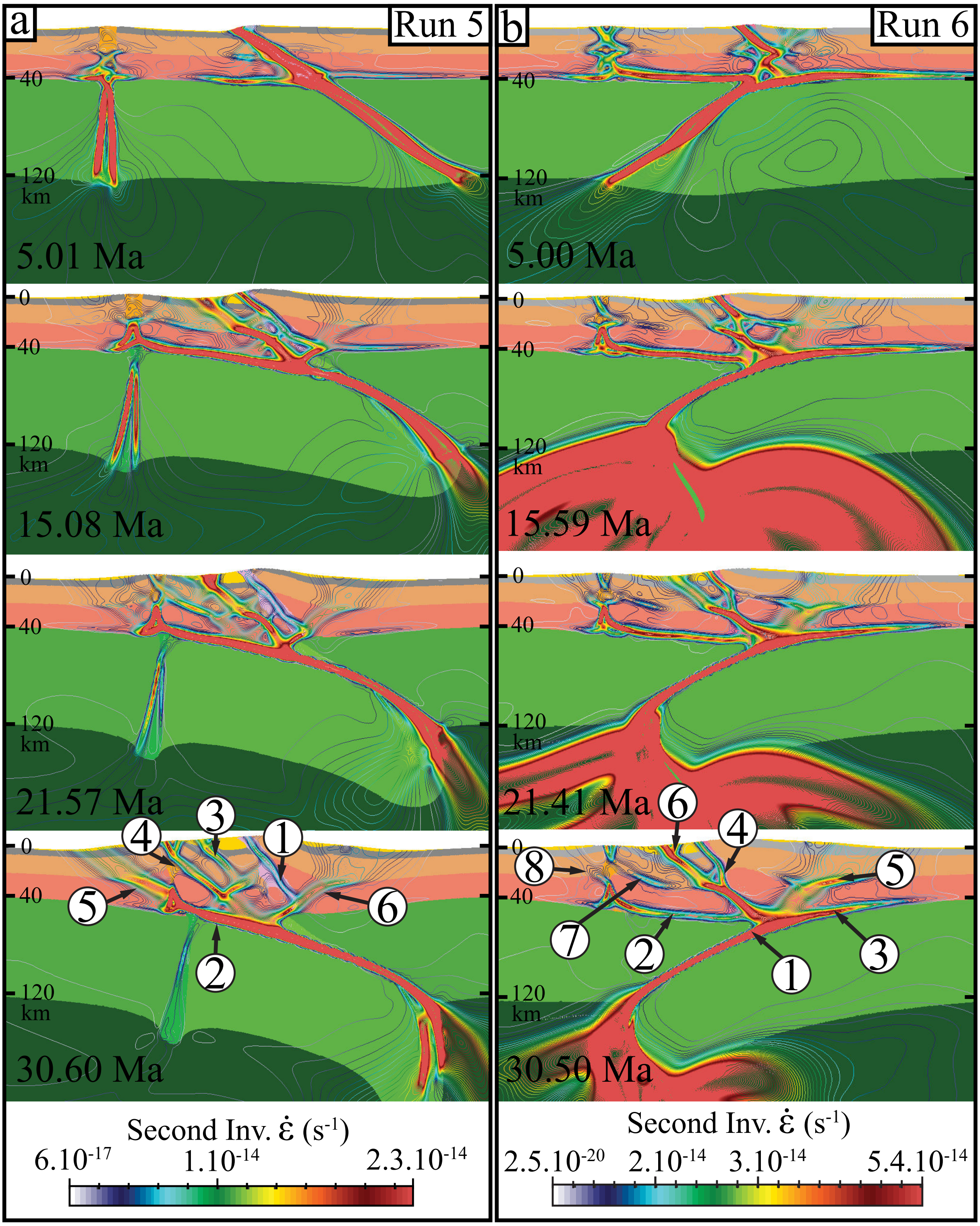

Figure 7: Simulations with both crustal and mantle weak zones (Runs 5 and 6). Colours represent the different phases of the model (see figure 4 for legend) while coloured lines represent the isovalues of second invariant of the strain rate tensor. a) Simulation 5 with a vertical and a 30° left dipping weak zones in the crust and mantle. b) Simulation 6 with a vertical and a folded weak zone in the crust and a left dipping weak zone in the mantle.

After 15 Myr, a new top-to-the-left thrust (structure 6 on Figure 7b) forms to the left of the folded suture, while the conjugate thrust becomes less active. At 20 Myr, the two shear zones (structures 4 and 6 on Figure 7b) deform the central block and its basin, and root at depth in the folded suture. At the same time, two flat shear zones develop in the central block at the Moho (structure 2 on Figure 7b) and at the upper-lower crust boundary (structure 7 on Figure 7b). Eventually, at 30 Myr, the latest shear zone (structure 7 on Figure 7b) emerges at the surface on the trace of the vertical suture while the other one seems to favour the propagation of a new top-to-the-left thrust (structure 8 on Figure 7b) on the left side of the model. On the right block, a newly formed shear zone (structure 5 on Figure 7b) connects with the large mantle shear zone (structure 1 on Figure 7b) and flattens between the upper and lower crust.

During the simulation, the crust of the right block is decoupled from the mantle lithosphere, which leads to its underthrusting beneath the central block.

After around 30 Myr of simulation, the topography reaches 7 km above the folded suture and the central basin has a thickness of 6 km. The crust is thickened from 40 km to 70 km but some parts of the right block crust are buried down to 100 km along the mantle shear zone.

We now discuss the results of the models in the light of existing constraints on the Kyrgyz Tien Shan crustal structure.

5. Validation of the models and crustal structure

5.1. *Validation of the models*

In order to discuss the validity of the different models, we compare them with geophysical data of the Tien Shan structures, imaged through topography data, a deep seismic profile, receiver functions, gravimetric anomalies, electric resistivity profiles and seismic events localization.

5.1.1. *Topography, crustal thickness and Moho geometry*

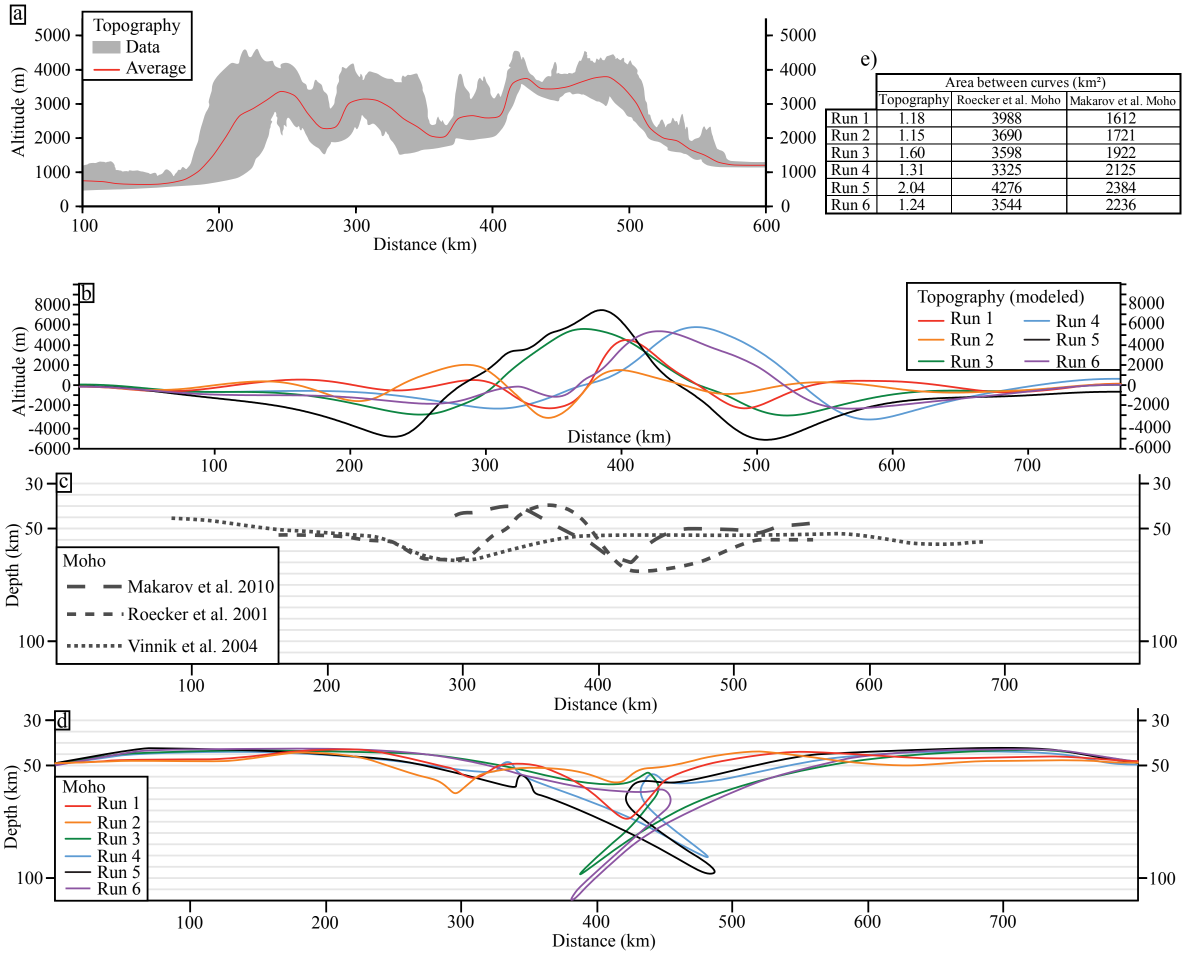

	Area between curves (km²)		
	Topography	Roecker et al. Moho	Makarov et al. Moho
Run 1	1.18	3988	1612
Run 2	1.15	3690	1721
Run 3	1.60	3598	1922
Run 4	1.31	3325	2125
Run 5	2.04	4276	2384
Run 6	1.24	3544	2236

Figure 8: a) Topography of the Kyrgyz Tien Shan from North to South along a 100 km thick swath. The grey area represents the data while the red line is the average topography calculated with a moving average technique. b) Modelled topography for all simulations at the last time-step of each model (see Figure 5). c) Published Moho geometries of the Kyrgyz Tien Shan along a North-South transect between the Issyk-Kul Lake and the Talas-Fergana Fault (see Figure 1 for locations). d) Modelled Moho for all simulations at the last time-step for each model (see Figure 5). e) Misfit estimate calculated as the area (in km²) between modelled and observed surface and Moho topographies. Moho geometry is from Roecker et al. (2001) and Makarov et al. (2010).

We extracted from the SRTM (Shuttle Radar Topography Mission) topographic database a 50 km-wide NNW-SSE area across the Kyrgyz Tien-Shan, and compute a mean topography in order to compare it with our models (Figure 8a).

After 30 Myr, Run 1 presents a topography characterized by two high relief zones located (i) around the northern suture zone with a relative elevation of 2500 m to 3000 m with respect to the basin surface and (ii) around the At-Bashi suture zone with a relative elevation of 5000 m to 6500 m (Figure 8b). These high topography zones correspond to the uplifted hanging walls of the main shear zones. The topography in Run 2 has approximately the same characteristics as in Run 1. It shows two uplifted zones with an elevation of 4000 m to 5000 m on the northern range and 3000 m to 3500 m on the southern one. The difference with Run 1 is that the northern peak is higher than the southern one. Runs 3 and 5 show only one 200 km – wide high relief zone located in the central part of the model, with two foreland basins on its sides. The elevation amplitude between the peak and the basins is of 12 km. Finally, the topography of Runs 4 and 6 also presents two uplifted zones separated by a basin. In this simulation, the contrast between the altitudes of the northern and southern ranges is more important than for Runs 1 and 2. To the north, the relative elevation is of about 1500 m while to south it reaches 6500 to 7000 m.

In summary, the topography of Runs 3 and 5 is significantly different from the observed one for two reasons: (i) the periodicity of highs and lows is not reproduced and (ii) the amplitude of the topography is clearly too large. In other runs, the location and magnitude of the topography is well represented, although in Runs 4 and 6 the two uplifted zones are more dissymmetrical than the observed ones. To better quantify the fit between the modelled and natural topography, the area separating the topographic curves extracted from the final stages of the different runs and the curve representing the average topography has been calculated (Figure 8b and 8e). The best fitting topographies corresponds to Runs 1 and 2.

Moho depths are extracted from previously published geophysical data and models along a similar profile (Zhiwei et al., 2009) (Figure 8c). For Run 1, crustal thicknesses are larger beneath the two high relief zones with Moho depths of 55 km and 70 km under the Nikolaev Line and the At-Bashi suture zone, respectively. The average crustal thickness elsewhere is about 40-45 km. The modelled Moho geometry is very similar to the one interpreted from MANAS experiment (Makarov et al., 2010) beneath the At-Bashi suture zone and to the one deduced from receiver function (Vinnik et al., 2004) beneath the Nikolaev Line (Figures 8c and 8d). The Moho geometry of Run 2 is rather similar to that of Run 1 but with a deepest Moho to the North (60-65 km) than to the South (55-60 km); as for Run 1, it is on average compatible with Moho depths from published geophysical data.

The Moho geometry of Runs 3 to 6 (Figure 8d) is characterized by the dragging of the central or right block lower crust (depending on the dip of the mantle weak zone) into the lithospheric mantle. The deepest part of the crust reaches 90 to more than 100 km along the suture zone. Even without considering the thin layer of underthrusted lower crust present in these models that would not be resolved in the data, this geometry is very different from both geophysically determined Moho depths (Figure 8c).

To summarize, among the six models, only Runs 1 and 2, and particularly Run 1, fit relatively well the Moho modelled by Makarov et al. (2010) as well as the topography. Both produce a topography characterized by two ranges supported by a 50 to 70 km thick crust. Run 1 presents a more pronounced crustal thickening beneath the Tarim, which is more compatible with deep seismic profile data where the Moho deepens from 40 km under the NTS to 60-65 km beneath the At-Bashi suture zone (Makarov et al., 2010).

5.1.2. *Strain localization*

We compare the finite strain of our simulations with the MT profile (shown in Figure 3c), assuming that the possible presence of fluids along major shear zones could significantly reduce their resistivity.

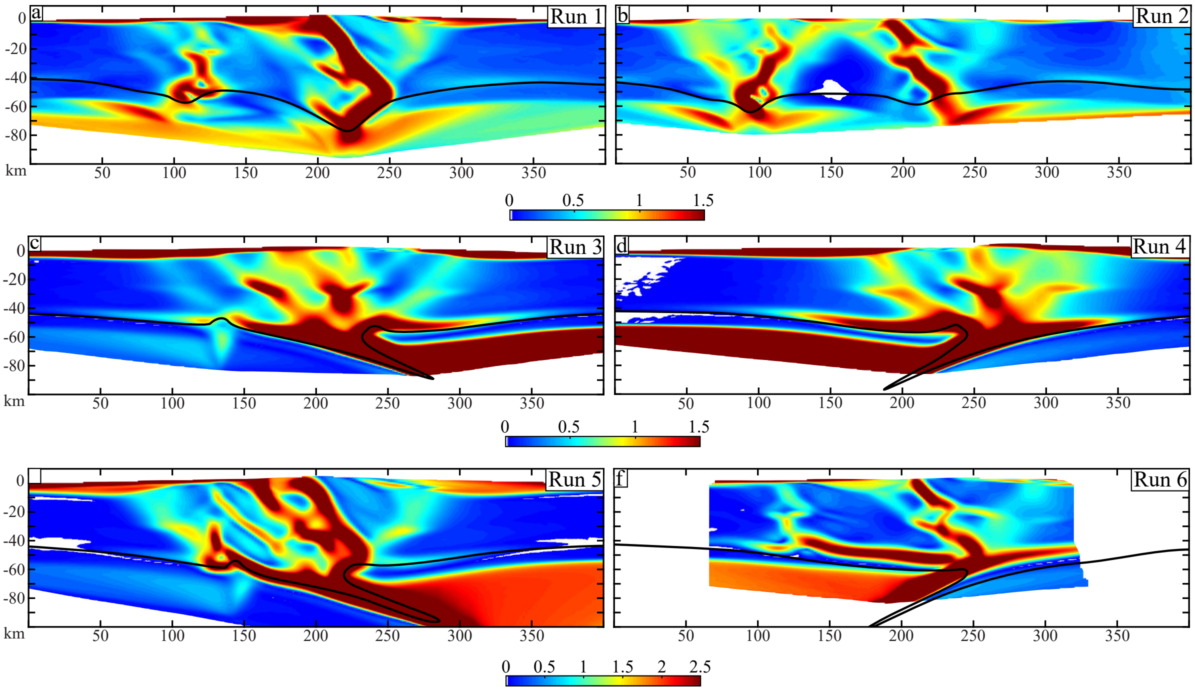

Figure 9: Modelled cumulated strain computed as the second invariant of the strain tensor for simulations 1 (a), 2 (b), 3(c), 4 (d), 5 (e) and 6 (f) at the last time-step for each model (see Figure 5).

For simulations 1 and 2, finite strain is localized along conjugate structures rooted at depth in the lower crust of both sutures. Deformation is more important on the southern suture in Run 1 and on the northern one in Run 2. Despite this difference, these two simulations (Figure 9a and 9b) produce deformation patterns that are in good agreement with the MT resistivity profile (Figure 3c).

The total finite strain computed for Runs 3 and 4 (Figure 9c and 9d) shows that most of the deformation localizes in the lithospheric mantle, particularly along the initial weak zone and at the crust-mantle interface. In the crust, the deformation is much more diffuse since there are no crustal weak zones guiding strain localization. The deformation pattern highlights wide zones of diffuse deformation in the crust, rooted in the mantellic shear zone. These results are not compatible with the deformation zones imaged with the MT profile.

Runs 5 and 6 show mostly top-to-the-North shear zones with a large finite strain that branch on a flat décollement at the Moho (Figures 9e and 9f). Model 5 also shows a conjugate thrust set on the southern side of the At-Bashi suture. This pattern is less compatible with resistivity variations imaged on the MT profile and with other structural data than models 1 and 2 (Figure 9). Oppositely to Runs 1 and 2, Runs 5 and 6 do not display any high strain zone affecting the central basin and rooted in the NL, which is also different from observed in the MT profile (Figure 3c).

The comparison between finite strain models and the electric resistivity profile (Batalev et al., 2011) indicates that Runs 1 and 2 give the most satisfying fit in terms of topography, Moho geometry (Figure 8) and distribution of seismic events (Figure 2a).

5.2. Deep structures and crustal cross-section

5.2.1. *Cenozoic underthrusting of the Tarim*

In this study, we were able to reproduce the underthrusting of the Tarim beneath the Tien Shan, which is ascribed to the Cenozoic convergence stage. This newly formed North-dipping thrust develops even if the Paleozoic At-Bashi suture was initially south-dipping. Indeed, all our experiments made with a 30° dipping suture (At-Bashi) display a decoupling level at lower crustal depths in the right block (Tarim) where the upper crust and the mantle are tear apart. While the upper crust is uplifted in the hanging wall of the inherited structure, the lithospheric mantle is underthrusted beneath the central block (MTS) along a newly formed thrust zone of opposite vergence.

This decoupling can be related to several causes, depending on the considered model. For Run 1 (Figure 5a), the formation of a top-to-the-South shear zone can be interpreted as a consequence of the downward bending of the Moho and lower crustal thickening of the MTS, which accommodates the relative convergence between the MTS and Tarim in the absence of a weak zone in the mantle. This flexure allows localizing a shear zone at the base of the crust in the MTS, which then propagates into the Tarim crust. Therefore, with an initially south-dipping crustal suture between the MTS and Tarim, and without any weak zone in the mantle beneath this suture, the Tarim crust becomes rapidly underthrusted northward beneath the MTS, which suggests that northward dipping reflectors and flexure observed on the deep seismic profile (Makarov et al., 2010) are not necessarily of Paleozoic age.

In the case of a south-dipping weak zone preserved in the mantle (Figure 7a), the development of the top-to-the-south thrust starts at around 13 Myr, i.e., later than for Run 1. The lowermost part of the Tarim crust and the base of the MTS crust are dragged downwards along the mantle weak zone together with the mantle lithosphere of the MTS. The southernmost shear zone accommodates the decoupling between the upper part of the Tarim block uplifted along the At-Bashi shear zone, and its lowermost part, which bends downwards.

The two simulations with a north-dipping At-Bashi suture in the lower crust and/or in the mantle also lead to the development of a North-dipping, top-to-the-South shear zone in the Tarim. However, in the simulation involving a folded suture zone with no weak zone in the mantle, strain rates along this shear zone are much lower than for the other models, i.e., around 7.10^{-16} to 1.10^{-15} s^{-1}. In the simulation involving a weak zone in the mantle, this shear zone localises less the deformation than in the first two models.

5.2.2. *Crustal cross-section*

Using published geological field studies (e.g. Alekseev et al., 2007; Bakirov and Maksumova, 2001; Biske et al., 2013; Burtman, 2008; Jourdon et al., 2017; Jukov et al., 2008; Karpovitch et al., 1964; Loury et al., 2015b; Osmonbetov et al., 1982), and geophysical data (Batalev et al., 2011; Makarov et al., 2010; Mikhailova et al., 2015a, 2015b; Vinnik et al., 2004) and comparing them to thermomechanical models (this study), we propose a new geological crustal-scale cross-section of the Kyrgyz Tien Shan (Figure 10).

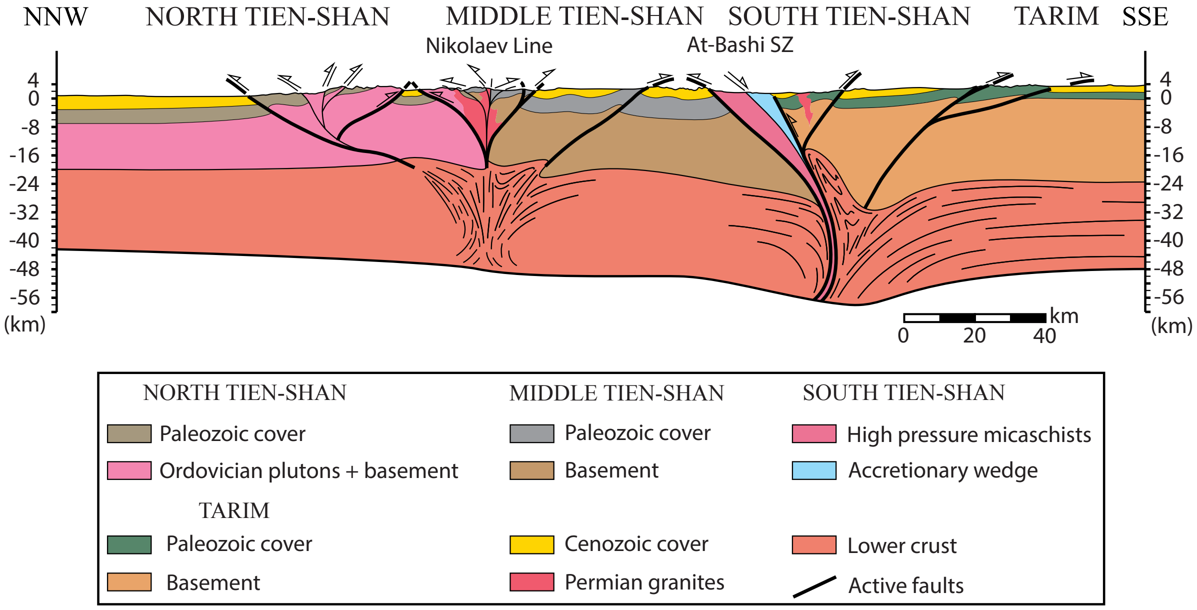

Figure 10: Interpretative crustal cross-section of the Kyrgyz Tien Shan along the thick black line in Figure 1, constructed from the geological data at the surface and the combination of geophysical data and a thermo-mechanical model (Run 1) presented in this study.

The principal crustal structures, that is to say, the top-to-the-South thrust fault on the northern boundary of the Tarim, the thrust faults in the Naryn basin and along the At-Bashi range have been described after surface observations and geophysical studies. The thermo-mechanical modelling allows us to propose a possible way to describe and interpret these structures at a crustal scale based on the best fitting model (Run 1) with a micaschist rheology for the At-Bashi suture and a homogeneous olivine rheology for the mantle.

The northward and southward verging of thrusts observed at the near surface root at depth into the suture zones. In the MTS, the central basin thrust, which separates the Naryn and At-Bashi basins, roots at depth into the Nikolaev Line and deforms the central intra-mountainous basin Cenozoic deposits. It is worth noting that some models also show a top-to-the North thrust in this central basin rooted into the At-Bashi suture, which also corresponds to tectonic structures observed in the Naryn basin (Goode et al., 2014). In the same way, the northernmost thrust, which uplifts the Ordovician plutonic bodies over the Cenozoic basin of Bishkek, roots into the Nikolaev Line. Exhumation of the Tarim lower crust along the At-Bashi suture zone coincides well with the structural setting of the Khan-Tengri and Pobeda regions where granulites, interpreted as coming from the Tarim lower crust (Loury et al., 2015b), overthrust Paleozoic metamorphic units. The age of this thrust is still unknown, but our experiments suggest that this exhumation, or at least a part of it, could be related to the Cenozoic deformation stage. Newly formed thrusts accommodate the uplift and overthrusting of the At-Bashi massif onto the Tarim basin.

6. Discussion

6.1. Influence of mantle versus crustal weak zones

6.1.1. *Deformation pattern*

The deformation patterns resulting from simulations with either crustal or mantle weak zones are very different. In absence of crustal weak zones, the mantle heterogeneities or lateral variation of the lithosphere strength controls the deformation in the crust. Nevertheless, as observed in Runs 3 and 4 this deformation is extremely localized in the mantle and along the crust-mantle boundary, and is much more distributed in the crust than in the runs where crustal weak zones are present. Moreover, the presence of weak mantle zones result in the sinking of the mantle lithosphere into the asthenosphere at depths of ~250-300 km, which is not consistent with the depth distribution of earthquakes (which are located in at crustal depths) nor with

geophysical images, although global tomography models of the Tien Shan are not accurate enough to determine the geometry of the deepest part of the lithosphere (Deng et al., 2017; Huang and Zhao, 2006; Lei and Zhao, 2007; Zhiwei et al., 2009).

When the inherited structures consist only of lateral variations of the whole lithospheric resistance between the different blocks (Figure S1e, f and g), the final deformation (Figure S6) and strain rate localization (Figure S5) poorly fit the available data (Table 2). However, when weak zones are only present in the crust, the topography (represented by peaks and basins), the Moho geometry and the crustal deformation show a better fit with the geophysical and geological data. Therefore, the most satisfying models with respect to existing geological and geophysical constrains are those with weak zones in the crust only. These modelling results rise interesting points:

1- Crustal weak zones are necessary to reproduce the first-order strain pattern in the Tien-Shan crust.

2- The presence or absence of weak mantle zone appears to exert a first-order control on the model results, as also evidenced by a recent study (Heron et al., 2016a, 2016b; Heron and Pysklywec, 2016). However, in the Tien-Shan area, the best-fitting models are those without weak zones in the mantle.

3- A too rigid Tarim lithosphere impedes the formation of the top to the south thrust in the Tarim. It is therefore essential that the northern boundary of Tarim and the Tien Shan lithospheres display similar strengths for the models to capture geological constraints.

	Model	WZ crust	WZ mantle	Thermal Age of the lithosphere (Ma)			Dip of the right WZ	Strong right block	Moho Type	Topo type	Strain pattern
				Left block	Central block	Right block					
Crustal control	1	Yes	No	100	100	100	R	No	A	A	A
	2	Yes	No	100	100	100	L	No	A	A	A
	9	Yes	No	500	500	500	R	No	A	A	A
	10	Yes	No	50	50	50	R	No	A	A	A
	11	Yes	No	100	100	100	R	No	A	A	A
	12	Yes	No	100	100	100	R	No	A	A	A
Mantellic control	3	No	Yes	100	100	100	R	No	B	B	C
	4	No	Yes	100	100	100	L	No	C	B	C
Mantellic control with crustal overprint	5	Yes	Yes	100	100	100	R	No	B	B	B
	6	Yes	Yes	100	100	100	L	No	C	C	B
	7	Yes	Yes	500	500	500	L	No	C	C	B
	8	Yes	Yes	50	50	50	L	No	C	A	B
Lithospheric heterogeneity control	14	Yes	Yes	100	100	500	L	Yes	A	B	B
	13	Yes	No	100	100	500	R	Yes	A	A	A
	15	No	No	500	100	500		Yes	D	B	A
	16	Yes	No	500	100	500	R	Yes	D	B	A

Table 2: Summary of all performed simulations and their first order results on Moho and topography shapes and on the cumulated strain pattern. Moho type: A = two distinct roots located beneath the crustal weak zones. B = underthrusting of the central block lower crust. C = underthrusting of the right block lower crust. D = one single deep crustal root beneath the central block. Topography type: A = two equally high relief areas separated by a central basin, and flexural basins on the right and left sides of the belt. B = one high relief area in the centre of the model surrounded by two flexural basins. C = one high relief area above the right crustal weak zone and a lower topography area located above the left crustal weak zone; both ranges are separated by a central basin. Two flexural basins are formed on the right and left parts of the belt. Strain Pattern: A = Strain localized in the crust and controlled by the crustal weak zones. B = Strain localized in the mantle and along the inclined initial crustal weak zone. C = Strain localized in the mantle and distributed in the crust.

Even if a stronger lithosphere could not lead to the formation of a thrust within the Tarim with the simulations we performed (Figure S5 and S6), we have to keep in mind that this represents only a small part of this continental block and it does not mean that the whole Tarim lithosphere is not strong. Moreover, the apparent influence of crust and mantle heterogeneities differs with the length scale at which the structures are analyzed. Recent studies (Calignano et al., 2015a, 2015b, Heron et al., 2016a, 2016b; Heron and Pysklywec, 2016) evidenced that mantle heterogeneities and lateral lithospheric strength variations are needed to localize deformation at the scale of plate tectonics (several thousands of km). The case of the Asian continent deformation in response to the India-Asia collision illustrates this long wavelength deformation pattern with localized deformation zones like the Tien Shan and weakly deformed zones like the Tarim that can be related to “weak” and “strong” lithospheres, respectively. Yet, at the scale of tectonic structures (~100’s km), like those which design the Tien Shan orogeny or the alpine orogeny (Bauville and Schmalholz, 2015; Lafosse et al., 2016; von Tscharner et al., 2016) crustal scale heterogeneities are primordial to explain the localization of the deformation as imaged by geological and geophysical data.

6.1.2. *Mantle healing*

The Tien Shan was formed by at least two subduction-collision event as highlighted by the presence of oceanic eclogites in the suture zones between (1) the NTS and the Kazakh Platform, and (2) the Tien Shan and the Tarim. Hence, a lithospheric-scale shear zone was involved in the final Paleozoic structuration of the South Tien-Shan. This shear zone must have presented, at least at the time of its activity, smaller grain sizes and fluid rich phases related to the subduction, i.e. two major softening actors (e.g. Mei and Kohlstedt, 2000,Bercovici and Ricard, 2012; Chu and Korenaga, 2012; Heron et al., 2016; Pili et al., 1997; Rovetta et al., 1987; Van Wijk, 2005; Vissers et al., 1995). According to Bercovici and Ricard, (2012) two phases peridotite (olivine, pyroxene) have very slow grain growth due to pinning processes. Theoretical healing time scale for these shear zones being be of the order of several hundred million years, they should have retained there weakness through the Cenozoic time. Yet, for Tien-Shan, our two simulations involving a strong and homogeneous mantle are more consistent with existing constraints on surface and deep structures. This suggests that Paleozoic mantle suture zones are no longer weak with respect to the current deformation stage.

Studies on Tien-Shan mantle xenoliths exhumed with basalts at around 70-75 Ma (Bagdassarov et al., 2011) show that there is only a very small fraction of water in these xenoliths, which possibly reflects the average composition of the Tien Shan lithospheric mantle. This statement is confirmed by the MT profile which shows high resistivity values in the mantle, which suggests that the mantle water content is low (Bagdassarov et al., 2011; Batalev et al., 2011). Hence, if there was a significant amount of water in the mantle in Paleozoic times, it seems not be the case since the Cenozoic.

At this stage we can only posit that pervasive alkaline volcanism that occurred during Permian (e.g., de Jong et al., 2009) and Cenozoic (e.g., Sobel and Arnaud, 2000) times may have dehydrated and heated the lithosphere and favored grain growth despite pinning.

Conclusions

The combination of field geological studies and available geophysical data with thermo-mechanical models allows us to propose a new crustal-scale cross section of the Tien Shan. In addition, the modelling approach leads us to test several mechanical and geometric hypotheses about the Tien Shan inherited structures. The key results of this study are the following:

- The mantle suture zones rheology strongly influences the localization of deformation and the geometry of the structures. For the simulations involving mantle suture zones, a weak mantle zone leads to the sinking of the lithosphere and to deformation localization on a décollement level at the base of crust.
- The most satisfying results are able to reproduce the crustal structure of the Tien Shan only with initial crustal weak zones instead of mantellic ones, which implies that the Tien Shan Cenozoic tectonics is mostly controlled by crustal deformation.
- The underthrusting of the Tarim block beneath the Tien Shan belt is shown to be a Cenozoic structure related to the formation of a North-dipping thrust in the Tarim crust. This structure can develop from either a South- or North-dipping At-Bashi suture zone.
- Although two simulations (1 and 2) provided good results concerning the current structure of the Kyrgyz Tien Shan, it seems that the strain localization, geometry of shear zones, topography and Moho geometry are more consistent with an initial South-dipping At-Bashi suture zone (Run 1).

Appendix A

This study uses pTatin2D, a parallel implementation of the finite element method, which employs an Arbitrary Lagrangian Eulerian discretization, together with the material point method. The codes solves for conservation of momentum

$$\frac{\partial \boldsymbol{\sigma}}{\partial \mathbf{x}} + \rho_{\mathrm{eff}}\mathbf{g} = 0 \tag{1}$$

for a viscous material of density ρ_{eff}, so that the full stress tensor

$$\boldsymbol{\sigma} = \boldsymbol{\sigma}^{\mathrm{d}} - \mathbf{I}P \tag{2}$$

is the sum of deviatoric stress σ^{d} for a material of effective viscosity η_{eff} and an isotropic pressure term P.

$$\boldsymbol{\sigma}^{\mathbf{d}} = 2\eta_{\mathrm{eff}}\dot{\boldsymbol{\varepsilon}} \tag{3}$$

Conservation of mass is approximated by enforcing incompressibility of the flow ***v***

$$\nabla.\mathbf{v} = 0 \tag{4}$$

The code is also coupled explicitly to heat conservation equation

$$\rho Cp\frac{\partial T}{\partial t} + \mathbf{v}.\nabla T = \nabla.(k\nabla T) + \rho H$$

in order to solve for temperature T using a constant thermal diffusivity κ.

The free surface boundary condition is accurately resolved through the use of high order stable elements (Q_2-P_1).

Material properties and history variables are assigned to material points contained within the computational domain that are advected with the velocity field of the solution. Effective viscosity is evaluated on material points using

$$\eta_{effv} = \frac{1}{4}(\dot{\varepsilon})^{\frac{1}{n}}\left(\frac{3}{4}A\right)^{-\frac{1}{n}} e^{\frac{Q+PV^*}{nRT}} \tag{6}$$

where coefficient A, n, Q define typical dislocation creep law and V^*, the activation volume, permits to increase activation energy with pressure.

If the deviatoric stress (eq. 3) predicted by dislocation creep exceed the Drucker-Prager yield criterion as expressed here as a function of friction angle ϕ and cohesion Co, the effective viscosity is re-evaluated as follow:

$$\eta_{effp} = \frac{\sin\phi P + \cos\phi Co}{\dot{\varepsilon}^{II}} \tag{7}$$

$$\eta_{eff} = \min(\eta_{effp}, \eta_{effv}) \tag{8}$$

Effective density of material points, i.e.

$$\rho_{eff} = \rho_0(1 - \alpha(T - T_0) + \beta(P - P_0)) \tag{9}$$

depends on a constant term ρ_0 defined by the lithology and varies linearly on Pressure and Temperature where α, β are the coefficients of thermal expansion and adiabatic compressibility respectively.

After being evaluated on material points, both viscosity and the density are then projected to the gauss points using Q_1 basis function together with harmonic and arithmetic averaging respectively.

Damage on faults is implemented through linear decrease of friction and/or cohesion coefficients with accumulated plastic strain ϵ

$$Co = \max\left(Co_\infty, Co_0 - \frac{\epsilon\,(Co_0 - Co_\infty)}{\epsilon_\infty}\right) \tag{10a}$$

$$\phi = \max\left(\phi_\infty, \phi_0 - \frac{\epsilon(\phi_0 - \phi_\infty)}{\epsilon_\infty}\right) \tag{10b}$$

Co_0/ϕ_0, Co_∞/ϕ_∞ and ϵ_∞ are respectively the initial (undamaged) cohesion/friction, the cohesion/friction at the end of the softening and the characteristic plastic strain after which final softening is achieved.

At each time steps, material point of sediment type are inserted on the current free surface, a new surface is computed according to Culling (1965) law:

$$K_e \frac{\partial^2 h}{\partial x^2} = \frac{\partial h}{\partial t} \tag{11}$$

The top surface is then remeshed so that only the sedimented markers remain. Sediment markers are given an age which corresponds to the time of deposition. This allows representing a crude stratigraphic information.

Details on implementation are similar to the 3D version of the code (Le Pourhiet et al., 2017; May et al., 2015, 2014). In 2D however, the linearized system of equation is small enough to be resolved with a direct sparse solver (umfpack) available through PETSc (Balay et al., 2014, 2013).

Supplementary material for:

The deep structure of Kyrgyz Tien Shan: modelling the past to better constrain the present

This supplementary material contains the setup (Figure S1) and results of 16 models (Figures S2 to S8) that we designed in order to assess and discuss the influence of the thermal state of the lithosphere, the rheology of the crust and the lateral variations of the lithospheric strength on the localization of the deformation. These runs are cited in the discussion and their results are reported in the Table 2 of the manuscript file but details are only presented here.

1. Impact of the lithospheric resistance

1.1. Impact of thermal age of the lithosphere

We have performed two "end member" simulations about the thermal age of the lithosphere (Figures S3c,d and S4a,b, runs 7, 8, 9 and 10) resulting in 4 different runs: two simulations using the same configuration as runs 1 and 6 with a thermal age of 500 Ma (Figure S3c and S4a, runs 7 and 9) and a lithospheric thickness of 140 km, and two simulations with the same configuration but for a thermal age of 50 Ma and a lithospheric thickness of 80 km (Figure S3d and S4b, runs 8 and 10).

Simulations performed with an old, strong lithosphere (Figure S3c and S4a) show a more localized deformation while simulations performed with a weaker lithosphere (Figure S3d and S4b) show a more distributed deformation. These results have already been largely presented and discussed in the literature about the behavior and deformation of the lithosphere depending on its rheology and resistance (Burov, 2011; Burov and Diament, 1995). Moreover, the control exerted by the mantle on the strain localization is much more important as the lithosphere is strong. Whereas the lithospheric strength affects the degree of strain localization, it does not change much the first order deformation pattern. Therefore, the 100 Ma old and 120 km thick lithosphere we use seems an acceptable approximation in order to discuss first order results.

1.2. Impact of the lithospheric resistance heterogeneity

In the previous runs, all blocks have the same strength, which forces strain localization to be controlled by mantellic and/or crustal weak zones. In order to assess the possible influence of a lithospheric strength contrast between blocks we designed several other tests (Figure S1e,f,g).

The first two runs use the geometry of runs 1 and 6 (Figure S1e and g, runs 13 and 14 respectively) and are characterized by a stronger lithosphere (thermal age of 500 Ma and 140 km thick) on the right block (corresponding to the Tarim) while other blocks are represented by a lithosphere with a thermal age of 100 Ma and a thickness of 100 km. Results show that the most rigid block is not or poorly deformed (Figure S6) while the other blocks accommodate the largest part of the deformation. The latter appears mainly accommodated by crustal weak zones and by the folding of the crust due to the indentation of the rigid block.

Then, two other runs involve a stronger lithosphere (thermal age of 500 Ma and 140 km thick) on the left and right blocks while the central one is weaker (thermal age of 100 Ma and a 100 km thickness), with either a homogeneous crust (Figure S5c, run 15) or with weak zones in the crust (Figure S5d, run 16). These two runs have been designed in order to determine if a lithospheric rheological contrast could be sufficient to explain the localization of the deformation observed in the Tien Shan or if inherited crustal structures are needed. Without crustal weak zones, the central block is highly folded and four important shear zones are formed (Figure S5s and S6), rooting into the weaker rheological interfaces of the lithosphere (upper crust-lower crust boundary and crust-mantle boundary). On the contrary, when crustal weak zones are present the central block is still highly deformed due to its relative weakness compared to the surrounding blocks, but the deformation is more controlled by the presence of initial weak zones than by the lithospheric strength contrast (Figure S5d and S6).

*1.3.**Impact of the crustal rheology***

In the previous models, we chose to simulate the continental crust with two rheological layers, a quartz rheology for the upper crust and a diorite rheology for the lower crust. We have tested the influence of a single rheological layer crust on the localization of the deformation with a whole quartz crust and a whole diorite crust using the configuration of run 1 (Figure S4 c and d, runs 11 and 12). In the case where the crust is only made of quartz (Figure S4d), the deformation expresses by the buckling of the crust with 100 km wavelength folds (Figure S4d and S6). On the other hand, with a diorite rheology the crust is barely folded and the deformation pattern is close to that obtained in the run 1 (Figure S4c and S6).

This observation allow us to consider that the lower crust has to be more resistant than a quartz rheology to obtain a result more consistent with data. Therefore a two layered crust seems to be a good approximation in order to simulate the deformation of the Tien Shan.

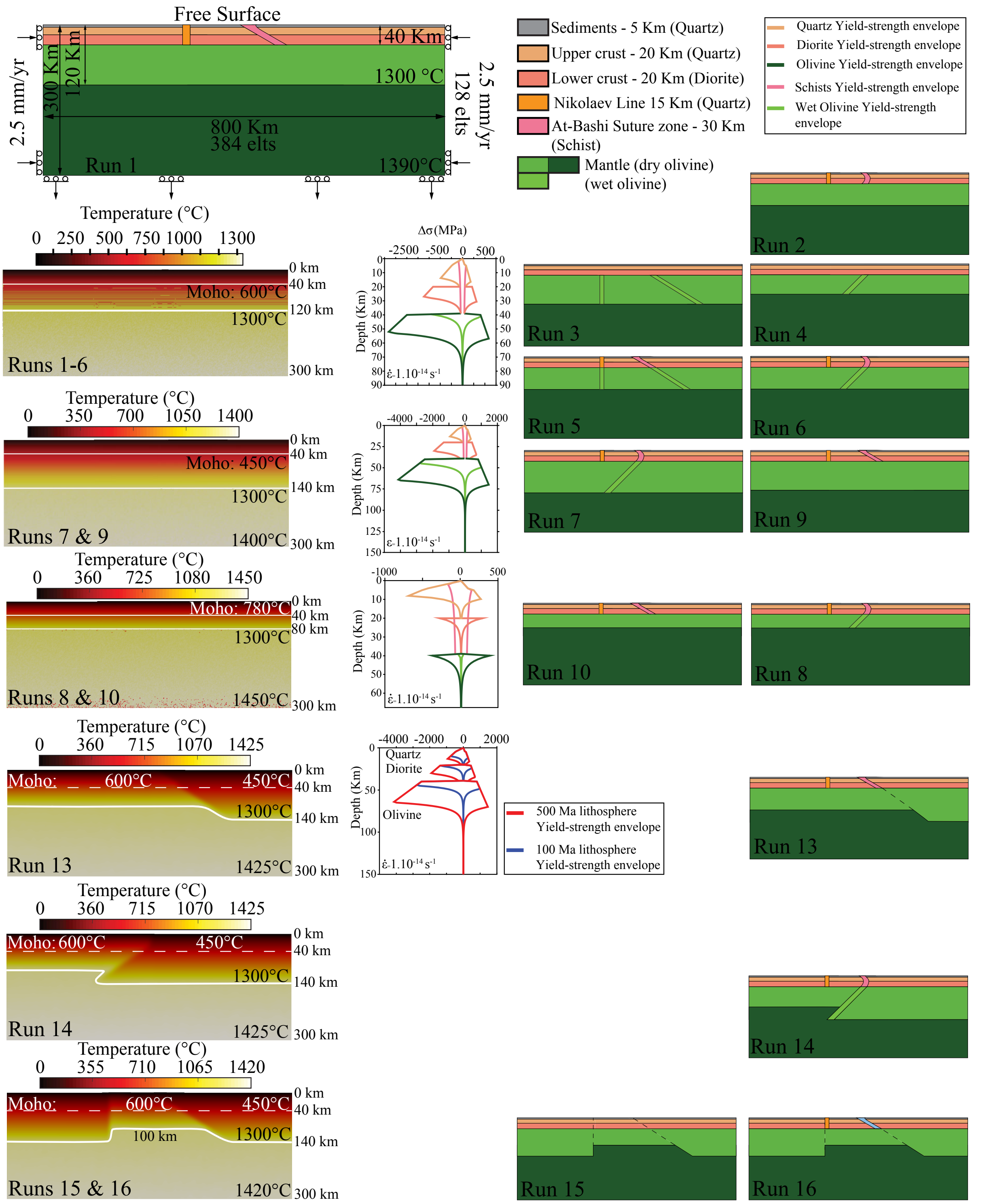

Figure S1: Initial setup of each run presented in this supplementary material. a. Geometry of model 1, with dimensions and boundary conditions for all simulations (elts = elements). On the left: initial thermal state of the lithosphere. On the right: initial geometry of different lithospheric layers and weak zones. b. 100 Ma lithosphere. c. 500 Ma lithosphere. d. 50 Ma lithosphere. e. and f. The right block lithosphere is simulated for a thermal age of 500 Ma, the two other blocks are simulated with a 100 Ma lithosphere. g. Left and right blocks lithospheres are simulated for a thermal age of 500 Ma, the central block is simulated with a 100 Ma lithosphere. The Yield-strength envelopes of simulated materials are calculated for a (b) 100 Ma, (c) 500 Ma and (d) 50 Ma lithosphere.

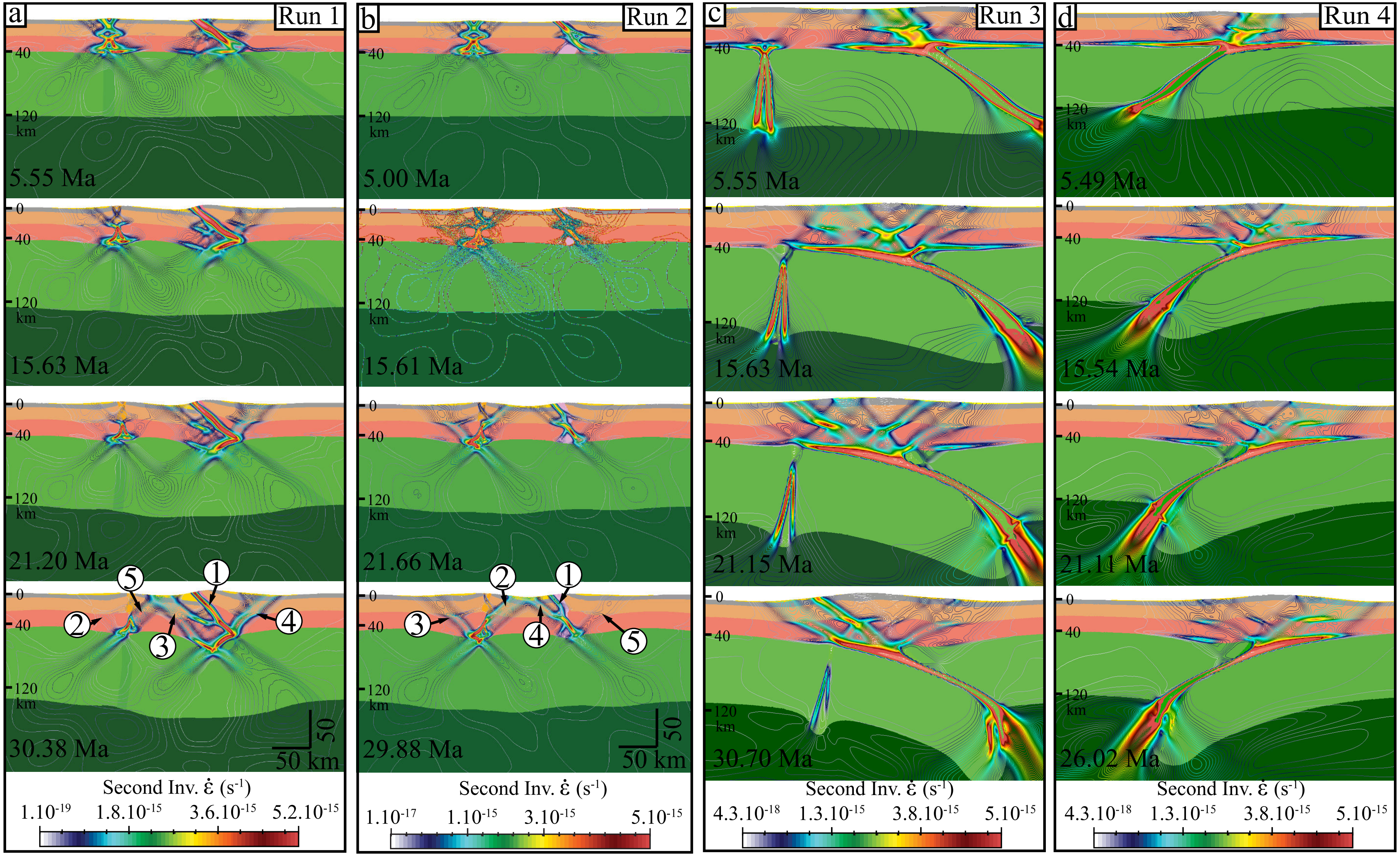

Figure S2: Modelling results for: a. and b. Crustal weak zones with a (a) rigth-dipping and (b) left dipping weak zone. c. and d. Mantellic weak zones with a (c) rigth-dipping and (d) left dipping weak zone. Colors represent the different phases of the model (see Figure S1 for legend) while colored lines represent the isovalues of second invariant of the strain rate tensor

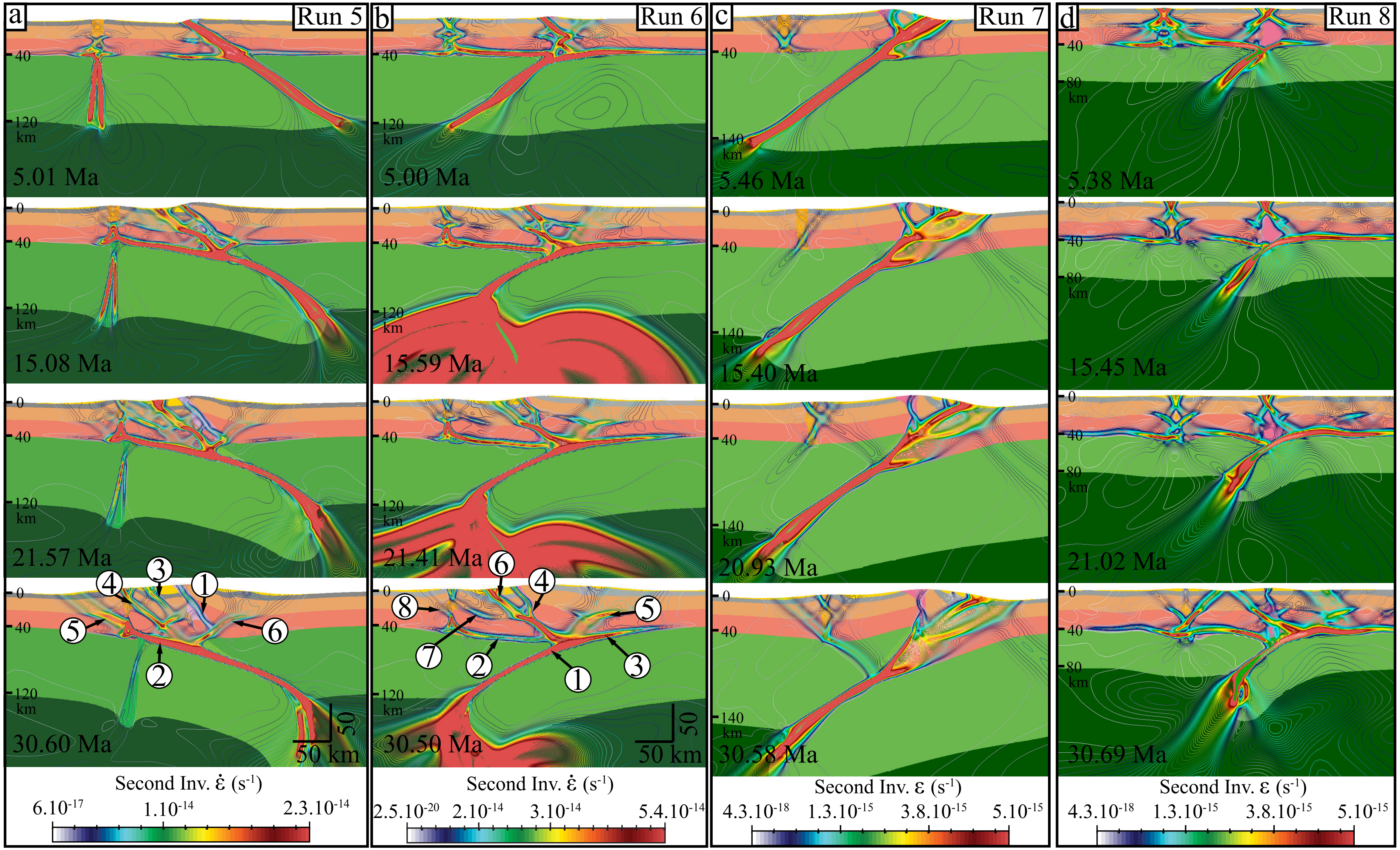

Figure S3: Modelling results for: a. and b. Crustal and mantellic weak zones with a (a) rigth-dipping and (b) left dipping weak zone. c. and d. Crustal and mantellic weak zones with a left dipping weak zone for a (c) 500 Ma lithosphere and a (d) 50 Ma lithosphere. Colors represent the different phases of the model (see Figure S1 for legend) while colored lines represent the isovalues of second invariant of the strain rate tensor

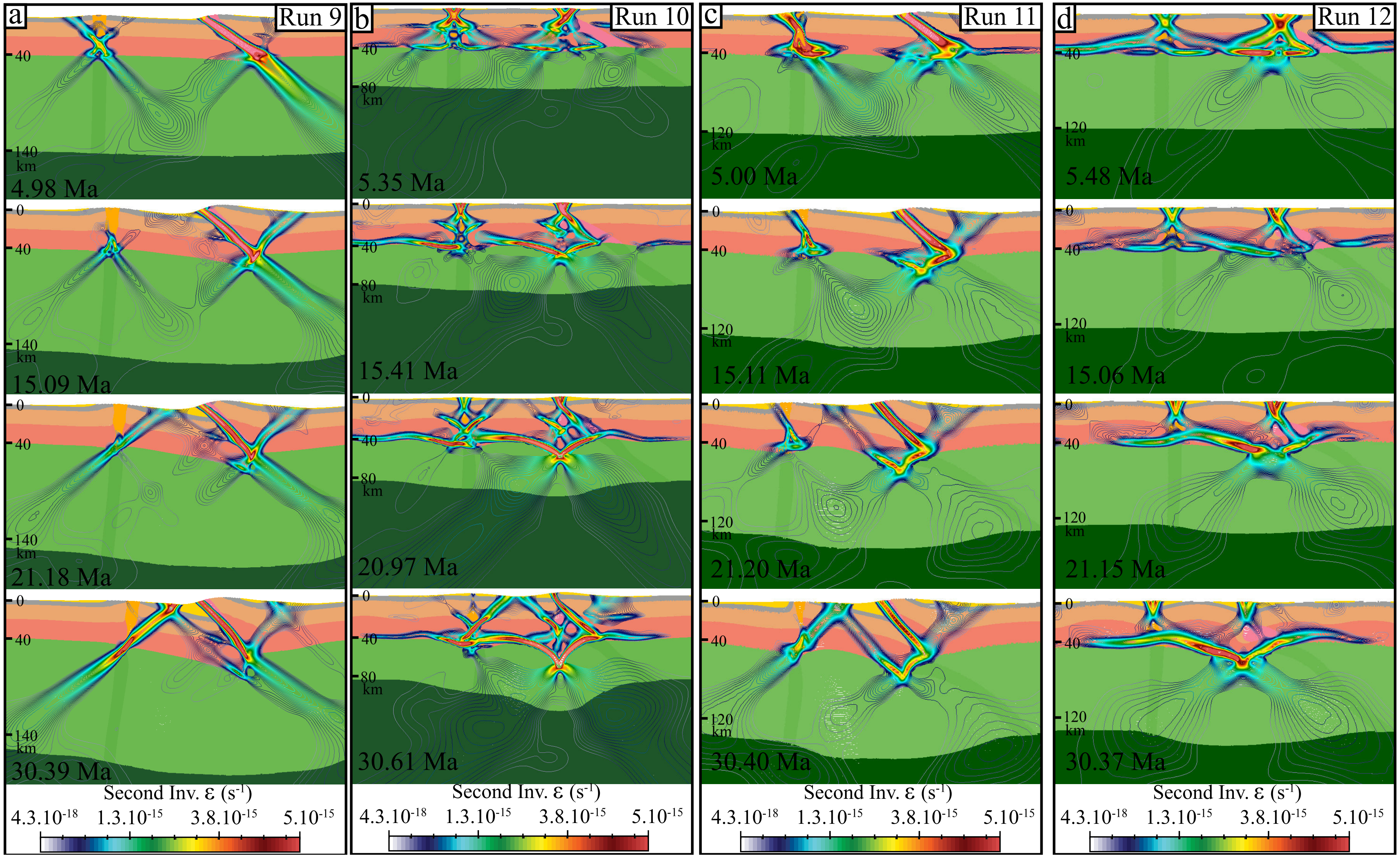

Figure S4: Modelling results for: a. and b. Crustal weak zones with a right-dipping weak zone for a (a) 500 Ma lithosphere and a (b) 50 Ma lithosphere. c. and d. Crustal weak zones with a right dipping weak zone for a (c) diorite rheology crust and a (d) quartz rheology crust. Colors represent the different phases of the model (see Figure S1 for legend) while colored lines represent the isovalues of second invariant of the strain rate tensor.

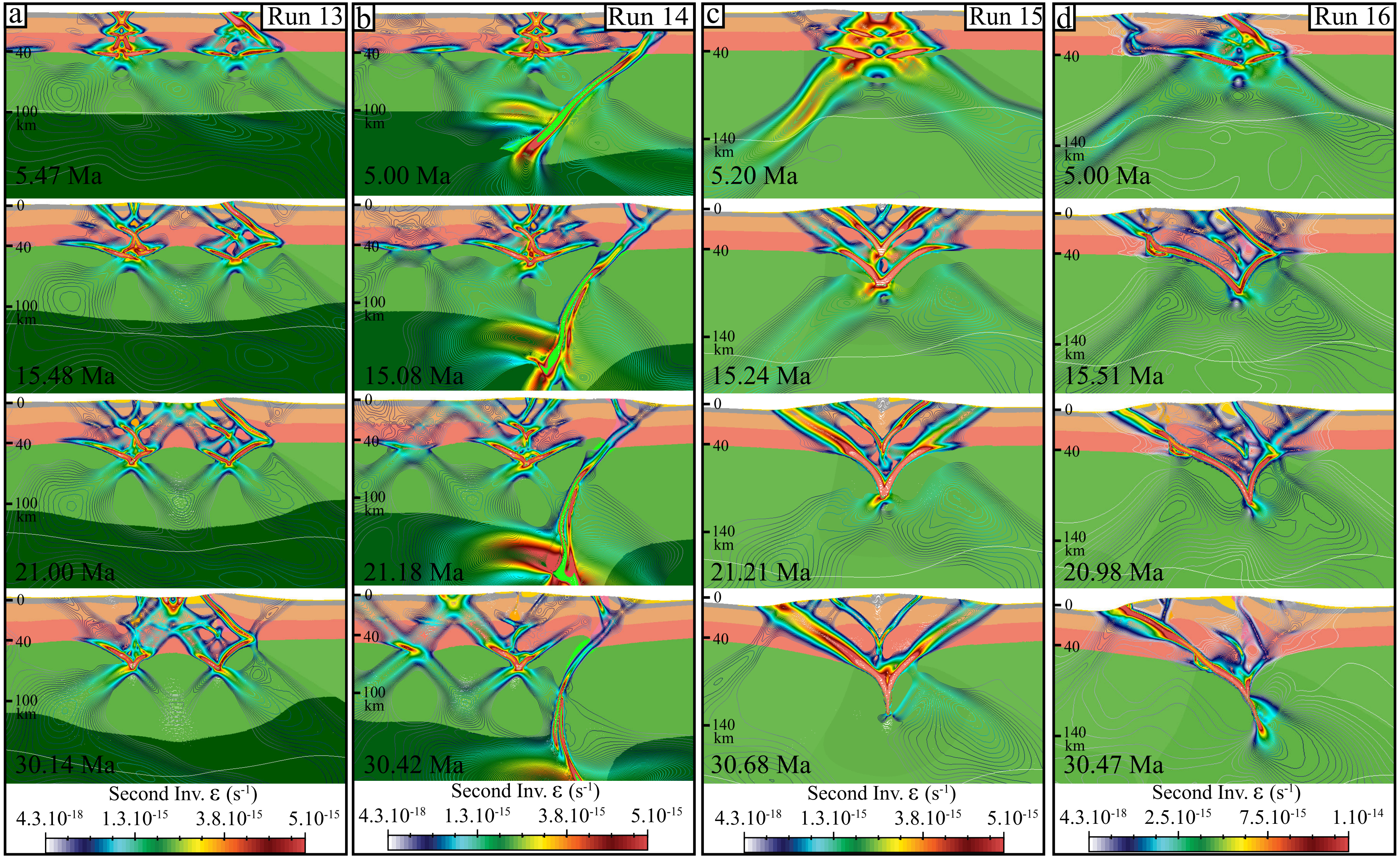

Figure S5: Modelling results for: a. Curstal and b. Crustal and mantellic weak zones with a (a) right dipping and a (b) left dipping weak zone. The lithosphere of the right block is simulated with a thermal age of 500 Ma while the two other blocks are simulated with a 100 Ma lithosphere. c. and d. The lithospheres of the right and left blocks are simulated with a thermal age of 500 Ma while the central block is simulated with a 100 Ma lithosphere with no weak zones (c) and crustal weak zones (d). Colors represent the different phases of the model (see Figure S1 for legend) while colored lines represent the isovalues of second invariant of the strain rate tensor

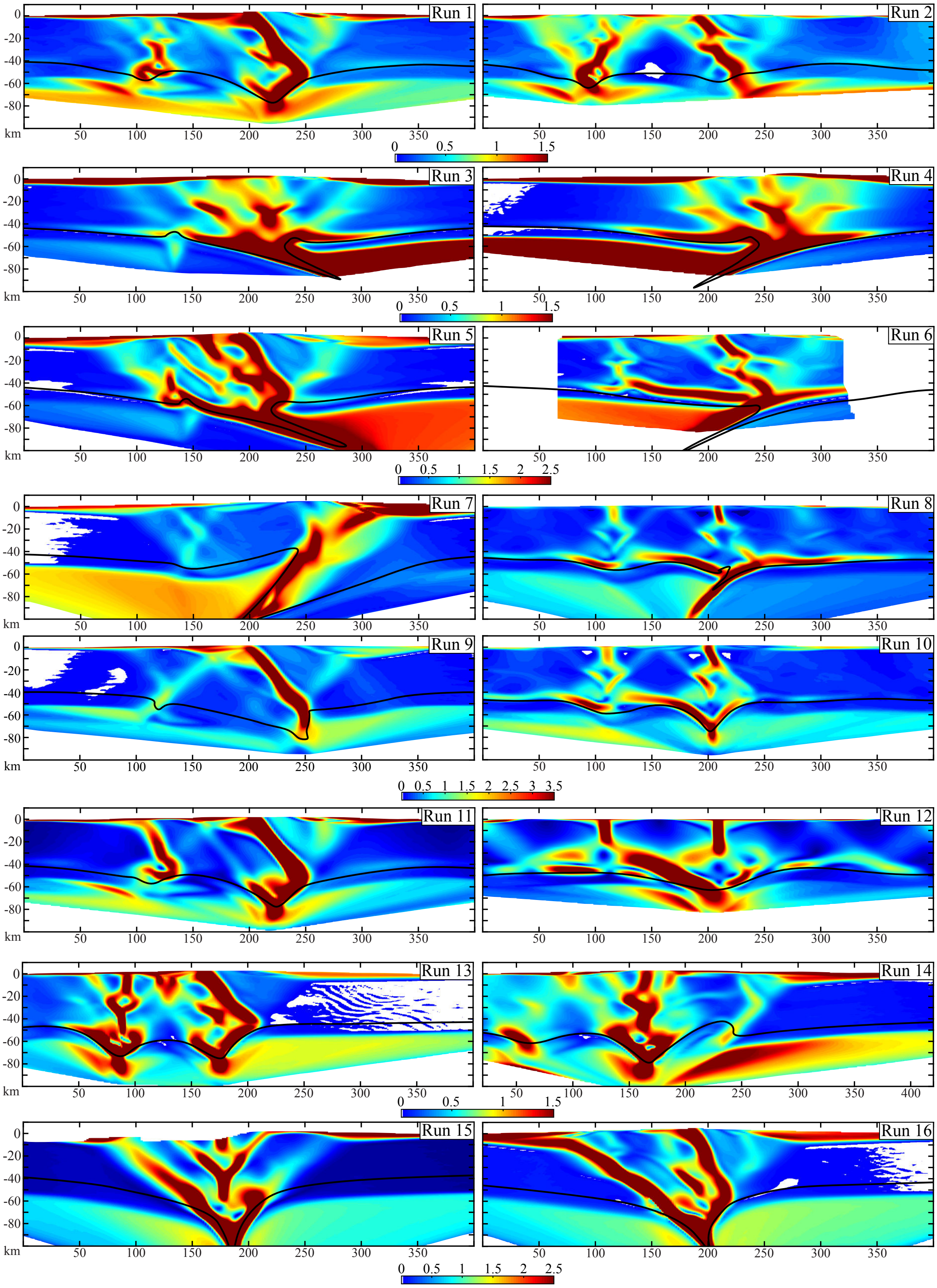

Figure S6: Total modeled strain for all simulations at the last time-step for each model. The total strain value (computed as the second invariant of the strain tensor) represents an augmentation or a diminution of the width/length with respect to the initial shape. A value of 1 means 100% of augmentation or diminution of its width or length

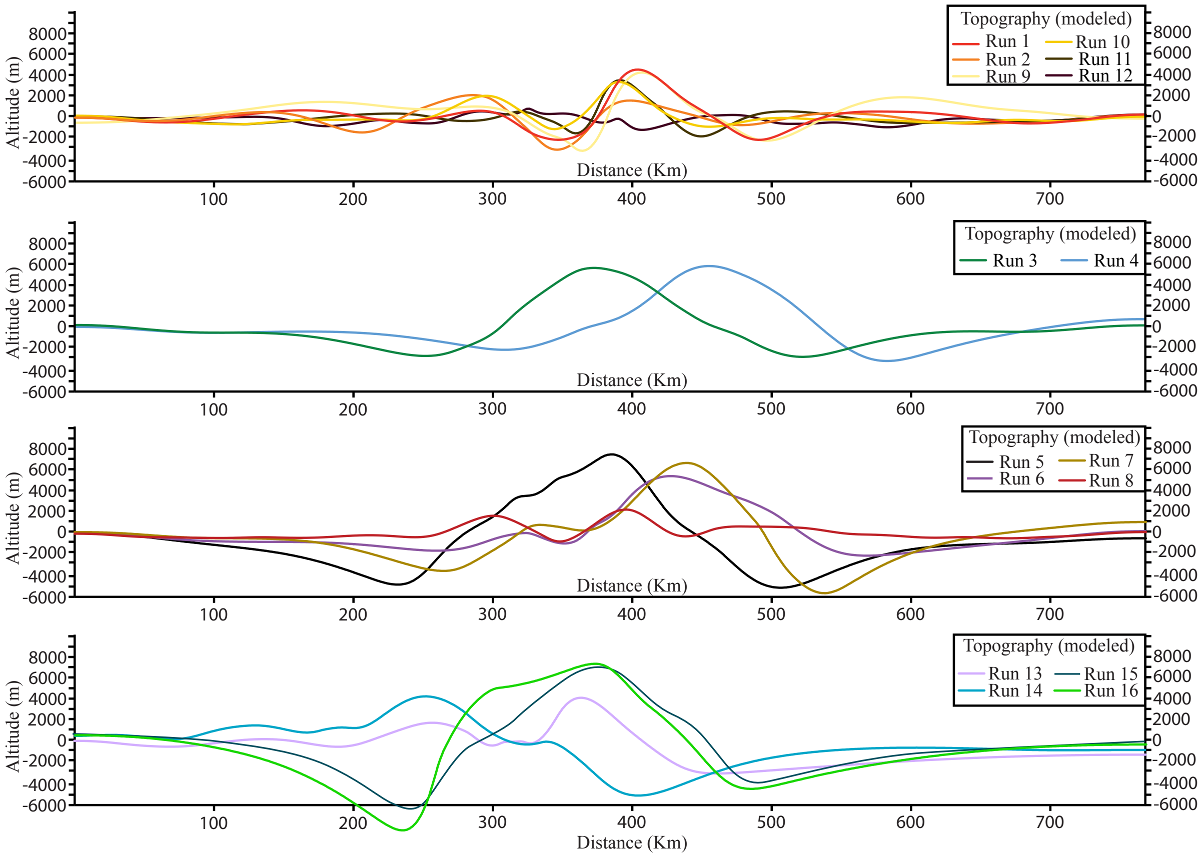

Figure S7: Modeled topography for each run at the last time-step.

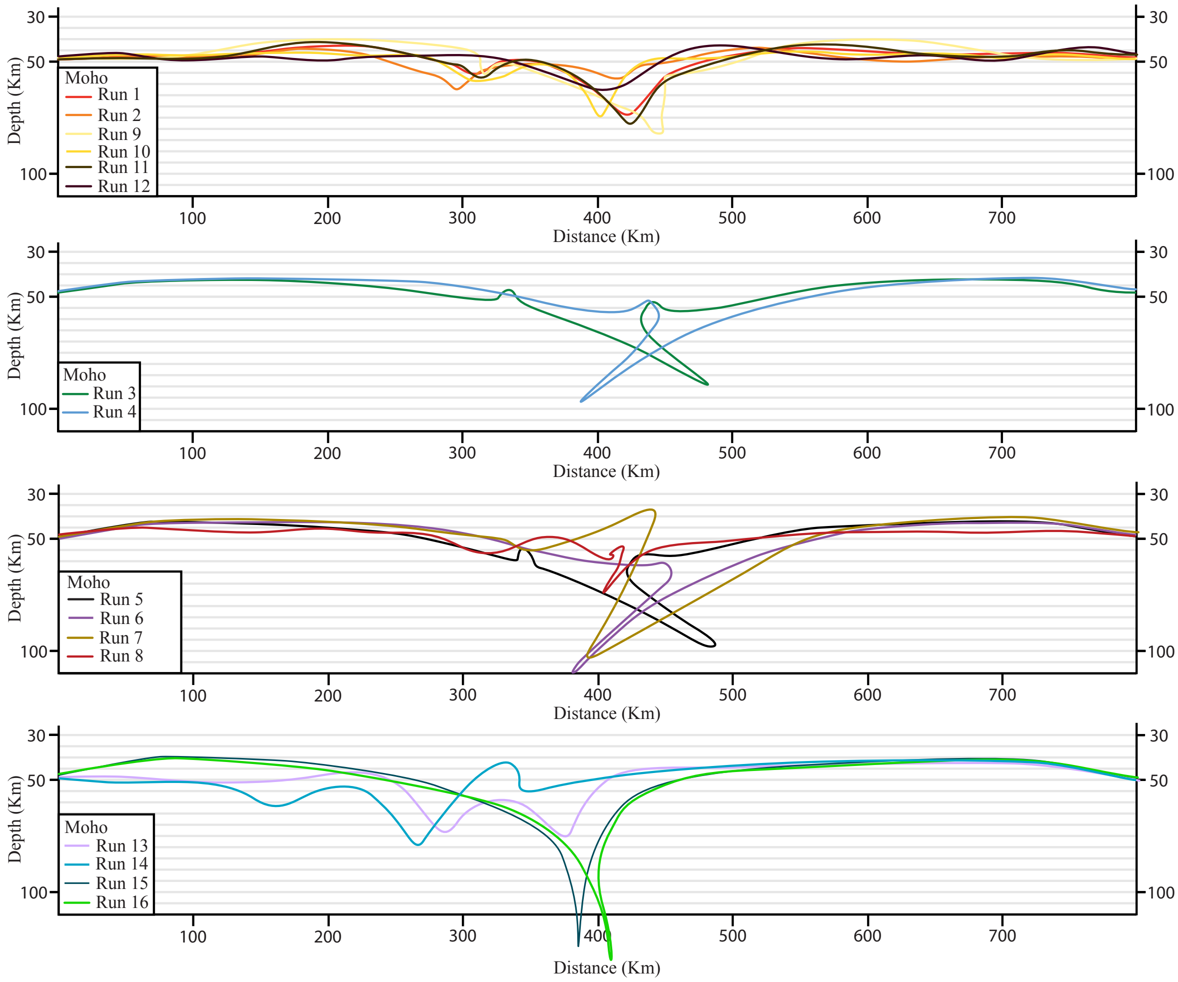

Figure S8: Modeled geometry of the Moho for each run at the last time step.

IV. Influence des processus de surface sur la tectonique et l'exhumation basse température.

La thermo-chronologie basse température est utilisée comme un marqueur d'événements se produisant à proximité de la surface, et représentant les dernières étapes de l'exhumation des roches par des phénomènes qui peuvent être liés à la fois à des processus d'érosion, des processus tectoniques ou des événements magmatiques.

Dans la chaîne du Tien Shan de nombreuses études basées sur les méthodes de datation de thermo-chronologie basse température (U-Th-He, traces de fission sur apatite et zircon) sont disponibles. Ces dernières permettent notamment de mettre en lumière la présence d'une période tectoniquement calme au cours du Mésozoïque avant la reprise en compression de la chaîne au Cénozoïque (Jolivet et al., 2013; Sobel and Arnaud, 2000). Cependant, les nombreuses datations effectuées, notamment dans la partie orientale du Tien Shan kirghize peuvent être utilisées pour identifier les structures actives au cours du Cénozoïque (Macaulay et al., 2014).

Les modèles thermomécaniques présentés précédemment visaient à comprendre comment la géométrie des structures héritées ainsi que la rhéologie de la lithosphère influençaient la déformation cénozoïque. Ceux-ci nous ont permis de montrer :

1- Que la déformation cénozoïque dans le Tien Shan kirghize est contrôlée par des structures crustales et que le manteau lithosphérique ne contient plus de traces rhéologiques des phases tectoniques paléozoïques.
2- Que la lithosphère de la bordure nord du Tarim est rhéologiquement similaire à la lithosphère du Tien Shan.
3- Que la zone de suture qui sépare le Tien Shan et le Tarim possédait un pendage vers le sud avant la tectonique cénozoïque.

Cependant, l'idée de ce chapitre est de comprendre quels sont les paramètres qui vont influencer l'exhumation à basse température. A partir de ces caractéristiques nous avons élaboré un nouvel état initial dans le but de comprendre l'influence des processus de surface (érosion-sédimentation) sur la répartition et l'exhumation des roches du Tien Shan au-delà de l'isotherme 120°C. En effet, cette isotherme correspond à la température en-dessous de laquelle les traces de fission sur les apatites (AFT) ne cicatrisent plus ce qui nous permet de comparer les résultats issus des modèles avec les données des AFT qui sont très abondantes dans le Tien Shan.

1. Trajets Température-temps.

Les données thermo-chronologiques basse température et notamment les histogrammes de longueur de traces permettent de déterminer les trajets température-temps qui caractérisent l'histoire thermique la plus probable d'un échantillon. Pour pouvoir comparer les résultats obtenus via la modélisation numérique à ceux obtenus sur les échantillons naturels il est nécessaire de pouvoir retracer cette histoire thermique dans les modèles.

Le code pTatin2D utilise des marqueurs sur lesquels sont enregistrés entre autres le numéro d'un point, sa position (x,z), la pression et la température à chaque pas de temps. Ces informations permettent de retracer spatialement et temporellement l'histoire thermo-barométrique d'un point situé dans le modèle. J'ai développé un code matlab permettant d'établir les chemins pression-température-temps et les âges traces de fission de points choisis à partir des fichiers de sortie du modèle (détails du code et explications en Annexes). Dans le cas qui nous intéresse ici seuls les trajets température-temps (T-t) sont considérés.

L'idée est donc de déterminer quels sont les points ayant subi un refroidissement à partir de températures supérieures ou égales à 120°C et à quel moment les trajectoires T-t ont croisé cette isotherme. Pour identifier ces points et sauvegarder leur âge il est nécessaire de mettre en place un algorithme qui va repérer chaque point à chaque pas de temps.

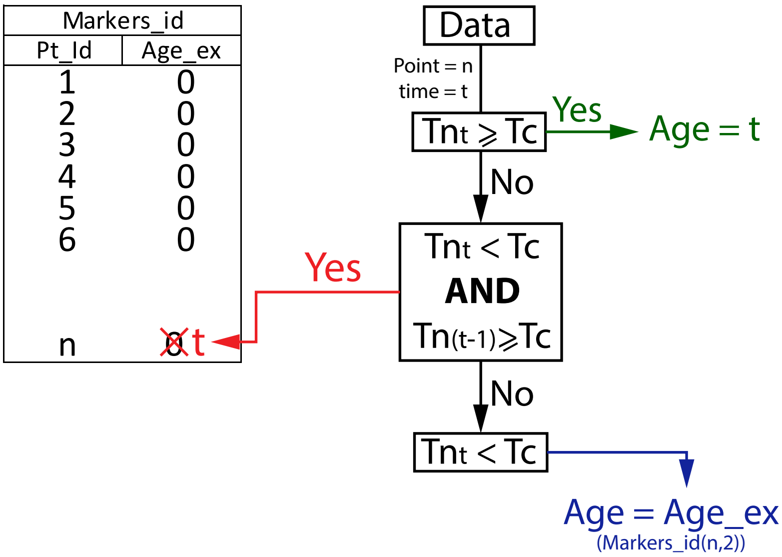

Figure IV-1 : Schéma de l'algorithme utilisé pour calculer et extraire l'âge d'exhumation de points issus des fichiers de sortie de pTatin2D

Une matrice de n lignes et 2 colonnes (markers_id sur la Figure) est créée avant que ne commence l'itération sur les pas de temps. Cette matrice enregistre le numéro du point dans la colonne 1 tandis que la colonne 2 est remplie de 0. Cette matrice va servir à identifier et garder en mémoire le temps t auquel un point n passe l'isotherme 120°C (dans le sens du refroidissement).

A chaque pas de temps :

- Si la température d'un point est supérieure à 120°C la valeur d'âge attribuée à ce point est celle de l'âge du modèle. Cette valeur sera écrasée au pas de temps d'après puisque le système chronométrique est considéré ouvert.
- Si la température est inférieure à 120°C et qu'au pas de temps précédent elle était supérieure à 120°C alors le point a traversé l'isotherme qui représente la fermeture du système chronométrique. Dans ce cas, la valeur d'âge attribuée à ce point est l'âge du modèle au pas de temps en cours et cette valeur est stockée dans la colonne 2 de la matrice markers_id.

- Si la température est inférieure à 120°C alors la valeur d'âge attribuée au point est la valeur stockée dans la deuxième colonne de la matrice markers_id.

Cette dernière étape permet d'attribuer l'âge 0 aux points ayant toujours résidé à des températures inférieures à 120°C mais également de fixer l'âge d'exhumation des points ayant traversé l'isotherme 120°C sans que celui-ci ne soit écrasé au pas de temps suivant.

Le fait d'attribuer la valeur 0 à l'âge des points dont la température a toujours été inférieure à 120°C peut paraître étrange au premier abord. En réalité le temps dans les modèles s'écoule positivement, or l'état initial représente le passé et l'état final le présent. C'est pourquoi une fois tous les pas de temps analysés il est nécessaire d'inverser le temps pour le faire correspondre à notre échelle. Nous prenons donc le pas de temps final comme étant 0 et le pas de temps initial devient $t_{init} = -t_{fin}$. De cette manière le pas de temps final peut être assimilé au présent. Nous calculons ensuite l'âge d'exhumation tel que :

$$age_{exhum} = t_{final} - age$$

Cet âge peut être comparé aux âges obtenus par thermo-chronologie basse température d'après la méthode des traces de fissions sur apatite.

2. Impact des processus d'éroion-sédimentation sur l'exhumation de roches de basse température dans les chaînes de montagnes : l'exemple du Tien Shan

Le travail présenté dans cette section fait l'objet d'un article court préparé dans le but d'être soumis au journal Terra Nova.

Résumé

Les modèles thermo-mécaniques 2D montrent que la formation des chaînes de montagnes est très sensible aux processus de surface qui affectent l'évolution tectonique en améliorant l'exhumation et l'affaiblissement thermique de la croûte ainsi qu'en déposant des sédiments moins résistants et plus froids dans les bassins. Alors que les structures tectoniques cylindriques sont bien reproduites par les modèles de déformation plane en 2D, les processus d'érosion et de sédimentation ne peuvent pas être approximés le long d'un profil 1D. Ce problème est bien illustré dans le Tien Shan, où les structures tectoniques, les bassins et les taux d'exhumations sont bien contraints. En utilisant la profondeur des bassins et le taux d'exhumation en tant que fonction coût à partir des résultats de nos modèles, nous pouvons montrer qu'il est impossible d'ajuster à la fois la taille des bassins et l'exhumation en utilisant un modèle 1D standard. Nous avons donc implémenté un transfert de masse perpendiculaire au plan dans lequel le modèle est défini afin de montrer comment cela affecte l'évolution tectonique du modèle. Finalement, nous montrons qu'en considérant des flux sédimentaires hors plan il est nécessaire d'évacuer 80% des sédiments par drainage latéral dans le but de minimiser le résidu entre les données et le modèle.

Impact of erosion-sedimentation processes on low temperature exhumation in mountain belts: the example of the Tien Shan

Anthony Jourdon[1], Laetitia Le Pourhiet[2], Carole Petit[1], Yann Rolland[1]

1- Université Côte d'Azur, CNRS, IRD, Observatoire de la Côte d'Azur, Géoazur, Valbonne, France

2- IsTeP, Université Pierre et Marie Curie, Paris, France

Abstract

2D thermo-mechanical models show that mountain building is very sensitive to surface processes, which affects tectonics by enhancing exhumation and thermal weakening of the crust, and depositing soft and cold sediments in surrounding basins. While cylindrical tectonic structures are well approximated by 2D plane strain models, erosion and sedimentation cannot be captured along 1D profile. The example of Tien Shan where structures, basins and exhumation rates are well constrained illustrate this issue. Using basin depths and exhumation rates as cost functions of our forward models, we first show that it is impossible to adjust both basin depths and exhumation rates using standard 1D models. We then implement out-of-plane mass transfer and show how it affects the tectonic evolution of the model. We finally invert the amount of out-of-plane sediments loss and find out that 80% of the sediments must be evacuated by lateral drainage in order to minimize the misfit.

Introduction

Processes controlling topographic evolution are responsible for thermal gradient perturbations and as such exert a significant control on the spatial and age repartition of exhumed rocks. This is especially true at low temperatures since these perturbations decrease exponentially with depth (Braun, 2002a, 2002b; Stüwe et al., 1994; Turcotte and Schubert, 2014). In active mountain belts, tectonics and erosion-sedimentation processes controls landscape changes and are linked through a positive feedback loop (e.g. Whipple, 2009; Willett, 1999).

In cylindrical mountain belts, the first order structure and tectonic evolution can be captured by 2D plane strain geodynamic models but paths between sediments sources and sinks depend on drainage network (Tucker and Slingerland, 1996). This drainage network permanently adapts to the topographic surface ongoing evolution. With time, some river beds tend to align themselves with cylindrical tectonic structures, i.e. normal to the tectonic model surface. As a result, a major proportion of sediments is routed far from the source by range-parallel networks, which influences mass balance and tectonics response.

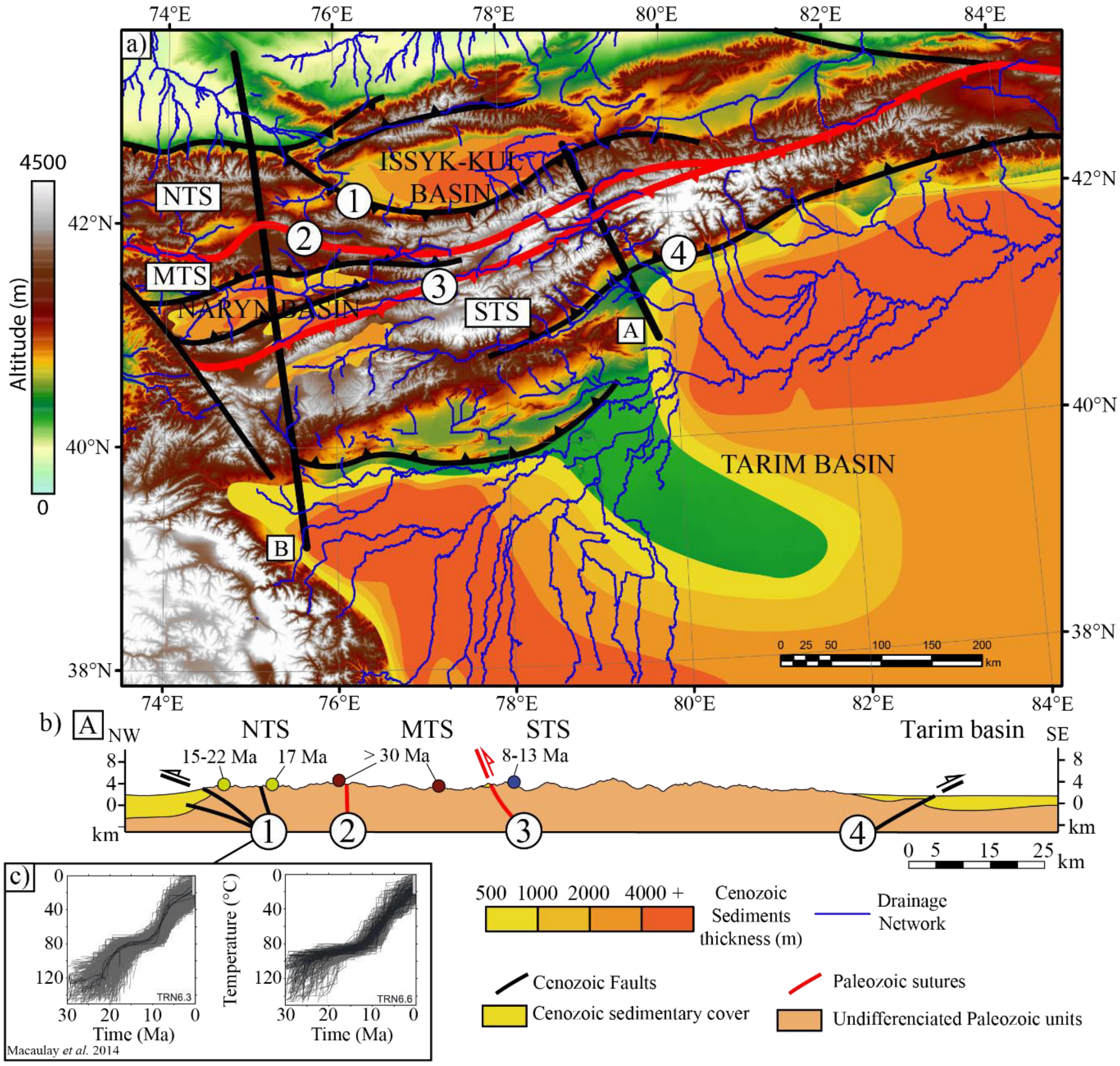

Figure 1: a) Topographic map of the Tien Shan and northern Tarim basin. The thickness of major Cenozoic basins are after (Metivier and Gaudemer, 1996; Wang et al., 1992) *in the Tarim basin and after* (Jukov et al., 2008) *in the Kyrgyz Tien Shan. The red lines represent the Paleozoic suture zones after* (Jourdon et al., 2017; Loury et al., 2015a; Xiao et al., 2013) *and the black lines the main Cenozoic faults after* (Macaulay et al., 2014; Thompson et al., 2002)*. NTS: North Tien Shan, MTS: Middle Tien Shan, STS: South Tien Shan. 1: Main Terskey Fault, 2: Nikolaev Line, 3: South Tien Shan Suture, 4: North Tarim Thrust. The thick black lines indicate cross-sections A (this study) and B (Jourdon et al. in rev.) location. b) Schematic geological cross-section along line A; coloured dots indicate Apatite Fission Tracks exhumation ages after* (De Grave et al., 2012; Glorie et al., 2011; Macaulay et al., 2013)*. c) Temperature-time paths of samples located along the Main Terskey Fault* (Macaulay et al., 2014).

The Kyrgyz Tien Shan (TS) is a typical example of an intracontinental range where active thrusts are responsible for significant uplift and subsequent erosion, which leads to the development of two flexural basins on both sides of the belt. To the north, the Issyk-Kul basin (Figure 1) displays a maximum Cenozoic sedimentary thickness of ~4 km (Jukov et al., 2008) while to the south the Tarim basin is filled of Oligocene to Quaternary sediments of variable thickness, up to 7 km (Makarov et al., 2010). While the tectonic structure can be considered as cylindrical, major rivers trend NE-SW parallel to the main topographic ranges and to the Cenozoic basins of Issyk-kul and Naryn (Figure 1). This current configuration of the drainage network is consistent with the fact that Cenozoic sedimentary flux is principally oriented E-W rather than N-S (Abdrakhmatov *et al.* 2001).

In this study, we aim at assessing how this lack of mass balance in 2D affects the dynamic of intracontinental belts. We designed a series of numerical experiments to test surface process parameters imposed on a thermo-mechanical model which has been calibrated to describe the Cenozoic evolution of the Kyrgyz Tien Shan (TS) (Jourdon et al., submitted). The target cross section has been chosen because both sedimentary basin depths and low temperature (LT) ages are available.

We first briefly describe the TS belt tectonic context and existing LT age constraints on exhumation. We then describe the numerical experiment. Finally, we discuss the influence of lateral sedimentary fluxes on the age and repartition of exhumed rocks below the 120°C isotherm which is the corresponding closure temperature of Apatite Fission Track (AFT) ages.

1. General overview on the Tien Shan and thermo-chronological constraints

In response to India-Asia collision, deformation has propagated towards the core of the Eurasian continent since the Cenozoic. Nowadays, the collisional deformation extends over several thousand kilometres, from the Himalayan front to the Siberian craton (e.g. Avouac *et al.*, 1993; Tapponnier *et al.*, 1986; Sobel and Dumitru, 1997). The TS belt is considered as a typical example of a recent intracontinental mountain belt, which develops on a Paleozoic orogen remnants. Paleozoic structures like collisional sutures and transcurrent shear zones influence the localization of the Cenozoic deformation (Jourdon et al., 2017) . The main tectonic units of TS correspond to three continental blocks: the North TS (NTS), Middle TS (MTS) and the Tarim basin, separated by two Paleozoic sutures: the Nikolaev Line (NL) and the South TS suture (STSs) (Figure 1).

The convergence in the TS is accomodated by N-S to NW-SE shortening. The principal Cenozoic structures in the Kyrgyz TS (Figure 1) are highlighted by geophysical (Makarov et al., 2010) and thermo-chronological data (Macaulay *et al.*, 2013; 2014; De Grave *et al.*, 2012; Glorie *et al.*, 2011; 2010). Along the northern border of the Tarim basin, seismic activity indicates a top-to-the-South thrust of the TS over the Tarim, as visible also on the MANAS seismic profile (Makarov et al., 2010). To the North, the basement of the NTS over-thrusts the Cenozoic basin of Lake Issyk-Kul along the Main Terskey Fault (MTF), which is interpreted as a Cenozoic thrust. Thermo-chronological data show that this structure was activated during the Late Oligocene (~25 Ma ago) and propagated eastward during the Miocene. In the Central part of the belt, the STSs is reactivated by a top-to-the-north thrust, which uplifted the STS suture units over the MTS from 20 Ma (Macaulay et al., 2014) to 8 Ma (Glorie et al., 2011).

Previous thermo-chronological studies provided AFT ages in the Eastern part of the Kyrgyz TS (Figure 1), which allowed constraining the onset of Cenozoic deformation and faults activity in this area. In the NTS, AFT ages range from the Late Oligocene (~25 Ma) in the western part of the Terskey range, to the Early Miocene (15 Ma) in its eastern part (Macaulay *et al.*, 2014). To the South, the NTS and MTS basements separated by the NL recorded older AFT ages ranging from 40 to >100 Ma, indicating lower exhumation rates. Southward, AFT ages between the MTS and the STS range from 8 Ma to 13 Ma (Glorie et al., 2011). The ages are interpreted as reflecting faster exhumation and deformation rates.

2. Modelling setup

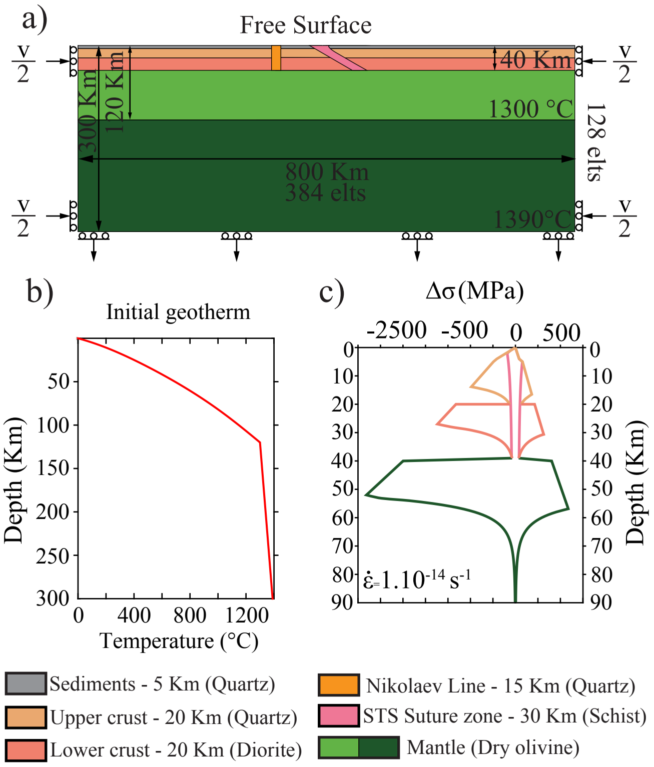

Figure 2: Models setup. a) Rheological phases and boundary conditions, v = 0.5 mm/a. b) Initial geotherm for all models. c) Yield strength envelope of the ductile flow laws of quartz (brown), diorite (salmon pink), schists (pink) and olivine (green) for a strain rate of 1.10^{-14} s^{-1}.

Jourdon et al. (in rev.) showed that pre-Cenozoic crustal heterogeneities like STSs and the NL exert a first order control on the localization of newly formed structures, the position of intra-mountain basins and the topography along cross section B (Figure 1) and that mantle inheritance is negligible. Building on these results and reducing the width of the MTS according to Paleozoic tectonic reconstructions (Alexeiev et al., 2016; Jourdon et al., 2017; Windley et al., 2007) to adapt the set-up to cross-section A where exhumation is constrained, the initial geometry of the all the models include inherited structures. A 15 km wide vertical zone represents the NL and a 30 km wide and 30° right (south-) dipping weak zone represents the STS metamorphic units (Figure 2).

Surface processes are modelled using Culling's (1965) law with a diffusivity (κ_e) that varies from 0 to 5.10^{-5} m².s^{-1}. We first assume that all eroded sediments are deposited in the model plane. Then, we implement a parameter allowing us to prescribe the proportion of eroded sediments that will be routed off the model space (hence not deposited). This parameter represents the transition from range-perpendicular to range-parallel drainage networks between mountains and basins.

In order to assess the influence of these parameters on low temperature exhumation ages provided by AFT data, we consider the 120°C isotherm as the temperature above which the age is constantly reset. We do not take into account fission track healing, which can occur at temperatures between 120°C and 100°C (Wagner, 1968).

3. Impact of erosion rate

At first order, exhumation ages show a strong dependency on the diffusion coefficient (Figures 3 and 4). For both shear zones the exhumation age residual is minimum for diffusion coefficients around 10^{-6} m^2.s^{-1}. When the erosion rate is too low (10^{-7} m^2.s^{-1}) no exhumation occurs and the belt remains cold. On the contrary, large erosion rates (10^{-5} m^2.s^{-1}) lead to a rapid rise of the 120°C isotherm and exhumation ages are too young.

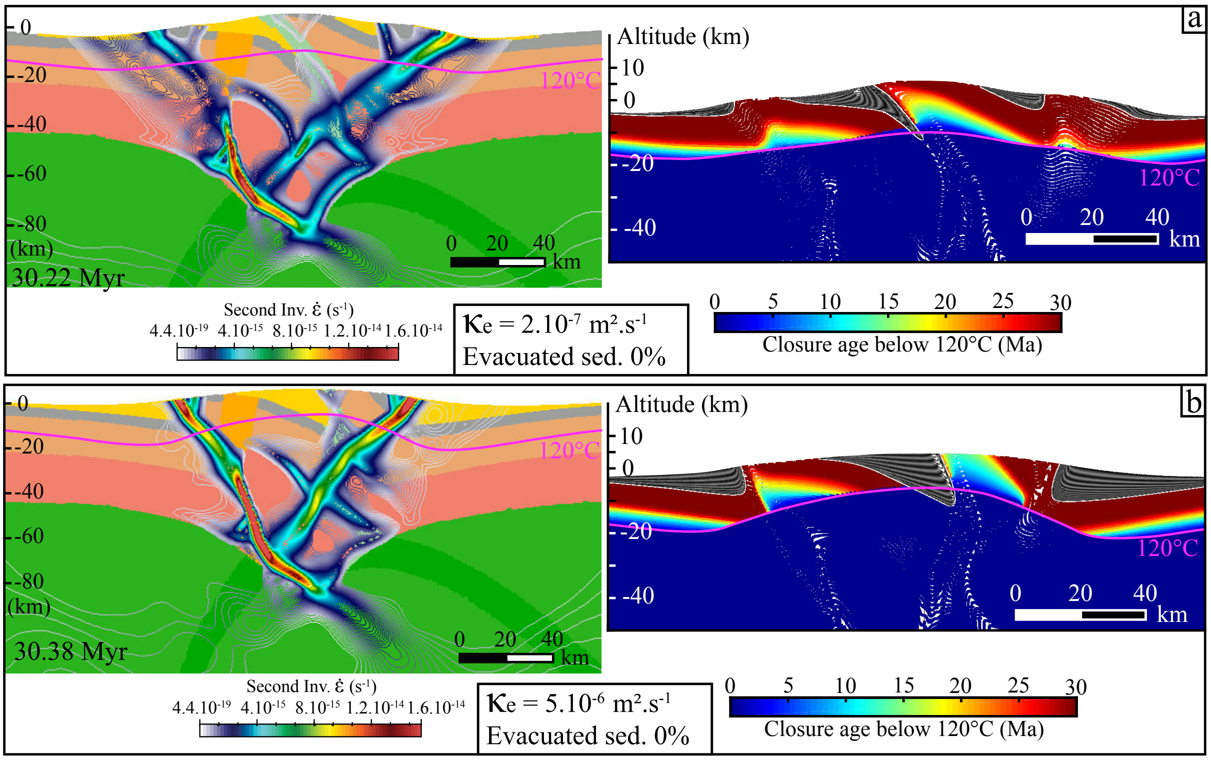

Figure 3: Final time step of two models with diffusion coefficient of a) 2.10^{-7} m^2.s^{-1} and b) 5.10^{-6} m^2.s^{-1} and no outward sediments fluxes. On the left, isolines represent the second invariant of the strain rate tensor. On the right, colours represent the age of exhumation at temperatures lower than the 120°C isotherm (purple line). Sedimentary basins are represented with stratigraphic layering of 1 Ma.

In the models with constant erosion rates and sediments remaining in the model plane, three major shear zones (SZ) localize the deformation (Figure 3). The left SZ is active during the whole simulation and controls the exhumation of its hanging wall. The central SZ, localized initially on the right dipping weak zone is active at the beginning of the exhumation history, then is progressively abandoned and gives rise to the right SZ, which contributes to the latest stage of exhumation by uplifting the central part of the belt. Depending on the erosion rate, the tectonic evolution can differ (Figure 3). Large erosion rates lead to the formation of a narrower belt with more localized deformation on two steeper reverse shear zones. Oppositely, lower erosion rates result in a more complex deformation pattern with more diffuse structures and a wider orogenic belt.

None of these 2D mass conservative models can be adjusted to fit both the known exhumation ages and basin depths. Either exhumation occurs but basins are too deep or vice versa. Therefore, we shall consider the out of plane sedimentary fluxes inferred by the belt-parallel drainage network in order to produce basins of more realistic sizes while having exhumation.

4. Quantification of out of plane drainage

We synthesize here the results of 37 tests in residual maps of exhumation ages and basins depths (Figure 4). Residuals are computed as $R = data - model$ and normalized such as $R_N = \frac{|R-\min(R)|}{|\max(R)-\min(R)|}$ (Figure 6).

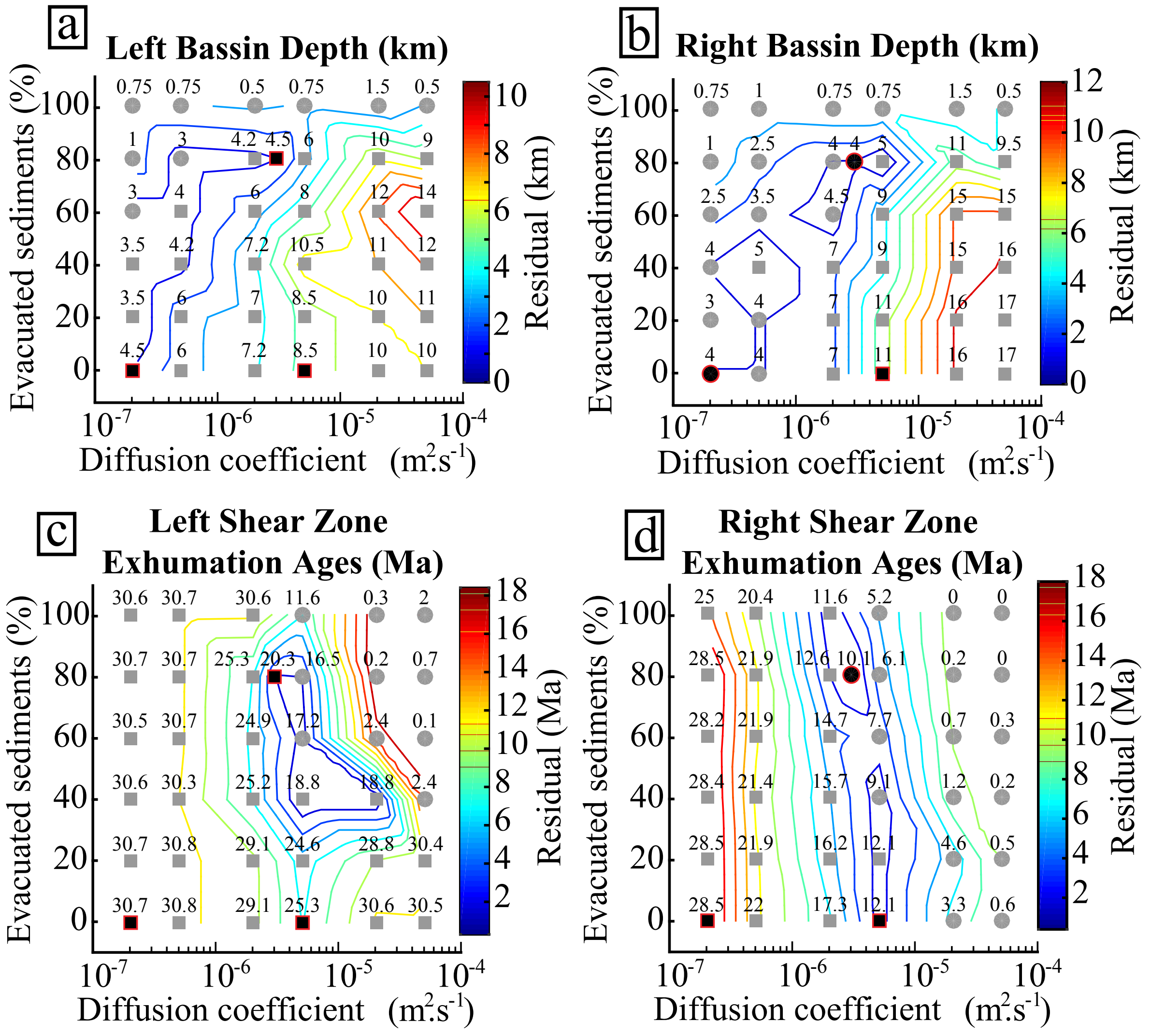

Figure 4: Modelled values and residuals of a) and b) left and right basins depth respectively compared with the Issyk-kul and Tarim basins depths. c) and d) left and right shear zones respectively compared with the MFT and STSS (see Figure 1 for location and abbreviations) exhumation ages on AFT. Grey dots and squares represent models for which the residue is positive and negative respectively (black dots indicate the models presented in Figures 3 and 5). Numbers represent the depth of modelled basins and the exhumation ages along the shear zones. Coloured lines represent the residual between data and models.

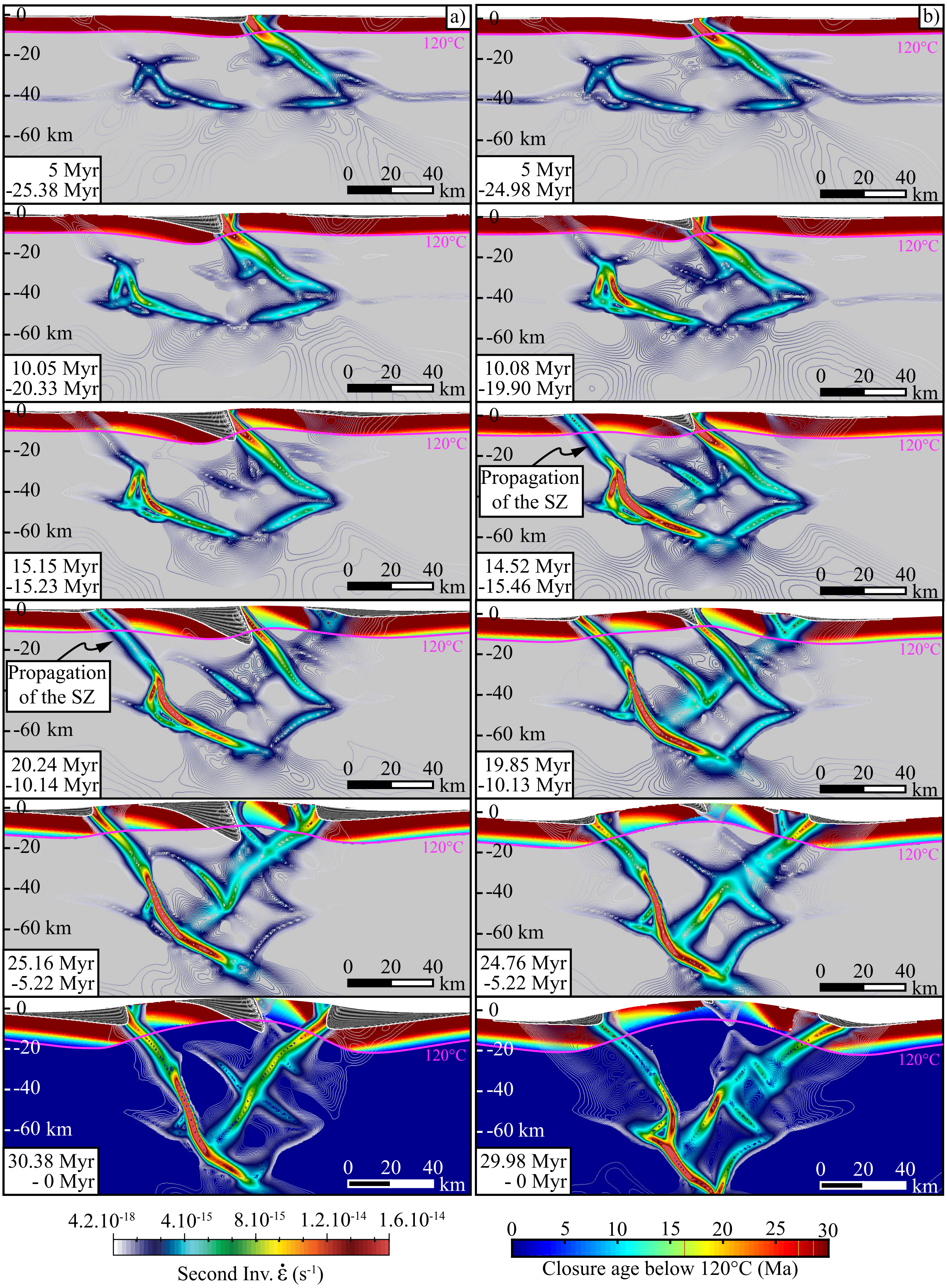

Figure 5: Model evolution with a diffusion coefficient and an amount of evacuated sediments of a) 5.10^{-6} $m^2.s^{-1}$ and 0% and b) 3.10^{-6} $m^2.s^{-1}$ and 80% respectively. Isolines represent the second invariant of strain rate tensor. The grey background represents the medium where the chronometer is considered open (temperature > 120°C, purple line). The backward time is indicated with a minus, and the forward time is indicated as positive. Sedimentary basins are represented with stratigraphic layering of 1 Ma.

The proportion of evacuated sediments does not influence exhumation ages of the right shear zone, but strongly affects the final depth of the associated basin (Figure 4). Minimum basins depth residuals occur for low diffusion coefficients (10^{-7} m².s^{-1}) and low percentages of evacuated sediments, or for higher diffusion coefficients (10^{-6} to 10^{-5} m².s^{-1}) with a high percentage of evacuated sediments (~80%). Largest residuals are observed for high diffusion coefficients (10^{-6} to 10^{-5} m².s^{-1}) and limited sedimentary outward flux (0-40%), leading to the development of very deep basins (>10 km).

Exhumation ages are more sensitive to the proportion of evacuated sediments for the left SZ. This different tectonic response relates to the mass of sediments deposited in the central basin, which develops in the central SZ footwall (Figure 5). The weight of this basin seems to delay strain localization in the left SZ, which is responsible for most of the exhumation. Therefore, the deeper the central basin, the later the left SZ is activated and thus the later the exhumation occurs. This explains the need of out of plane sedimentary fluxes to fit exhumation ages on the left SZ. Basin depths also affect the SZ dip angles such as deeper basins lead to steeper SZ (Figure 5).

To summarize, basin depth and exhumation rates, though exerting different roles on the mountain belt deformation pattern, appear to be two useful independent data that can be used to efficiently rule out both the diffusion coefficient and the amount of evacuated sediments.

5. Comparison with the Tien Shan belt

The best fitting model minimizes residuals for exhumation ages and basins depth according to an average of normalised residuals $R_{N_{total}} = \frac{1}{4}\sum_{i=1}^{4} R_{N_i}$ (Figure 6). It corresponds to an intermediate diffusion coefficient (3.10^{-6} m².s^{-1}) and an important outward sedimentary flux (~80%).

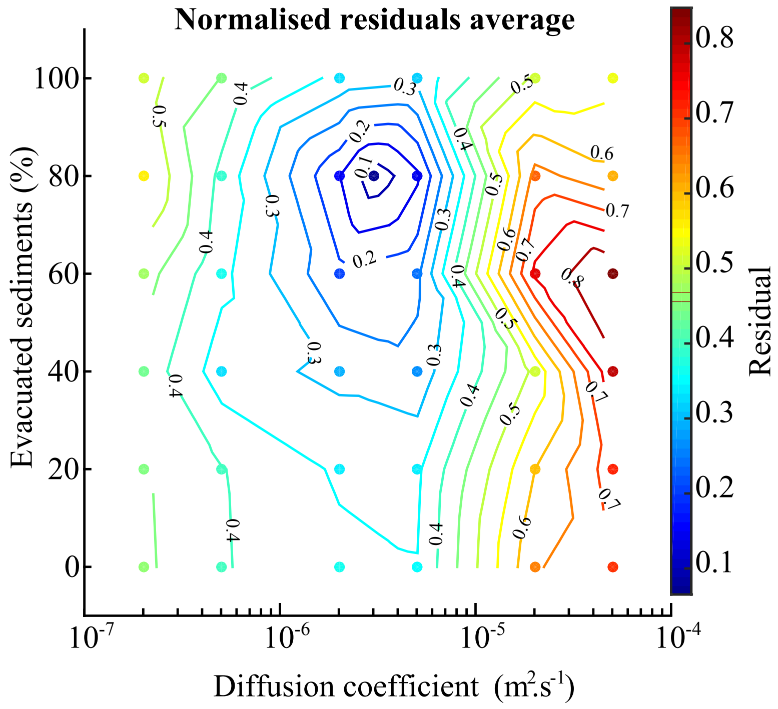

Figure 6: Normalised residuals average computed for each models taking into account both basins depth and exhumation ages (see text for details on the computing). Colours represent the values of the residual and lines represent isovalues of this residual.

In this model, predicted AFT age misfits (2-4 Ma) are in the error range for natural samples. Temperature-time (T-t) paths obtained from fission track lengths near the MTF (Macaulay *et al.*, 2014; samples TRN6.3, and TRN6.6) are compared with modelled ones near the shear zone representing the MTF (Figure 7).

T-t paths of virtual samples 1 to 5 follow a warmer path between 25 Ma and 10 Ma than natural samples, and do not display any clear stagnation at ~80-90°C during this time. However, the average cooling rate is well reproduced, especially between 10 and 0 Ma. For the natural samples, the increasing cooling rate at 10-15 Ma is interpreted as an acceleration of the basement uplift rate, and can be associated to the strain rate increase observed in our model during this period.

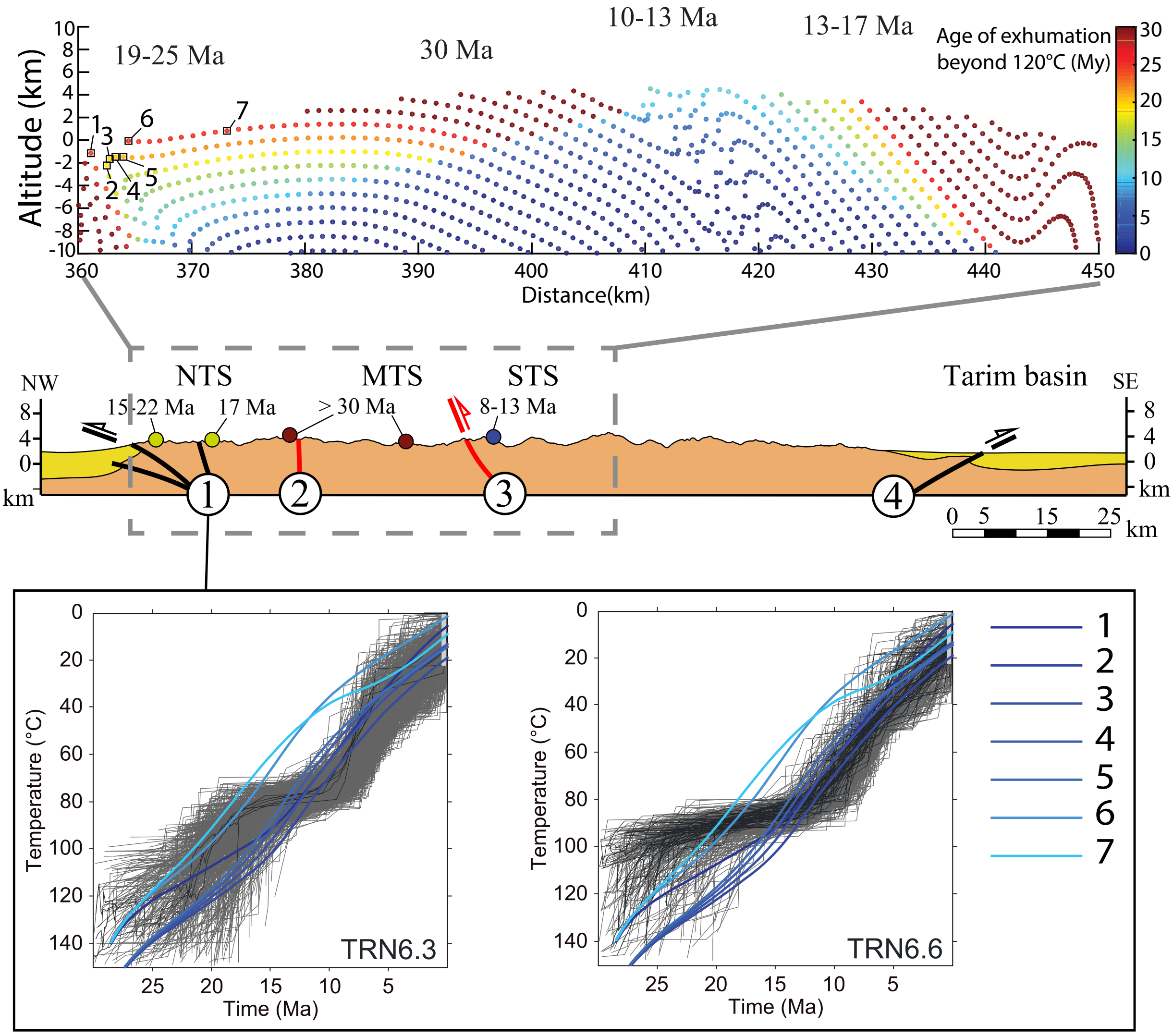

Figure 7: a) Exhumation age and numerical sampling for the model with a diffusion coefficient of 3.10^{-6} m^2.s-1 and 80% of evacuated sediments which correspond to the model with a minimal residual. b) Comparison of two samples T-t paths from Macaulay et al. *(2014) localized along the MTF with numerical samples 1 to 7. c) Cross-section of the eastern Kyrgyz Tien Shan and exhumation ages from AFT* (De Grave et al., 2012; Glorie et al., 2011; Macaulay et al., 2014).

According to the reconstruction proposed by Macaulay *et al.* (2014), cooling rates changes between 25 Ma and 20 Ma and between 15 Ma and 5 Ma can be related to regional-scale tectonic events. Sedimentation rates in the northern part of the Tarim basin show an acceleration around ~12 Ma which seems related to the regional tectonic activity (Chen et al., 2015). In our models, the cooling rate of samples near the right SZ increases around 10 Myr, as a result of the strain rate increase in this SZ, which is consistent with their data.

6. Discussion

In our models, AFT exhumation ages can be fitted by adjusting the erosion rate (Figure 4) which agrees with previous studies (e.g. Willett, 1999; Whipple, 2009; Braun, 2002b). However, for an erosion rate fitting well the AFT data, sedimentary basins are much too deep (>15 km instead of a few km) if we consider that all the eroded matter is deposited in the model plane. Accounting for range-parallel sediment fluxes helps solving this issue. Moreover, for the left SZ, the weight of the central basin has a direct feedback on strain localization. The feedback between sedimentation and exhumation depends on whether pre-exiting structures are well oriented or not. The rate of exhumation along the well oriented right shear zone is not affected by sedimentation because the kinematics is not affected at first order by the basin size (Figure 5). However, inherited structures oriented at a high angle of compression direction only serve as locus for shortcut faults (left SZ) but the basin weight exerts a control on their kinematics. In order to obtain coherent exhumation ages, basin depths and tectonic features in agreement with the data we conclude that 80% of the sediments are rooted outward of our model (Figure 6).

Active tectonic structures contribute to the rising of topographic barriers leading to a change in the drainage network and therefore in the sedimentary fluxes (Tucker and Slingerland, 1996). Cylindrical belts will enhance the development of range-parallel drainage. This process exerts a strong influence on the sedimentary mass repartition at the surface by controlling basins depth and extent, which in turn affects tectonics: the thicker the sedimentary basin, the more delayed and steeper the shear zones.

In the Tien Shan, the sedimentary basins depth and repartition can be variable from East to West. All basins are oriented E-W (parallel to the belt) and the deepest one is the Naryn basin with a thickness of 5-6 km (Jukov et al., 2008). In the Tarim basin the thickest sedimentary sequences related to the Tien Shan erosion are located on the Western border, along the Pamir-TS collision and in the North-Eastern part along the North Tarim Thrust (Metivier and Gaudemer, 1996; Wang et al., 1992). This infill geometry can be related to the flexural deformation but also to the E-W drainage network carrying sediments from the TS to the East of the Tarim.

V. Discussion

La chaîne du Tien Shan, actuellement active et située en domaine intracontinental, possède une histoire bien plus ancienne qui s'est déroulée au cours du Paléozoïque (550-250 Ma).

En effet, malgré la forte empreinte de la tectonique tertiaire, la structure actuelle du Tien Shan est toujours marquée par l'empreinte des grandes phases orogéniques du Paléozoïque : la phase Calédonienne (de l'Ordovicien au Dévonien, 480-350 Ma), et la phase hercynienne (Carbonifère à Permien, 350-250 Ma). Ces évènements tectoniques aboutissent à la formation de grandes structures lithosphériques suturant les blocs (continentaux ou arc volcaniques) entre eux et laissant une empreinte rhéologique dans la lithosphère continentale.

Cependant, bien que ces grandes structures héritées soient connues et identifiées, il demeure de nombreuses questions et discussions à propos de leurs origines.

Ce chapitre n'a pas pour vocation de traduire en français les discussions des précédents chapitres mais plutôt de proposer une ouverture et une discussion à toute l'échelle du Tien Shan (kirghize et chinois) sur la tectonique paléozoïque et son implication dans la déformation Cénozoïque.

1. Tectonique paléozoïque du Tien Shan

Comme présenté dans la section I.1.2., l'histoire paléozoïque du Tien Shan reste débattue notamment sur la vergence de la subduction carbonifère conduisant à la collision entre le Tarim et le Tien Shan. Cependant, alors que la majeure partie des débats s'orchestrent autour de cette subduction, la formation de la zone de suture entre le NTS et le MTS au Kirghizstan soulève plusieurs interrogations rarement discutées.

1.1. La Nikolaev Line, zone de suture d'une subduction ou faille transformante ?

La Nikolaev Line représente la zone de suture entre le NTS, marge active ordovicienne, et le MTS (voir Figure I-3 pour la localisation des sutures) (Bakirov and Maksumova, 2001; Maksumova et al., 2001), constitué d'un socle Protérozoïque (Glorie et al., 2011; Keselev et al., 1982; Kiselev et al., 1993; Kröner et al., 2012a) et de flyschs ordoviciens à dévoniens surmontés par une plateforme carbonatée carbonifère (Jukov et al., 2008; Karpovitch et al., 1964; Mikolaichuk et al., 1997). La majeure partie du socle du NTS résulte d'une subduction vers le Nord initiée au cours du Cambrien et prenant fin à l'Ordovicien supérieur-Dévonien inférieur (Bakirov and Maksumova, 2001; Kröner et al., 2012a; Maksumova et al., 2001). Cette époque semble également marquer l'accrétion du MTS avec le NTS et la fin du magmatisme calco-alcalin. Le long de la Nikolaev Line une formation d'ophiolite non métamorphique caractérisée par une séquence complète de roches ultra-mafiques, gabbros et pillow-lava est parfois retrouvée (Figure V-I). Cette ophiolite est datée du Cambrien-Ordovicien inférieur grâce à la présence de faunes fossiles dans les formations sédimentaires associées (Bakirov and Maksumova, 2001).

L'accrétion du MTS et du NTS est considérée à l'heure actuelle comme étant liée à une collision entre ces blocs continentaux à la suite de la fermeture de l'Océan Terskey. Cependant, aucune unité métamorphique de haute pression (schistes bleus-éclogites) ni de moyenne température (faciès amphibolite) n'est retrouvée le long de cette suture. Mis à part la présence d'une ophiolite non métamorphique, il n'existe actuellement pas de traces de collision à proprement parler entre le NTS et le MTS. En revanche, la présence du magmatisme calco-alcalin largement répandu dans le NTS ainsi que cette ophiolite laissent peu de doute quant à la présence de la subduction de l'Océan Terskey sous le NTS au cours de l'Ordovicien.

Figure V-1 : Photo de l'assemblage ophiolitique (Serpentine-Gabbro-basalte) situé entre le NTS et le MTS.

De plus, la déformation au Carbonifère supérieur le long de la NL est associée à une grande zone de décrochement dextre présentant les caractéristiques d'une structure en fleur (section II.3.1. et II.4.1., Jourdon et al., 2017). Cette zone de décrochement est formée à la faveur d'un partitionnement de la déformation entre la suture du STS et celle du NTS/MTS. Un tel partitionnement ne peut se produire que grâce à la présence d'une structure verticale préexistante qui pourrait être réactivée au Carbonifère.

De ce fait, il est possible de proposer une interprétation différente de la collision classique pour expliquer l'accrétion du NTS et du MTS notamment par analogie avec l'Ouest américain et la Californie. En effet, dans cette zone, la convergence oblique entre les plaques Amérique du Nord et Pacifique est accommodée par une tectonique décrochante notamment le long de la très célèbre faille de San-Andreas (Figure V-2) (Atwater, 1989, 1970; Atwater and Stock, 1998; Nicholson et al., 1994). Au cours du Cénozoïque la ride séparant la plaque Pacifique et la plaque Farallon se retrouve au niveau de la fosse de subduction et bloque localement cette dernière. Ceci a pour effet la remontée vers le Nord de la Californie le long d'une grande zone de faille transformante.

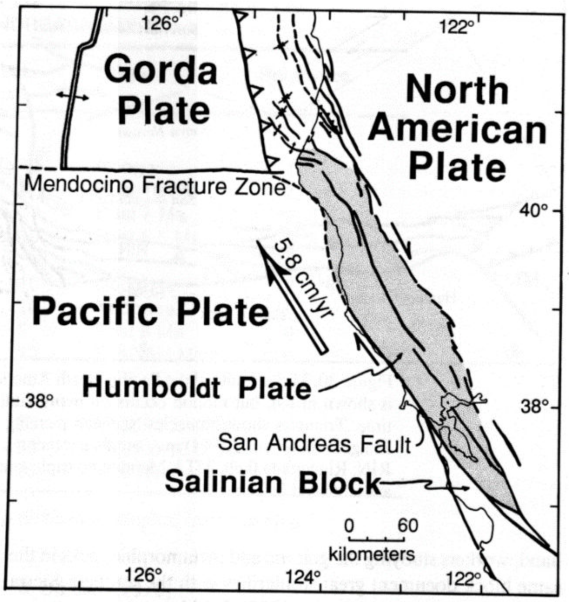

Figure V-2 : Mouvement relatif des plaques Pacifique, et Nord Amérique le long de la faille de San Andreas (Atwater, 1989)

Dans le Tien Shan, au cours de l'Ordovicien la zone de subduction de l'Océan Terskey borde le Sud du continent Kazakh-NTS-Yili du Kirghizstan à la Chine (en coordonnées actuelles). Par analogie avec la tectonique de la côte Ouest américaine, le bloc du MTS pourrait alors avoir migré d'Est en Ouest à la faveur d'un grand décrochement similaire à la faille de San Andreas. Cette interprétation permettrait d'expliquer l'absence de roches métamorphiques de haute pression et la présence d'ophiolites non métamorphiques le long de la Nikolaev Line, ainsi que la présence d'une zone de déformation verticale favorablement orientée pour accommoder le partitionnement de la déformation au cours de la collision Tarim-Tien Shan.

1.2.Tectonique hercynienne, de la subduction à la collision

L'histoire hercynienne du Tien Shan représente la dernière phase tectonique majeure avant la collision Inde-Asie et la réactivation de la chaîne. Elle s'inscrit dans la continuité de la phase orogénique calédonienne et prend fin au Permien avec une tectonique majoritairement décrochante (Alekseev et al., 2007; Konopelko et al., 2013; Mikolaichuk et al., 1997; Rolland et al., 2013; Wang et al., 2007a) et un magmatisme intense disséminé dans toute la chaîne et qui s'étend au sein du Tarim (Konopelko et al., 2009, 2007, Wang et al., 2014, 2009; Wei et al., 2014; Xu et al., 2014; Yang et al., 2013). Ce chapitre est consacré à la discussion des deux grandes hypothèses sur le sens de la subduction et des implications tectoniques de ces modèles.

Mais avant tout, pour discuter de la tectonique dévono-carbonifère, il est nécessaire de repartir de la configuration cambro-ordovicienne de la région. Comme présenté dans la section I.1.2., plusieurs auteurs proposent qu'au début du Paléozoïque l'Océan Terskey était, à l'image du Pacifique aujourd'hui, dans une situation de double subduction (Bazhenov et al., 2003; Gao et al., 2009; Lomize et al., 1997). La subduction sous le bloc Kazakhstan-NTS-Yili vers le Nord étant traitée dans la section V.1.1., cette partie se concentrera sur la discussion de la subduction de l'autre côté du domaine océanique.

Le Tien Shan chinois et le Tien Shan kirghize partagent une histoire commune, cependant certaines unités tectoniques ne sont pas continus d'un bout à l'autre de la chaîne. Pour permettre une reconstitution temporelle et spatiale des évènements tectoniques majeurs de la chaîne il est nécessaire d'avoir une approche en trois dimensions. L'évolution du Tien Shan sera donc présentée et discutée ici à travers des cartes ainsi que des coupes représentant des hypothèses sur la situation géodynamique du Tien Shan kirghize et du Tien Shan chinois.

Avant d'entrer réellement dans la discussion quant à la vergence de la subduction entre le Tarim et le Tien Shan, il faut noter que les deux modèles partent d'une situation assez similaire jusqu'au Dévonien. En effet, dans le Tien Shan chinois, le Central Tien Shan est constitué de séries magmatiques d'arc datées du Silurien au Dévonien moyen (Charvet et al., 2011; Gao et al., 2009; Liu et al., 2014; Wang et al., 2011; Xiao et al., 2013). Cet arc est actuellement situé entre le NTS et le STS en Chine. Il est séparé du NTS, au Nord, par la « *Central Tien Shan Suture Zone* » (CTS SZ) et du STS, au Sud, par la « *South Tien Shan Suture Zone* » (STS SZ). Cette dernière est marquée par la présence de morceaux de lithosphère océanique ayant une signature d'arrière arc (Gao et al., 2009; Wang et al., 2011). La présence de l'arc du CTS ainsi que des roches d'arrière-arc dans la suture Sud témoignent d'une subduction sous la marge du Tarim au Silurien qui va ensuite entraîner l'ouverture d'un bassin arrière-arc et séparer le CTS du Tarim au cours du Dévonien (Figure V-3).

Dans le Tien Shan kirghize en revanche, on ne trouve pas d'arc magmatique semblable au CTS. Cependant, le long de la suture sud (nommée localement At-Bashi-Kokshaal, mais qui correspond à la STS SZ) une ophiolite non métamorphique démembrée est retrouvée (Alekseev et al., 2007; Jourdon et al., 2017; Loury et al., 2015). Cette ophiolite pourrait témoigner d'une subduction intra-océanique entre l'Océan Terskey et l'Océan Sud Tien Shan qui aurait ensuite conduit à l'obduction de morceaux de l'Océan STS sur le MTS entre le Dévonien et le Carbonifère. Cette partie est plus détaillée dans la discussion sur les différents modèles.

Quoiqu'il en soit, c'est à partir du Dévonien que les deux grandes hypothèses sur la vergence de la subduction qui conduira à la collision entre le Tarim et le Tien Shan divergent.

1.2.1. Modèle de subduction vers le Sud

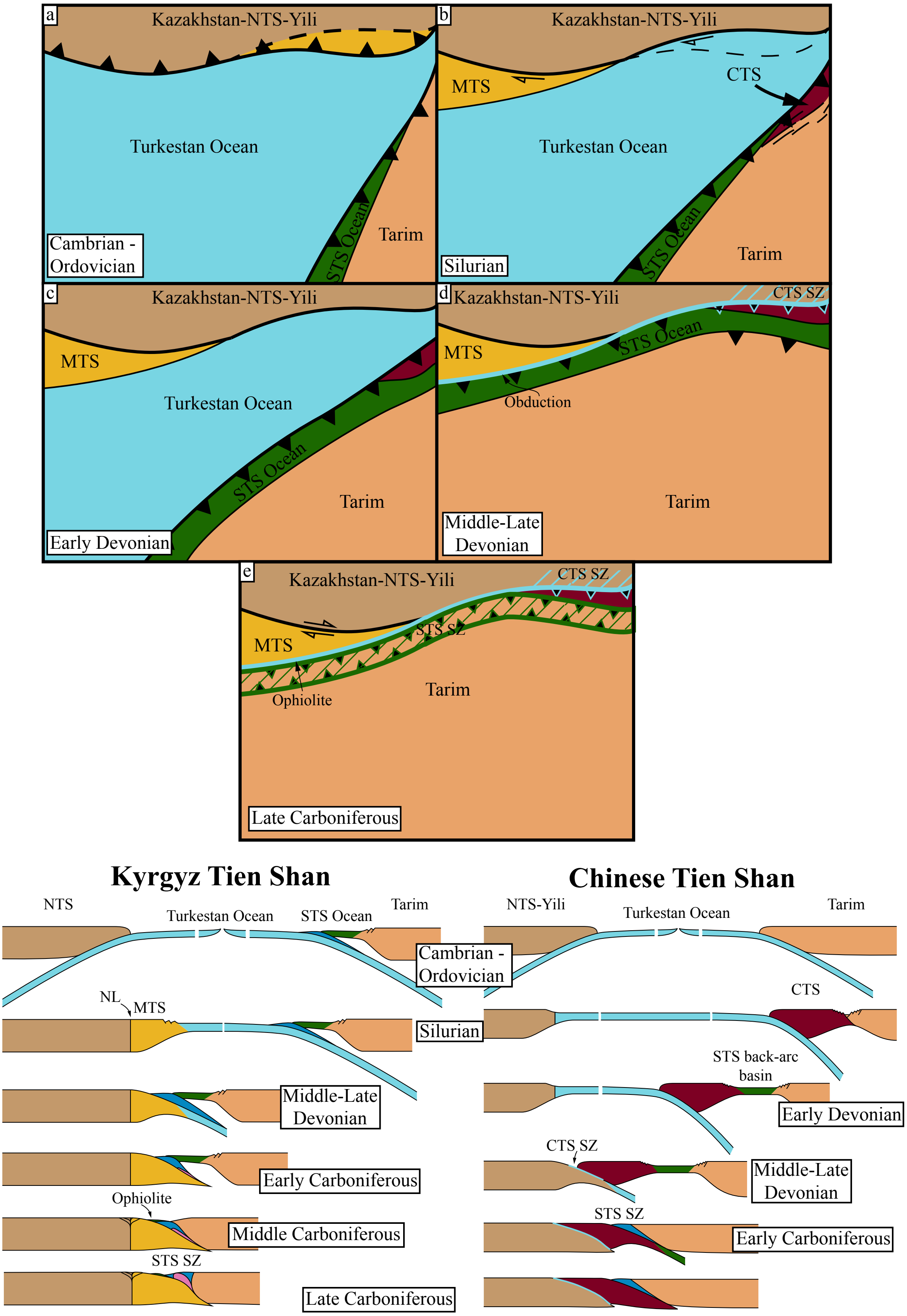

Figure V-3 : Modèle conceptuel de la formation et de l'évolution du Tien Shan de l'Ordovicien au Carbonifère supérieur en carte et en coupe au niveau du Tien Shan kirghize et chinois dans l'hypothèse d'une subduction de l'océan séparant le Tarim et le Tien Shan vers le Sud

Dans le Tien Shan chinois, à partir du Dévonien, la subduction de l'Océan Terskey vers le Sud responsable de la formation de l'arc du CTS entraîne l'ouverture arrière arc détachant le CTS du Tarim (Charvet et al., 2011; Gao et al., 2009; Liu et al., 2014; Wang et al., 2011; Xiao et al., 2013). La fermeture de l'Océan Terskey se produit vers la fin du Dévonien et permet l'accrétion du CTS et du NTS (Figure V-3). Cette collision transfère alors la subduction vers le domaine arrière-arc qui plonge sous le Tarim. La fermeture de ce domaine océanique s'accompagne alors de la collision entre le Tarim et le CTS à l'Est et entre le Tarim et le NTS à l'Ouest. Les interprétations des datations ^{39}Ar-^{40}Ar sur les roches de haute pression ont notamment permis d'établir une chronologie. Selon les auteurs, en Chine, le pic de pression des roches exhumées est atteint entre 345 et 341 Ma (Gao and Klemd, 2003) et l'exhumation se produit au cours de la collision entre le Tarim et le NTS entre 331 et 316 Ma (Gao and Klemd, 2003; Wang et al., 2010).

Ce modèle de subduction vers le Sud en Chine s'appuie principalement sur des données structurales dans le STS. En effet, d'après plusieurs auteurs (Charvet et al., 2011, 2007, Ge et al., 2014, 2012; Lei et al., 2011; Lin et al., 2013; Wang et al., 2007a), l'étude de la déformation montre un transport de nappes du Sud vers le Nord associé à des failles inverses à vergence Nord et des détachements à vergence Sud.

Dans le Tien Shan kirghize, on ne trouve pas d'équivalent du CTS. En revanche, comme énoncé précédemment, on retrouve une ophiolite non métamorphique au niveau de la suture d'At-Bashi (Alekseev et al., 2007; Jourdon et al., 2017; Loury et al., 2015a, 2015b). Cette unité chevauche le socle du MTS vers le Nord et est chevauchée par les unités de haute pression. La

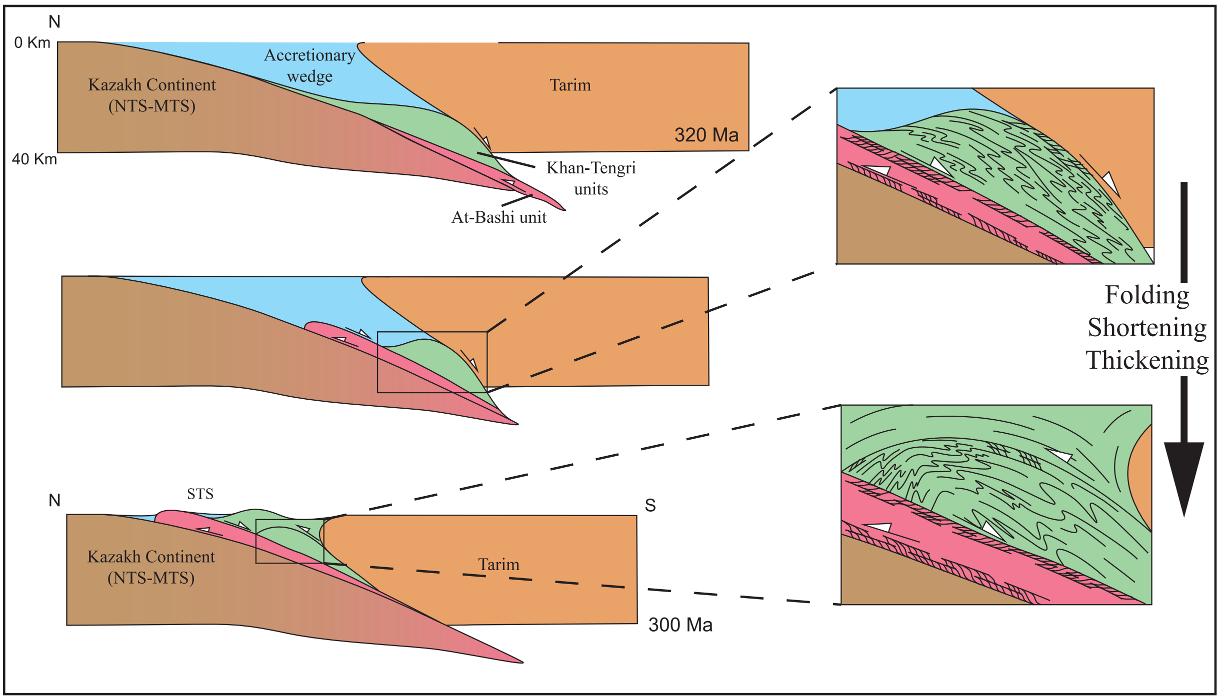

Figure V-4 : Modèle conceptuel d'exhumation des unités sous-charriées lors de la collision entre le Tarim et le Tien Shan dans le cas où la subduction était initialement dirigée vers le Sud position structurale et l'absence de métamorphisme au sein de cette ophiolite peut être interprété comme le témoignage d'un sous charriage du MTS sous une partie de l'Océan STS, ce qui impliquerait une subduction vers le Sud avant la mise en place des unités de haute pression et la collision avec le Tarim c'est-à-dire entre le Dévonien et le Carbonifère moyen (Figure V-3). Malheureusement le manque de données sur cette ophiolite ne permet pas d'appuyer cette interprétation. Malgré tout, les roches de haute pression exhumées montrent un processus de subduction actif au Carbonifère moyen avec des datations interprétées comme reflétant le pic de pression entre 330 Ma et 320 Ma ainsi qu'un âge d'exhumation aux alentours de 316 Ma (Hegner et al., 2010; Loury et al., 2015a; Simonov et al., 2008).

Une fois encore, ce modèle de subduction vers le Sud s'appuie principalement sur des arguments structuraux dans le STS avec la présence de chevauchements vers le Nord des unités de haute pression et une diminution du degré de métamorphisme du Nord vers le Sud dont les faciès sont séparés par des détachements à vergence Sud (Figure V-4) (Jourdon et al., 2017; Loury et al., 2015a, 2015b).

1.2.2. Modèle de subduction vers le Nord

Dans le modèle dans lequel une subduction vers le Nord est à l'origine de la collision entre le Tarim et le Tien Shan, la situation au Dévonien inférieur serait sensiblement la même que dans le cas d'une subduction vers le Sud (Figure V-5). En effet, la présence de l'arc du CTS implique qu'au cours du Silurien et jusqu'au Dévonien une subduction de l'Océan Terskey vers le Sud est en cours (Lin et al., 2009; Wang et al., 2011, 2008). Avant de discuter du changement de vergence de la subduction plusieurs hypothèses sont à présenter :

1- La subduction vers le Sud de l'Océan Terskey n'est pas continue d'Est en Ouest et s'effectue seulement sous le CTS, dans ce cas le MTS et le Tarim sont en condition de marge passive et il n'y a pas de subduction intra-océanique. Bien que cela soit possible, cette hypothèse impliquerait la présence de grandes structures lithosphériques permettant le transfert d'une zone de convergence à l'Est (sous le CTS) vers une zone soit en divergence soit passive à l'Ouest. Cependant, dans le Tien Shan actuel la zone de contact entre le STS et le reste de la chaîne est continue et aucune structure de cet ordre ne semble être présente.

2- La subduction vers le Sud de l'Océan Terskey est continue passant d'une subduction océan-continent à l'Est à une subduction intra-océanique à l'Ouest. Cette interprétation permet d'expliquer ici aussi la présence de l'ophiolite non métamorphique sous la suture d'At-Bashi dans le STS kirghize (Figure V-5).

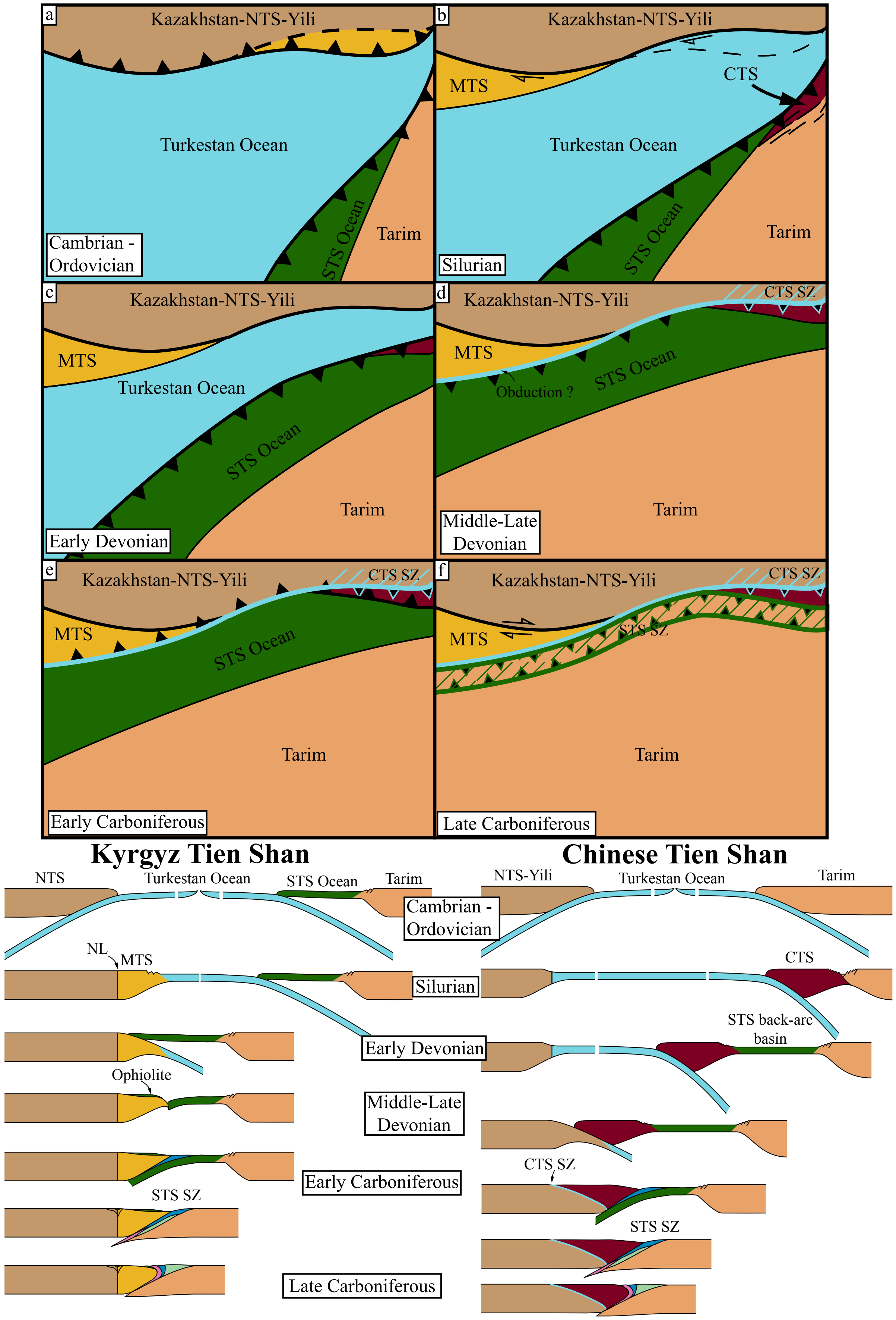

Figure V-5 : Modèle conceptuel de la formation et de l'évolution du Tien Shan de l'Ordovicien au Carbonifère supérieur en carte et en coupe au niveau du Tien Shan kirghize et chinois dans l'hypothèse d'une subduction de l'océan séparant le Tarim et le Tien Shan vers le Nord.

Quelle que soit l'interprétation préférée, la subduction sous le CTS est dirigée vers le Sud au cours du Dévonien. Un changement de vergence est donc nécessaire pour expliquer le modèle de subduction vers le Nord.

Dans le Tien Shan chinois, l'accrétion du CTS avec le NTS s'effectue au cours du Dévonien moyen à supérieur, impliquant la fermeture de l'espace océanique séparant ces deux blocs (e.g. Charvet et al., 2011; Gao et al., 2009; Han et al., 2011; Wang et al., 2010; Windley et al., 1990; Xiao et al., 2014). A partir de cette configuration, l'Océan STS ouvert en contexte arrière-arc entre le Tarim et le CTS entre en subduction vers le Nord sous le CTS au cours du Carbonifère inférieur (Figure V-5) (Gao et al., 2009, 1998, Xiao et al., 2014, 2013, 2004) jusqu'à sa fermeture complète entraînant le sous-charriage du Tarim sous le Tien Shan entre 330 et 320 Ma d'après les âges obtenus sur les roches de haute pression (Gao and Klemd, 2003; B. Wang et al., 2010).

Dans le Tien Shan kirghize, la fermeture de l'Océan Terskey s'effectuerait au cours du Dévonien entraînant cette fois ci le sous charriage de la marge Sud du MTS sous l'Océan STS ce qui permettrait la mise en place d'une ophiolite au-dessus du socle du MTS (Figure V-5). L'âge d'un tel événement ne peut malheureusement être contraint du fait du manque de données sur cette ophiolite. Toutefois, le sous-charriage du bloc continental du MTS marque alors la fermeture de l'Océan Terskey et donc la fin de la subduction à vergence Sud. Ceci permettrait alors à l'Océan STS d'entrer à son tour en subduction sous le MTS au cours du Carbonifère inférieur (pic de pression daté à 330 Ma dans le roches de haute pression) jusqu'à sa fermeture

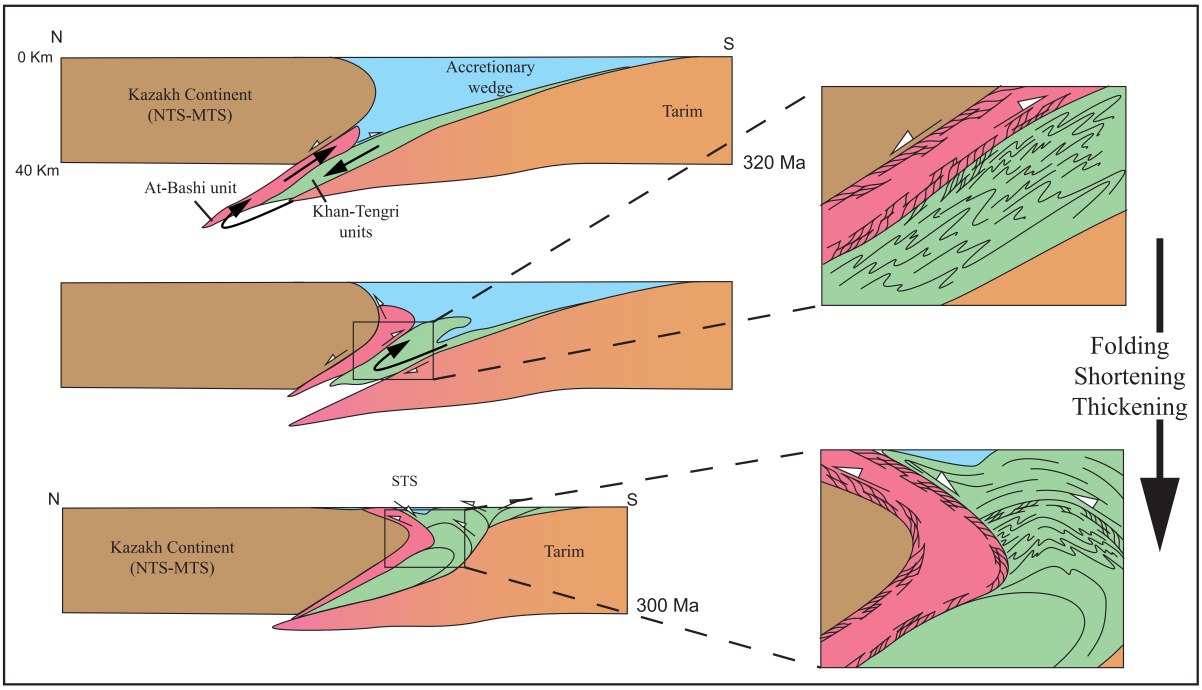

Figure V-6 : Modèle conceptuel d'exhumation des unités sous-charriées lors de la collision entre le Tarim et le Tien Shan dans le cas où la subduction était initialement dirigée vers le Nord. Les trajet des unités exhumées sont inspirés de modèles numériques d'exhumation d'après (Butler et al., 2013; Warren et al., 2008; Yamato et al., 2008) conduisant au sous charriage du Tarim sous le Tien Shan vers 320 Ma (Figure V-5) (Hegner et al., 2010; Loury et al., 2016; 2015a).

Etant donné que les données structurales montrent un transport du Sud vers le Nord à la fois en Chine et au Kirghizstan, une subduction vers le Nord impliquerait qu'au cours de la collision les unités métamorphiques qui composent les complexes d'accrétions s'exhument le long de rétro-chevauchements (Figure V-6).

1.3.Synthèse

La formation du Tien Shan au cours du Paléozoïque reste donc âprement débattue notamment sur la phase finale impliquant la collision entre le Tarim et le Tien Shan qui scelle la longue histoire de la CAOB dans cette partie de la chaîne. Cependant, comme présenté dans cette discussion, les deux modèles de subduction sont possibles et les données actuelles ne permettent pas réellement une décision objective d'un modèle face à un autre.

Les partisans du modèle de subduction vers le Sud (Charvet et al., 2011, 2007, Ge et al., 2014, 2012; Lei et al., 2011; Lin et al., 2013; Wang et al., 2007a) invoquent la vergence des structures tectoniques mise en lumière par la géologie avec des chevauchements à vergence Nord et des détachements à vergence Sud le long de la zone de suture du STS. Ce modèle implique une exhumation des unités de haute et moyenne pression dans une position structurale « normale », avec les unités de plus au degré métamorphique remontant le long du front de collision et séparées des unités de plus bas degré métamorphique par des détachements, de même type que la subduction Egéenne (e.g. Jolivet and Brun, 2010).

D'un autre côté les partisans du modèle de subduction à vergence Nord (Chen et al., 1999; Gao et al., 2009, 1998; Liu et al., 2014; Xiao et al., 2013, 2009) se basent sur les données géophysiques et notamment sur le profil sismique MANAS qui montre un sous-charriage actuel du Tarim sous le Tien Shan qui correspondrait à la structure héritée de la suture STS (Makarov et al., 2010). Ce modèle implique quant à lui une exhumation « inverse » des unités métamorphiques avec les unités de haute pression à l'arrière du prisme et les unités de plus bas degré métamorphique à l'avant, de même type que la subduction Alpine (e.g. Agard et al., 2009; Ernst, 1973; Saliot, 1978; Yamato et al., 2008).

Dans les deux cas il existe des analogues et les arguments en faveur d'un modèle sont souvent transposables à l'autre. Cependant, la déformation liée à la tectonique paléozoïque dans le Tien Shan a laissé une forte empreinte rhéologique dans la lithosphère. Les études menées dans cette thèse sur l'implication de l'héritage structural dans la localisation de la déformation cénozoïque montrent que la tectonique paléozoïque a une influence capitale. Elles nous permettent également d'apporter des éléments de réponse sur la structure à l'échelle lithosphérique de la chaîne et sur l'état initial précédant la tectonique Cénozoïque. En ce qui concerne le débat sur la vergence de la subduction quelques éléments de réponse sont mis en avant par les modèles numériques. Tout d'abord, le sous charriage du Tarim sous le Tien Shan actuellement observé advient quel que soit le pendage initial de la suture du STS : cette déformation est donc d'âge tertiaire et n'indique en rien le pendage de la zone de suture au Paléozoïque. Or la présence de ce sous charriage représente l'un des arguments majeur des auteurs proposant une subduction vers le Nord au Carbonifère. Ensuite, malgré la forte similitude entre les modèles ayant une zone de faiblesse crustale à pendage Sud et Nord (Modèles 1 et 5, section III, Figures 5 et 7), on retrouve une meilleure corrélation entre les données géologiques et géophysiques et le modèle présentant une suture à pendage Sud avant la déformation Cénozoïque. Il est donc probable que la partie crustale de la suture du STS ait été à pendage Sud avant la phase de déformation cénozoïque, même si cela n'implique pas forcément que la subduction ait été dirigée sous le Tarim.

2. Déformation intracontinentale, réactivation et rhéologie de la lithosphère : l'exemple de la déformation cénozoïque de l'Asie

La chaîne du Tien Shan, actuellement située à plus de 1000 km de toute limite de plaque, représente un exemple unique de chaîne intracontinentale. Tel que cela a été présenté précédemment, l'histoire Paléozoïque du Tien Shan joue un rôle majeur dans la localisation de la déformation Cénozoïque, notamment à cause de zones de faiblesses crustales. Cependant la

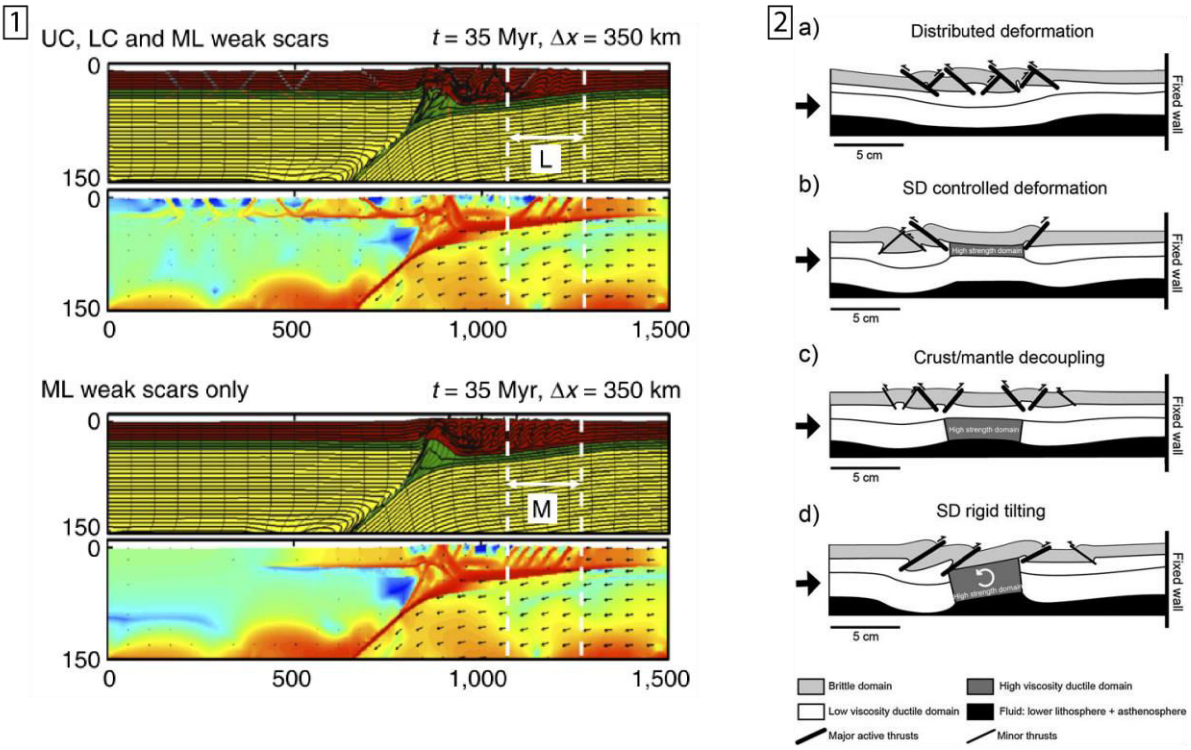

Figure V-7 :1 : modèles numériques montrant la localisation de la déformation dans une lithosphère continentale pré-fracturée (« weak scars »), UC : Croûte supérieure, LC : Croûte inférieure, ML : Manteau lithosphérique. Les couleurs montrent les différentes phases (en haut) et le second invariant du tenseur des vitesses de déformation (en bas), (Heron et al., 2016a). *2 : Interprétation de modèles analogiques, a) une lithosphère sans contraste rhéologique entraîne une déformation distribuée, b) la présence d'un milieux rigide dans la croûte inférieure localise la déformation sur les bords de ce domaine, c) la présence d'un bloc rigide dans le manteau lithosphérique entraîne un découplage de la déformation mantellique et crustale, d) la présence d'un bloc rigide du manteau lithosphérique à la croûte inférieure entraîne la rotation rigide du bloc et localise la déformation sur les bords de ce bloc dans les domaines moins résistants de la croûte et du manteau (Calignano et al., 2015b)* déformation très contrastée du continent asiatique témoigne probablement de la présence d'hétérogénéités rhéologiques à plusieurs échelles.

Molnar et Tapponnier (1981) ont proposé que la localisation de la déformation en Asie soit directement reliée à l'âge thermique de la croûte et plus généralement de la lithosphère. En effet, il existe une corrélation négative à l'échelle du continent entre l'âge de la dernière phase orogénique et l'intensité de la déformation cénozoïque. La résistance visqueuse de la lithosphère est très dépendante de son état thermique, surtout en ce qui concerne l'olivine (Burov et al., 2014; Burov and Diament, 1995) minéral principal des péridotites et donc représentant la rhéologie du manteau lithosphérique.

D'autres auteurs (Calignano et al., 2015b; Heron et al., 2016a, 2016b; Heron and Pysklywec, 2016) proposent également que la présence de zones de faiblesse et de contrastes rhéologiques persistants dans le manteau lithosphérique soit essentielle pour expliquer une telle distribution de la déformation à l'échelle d'une plaque tectonique (Figure V-7) (plusieurs milliers de kilomètres).

Enfin, dans cette thèse il a été montré que l'héritage structural à l'échelle crustale était primordial pour expliquer la localisation de la déformation dans le Tien Shan. Les résultats et propositions de ces différentes études montrent donc une forte dépendance entre les processus de déformation et l'échelle à laquelle ils sont observés et analysés.

La distribution de la déformation du continent asiatique à grande échelle, présentant des zones très déformées telles que le Tien Shan ou le Tibet et des zones peu déformées telles que le Tarim, peut être reliée à la présence de zone de faiblesses lithosphériques et/ou contrastes rhéologiques tels que décrits et représentés par Heron et al. (2016a) ou encore Molnar et Tapponnier (1981). En effet, le Tien Shan ou le Tibet sont fortement marqués par les épisodes tectoniques ayant formé ces domaines continentaux. Le Tien Shan se construit au cours du Paléozoïque par des épisodes de subductions et de collisions qui structurent la lithosphère. De la même manière le Tibet subit une histoire similaire faite de subductions et de collisions au cours du Mésozoïque. Ces deux zones sont donc affectées par une structuration lithologique et thermique de la lithosphère foncièrement différente du bassin du Tarim dont les bordures sont impliquées dans ces événements passés mais dont le centre, zone la moins déformée, reste intact. Il en résulte, à l'échelle de la plaque asiatique, des variations de rhéologie fortes qui impactent la localisation de la déformation dans le continent.

En revanche, à l'échelle de la chaîne du Tien Shan, la longueur d'onde de la déformation est plurikilométrique. Elle se localise sur des zones de failles héritées, telles que la suture STS ou encore la faille de Talas-Ferghana, ainsi que sur des zones de faille néoformées qui viennent se connecter en profondeur le long des discontinuités majeures (croûte sup.-croûte inf. et croûte-manteau) aux zones de déformations préexistantes.

De même, nous avons montré que la bordure Nord du bassin du Tarim ne représente pas une variation significative de rhéologie par rapport au reste du Tien Shan. En effet, cette bordure localise même la majeure partie de la déformation actuelle. Un bloc trop rigide représenterait un contraste de rhéologie trop important et n'admettrait pas de se déformer de cette manière. Cela n'implique pas que toute la lithosphère du Tarim soit d'une rhéologie proche de celle du Tien Shan mais plutôt que la transition entre une lithosphère « perturbée » par les anciennes orogénèses et une lithosphère « cratonique » est diffuse, et ne constitue pas une zone de faiblesse localisée ou un contraste de rhéologie brutal.

Pour résumer ce que l'ensemble de ces études nous apprend, il semble qu'à l'échelle de la chaîne se sont les variations de rhéologie de la croûte qui contrôlent la structure lithosphérique du Tien Shan, alors qu'à l'échelle de plusieurs milliers de kilomètres ce sont les variations de rhéologie lithosphériques qui contrôlent la localisation de la déformation dans le continent.

L'influence de l'héritage tectonique sur la construction des chaînes de montagnes peut être abordée à travers d'autres exemples et notamment par l'étude d'une chaîne bien connue de la communauté européenne que sont les Pyrénées. Bien que les processus à l'origine de la construction des Pyrénées et du Tien Shan soient très différents, (rift intracontinental inversé contre réactivation d'une ancienne chaîne de montagne en domaine intracontinental) il n'en reste pas moins intéressant de comparer les processus et mécanismes ayant conduit à la réactivation des structures héritées.

Les modèles numériques montrent que dans le cas de la réactivation de zones de faiblesses dans le manteau lithosphérique, celles-ci exerce un contrôle de premier ordre sur la localisation de la déformation. Toutefois, dans le cadre du Tien Shan, les deux phases tectoniques sont des phases de compression séparées de 250 Ma. Au cours de cette période le manteau a pu cicatriser par croissance de grains et/ou recristallisation. En revanche, en ce qui concerne la chaîne pyrénéenne la phase de rift intracontinental entraîne un réchauffement de la lithosphère et conduit à une forte hétérogénéité rhéologique au sein de cette dernière (e.g. Vacherat et al., 2014) qui permet la localisation de grandes structures extensives. La grande structure qu'est la faille nord-pyrénéenne est elle-même interprétée comme une faille transformante héritée qui séparait initialement l'Ibérie de l'Eurasie (e.g. Choukroune, 1976). Cet héritage semble contrôler une grande partie de l'évolution et de la déformation finie de la chaîne notamment en ce qui concerne son asymétrie et le style de la déformation type tectonique de socle (e.g. Jammes and Huismans, 2012). Enfin, dans le cas des Pyrénées, la reprise en compression s'effectue immédiatement après l'arrêt de l'extension. Cette inversion se produit donc alors que le manteau est toujours faible et la lithosphère thermiquement rajeunie. Dans ce contexte, les grandes zones déformées dans le manteau (détachements ductiles par exemple) sont toujours des zones de faiblesse privilégiées où la déformation peut se localiser.

Perspectives

Au cours de cette thèse, une approche combinée géologie de terrain-modélisation numérique a été utilisée. Les modèles numériques ont pu être comparés avec de nombreuses données de géologie (géologie de terrain et études de thermo-chronologie basse température) et de géophysique (profil sismique, profil magnéto-tellurique, catalogue de sismicité, vitesse GPS) afin de contraindre au mieux la structure lithosphérique et l'évolution du Tien Shan kirghize.

Bien que la tectonique du Tien Shan soit déjà bien étudiée, il reste de nombreuses questions en suspens notamment sur la déformation et l'histoire paléozoïques. Tout d'abord la présence des unités d'ophiolites non métamorphiques au niveau des zones de suture entre NTS-MTS et MTS-STS reste très peu étudiée. Il n'existe pas de données quant à l'âge de ces unités, leur mode et leur âge de mise en place dans leur position structurale actuelle. Or leur étude pourrait fournir de précieuses informations sur l'histoire des phases de subduction-collision/accrétion dans le Tien Shan kirghize. Dans cette même optique il serait intéressant de tester à l'aide de modèles numériques les différentes hypothèses et scénarii à propos de la construction paléozoïque du Tien Shan (nombre et vergence des subductions).

D'après l'étude menée sur le terrain nous avons également pu mettre en évidence la présence d'un partitionnement de la déformation au cours de la collision. Notre interprétation propose que l'obliquité de la convergence entre le Tarim et le Tien Shan soit à l'origine de ce partitionnement. Cependant, il serait intéressant là aussi de tester, à partir de modèles thermo-mécaniques, si cela est mécaniquement réalisable et dans quelles mesures. De plus si le Tien Shan représente la plaque inférieure (ce qui reste à démontrer clairement) un tel partitionnement de la déformation n'a jamais été démontré. En revanche si le Tien Shan est en position de plaque supérieure plusieurs études (e.g. Barnes et al., 1998; Chemenda et al., 2000) ont montré qu'il était possible, notamment dans les contextes de subduction intra-océanique, de partitionner la déformation entre un front chevauchant et une zone décrochante.

En ce qui concerne la déformation cénozoïque, il serait également intéressant d'avoir des données sur l'exhumation basse température des plutons situés dans le Sud Tien Shan côté chinois bien que les conditions d'accès soient compliquées étant donnée l'altitude de ces zones. Cela pourrait permettre de comparer les résultats des modèles numériques avec les données, sachant que nos modèles prédisent une exhumation dans le Sud Tien Shan le long de la zone de suture réactivée mais également plus au Sud.

Enfin, l'étude de l'influence de l'héritage structural à partir de la modélisation numérique a été menée à travers la définition de zones de faiblesses initiales. Ces zones sont rendues faibles par l'introduction d'un angle de friction et/ou d'une loi de fluage plus faible que le milieu environnant. Cependant, il serait intéressant d'utiliser non pas la loi fluage d'un matériau différent mais plutôt de prendre en compte une loi de fluage pour un même matériau prenant en compte une anisotropie. Toutefois, même si certaines lois prennent en compte l'anisotropie des minéraux et les directions préférentielles de glissement, il existe une complexité à intégrer ces lois dans les codes thermo-mécaniques appliqués à la déformation de la lithosphère sur de longues échelles de temps.

Annexes

Minutes de terrain

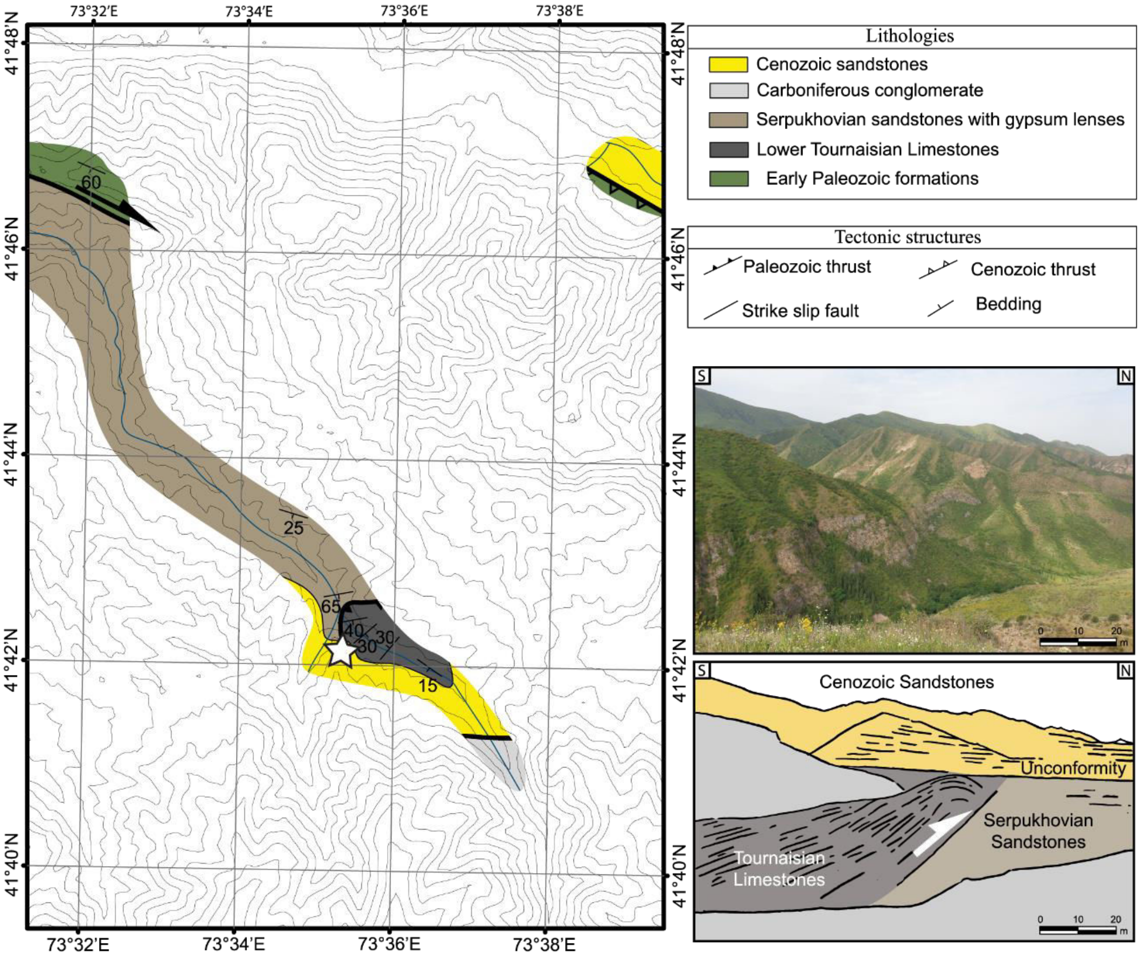

Minute de terrain de la zone de Toktogul (Figure 3, chapitre II)

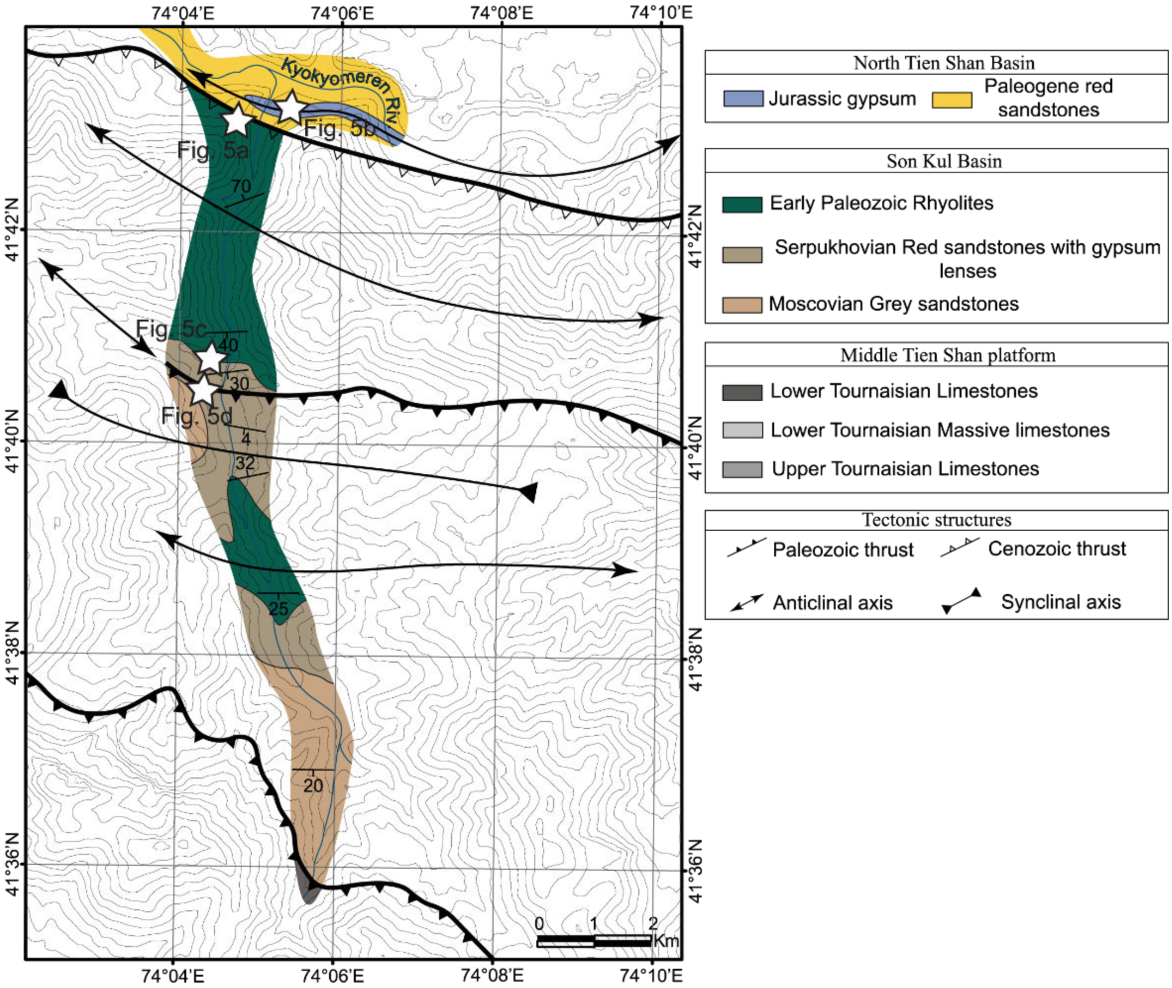

Minute de terrain de la zone centrale de Song-Kul (Figure 4, chapitre II)

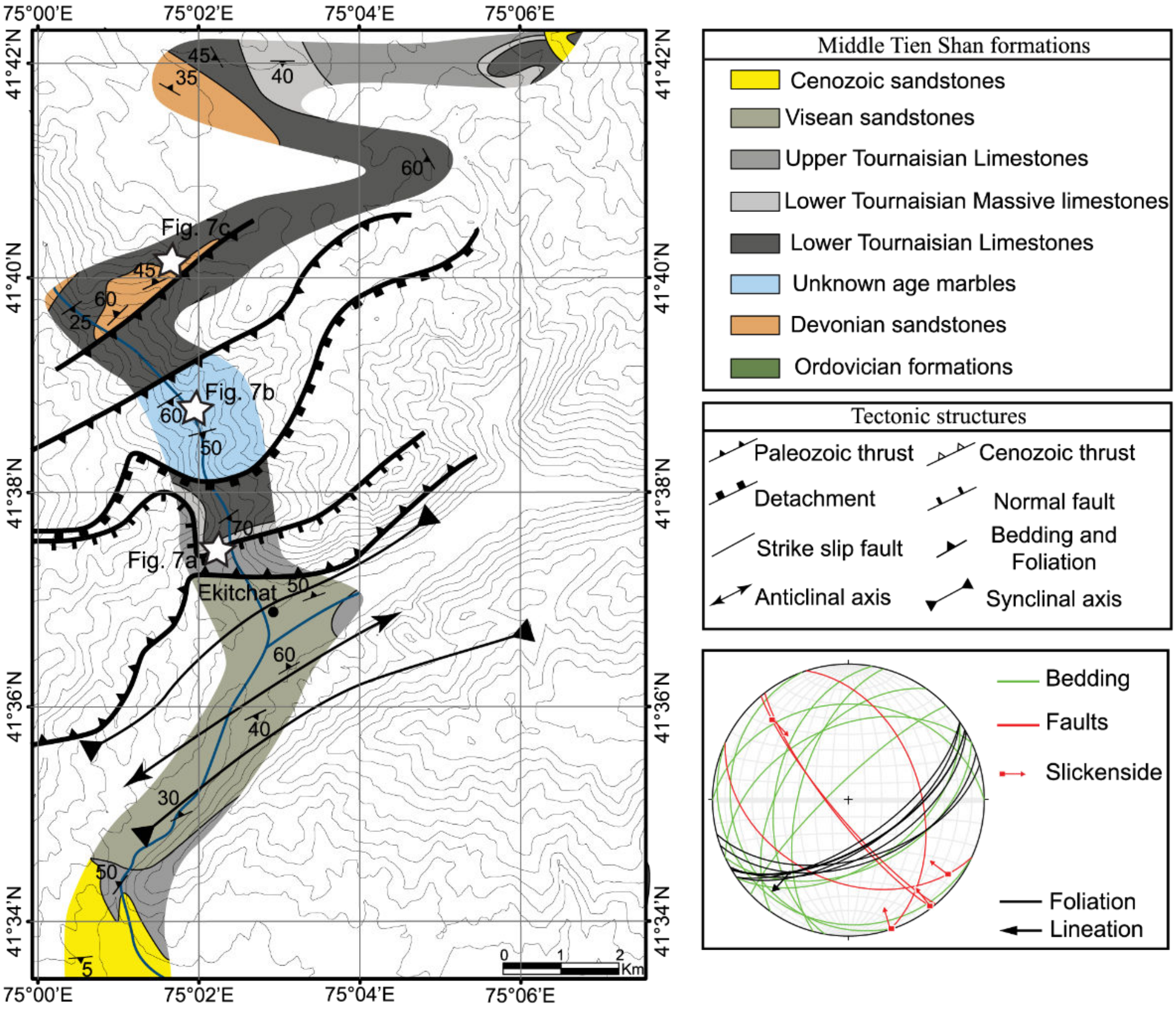

Minute de terrain de la zone de Song-Kul (Figure 6, chapitre II)

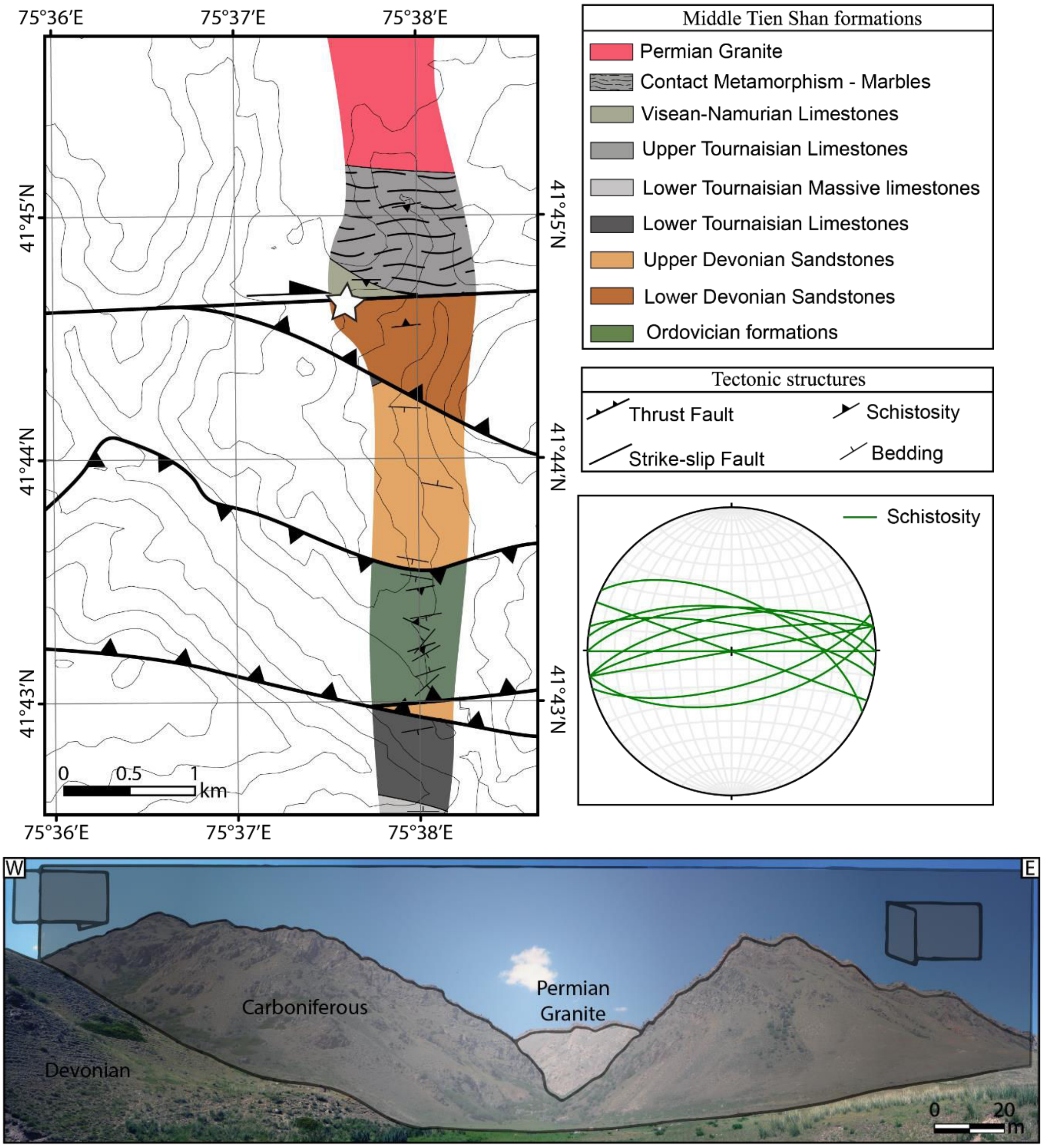

Minute de terrain de la zone Song-Kul Est (Figure 8, chapitre II)

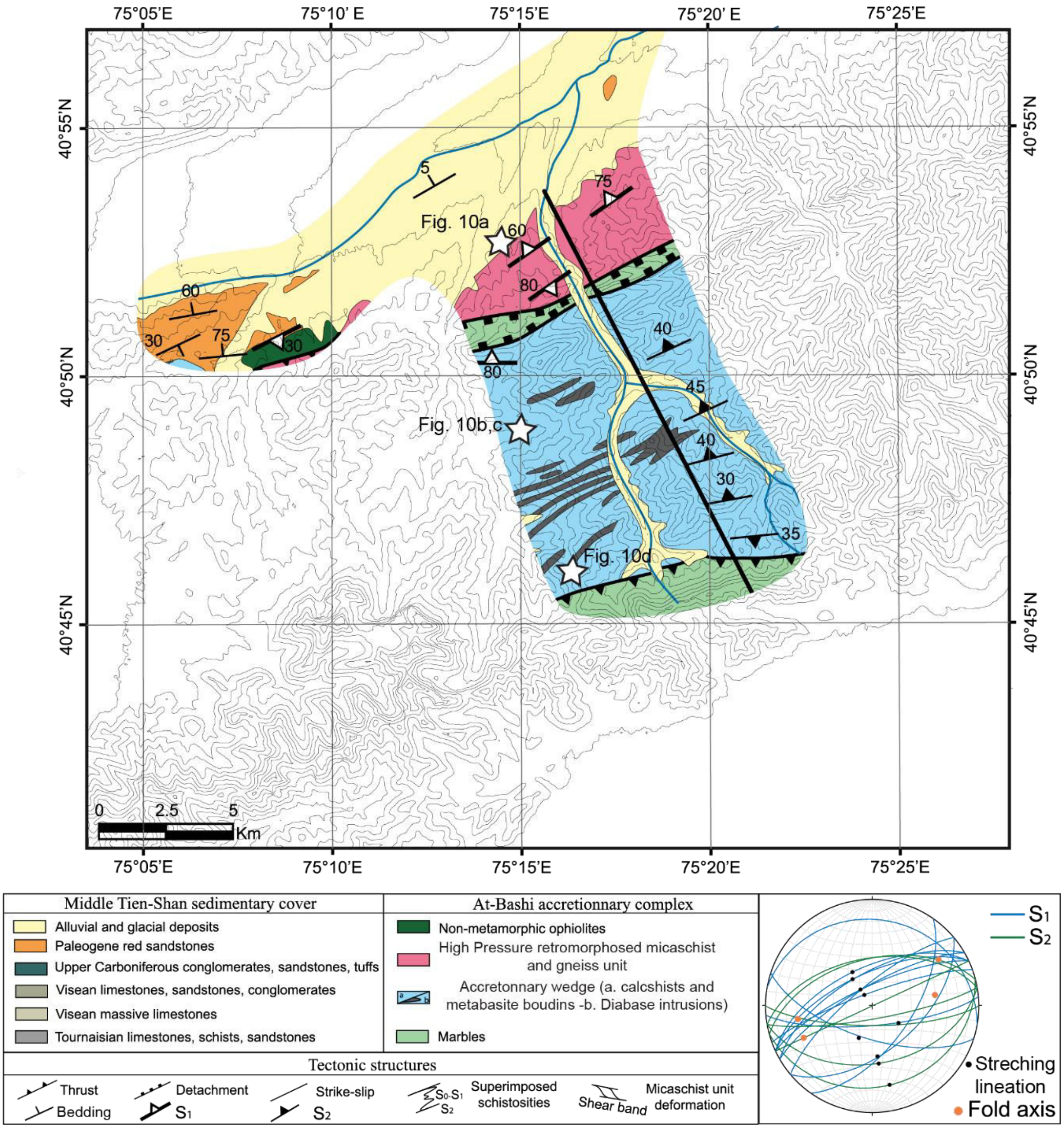

Minute de terrain de la zone d'At-Bashi (Figure 9, chapitre II)

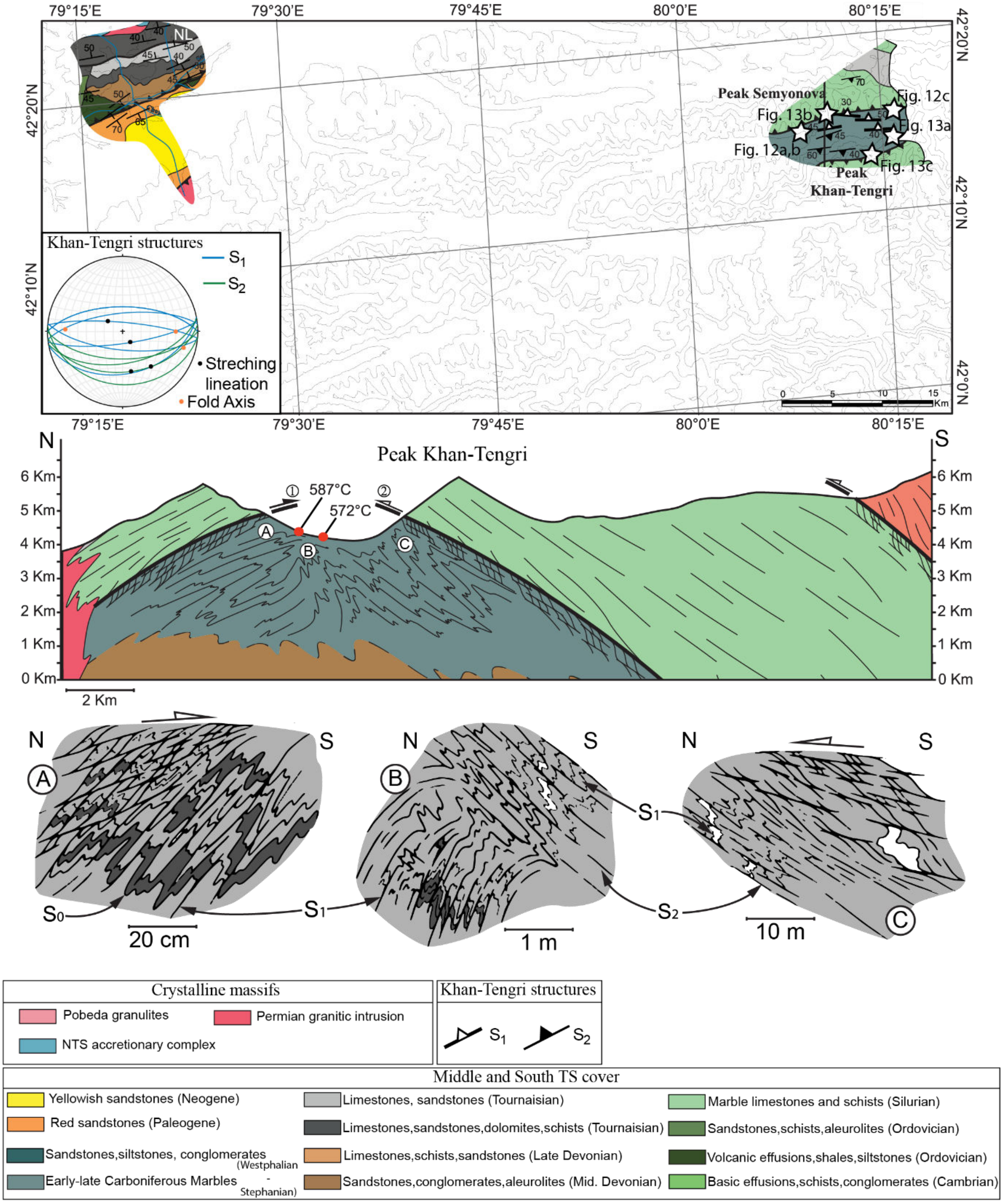

Minute de terrain de la zone du Khan-Tengri (Figure 11, chapitre II)

Routines Matlab pour les trajets P-T-t d'après pTatin2D

Introduction

P_T_t_fromPtatin is a matlab program aiming to compute Depth-Pressure-Temperature-time paths from pTatin2D simulations results. It is composed of three functions (Interface2, Age, and Path) which will be described further. The Figure 1 shows an example of obtained results.

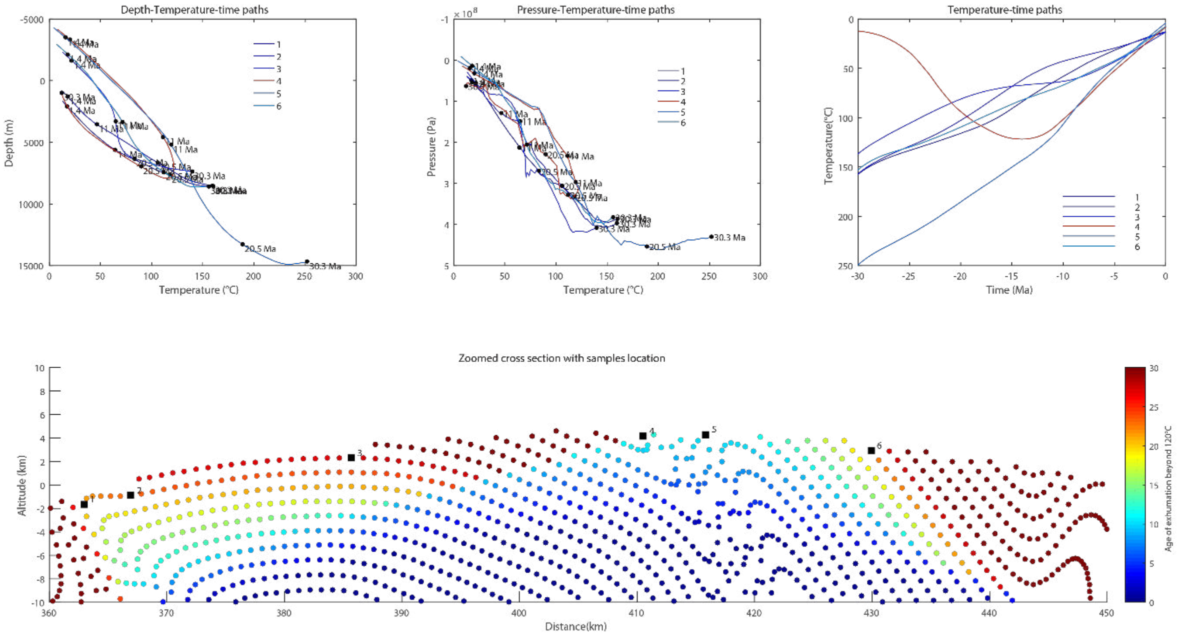

Figure 1: Example of figure obtained after P_T_tfromPtatin run.

The user chooses the points by clicking on them and the age of exhumation beyond a temperature is computed with the T-t, P-T-t and Depth-Temperature-time paths. This program works for parallel simulations by using data contained in the Passive_PT-subdomain files.

Functions

Interface function

When the **P_T_t_fromPtatin** script is launched, a window opens to ask the parameters needed to compute ages and paths to the user. This function saves the parameters given by user returning outputs [Repertoire, nb_block, num_block, zmin, dstep, step_nbr, closure_temp, last_step] respectively corresponding to the text boxes in the order presented by Figure 2.

In order to locate the Passive_PT-subdomain files, the **directory** where these files are located needs to be indicated in the **Directory text box**.

The **second text box** needs the **number of Passive_PT-subdomain** which **contains data**. Indeed, every file does not contain the data required, generally the first subdomains contain the time of the selected time step while the next subdomains contain the number of the point, the depth, the temperature, the position of the point and the pressure (not in this order). They are the same for each time step, therefore the user needs to indicate **how many subdomains contain data for one time step**.

The **third text box** is in relation with the second one. Indeed, as explain for the second text box, all the subdomains do not have the data in which we are interested. Therefore the user has to indicate the **number of the first subdomain containing data**.

In the **fourth text box** the **maximal depth of the points to consider** has to be given by the user in order to not take into account all the points of the simulation for time and space issues.

For the **fifth text box**, the **Step frequency of outputs** represents the frequency chosen by the user for saving pTatin simulations results. In the **ptatin.options** file it is characterized by the option **–output_frequency**.

The **Number of Step text box** needs the number of **saved time steps** regarding the **output frequency chosen**. In order to know this number the user needs to **divide the total time steps by the output frequency**.

In the **closure temperature text box** the user has to indicate the **temperature from which the age of a sample exhumed has to be counted**.

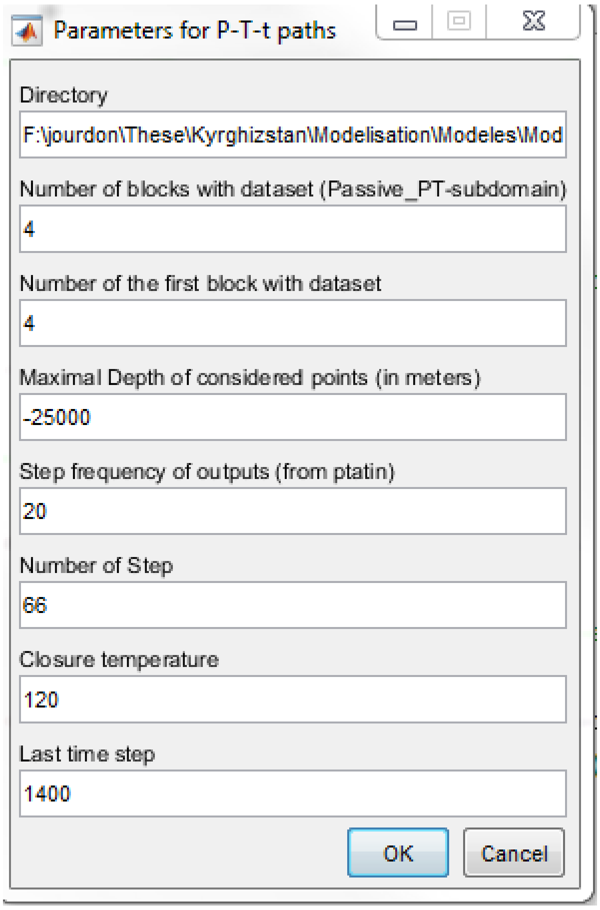

Parameters for P-T-t paths

Directory
F:\jourdon\These\Kyrghizstan\Modelisation\Modeles\Mod

Number of blocks with dataset (Passive_PT-subdomain)
4

Number of the first block with dataset
4

Maximal Depth of considered points (in meters)
-25000

Step frequency of outputs (from ptatin)
20

Number of Step
66

Closure temperature
120

Last time step
1400

Figure 2: Window opening when the script is launched in order to enter information required to run the program.

The **Last time step text box** needs the time step from which the user wants to **consider the end time of the simulation**. It is **not necessarily the true last time step**. Example: You want to consider a P-T-t history of 30 Myr but your simulation has run for 40 Myr, you will have to search what is the time step corresponding to 30 Myr and not the true last time step of your simulation.

Once these parameters have been indicated by the user they are saved and they will be used by the next function.

To create this interface, the matlab function used is called “prompt”. Default answers are already entered but can be changed by the user in the line 9 of Interface2 function : default = {'F:\jourdon\These\Kyrghizstan\Modelisation\Modeles\ModelesErosion\Est_ero6_SPM08_epsmax05_all_NLphi30\','4', '4', '-25000', '20', '66', '120','1400'}; where each coma separates each default values.

Age function

Once the user has finished to enter the needed parameters, the function Interface stops and the function Age is launched. This function will compute the age of exhumation above the isotherm indicated by the closure temperature for all points between the surface and the maximal depth entered previously.

Firstly, this function will open the first Passive_PT-subdomain called step00000_Passive_PT-subdomain00001.dat in order to fix the starting point for time. Secondly, the last time step indicated by the user is read in order to fix the final time of the simulation.

Then the subdomains containing data will be open to compute the characteristics of each considered points at the beginning of the simulation. Five vectors are created:

- **pid0** is the Id of each point
- **x0** is the x position of each point
- **z0** is the depth of each point
- **P0** is the pressure of each point
- **t0** is the temperature of each point

Then a matrix **step0** is created containing all the points of each subdomains with data, in which the points with a depth greater than the maximal depth entered previously will be deleted from the step0 matrix.

After that, the time loop begins and the previous operation will be done for every time steps. A step1 matrix is constructed and erased for each new time step. Moreover, the time of each time step is saved as the variable **agemodel**. Then, the age of each point will be calculated and saved in a variable named **age**.

For each time step:

- If the temperature of a point is over the closure temperature, the point will have the age of the model at this time step which will be erased by the age of the next time step.
- If the temperature of a point is smaller than the closure temperature and its temperature was greater at the previous time step, then the age of this point is the age of the model at this time step. But this one will not be reseted. Indeed, the age is saved and will not be affected by the evolving time as long as the point do not cross again the isotherm defined by the closure temperature.
- Finally, if the temperature of a point is smaller than the closure temperature its age is set to 0.

Several things have to be clearly explained here. Firstly, do not forget that in the simulation the time is going forward, so at the end of the time step loops we will recalculate the age of the points in the model by taking the final time step time as the reference age 0 Myr as if it was today, and the first time step as if it was the past. This is why the age of the points which are always at temperatures smaller than the closure temperature is set to 0 Myr.

Secondly, how do we save the age of an exhumed point? Between Lines 48 and 52 a matrix named markers_id is created. The figure 3 illustrates how this matrix is filled. The first column of this matrix contain the Id of the points and the second column is set to 0. Then, during the age computation of the points at each time step (Lines 125 to 131) this matrix will be used. When a point crosses (from higher to lower temperature) the closure temperature, the age at which this happened is saved in the second column of the markers_id matrix. Then if the point stays at a temperature smaller than the closure temperature its age is set to be equal to its value in the second column of the markers_id matrix. That means that if a point has always been in temperatures smaller than the closure temperature his age is 0, but if at a time this point has been exhumed then the age of this exhumation was saved in the second column of the markers_id matrix and this age is attributed to the corresponding point.

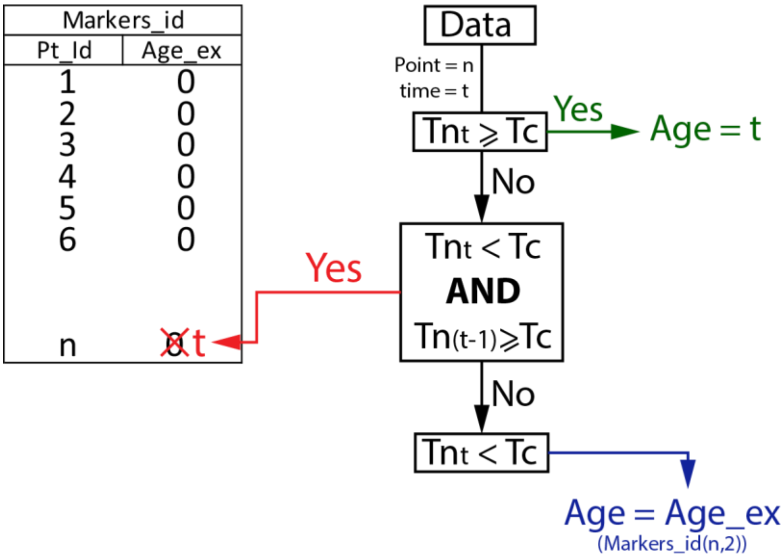

Figure 3: Illustration of the algorithm used to compute the age of the points in the simulation. T: Temperature, n: the considered point, Tc: closure temperature, t: current time of the model.

This allows to not reset the age of exhumation at each time step except if it crosses again the closure temperature isotherm since the age will be set to be the age of the current time step. The position of the points is computed at each time step.

Once it has been done for all time steps, the age of exhumation is calculated by subtracting the time of the final time step by the age of exhumation in order to have a backward time and not a forward time (Line 154 age_exhum = agefin-age).

Two figures are drawn, the first one represents all the points considered with their age (Figure 4). The second one is a zoom (Figure 5), of course you may need to change the x and z limits depending on what is the size of the simulation and the size of the zone where you need to compute P-T-t paths. This figure is clickable, the user will have to click on the points for which P-T-t paths and exact ages are wanted. If a click outside of a point is done, the nearest point will be considered.

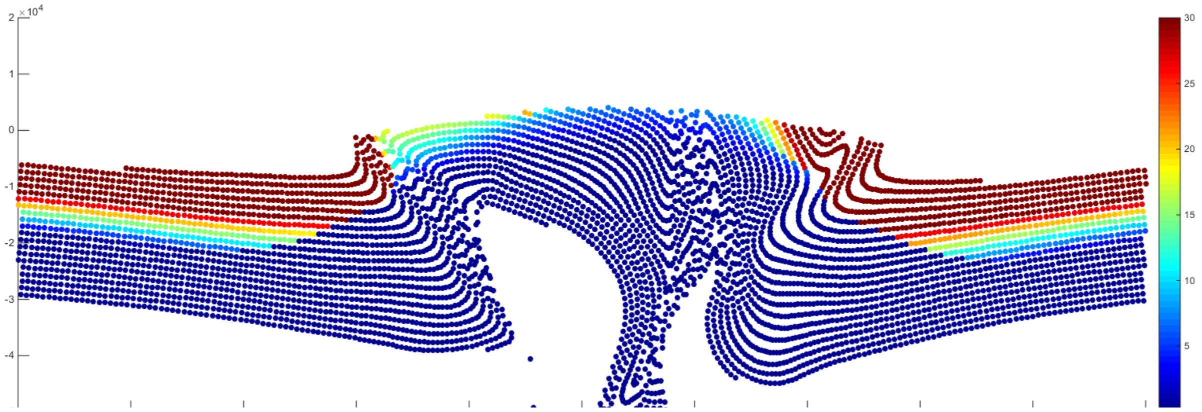

Figure 4 : Age of the points considered in the model regarding the closure temperature entered. The value 0 means that the point did not cross (from higher to lower temperature) the closure temperature, while the maximum value (30 in this example) represents points which have never been at temperatures equal or higher than the closure temperature. All the intermediate values represents the exhumation age of the points at temperatures lower than the closure temperature

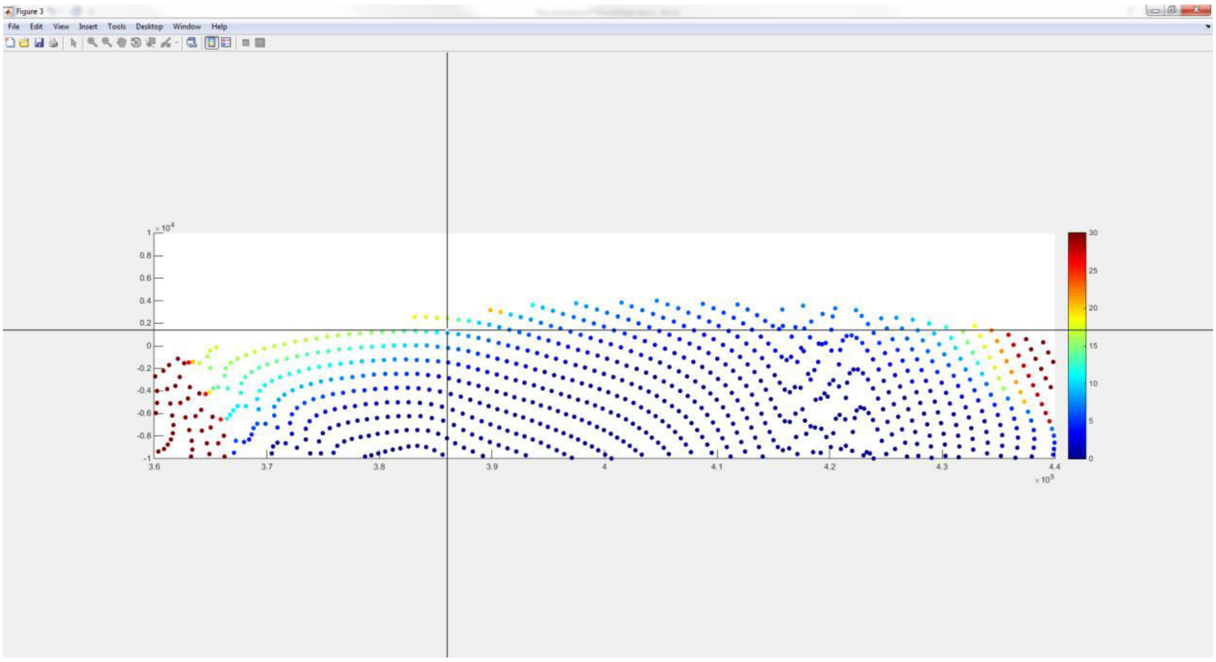

Figure 5: Zoomed cross-section opening at the end of the Age function to allow the user to click on the desired points in order to compute their Depth-Temperature-time, P-T-t and T-t paths and save their ages in a matrix.

The clicked point will then be used to calculate their Depth-Temperature-time and Temperature-time paths by the Path function.

Path function

This function is doing the exact same process than the function Age except that the considered points are the one chosen by the user at the end of the Age function.

A figure (Figure 6) is then drawn showing the Depth-Temperature-time path, the Pressure-Temperature-time path, the Temperature-time path and the clicked points on the cross section with a number corresponding to the order in which the user has clicked.

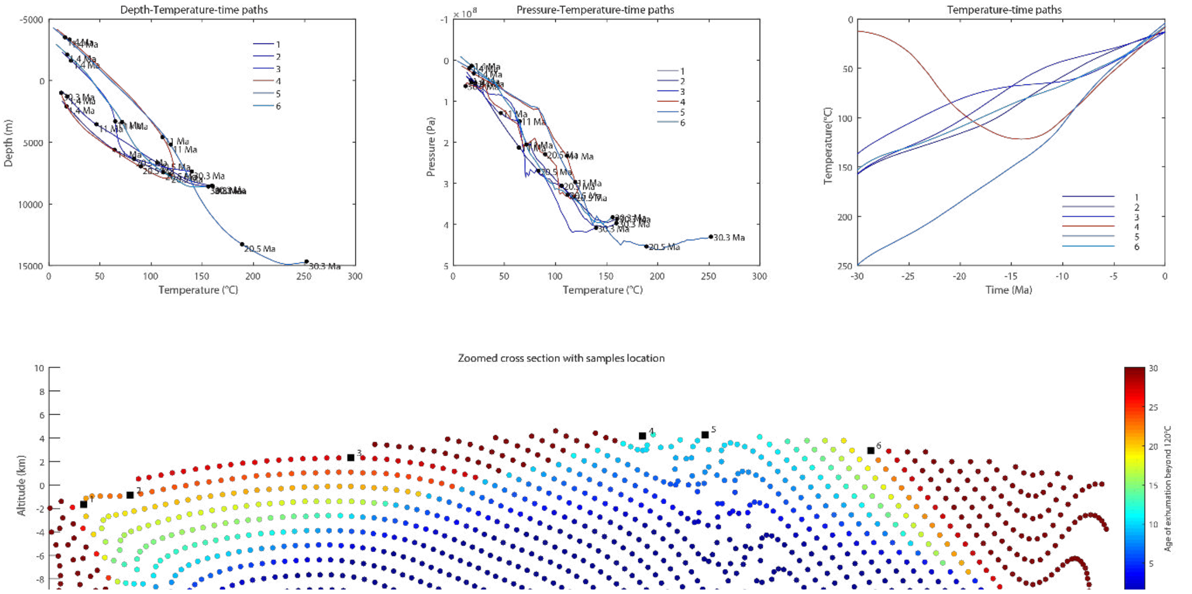

Figure 6: final figure obtained at the end of the P_T_tfromPtatin script. A Depth-Temperature-time path (corner left), a Pressure-Temperature-time path (central), a Temperature-time path (corner right) are obtained as well as a cross section indicating the exhumation age of the points in the simulation on which the clicked points are represented.

A table is also saved with the point id and its age of exhumation, the order is also the order of the clicked points.

Pt_id	Age forward (seconds)	Age backward (Myr)
15613	3.6564E+14	20.20159236
15242	4.5372E+14	17.39649682
15296	3.4275E+14	20.93057325
22357	7.7683E+14	7.106369427
23915	1.2272E+14	27.93789809

Table obtained at the end of the simulation indicating the Id of the clicked points, the Age forward and the age backward

Scripts pour trajets P-T-t

1. Calcul des âges d'exhumation puis des trajets

```
  %%% This script will compute exhumation age and P-T-t path
from ptatin2d
  %%% run result

  clear all
  close all
  % This function opens an interface to allows user to defines
parameters for
  % P-T-t paths computing
  [Repertoire,nb_block,num_block,zmin,dstep,step_nbr,closure_t
emp,last_step] = Interface2;

  % This function computes the exhumation age of the
considered
  % points
  [pt_id,xpos,zpos,age_exhum] =
Age(Repertoire,nb_block,num_block,zmin,step_nbr,dstep,closure_
temp,last_step);

  % This function computes the P-T-t paths of clicked points
(asked to user
  % at the end of the precedent function)
  [age_pt] =
Path(Repertoire,nb_block,num_block,step_nbr,pt_id,xpos,zpos,ag
e_exhum,dstep,closure_temp,last_step);
  % Age_pt is a table containing the number of the clicked
point (in original
  % file), and the age of exhumation (3rd row is in Ma)
```

2. Ages d'exhumation

```
   function [pt_id,xpos,zpos,age_exhum] =
Age(Repertoire,nb_block,num_block,zmin,step_nbr,dstep,closure_
temp,last_step)

   %%% OPENS Passive Tracer FILES FROM PTATIN

   close all;

   delimiterIn = ' ';
   headerlinesIn = 2;

   %%% reads first step for temperatures and markers
     filename0 = [Repertoire,'step00000_Passive_PT-
subdomain00001.dat'];
     fid       = fopen(filename0);
              A     = fscanf(fid,'%s',6);
              age_0 = fscanf(fid,'%f',1);
     fclose (fid);

     %%% reads last step for time
     filename0 = [Repertoire,'step0',last_step,'_Passive_PT-
subdomain00001.dat'];
     fid       = fopen(filename0);
              A       = fscanf(fid,'%s',6);
              age_end = fscanf(fid,'%f',1);
     fclose (fid);

     %%% k = Numbers of the block with data
     for k=1:nb_block
         blocknum  = k+(num_block-1);
         filename0 = [Repertoire,'step00000_Passive_PT-
subdomain0000',num2str(blocknum),'.dat'];
         A0   =
importdata(filename0,delimiterIn,headerlinesIn);
         pid0 = A0.data(:, 1);
         x0   = A0.data(:, 3);
         z0   = A0.data(:, 4);
         P0   = A0.data(:, 5);
         t0   = A0.data(:, 6);

        step00=[pid0 x0 z0 P0 t0];
         if k==1
           step0=step00;
         else
           step0=[step0; step00];
         end
       end
       step0=sortrows(step0,1);

       %%% selects starting points depth
       %%% Selects points between 0 and zmin
```

```
       markers = find(step0(:,3)>zmin);

       for k=1:size(markers,1)
       l = markers(k);
       markers_id(k,1) = step0(l,1);
       markers_id(k,2) = 0;
       end

     %%% Loop on time steps

   for j=1:step_nbr  % number of time steps
       init = j*dstep

       %%% number of zeros in file name
       if init < 10
           dk = ['0000',num2str(init)];
       elseif init >=10 && init<100
           dk = ['000',num2str(init)];
       elseif init >=100 && init<1000
           dk = ['00',num2str(init)];
       else
           dk = ['0',num2str(init)];
       end

       %%%  !!!! add another "zero" test if the number of
subdomains is > 9 !!!

   %%% reads initial state files for 4 blocks (starting from
block x)
   %%% change the number of blocks if necessary
         filename1 =
[Repertoire,'step',num2str(dk),'_Passive_PT-
subdomain00001.dat'];
         fid       = fopen(filename1);
              A        = fscanf(fid,'%s',6);
              agemodel = fscanf(fid,'%f',1)
         fclose(fid);

       for k=1:nb_block
         blocknum   = k+(num_block-1);
         filename1 =
[Repertoire,'step',num2str(dk),'_Passive_PT-
subdomain0000',num2str(blocknum),'.dat'];
         A1    =
importdata(filename1,delimiterIn,headerlinesIn);
         pid1 = A1.data(:, 1);
         x1   = A1.data(:, 3);
         z1   = A1.data(:, 4);
         P1   = A1.data(:, 5);
         t1   = A1.data(:, 6);
        step01=[pid1 x1 z1 P1 t1];
```

```
        if k==1
          step1=step01;
        else
          step1=[step1; step01];
        end
      end
      step1=sortrows(step1,1);


      %%% finds surface points
      linesurf = find(step1(:,5)<13);
      for k=1:size(linesurf,1)
          xsurf(k) = step1(linesurf(k),2);
          zsurf(k) = step1(linesurf(k),3);
      end

      %%% finds marked points
      lmark = size(markers_id,1);

      for i=1:lmark

         line = find(step1(:,1)==markers_id(i,1));

         if j==1
           age(i)  = agemodel;
           xpos(i) = step1(line,2);
           zpos(i) = step1(line,3);
           P(i)    = step1(line,4);
         else

            if (isempty(line)~=1)
            temp(i,j) = step1(line,5);
            id = step1(line,1);


               if temp(i,j) >= closure_temp
                age(i) = agemodel;

               elseif temp(i,j)<closure_temp && temp(i,j-
1)>=closure_temp
                markers_id(i,2) = agemodel;
                age(i)          = agemodel;
               else age(i) = markers_id(i,2);

               end

             xpos(i) = step1(line,2);
             zpos(i) = step1(line,3);
             P(i)    = step1(line,4);
            else
             xpos(i) = -200000;
```

```
                zpos(i) = -200000;
                age(i)  = 3e17;
               end
            end

         end

         age    = age/3.14E13;
         exhum  = markers_id(:,2)/3.14E13;
         agefin = age_end/3.14E13;


     end

     age_exhum = agefin-age;

     figure (2);
       scatter(xpos,zpos,30,age_exhum,'filled')
       axis equal
       axis([300000 500000 -50000 20000])
       caxis([0 30])
       colorbar
       colormap jet
       hold off

     %%% contourf

     % x = 300000:1000:500000;
     % z = -15000:1000:10000;
     % [XG,ZG] = meshgrid(x,z);
     % age_interp = griddata(xpos,zpos,agefin-
   age,XG,ZG,'linear');
     %
     % figure(2)
     % contourf(x,z,age_interp,0:2:30)
     % axis equal
     % axis([300000 500000 -50000 20000])
     % caxis([0 30])
     % colorbar

     %%% Graphical Input from mouse

     figure (3)
     scatter(xpos,zpos,30,age_exhum,'filled')
     axis equal
     axis([340000 460000 -15000 10000])
     caxis([0 30])
     colorbar
     colormap jet

     % Stock coordinates of clicked points
```

```
   [xpt,zpt] = ginput;

   for i = 1:length(xpt)
       for k = 1:length(step1)

           dist(k)=(xpt(i)-step1(k,2))^2+(zpt(i)-step1(k,3))^2;

       end

       [a,b]     = min(dist);
       pt_id(i) = step1(b,1);
   end

   end
```

3. *Trajets*

```
   function [age_pt] =
Path(Repertoire,nb_block,num_block,step_nbr,pt_id,xpos,zpos,ag
e_exhum,dstep,closure_temp,last_step)

   delimiterIn = ' ';
   headerlinesIn = 2;

   %%% reads first step for temperatures and markers
     filename0 = [Repertoire,'step00000_Passive_PT-
subdomain00001.dat'];
     fid = fopen(filename0);
              A=fscanf(fid,'%s',6);
              age_0=fscanf(fid,'%f',1);
     fclose (fid);

     %%% reads last step for time
     filename0 = [Repertoire,'step0',last_step,'_Passive_PT-
subdomain00001.dat'];
     fid = fopen(filename0);
              A=fscanf(fid,'%s',6);
              age_end=fscanf(fid,'%f',1);
     fclose (fid);

     %%% k = Number of the blocks with data
     for k=1:nb_block
         blocknum = k+(num_block-1);
         filename0 = [Repertoire,'step00000_Passive_PT-
subdomain0000',num2str(blocknum),'.dat'];
         A0    =
importdata(filename0,delimiterIn,headerlinesIn);
         pid0 = A0.data(:, 1);
         x0   = A0.data(:, 3);
         z0   = A0.data(:, 4);
         P0   = A0.data(:, 5);
```

```
        t0   = A0.data(:, 6);

       step00=[pid0 x0 z0 P0 t0];
        if k==1
          step0=step00;
        else
          step0=[step0; step00];
        end
     end
      step0=sortrows(step0,1);

      %%% selects starting points depth

  for k=1:size(pt_id,2)
      l=pt_id(k);
      markers_id(k,1) = step0(l,1);
      markers_id(k,2) = 0;
  end
    %%% Loop on time steps

  for j=1:step_nbr  % number of time steps
      init = j*dstep

      %%% number of zeros in file name
      if init < 10
          dk = ['0000',num2str(init)];
      elseif init >=10 && init<100
          dk = ['000',num2str(init)];
      elseif init >=100 && init<1000
          dk = ['00',num2str(init)];
      else
          dk = ['0',num2str(init)];
      end

      %%%  !!!! add another "zero" test if the number of
subdomains is > 9 !!!

  %%% reads initial state files for 4 blocks (starting from
block x)
  %%% change the number of blocks if necessary
        filename1 =
[Repertoire,'step',num2str(dk),'_Passive_PT-
subdomain00001.dat'];
        fid = fopen(filename1);
             A=fscanf(fid,'%s',6);
             agemodel=fscanf(fid,'%f',1)
        fclose(fid);

      for k=1:nb_block
        blocknum = k+(num_block-1);
```

```
        filename1 =
[Repertoire,'step',num2str(dk),'_Passive_PT-
subdomain0000',num2str(blocknum),'.dat'];
        A1   =
importdata(filename1,delimiterIn,headerlinesIn);
        pid1 = A1.data(:, 1);
        x1   = A1.data(:, 3);
        z1   = A1.data(:, 4);
        P1   = A1.data(:, 5);
        t1   = A1.data(:, 6);
       step01=[pid1 x1 z1 P1 t1];
        if k==1
          step1=step01;
        else
          step1=[step1; step01];
        end
      end
      step1=sortrows(step1,1);


      %%% finds surface points
      linesurf = find(step1(:,5)<13);
      for k=1:size(linesurf,1)
          xsurf(k)=step1(linesurf(k),2);
          zsurf(k)=step1(linesurf(k),3);
      end

      %%% finds marked points
      lmark = size(pt_id,2);

      for i=1:lmark

         line = find(step1(:,1)==pt_id(i))   ;

         if j==1
           age(i)= agemodel;
           xpos_pt(i) = step1(line,2);
           zpos_pt(i) = step1(line,3);
           P_pt(i)    = step1(line,4);
         else

            if (isempty(line)~=1)
            temp(i,j) = step1(line,5);
            time(i,j) = (age_end-agemodel)/3.14e13;
            id        = step1(line,1);

               if temp(i,j) >= closure_temp
                age(i) = agemodel;

               elseif temp(i,j)<closure_temp && temp(i,j-
1)>=closure_temp
```

```
                 markers_id(i,2)= agemodel;
                 age(i)          = agemodel;
                else age(i)      = markers_id(i,2);

                end

              xpos_pt(i)     = step1(line,2);
              zpos_pt(i,j)   = step1(line,3);
              zpos_pt_end(i) = step1(line,3);
              P_pt(i,j)      = step1(line,4);
              P_pt_end(i)    = step1(line,4);
             else
              xpos_pt(i)     = -200000;
              zpos_pt(i,j)   = -200000;
              zpos_pt_end(i) = -200000;
              age(i)         = 3e17;
             end
          end

       end

       age = age/3.14E13;

       agefin = age_end/3.14E13;

   end

   figure (4)

   subplot(2,3,1)
   c = colormap(jet);
   for n = 1:lmark
   %plot(-time(n,2:size(time,2)),temp(n,2:size(temp,2)))
   plot(temp(n,2:size(time,2)),-
zpos_pt(n,2:size(temp,2)),'Color',c(n*3,:))
   hold on
   plot(200:220,(-4e3+n*1e3)*ones(1,21),'Color',c(n*3,:))
   text(222,(-4e3+n*1e3),num2str(n))
   for k=2:20:size(time,2)
   scatter(temp(n,k),-zpos_pt(n,k),20,'k','filled')
   text(temp(n,k)+2,-
zpos_pt(n,k)+3e2,[num2str(round(time(n,k),1)),' Ma'])
   end
   end
   axis ij
   hold off
   xlabel('Temperature (°C)')
   ylabel('Depth (m)')
   title('Depth-Temperature-time paths')

   subplot(2,3,2)
```

```
 c = colormap(jet);
 for n = 1:lmark
 %plot(-time(n,2:size(time,2)),temp(n,2:size(temp,2)))
 plot(temp(n,2:size(time,2)),P_pt(n,2:size(temp,2)),'Color',c
(n*3,:))
 hold on
 plot(200:220,(0+n*0.25e8)*ones(1,21),'Color',c(n*3,:))
 text(222,(0+n*0.25e8),num2str(n))
 for k=2:20:size(time,2)
 scatter(temp(n,k),P_pt(n,k),20,'k','filled')
 text(temp(n,k)+2,P_pt(n,k)+3e2,[num2str(round(time(n,k),1)),
' Ma'])
 end
 end
 axis ij
 hold off
 xlabel('Temperature (°C)')
 ylabel('Pressure (Pa)')
 title('Pressure-Temperature-time paths')

 subplot(2,3,3)
 c = colormap(jet);
 for n = 1:lmark
 plot(-
time(n,2:size(time,2)),temp(n,2:size(temp,2)),'Color',c(n*3,:)
)
 hold on
 plot(-10:-5,(170+n*10)*ones(1,6),'Color',c(n*3,:))
 text(-3,(170+n*10),num2str(n))
 end
 axis ij
 axis([-30 0 0 300])
 hold off
 xlabel('Time (Ma)')
 ylabel('Temperature(°C)')
 title('Temperature-time paths')

 subplot(2,3,[4,6])
 scatter(xpos*1e-3,zpos*1e-3,30,age_exhum,'filled')
 hold on
 scatter(xpos_pt*1e-3,zpos_pt_end*1e-
3,80,'k','filled','square')
 for i = 1:lmark
     text(xpos_pt(i)*1e-3+0.5,zpos_pt_end(i)*1e-
3+0.5,num2str(i))
 end
 axis equal
 axis([340 460 -15 10])
 caxis([0 30])
 h = colorbar;
```

```
  h.Label.String = ['Age of exhumation beyond
',num2str(closure_temp),'°C'];
  colormap jet
  xlabel('Distance(km)')
  ylabel('Altitude (km)')
  title('Zoomed cross section with samples location')
  hold off

  % Table of exhumation ages for clicked points (raw 3 in Myr)
  age_pt = markers_id;

  for i = 1:lmark
      age_pt(i,3) = (age_end-markers_id(i,2))/3.14e13;
  end

  end
```

4. *Interface*

```
  function
[Repertoire,nb_block,num_block,zmin,dstep,step_nbr,closure_tem
p,last_step] = Interface2
  prompt = {'Directory','Number of blocks with dataset
(Passive_PT-subdomain)',...
      'Number of the first block with dataset',...
      'Maximal Depth of considered points (in meters)',...
      'Step frequency of outputs (from ptatin)',...
      'Number of Step',...
      'Closure temperature',...
      'Last time step'};
  default =
{'F:\jourdon\These\Kyrghizstan\Modelisation\Modeles\ModelesEro
sion\Est_ero6_SPM08_epsmax05_all_NLphi30\',...
      '4', '4', '-25000', '20', '66', '120','1400'};
  answer1 = inputdlg(prompt,'Parameters for P-T-t
paths',1,default);


  Repertoire = char(answer1(1));
  nb_block = str2num(char(answer1(2)));
  num_block = str2num(char(answer1(3)));
  zmin = str2num(char(answer1(4)));
  dstep = str2num(char(answer1(5)));
  step_nbr = str2num(char(answer1(6)));
  closure_temp = str2num(char(answer1(7)));
  last_step = char(answer1(8));
  end
```

Références

Abdrakhmatov, K., Weldon, R., Thompson, S.C., Burbank, D.W., Rubin, C., Miller, M., Molnar, P., 2001. Onset, style and current rate of shortening in the central Tien Shan, Kyrgyz Republic. Russian Geology and Geophysics 42, 1585–1609.

Abdrakhmatov, K.E., Aldazhanov, S.A., Hager, B.H., Hamburger, M.W., Herring, T.A., Kalabaev, K.B., Makarov, V.I., Molnar, P., Panasyuk, S. V., Prilepin, M.T., Reilinger, R.E., Sadybakasov, I.S., Souter, B.J., Trapeznikov, Y.A., Tsurkov, V.Y., Zubovich, A. V., 1996. Relatively recent construction of the Tien Shan inferred from GPS measurements of present-day crustal deformation rates. Nature 384, 450–453.

Agard, P., Yamato, P., Jolivet, L., Burov, E., 2009. Exhumation of oceanic blueschists and eclogites in subduction zones: Timing and mechanisms. Earth-Science Reviews 92, 53–79. doi:10.1016/j.earscirev.2008.11.002

Albare, F., 1998. The growth of continental crust. Tectonophysics 296, 1–14.

Alekseev, D. V., Aristov, V. a., Degtyarev, K.E., 2007. The age and tectonic setting of volcanic and cherty sequences in the ophiolite complex of the Atbashe Ridge (Southern Tien Shan). Doklady Earth Sciences 413, 380–383. doi:10.1134/S1028334X07030130

Alekseev, D. V., Degtyarev, K.E., Kotov, a. B., Sal'nikova, E.B., Tret'yakov, a. a., Yakovleva, S.Z., Anisimova, I. V., Shatagin, K.N., 2009. Late Paleozoic subductional and collisional igneous complexes in the Naryn segment of the Middle Tien Shan (Kyrgyzstan). Doklady Earth Sciences 427, 760–763. doi:10.1134/S1028334X09050122

Alexeiev, D. V., Kröner, A., Hegner, E., Rojas-Agramonte, Y., Biske, Y.S., Wong, J., Geng, H.Y., Ivleva, E.A., M??hlberg, M., Mikolaichuk, A. V., Liu, D., 2016. Middle to Late Ordovician arc system in the Kyrgyz Middle Tianshan: From arc-continent collision to subsequent evolution of a Palaeozoic continental margin. Gondwana Research 39, 261–291. doi:10.1016/j.gr.2016.02.003

Ali, J.R., Thompson, G.M., Zhou, M., Song, X., 2005. Emeishan large igneous province , SW China. Lithos 79, 475–489. doi:10.1016/j.lithos.2004.09.013

Allen, M.B., Vincent, J., Wheeler, P.J., 1999. Late Cenozoic tectonics of the Kepingtage thrust zone : Interactions of the Tien Shan and Tarim Basin , northwest China. Tectonics 18, 639–654. doi:10.1029/1999TC900019

Allen, M.B., Windley, B.F., Zhang, C., 1993. Palaeozoic collisional tectonics and magmatism of the Chinese Tien Shan, central Asia. Tectonophysics 220, 89–115. doi:10.1016/0040-1951(93)90225-9

Atwater, T., 1970. Implications of Plate Tectonics for the Cenozoic Tectonic Evolution of Western North America. Geological Society of America Bulletin 81, 3513–3536.

Atwater, T., 1989. Plate Tectonic History of the Northeast Pacific and Western North America, in: Winterer, E.L., Hussong, D.M., Decker, R.W. (Eds.), The Eastern Pacific Ocean and Hawaii. Boulder, Colorado, pp. 499–522.

Atwater, T., Stock, J., 1998. Pacific-North America Plate Tectonics of the Neogene Southwestern United States - An Update. International Geological Review 40, 375–402.

Avouac, J.P., Tapponier, P., Bai, M., You, H., Wang, G., 1993. Active thrusting and folding around the northern Tien Shan and late Cenozoic rotation of the Tarim relative to Dzungaria and Kazakhstan. Journal of Geophysical Research 98, 6755–6804.

Bagdassarov, N., Batalev, V., Egorova, V., 2011. State of lithosphere beneath Tien Shan from petrology and electrical conductivity of xenoliths. Journal of Geophysical Research 116, 1–22. doi:10.1029/2009JB007125

Bakirov, A.B., Maksumova, R.A., 2001. Geodynamic evolution of the Tien Shan Litosphere. Russian Geology and Geophysics 42, 1359–1366.

Balay, S., Abhyankar, S., Adams, M., Brown, J., Brune, P., Buschelman, K., Eijkhout, V., Gropp, W., Kaushik, D., Knepley, M., Mcinnes Curfman, L., Rupp, K., Smith, B., Zhang, H., 2013. PETSc Web page [WWW Document]. URL http://www.mcs.anl.gov/petsc

Balay, S., Abhyankar, S., Adams, M., Brown, J., Brune, P., Buschelman, K., Eijkhout, V., Gropp, W., Kaushik, D., Knepley, M., Mcinnes Curfman, L., Rupp, K., Smith, B., Zhang, H., 2014. PETSc Users Manual. Argonne National Laboratory ANL-95/11-Revision 3.5.

Bande, A., Sobel, E.R., Mikolaichuk, A., Acosta, V.T., 2015. Talas – Fergana Fault Cenozoic timing of deformation and its relation to Pamir indentation. Geological Society of London, Special publication 427, SP427-1.

Barnes, P.M., de Lépinay, B.M., Collot, J.-Y., Delteil, J., Audru, J.-C., 1998. Strain partitioning in the transition area between oblique subduction and continental collision, Hikurangi margin, New Zealand. Tectonics 17, 534–557. doi:10.1029/98TC00974

Baslakunov, J., Takasu, A., Tagiri, M., Bakirov, A., Sakiev, K., 2007. Two modes of occurrence of eclogites from the Atbashy Range, southern Tien-Shan, Kyrgyzstan, in: American Geophysical Union Fall Meeting. p. Abstract V41C0730B.

Batalev, V.Y., Bataleva, E.A., Egorova, V. V, Matyukov, V.E., Rybin, A.K., 2011. The lithospheric structure of the Central and Southern Tien Shan : MTS data correlated with petrology and laboratory studies of lower-crust and upper-mantle xenoliths. Russian Geology and Geophysics 52, 1592–1599. doi:10.1016/j.rgg.2011.11.005

Bauville, A., Schmalholz, S.M., 2015. Transition from thin- to thick-skinned tectonics and consequences for nappe formation: Numerical simulations and applications to the Helvetic nappe system, Switzerland. Tectonophysics 665, 101–117. doi:10.1016/j.tecto.2015.09.030

Bazhenov, M.L., Collins, A.Q., Degtyarev, K.E., Levashova, N.M., Mikolaichuk, A. V., Pavlov, V.E., Van der Voo, R., 2003. Paleozoic northward drift of the North Tien Shan (Central Asia) as revealed by Ordovician and Carboniferous paleomagnetism. Tectonophysics 366, 113–141. doi:10.1016/S0040-1951(03)00075-1

Beaumont, C., Jamieson, R. a., Butler, J.P., Warren, C.J., 2009. Crustal structure: A key constraint on the mechanism of ultra-high-pressure rock exhumation. Earth and Planetary Science Letters 287, 116–129. doi:10.1016/j.epsl.2009.08.001

Bellahsen, N., Jolivet, L., Lacombe, O., Bellanger, M., Boutoux, A., Garcia, S., Mouthereau, F., 2012. Tectonophysics Mechanisms of margin inversion in the external Western Alps : Implications for crustal rheology. Tectonophysics 560–561, 62–83. doi:10.1016/j.tecto.2012.06.022

Bellahsen, N., Mouthereau, F., Boutoux, A., Bellanger, M., Lacombe, O., Jolivet, L., Rolland, Y., 2014. Collision kinematics in the western external Alps. Tectonics 33, 1055–1088. doi:10.1002/2013TC003453

Bercovici, D., Ricard, Y., 2012. Mechanisms for the generation of plate tectonics by two-phase grain-damage and pinning. Physics of Earth and Planetary Interiors 202–203, 27–55. doi:10.1016/j.pepi.2012.05.003

Beyssac, O., Bollinger, L., Avouac, J.P., Goffé, B., 2004. Thermal metamorphism in the lesser Himalaya of Nepal determined from Raman spectroscopy of carbonaceous material. Earth and Planetary Science Letters 225, 233–241. doi:10.1016/j.epsl.2004.05.023

Beyssac, O., Goffé, B., Chopin, C., Rouzaud, J.N., 2002. Raman spectra of carbonaceous material in metasediments: A new geothermometer. Journal of Metamorphic Geology 20, 859–871. doi:10.1046/j.1525-1314.2002.00408.x

Beyssac, O., Goffé, B., Petitet, J.-P., Froigneux, E., Moreau, M., Rouzaud, J.-N., 2003. On the characterization of disordered and heterogeneous carbonaceous materials by Raman spectroscopy. Spectrochimica Acta Part A: Molecular and Biomolecular Spectroscopy 59, 2267–2276. doi:10.1016/S1386-1425(03)00070-2

Bielinski, R.A., Park, S.K., Sears, C., 2003. Lithospheric heterogeneity in the Kyrgyz Tien Shan imaged by magnetotelluric studies. Geophysical Research Letters 30, 1–4. doi:10.1029/2003GL017455

Bird, P., 2003. An updated digital model of plate boundaries. Geochemistry, Geophysics, Geosystems 4. doi:10.1029/2001GC000252

Biske, Y.S., 1996a. Paleozoic Structure and History of South Tian-Shan (in Russian). Sankt-Pete. St Petersburg.

Biske, Y.S., 1996b. Late Paleozoic collision of the Tarimskiy and Kirghiz-Kazakh paleocontinents. Geotectonics 29, 26–34.

Biske, Y.S., Konopelko, D.L., Seltmann, R., 2013. Geodynamics of late Paleozoic magmatism in the Tien Shan and its framework. Geotectonics 47, 291–309. doi:10.1134/S001685211304002X

Biske, Y.S., Seltmann, R., 2010. Paleozoic Tian-Shan as a transitional region between the Rheic and Urals-Turkestan oceans. Gondwana Research 17, 602–613. doi:10.1016/j.gr.2009.11.014

Biske, Y.S., Zubtov, Y.S., Porshnyakov, G.S., 1985. Hercynides of the Atbashi Kokshaal Region Ou the Southern Tian-Shan (in Russian). Leningrad.

Braun, J., 2002a. Quantifying the effect of recent relief changes on age-elevation relationships. Earth and Planetary Science Letters 200, 331–343. doi:10.1016/S0012-821X(02)00638-6

Braun, J., 2002b. Estimating exhumation rate and relief evolution by spectral analysis of age-elevation datasets. Terra Nova 14, 210–214. doi:10.1046/j.1365-3121.2002.00409.x

Buiter, S.J.H., Pfiffner, O.A., 2003. Numerical models of the inversion of half-graben basins. Tectonics 22, 1–16. doi:10.1029/2002TC001417

Bullen, M.E., Burbank, D.W., Garver, J.I., Abdrakhmatov, K.Y., 2001. Late Cenozoic tectonic evolution of the northwestern Tien Shan: New age estimates for the initiation of mountain building. Geological Society of America Bulletin. doi:10.1130/0016-7606(2001)113<1544:LCTEOT>2.0.CO;2

Burbank, D.W., McLean, J.K., Bullen, M., Abdrakhmatov, K.Y., Miller, M.M., 1999a. Partitioning of intermontane basins by thrust-related folding, Tien Shan, Kyrgyzstan. Basin Research 11, 75–92. doi:10.1046/j.1365-2117.1999.00086.x

Burbank, D.W., McLean, J.K., Bullen, M., Abdrakhmatov, K.Y., Miller, M.M., 1999b. Partitioning of intermontane basins by thrust-related folding, Tien Shan, Kyrgyzstan. Basin Research 11, 75–92.

Burov, E., Francois, T., Agard, P., Le Pourhiet, L., Meyer, B., Tirel, C., Lebedev, S., Yamato, P., Brun, J.P., 2014. Rheological and geodynamic controls on the mechanisms of subduction and HP/UHP exhumation of crustal rocks during continental collision: Insights from numerical models. Tectonophysics 631, 212–250. doi:10.1016/j.tecto.2014.04.033

Burov, E.B., 2011. Rheology and strength of the lithosphere. Marine and Petroleum Geology 28, 1402–1443. doi:10.1016/j.marpetgeo.2011.05.008

Burov, E.B., Diament, M., 1995. The effective elastic thickness (Te) of continental lithosphere: What does it really mean ? Journal of Geophysical Research 100, 3905–3927.

Burtman, V.S., 2008. Nappes of the southern Tien Shan. Russian Journal of Earth Sciences 10, 1–35. doi:10.2205/2007ES000223

Buslov, M.M., De Grave, J., Bataleva, E. a V, Batalev, V.Y., 2007. Cenozoic tectonic and geodynamic evolution of the Kyrgyz Tien Shan Mountains: A review of geological, thermochronological and geophysical data. Journal of Asian Earth Sciences 29, 205–214. doi:10.1016/j.jseaes.2006.07.001

Butler, J.P., Beaumont, C., Jamieson, R. a., 2013. The Alps 1: A working geodynamic model for burial and exhumation of (ultra)high-pressure rocks in Alpine-type orogens. Earth and Planetary Science Letters 377–378, 114–131. doi:10.1016/j.epsl.2013.06.039

Butler, R.W.H., Tavarnelli, E., Grasso, M., 2006. Structural inheritance in mountain belts : An Alpine e Apennine perspective. Journal of Structural Geology 28, 1893–1908. doi:10.1016/j.jsg.2006.09.006

Calignano, E., Sokoutis, D., Willingshofer, E., Gueydan, F., Cloetingh, S., 2015a. Asymmetric vs. symmetric deep lithospheric architecture of intra-plate continental orogens. Earth and Planetary Science Letters 424, 38–50. doi:10.1016/j.epsl.2015.05.022

Calignano, E., Sokoutis, D., Willingshofer, E., Gueydan, F., Cloetingh, S., 2015b. Strain localization at the margins of strong lithospheric domains: Insights from analog models. Tectonics 34, 396–412. doi:10.1002/2014TC003756

Carter, N.L., Tsenn, M.C., 1987. Flow properties of continental lithosphere. Tectonophysics 136, 27–63.

Cawood, P.A., Kröner, A., Collins, W.J., Kusky, T.M., Mooney, W.D., Windley, B.F., 2009. Earth Accretionary systems in space and time. Geological Society of London, Special publication 318, 1–36.

Charvet, J., Shu, L.L.S., Laurent-Charvet, S., 2007. Paleozoic structural and geodynamic evolution of eastern Tianshan (NW China): welding of the Tarim and Junggar plates. Episodes 30, 162–172.

Charvet, J., Shu, L.S., Laurent-Charvet, S., Wang, B., Faure, M., Cluzel, D., Chen, Y., de Jong, K., 2011. Palaeozoic tectonic evolution of the Tianshan belt, NW China. Science China

Earth Sciences 54, 166–184. doi:10.1007/s11430-010-4138-1

Chemenda, A., Lallemand, S., Bokun, A., 2000. Strain partitioning and interplate friction in oblique subduction zones: Constraints provided by experimental modeling. Journal of Geophysical Research 105, 5567. doi:10.1029/1999JB900332

Chen, C., Lu, H., Jia, D., Cai, D., Wu, S., 1999. Closing history of the southern Tianshan oceanic basin, western China: An oblique collisional orogeny. Tectonophysics 302, 23–40. doi:10.1016/S0040-1951(98)00273-X

Chen, H.L., Yang, S.F., Li, Z.L., Yu, X., Luo, J.C., He, G.Y., Lin, X.B., Wang, Q.H., 2009. Spatial and temporal characteristics of Permian large igneous province in Tarim Basin. Xinjiang Pet. Geol. 30, 179–182.

Chen, X., Chen, H., Cheng, X., Shen, Z., Lin, X., 2015. Sedimentology and magnetostratigraphy of the Tierekesazi Cenozoic section in the foreland region of south West Tian Shan in Western China. Tectonophysics 654, 156–172. doi:10.1016/j.tecto.2015.05.009

Chenin, P., Manatschal, G., Picazo, S., Müntener, O., Karner, G., Johnson, C., Ulrich, M., 2017. Influence of the architecture of magma-poor hyperextended rifted margins on orogens produced by the closure of narrow versus wide oceans. Geosphere GES01363-1. doi:10.1130/GES01363.1

Choukroune, P., 1976. Structure et évolution tectonique de la zone nord-pyrénéenne. Analyse de la déformation dans une portion de chaîne à schistosité verticale. Mémoire de la Société géologique de France 127, Montpellier.

Choulet, F., Chen, Y., Wang, B., Faure, M., Cluzel, D., Charvet, J., Lin, W., Xu, B., 2011. Late Paleozoic paleogeographic reconstruction of Western Central Asia based upon paleomagnetic data and its geodynamic implications. Journal of Asian Earth Sciences 42, 867–884. doi:10.1016/j.jseaes.2010.07.011

Choulet, F., Faure, M., Cluzel, D., Chen, Y., Lin, W., Wang, B., 2012. From oblique accretion to transpression in the evolution of the Altaid collage: New insights from West Junggar, northwestern China. Gondwana Research 21, 530–547. doi:10.1016/j.gr.2011.07.015

Chu, X., Korenaga, J., 2012. Olivine rheology , shear stress , and grain growth in the lithospheric mantle : Geological constraints from the Kaapvaal craton. Earth and Planetary Science Letters 333–334, 52–62. doi:10.1016/j.epsl.2012.04.019

Cottle, J.M., Waters, D.J., Riley, D., Beyssac, O., Jessup, M.J., 2011. Metamorphic history of the South Tibetan Detachment System, Mt. Everest region, revealed by RSCM thermometry and phase equilibria modelling. Journal of Metamorphic Geology 29, 561–582. doi:10.1111/j.1525-1314.2011.00930.x

Culling, W.. E.. H.., 1965. Theory of Erosion on Soil-Covered Slopes. The Journal of Geology 73, 230–254.

De Boisgrollier, T., Petit, C., Fournier, M., Leturmy, P., Ringenbach, J.C., San'kov, V. a., Anisimova, S. a., Kovalenko, S.N., 2009. Palaeozoic orogeneses around the Siberian craton: Structure and evolution of the Patom belt and foredeep. Tectonics 28. doi:10.1029/2007TC002210

De Grave, J., Buslov, M.M., Van den Haute, P., 2004. Intracontinental deformation in Central Asia : distant effects of India-Eurasia convergence revealed by apatite fission-track thermochronology. Himalayan journal of Sciences 2, 121–122.

De Grave, J., Glorie, S., Buslov, M.M., Izmer, A., Fournier-Carrie, A., Batalev, V.Y., Vanhaecke, F., Elburg, M., Van den haute, P., 2011. The thermo-tectonic history of the Song-Kul plateau, Kyrgyz Tien Shan: Constraints by apatite and titanite thermochronometry and zircon U/Pb dating. Gondwana Research 20, 745–763. doi:10.1016/j.gr.2011.03.011

De Grave, J., Glorie, S., Ryabinin, a., Zhimulev, F., Buslov, M.M., Izmer, a., Elburg, M., Vanhaecke, F., Van den haute, P., 2012. Late Palaeozoic and Meso-Cenozoic tectonic evolution of the southern Kyrgyz Tien Shan: Constraints from multi-method thermochronology in the Trans-Alai, Turkestan-Alai segment and the southeastern Ferghana Basin. Journal of Asian Earth Sciences 44, 149–168. doi:10.1016/j.jseaes.2011.04.019

de Sigoyer, J., Chavagnac, V., Blichert-Toft, J., Villa, I.M., Luais, B., Guillot, S., Cosca, M., Mascle, G., 2000. Dating the Indian continental subduction and collisional thickening in the northwest Himalaya: multichronology of the Tso Morari eclogites. Geology 487–490.

Demets, C., Gordon, R.G., Argus, D.F., Stein, S., 1990. Current plate motions 71, 425–478. doi:10.1111/j.1365-246X.1990.tb06579.x

DeMets, C., Gordon, R.G., Argus, D.F., Stein, S., 1994. Effect of recent revisions to the geomagnetic reversal time scale on estimates of current plate motions. Geophysical Research Letters 21, 2191–2194.

Deng, Y., Levandowski, W., Kusky, T., 2017. Lithospheric density structure beneath the Tarim basin and surroundings, northwestern China, from the joint inversion of gravity and topography. Earth and Planetary Science Letters 460, 244–254. doi:10.1016/j.epsl.2016.10.051

Desegaulx, P., Rowe, F., Villein, A., 1990. Structural evolution of the Pyrenees : tectonic inheritance and flexural behaviour in the continental crust. Tectonophysics 182, 211–225.

Dong, Y., Zhang, G., Neubauer, F., Liu, X., Hauzenberger, C., Zhou, D., Li, W., 2011. Syn- and post-collisional granitoids in the Central Tianshan orogen: Geochemistry, geochronology and implications for tectonic evolution. Gondwana Research 20, 568–581. doi:10.1016/j.gr.2011.01.013

Dong, Y.P., Zhou, D.W., Zhang, C.L., Xia, L.Q., Xu, X.Y., Li, X.M., 2005. Tectonic setting of the Wuwamen ophiolite at the southern margin of Middle Tianshan Belt. Acta Petrologica Sinica 21, 37–44.

Dong, Y.P., Zhou, D.W., Zhang, G.W., Zhao, X., Luo, J.H., Xu, J.G., 2006. Geology and geochemistry of the Gangou ophiolitic mélange at the northern margin of the Middle Tianshan Belt. Acta Petrologica Sinica 22, 49–56.

Duretz, T., Gerya, T. V., 2013. Slab detachment during continental collision: Influence of crustal rheology and interaction with lithospheric delamination. Tectonophysics 602, 124–140. doi:10.1016/j.tecto.2012.12.024

Ekström, G., Nettles, M., Dziewonski, A.M., 2012. The global CMT project 2004 – 2010 : Centroid-moment tensors for 13,017 earthquakes. Physics of the Earth and Planetary interiors 200–201, 1–9. doi:10.1016/j.pepi.2012.04.002

England, P., Molnar, P., 1997. Active Deformation of Asia : From Kinematics to Dynamics.

Science 278, 647–650. doi:10.1126/science.278.5338.647

England, P., Molnar, P., 2005. Late Quaternary to decadal velocity fields in Asia. Journal of Geophysical Research: Solid Earth 110, 1–27. doi:10.1029/2004JB003541

Ernst, W.G., 1973. Interpretative Synthesis of Metamorphism in the Alps. Geological Society of America Bulletin 84, 2053–2078. doi:10.1130/0016-7606(1973)84<2053:ISOMIT>2.0.CO;2

Faccenda, M., Gerya, T. V., Chakraborty, S., 2008. Styles of post-subduction collisional orogeny: Influence of convergence velocity, crustal rheology and radiogenic heat production. Lithos 103, 257–287. doi:10.1016/j.lithos.2007.09.009

Flesch, L.M., Haines, A.J., Holt, W.E., 2001. Dynamics of the India-Eurasia collision zone. Journal of Geophysical Research 106, 16435–16460. doi:10.1029/2001JB000208

Furlong, K.P., Hugo, W.D., Zandt, G., 1989. Geometry and Evolution of the San Andreas Fault Zone in Northern California. Journal of Geophysical Research 94, 3100–3110.

Gao, J., Klemd, R., 2003. Formation of HP-LT rocks and their tectonic implications in the western Tianshan Orogen, NW China: Geochemical and age constraints. Lithos 66, 1–22. doi:10.1016/S0024-4937(02)00153-6

Gao, J., Li, M., Xiao, X., Tang, Y., He, G., 1998. Paleozoic tectonic evolution of the Tianshan Orogen, northwestern China. Tectonophysics 287, 213–231. doi:10.1016/S0040-1951(98)80070-X

Gao, J., Long, L., Klemd, R., Qian, Q., Liu, D., Xiong, X., Su, W., Liu, W., Wang, Y., Yang, F., 2009. Tectonic evolution of the South Tianshan orogen and adjacent regions, NW China: Geochemical and age constraints of granitoid rocks. International Journal of Earth Sciences 98, 1221–1238. doi:10.1007/s00531-008-0370-8

Ge, R., Zhu, W., Wilde, S. a., He, J., Cui, X., Wang, X., Bihai, Z., 2014. Neoproterozoic to Paleozoic long-lived accretionary orogeny in the northern Tarim Craton. Tectonics 33, 302–329. doi:10.1002/2013TC003501

Ge, R., Zhu, W., Wu, H., Zheng, B., Zhu, X., He, J., 2012. The Paleozoic northern margin of the Tarim Craton: Passive or active? Lithos 142–143, 1–15. doi:10.1016/j.lithos.2012.02.010

Gillcrist, R., Coward, M., Mugnier, J., 1987. Structural inversion and its controls: examples from the Alpine foreland and the French Alps. Geodinamica Acta 1, 5–34.

Glorie, S., De Grave, J., 2016. Exhuming the Meso-Cenozoic Kyrgyz Tianshan and Siberian Altai-Sayan: A review based on low-temperature thermochronology. Geoscience Frontiers 7, 155–170. doi:10.1016/j.gsf.2015.04.003

Glorie, S., De Grave, J., Buslov, M.M., Elburg, M. a., Stockli, D.F., Gerdes, a., Van den haute, P., 2010. Multi-method chronometric constraints on the evolution of the Northern Kyrgyz Tien Shan granitoids (Central Asian Orogenic Belt): From emplacement to exhumation. Journal of Asian Earth Sciences 38, 131–146. doi:10.1016/j.jseaes.2009.12.009

Glorie, S., De Grave, J., Buslov, M.M., Zhimulev, F.I., Stockli, D.F., Batalev, V.Y., Izmer, a., Van Den Haute, P., Vanhaecke, F., Elburg, M. a., 2011. Tectonic history of the Kyrgyz South Tien Shan (Atbashi-Inylchek) suture zone: The role of inherited structures during deformation-propagation. Tectonics 30. doi:10.1029/2011TC002949

Goetze, C., Evans, B., 1979. Stress and temperature in the bending lithosphere as constrained by experimental rock mechanics. Geophypsical Journal of the Royal Astronomical Society 59, 463–478.

Goetze, C., Evans, B., 1979. Stress and temperature in the bending lithosphere as constrained by experimental rock mechanics. Geophysical Journal International 59, 463–478. doi:10.1111/j.1365-246X.1979.tb02567.x

Goode, J.K., Burbank, D.W., Bookhagen, B., 2011. Basin width control of faulting in the Naryn Basin, south-central Kyrgyzstan. Tectonics 20. doi:10.1029/2011TC002910

Goode, J.K., Burbank, D.W., Bookhagen, B., 2011. Basin width control of faulting in the Naryn Basin, south-central Kyrgyzstan. Tectonics 30, 1–14. doi:10.1029/2011TC002910

Goode, J.K., Burbank, D.W., Ormukov, C., 2014. Pliocene-Pleistocene initiation, style, and sequencing of deformation in the central Tien Shan. Tectonics 33, 464–484. doi:10.1002/2013TC003394

Guillot, S., Garzanti, E., Baratoux, D., Marquer, D., Mahéo, G., De Sigoyer, J., 2003. Reconstructing the total shortening history of the NW Himalaya. Geochemistry, Geophysics, Geosystems 4. doi:10.1029/2002GC000484

Guo, J., Shu, L., Charvet, J., Laurent Charvet, S., Sun, S., 2002. Geochemical features of the two early paleozoic ophiolitic zones and volcanic rocks in the central-southern Tianshan Region, Xinjiang. Chinese Journal of Geochemistry 21, 308–321. doi:10.1007/BF02831532

Hacker, B.R., Kelemen, P.B., Behn, M.D., 2011. Differentiation of the continental crust by relamination. Earth and Planetary Science Letters 307, 501–516. doi:10.1016/j.epsl.2011.05.024

Han, B.F., He, G.Q., Wang, X.C., Guo, Z.J., 2011. Late Carboniferous collision between the Tarim and Kazakhstan-Yili terranes in the western segment of the South Tian Shan Orogen, Central Asia, and implications for the Northern Xinjiang, western China. Earth-Science Reviews 109, 74–93. doi:10.1016/j.earscirev.2011.09.001

Hegner, E., Klemd, R., Kröner, a., Corsini, M., Alexeiev, D. V., Iaccheri, L.M., Zack, T., Dulski, P., Xia, X., Windley, B.F., 2010. Mineral ages and p-t conditions of late paleozoic high-pressure eclogite and provenance of mélange sediments from atbashi in the south tianshan orogen of kyrgyzstan. American Journal of Science 310, 916–950. doi:10.2475/09.2010.07

Heron, P.J., Pysklywec, R.N., 2016. Inherited structure and coupled crust-mantle lithosphere evolution: Numerical models of Central Australia. Geophysical Research Letters 43, 4962–4970. doi:10.1002/2016GL068562

Heron, P.J., Pysklywec, R.N., Stephenson, R., 2016a. Identifying mantle lithosphere inheritance in controlling intraplate orogenesis. Journal of Geophysical Research: Solid Earth 121, 6966–6987. doi:10.1002/2016JB013460

Heron, P.J., Pysklywec, R.N., Stephenson, R., 2016b. Lasting mantle scars lead to perennial plate tectonics. Nature Communications 7, 1–7. doi:10.1038/ncomms11834

Hirth, G., Kohlstedt, D.L., 1996. Water in the oceanic upper mantle: implications for rheology, melt extraction and the evolution of the lithosphere. Earth and Planetary Science Letters 144, 93–108. doi:10.1016/0012-821X(96)00154-9

Huang, J., Zhao, D., 2006. High-resolution mantle tomography of China and surrounding regions. Journal of Geophysical Research: Solid Earth 111, 1–21. doi:10.1029/2005JB004066

Isaks, B.L., 1988. Uplift of the Central Andean Plateau and bending of the Bolivian orocline. Journal of Geophysical Research 93, 3211–3231. doi:10.1029/JB093iB04p03211

Jammes, S., Huismans, R.S., 2012. Structural styles of mountain building: Controls of lithospheric rheologic stratification and extensional inheritance. Journal of Geophysical Research: Solid Earth 117, 1–22. doi:10.1029/2012JB009376

Jammes, S., Huismans, R.S., Mu, J.A., 2014. Lateral variation in structural style of mountain building : controls of rheological and rift inheritance. Terra Nova 26, 201–207. doi:10.1111/ter.12087

Jolivet, L., Brun, J.P., 2010. Cenozoic geodynamic evolution of the Aegean. International Journal of Earth Sciences 99, 109–138. doi:10.1007/s00531-008-0366-4

Jolivet, M., Dominguez, S., Charreau, J., Chen, Y., Li, Y., Wang, Q., 2010. Mesozoic and Cenozoic tectonic history of the central Chinese Tian Shan: Reactivated tectonic structures and active deformation. Tectonics 29. doi:10.1029/2010TC002712

Jolivet, M., Heilbronn, G., Robin, C., Barrier, L., Bourquin, S., Guo, Z., Jia, Y., Guerit, L., Yang, W., Fu, B., 2013. Reconstructing the Late Palaeozoic - Mesozoic topographic evolution of the Chinese Tian Shan: Available data and remaining uncertainties. Advances in Geosciences 37, 7–18. doi:10.5194/adgeo-37-7-2013

Jong, K. De, Wang, B., Faure, M., Shu, L., Cluzel, D., Charvet, J., Ruffet, G., Chen, Y., 2009. New 40 Ar / 39 Ar age constraints on the Late Palaeozoic tectonic evolution of the western Tianshan (Xinjiang , northwestern China), with emphasis on Permian fluid ingress. International Journal of Earth Sciences 98, 1239–1258. doi:10.1007/s00531-008-0338-8

Jourdon, A., Petit, C., Rolland, Y., Loury, C., Bellahsen, N., Guillot, S., Le Pourhiet, L., Ganino, C., 2017. New structural data on Late Paleozoic tectonics in the Kyrgyz Tien Shan (Central Asian Orogenic Belt). Gondwana Research 46, 57–78. doi:10.1016/j.gr.2017.03.004

Jourdon, A., Rolland, Y., Petit, C., Bellahsen, N., 2014. Style of Alpine tectonic deformation in the Castellane fold-and-thrust belt (SW Alps, France): Insights from balanced cross-sections. Tectonophysics 633, 143–155. doi:10.1016/j.tecto.2014.06.022

Jukov, Y. V., Zakharov, I.L., Berezanskyi, A.V., Izraileva, R.M., 2008. Geological map of the Kyrgyz Republic 1:500 000.

Karpovitch, E.., Kolesnikov, V.A., Lunev, V.P., 1964. Geological map of the former USSR, 1:200 000 sheets. Alay-Kokshaal series K-43-XXVIII.

Keselev, V.V., Zhukov, Y.V., Israileva, R.M., Komarevstev, V.T., Tsyganok, E.N., 1982. Radiological Evidence for the Grenville Tectono-Magmatic Stage in the Northern Tianshan. Izvestiya Academy of Sciences of the Kyrgyz SSR 6, 26–30 (in Russian).

Kiselev, V. V., Apayarov, F.K., Komartsev, V.T., Tsyganok, E.N., Lukashova, E.M., 1993. Isotopic ages of zircons from crystalline complexes of the Tianshan, in: Kozakov, I.K. (Ed.), Early Precambrian of the Central Asia Folded Belt. St. Petersbourg, pp. 99–115.

Klemd, R., Gao, J., Li, J., Meyer, M., 2014. Metamorphic evolution of (ultra) -high-pressure subduction-related transient crust in the South Tianshan Orogen (Central Asian Orogenic Belt): Geodynamic implications. Gondwana Research. doi:10.1016/j.gr.2014.11.008

Kong, X., Bird, P., 1996. Neotectonics of Asia: Thin-shell finite-element models with faults, in: Yin, A., Harrison, T.M. (Eds.), Tectonic Evolution of Asia. Cambridge University Press, New York, pp. 18–34.

Konopelko, D., Biske, G., Seltmann, R., Eklund, O., Belyatsky, B., 2007. Hercynian post-collisional A-type granites of the Kokshaal Range, Southern Tien Shan, Kyrgyzstan. Lithos 97, 140–160. doi:10.1016/j.lithos.2006.12.005

Konopelko, D., Biske, G., Seltmann, R., Kiseleva, M., Matukov, D., Sergeev, S., 2008. Deciphering Caledonian events: Timing and geochemistry of the Caledonian magmatic arc in the Kyrgyz Tien Shan. Journal of Asian Earth Sciences 32, 131–141. doi:10.1016/j.jseaes.2007.10.017

Konopelko, D., Seltmann, R., Apayarov, F., Belousova, E., Izokh, a., Lepekhina, E., 2013. U-Pb-Hf zircon study of two mylonitic granite complexes in the Talas-Fergana fault zone, Kyrgyzstan, and Ar-Ar age of deformations along the fault. Journal of Asian Earth Sciences 73, 334–346. doi:10.1016/j.jseaes.2013.04.046

Konopelko, D., Seltmann, R., Biske, G., Lepekhina, E., Sergeev, S., 2009. Possible source dichotomy of contemporaneous post-collisional barren I-type versus tin-bearing A-type granites , lying on opposite sides of the South Tien Shan suture. Ore Geology Reviews 35, 206–216. doi:10.1016/j.oregeorev.2009.01.002

Kreemer, C., Holt, W.E., Haines, A.J., 2003. An integrated global model of present-day plate motions and plate boundary deformation. Geophysical Journal International 154, 8–34. doi:10.1046/j.1365-246X.2003.01917.x

Kröner, a., Alexeiev, D. V., Hegner, E., Rojas-Agramonte, Y., Corsini, M., Chao, Y., Wong, J., Windley, B.F., Liu, D., Tretyakov, a. a., 2012a. Zircon and muscovite ages, geochemistry, and Nd-Hf isotopes for the Aktyuz metamorphic terrane: Evidence for an Early Ordovician collisional belt in the northern Tianshan of Kyrgyzstan. Gondwana Research 21, 901–927. doi:10.1016/j.gr.2011.05.010

Kröner, a., Alexeiev, D. V., Hegner, E., Rojas-Agramonte, Y., Corsini, M., Chao, Y., Wong, J., Windley, B.F., Liu, D., Tretyakov, a. a., 2012b. Zircon and muscovite ages, geochemistry, and Nd-Hf isotopes for the Aktyuz metamorphic terrane: Evidence for an Early Ordovician collisional belt in the northern Tianshan of Kyrgyzstan. Gondwana Research 21, 901–927. doi:10.1016/j.gr.2011.05.010

Kröner, a., Alexeiev, D. V., Rojas-Agramonte, Y., Hegner, E., Wong, J., Xia, X., Belousova, E., Mikolaichuk, a. V., Seltmann, R., Liu, D., Kiselev, V. V., 2013. Mesoproterozoic (Grenville-age) terranes in the Kyrgyz North Tianshan: Zircon ages and Nd-Hf isotopic constraints on the origin and evolution of basement blocks in the southern Central Asian Orogen. Gondwana Research 23, 272–295. doi:10.1016/j.gr.2012.05.004

Kröner, a., Kovach, V., Belousova, E., Hegner, E., Armstrong, R., Dolgopolova, a., Seltmann, R., Alexeiev, D. V., Hoffmann, J.E., Wong, J., Sun, M., Cai, K., Wang, T., Tong, Y., Wilde, S. a., Degtyarev, K.E., Rytsk, E., 2014. Reassessment of continental growth during the accretionary history of the Central Asian Orogenic Belt. Gondwana Research 25, 103–125. doi:10.1016/j.gr.2012.12.023

Kusky, T.M., 2011. Geophysical and geological tests of tectonic models of the North China

Craton. Gondwana Research 20, 26–35. doi:10.1016/j.gr.2011.01.004

Lafosse, M., Boutoux, A., Bellahsen, N., Le Pourhiet, L., 2016. Role of tectonic burial and temperature on the inversion of inherited extensional basins during collision. Geological Magazine 153, 811–826. doi:10.1017/S0016756816000510

Lasovski, A.G., Mozolev, N., 1960. Geological map of the former USSR, 1:200 000 sheets. North-Tien-Shan series, K-43-XXII.

Laurent-Charvet, S., 2001. Accrétions continentales en Asie évolution géodynamique et structurale du Tianshan et du Junggar oriental (nord-ouest Chine) au Paléozoïque. Université d'Orléans, France.

Laurent-Charvet, S., Charvet, J., Monié, P., Shu, L., 2003. Late Paleozoic strike-slip shear zones in eastern central Asia (NW China): New structural and geochronological data. Tectonics 22, 1009. doi:10.1029/2001TC901047

Laurent-Charvet, S., Charvet, J., Shu, L., Ma, R., Lu, H., 2002. Palaeozoic late collisional strike-slip deformations in Tianshan and Altay, Eastern Xinjiang, NW China. Terra Nova 14, 249–256. doi:10.1046/j.1365-3121.2002.00417.x

Lavier, L., Buck, W.R., Poliakov, A.N., 1999. Self-consistent rolling-hinge model for the evolution of large-offset low-angle normal faults. Geology 27, 1127–1130.

Le Fort, P., 1975. Himalayas: the collided range. Present knowledge of the continental arc. American Journal of Science 275, 44.

Le Pourhiet, L., Burov, E., Moretti, I., 2004. Rifting through a stack of inhomogeneous thrusts (the dipping pie concept). Tectonics 23, 1–16. doi:10.1029/2003TC001584

Le Pourhiet, L., May, D.A., Huille, L., Watremez, L., Leroy, S., 2017. A Genetic Link Between Transform and Hyper-Extended Margins. Earth and Planetary Science Letters. doi:10.1016/j.epsl.2017.02.043

Lei, J., Zhao, D., 2007. Teleseismic P-wave tomography and the upper mantle structure of the central Tien Shan orogenic belt. Physics of the Earth and Planetary Interiors 162, 165–185. doi:10.1016/j.pepi.2007.04.010

Lei, R.X., Wu, C.Z., Gu, L.X., Zhang, Z.Z., Chi, G.X., Jiang, Y.H., 2011. Zircon u-pb chronology and hf isotope of the xingxingxia granodiorite from the central tianshan zone (nw china): Implications for the tectonic evolution of the southern altaids. Gondwana Research 20, 582–593. doi:10.1016/j.gr.2011.02.010

Lemoine, M., Cnrs, L.D.G.S.U.A., Bas, T., Arnaud-vanneau, A., Arnaud, H., Cnrs, I.D.U.A., 1986. The continental margin of the Mesozoic Tethys in the Western Alps. Marine and Petroleum Geology 3, 179–199.

Li, Q.L., Lin, W., Su, W., Li, X.H., Shi, Y.H., Liu, Y., Tang, G.Q., 2011. SIMS U-Pb rutile age of low-temperature eclogites from southwestern Chinese Tianshan, NW China. Lithos 122, 76–86. doi:10.1016/j.lithos.2010.11.007

Li, Z.H., Xu, Z.Q., Gerya, T. V., 2011. Flat versus steep subduction: Contrasting modes for the formation and exhumation of high- to ultrahigh-pressure rocks in continental collision zones. Earth and Planetary Science Letters 301, 65–77. doi:10.1016/j.epsl.2010.10.014

Lin, W., Chu, Y., Ji, W.B., Zhang, Z.P., Shi, Y.H., Wang, Z.Y., Li, Z., Wang, Q.C., 2013. Geochronological and geochemical constraints for a middle Paleozoic continental arc on the northern margin of the Tarim block: Implications for the Paleozoic tectonic evolution of the South Chinese Tianshan. Lithosphere 5, 355–381.

Lin, W., Faure, M., Shi, Y., Wang, Q., Li, Z., 2009. Palaeozoic tectonics of the south-western Chinese Tianshan: New insights from a structural study of the high-pressure/low-temperature metamorphic belt. International Journal of Earth Sciences 98, 1259–1274. doi:10.1007/s00531-008-0371-7

Liu, X., Su, W., Gao, J., Li, J., Jiang, T., Zhang, X., Ge, X., 2014. Lithos Paleozoic subduction erosion involving accretionary wedge sediments in the South Tianshan Orogen : Evidence from geochronological and geochemical studies on eclogites and their host metasediments. LITHOS 210–211, 89–110. doi:10.1016/j.lithos.2014.09.017

Lomize, M.G., Demina, L.I., Zarshchicov, A.V., 1997. The Kyrgyz–Terskei paleoceanic basin in the Tien Shan. Geotectonics (in Russian with english abstract) 30, 463–482.

Loury, C., 2016. Evolution géodynamique du Tien-Shan (Ceinture Orogénique d'Asie Centrale) au Paléozoïque et réactivation tectonique. Université de Nice-Sophia Antipolis.

Loury, C., Rolland, Y., Cenki-Tok, B., Lanari, P., Guillot, S., 2015a. Late Paleozoic evolution of the South Tien Shan : Insights from P-T estimates and allanite geochronology on retrogressed eclogites. Journal of Geodynamics. doi:10.1016/j.jog.2015.06.005

Loury, C., Rolland, Y., Guillot, S., Mikolaichuk, A. V, Lanari, P., Bruguier, O., Bosch, D., 2015b. Crustal-scale structure of South Tien Shan : implications for subduction polarity and Cenozoic reactivation. Geological Society of London, Special publication 427. doi:10.1144/SP427.4

Ma, R., Wang, C., Ye, S., 1993. Tectonic framework and crustal evolutional of Eastern Tianshan mountains. Publishing House of Nanjing University, Nanjing 1–225 (in Chinese with english abstract).

Macaulay, E. a., Sobel, E.R., Mikolaichuk, A., Kohn, B., Stuart, F.M., 2014. Cenozoic deformation and exhumation history of the Central Kyrgyz Tien Shan. Tectonics 33, 135–165. doi:10.1002/2013TC003376

Macaulay, E. a., Sobel, E.R., Mikolaichuk, A., Landgraf, A., Kohn, B., Stuart, F., 2013. Thermochronologic insight into late Cenozoic deformation in the basement-cored Terskey Range, Kyrgyz Tien Shan. Tectonics 32, 487–500. doi:10.1002/tect.20040

Makarov, V.I., Alekseev, D. V., Batalev, V.Y., Bataleva, E. a., Belyaev, I. V., Bragin, V.D., Dergunov, N.T., Efimova, N.N., Leonov, M.G., Munirova, L.M., Pavlenkin, a. D., Roecker, S., Roslov, Y. V., Rybin, a. K., Shchelochkov, G.G., 2010. Underthrusting of Tarim beneath the Tien Shan and deep structure of their junction zone: Main results of seismic experiment along MANAS Profile Kashgar-Song-Köl. Geotectonics 44, 102–126. doi:10.1134/S0016852110020020

Maksumova, R.A., Dzhenchuraeva, A.V., Berezanskii, A.V., 2001. Structure and evolution of the Tien Shan nappe-folded orogen. Russian Geology and Geophysics 42, 1367–1374.

May, D.A., Brown, J., Le Pourhiet, L., 2014. pTatin3D : High-Performance Methods for Long-Term Lithospheric Dynamics, in: Proceeding SC'14 Proceedings of the International Conference for High Performance Computing, Networking, Storage and Analysis. pp. 274–284. doi:10.1109/SC.2014.28

May, D.A., Brown, J., Le Pourhiet, L., 2015. A scalable , matrix-free multigrid preconditioner for finite element discretizations of heterogeneous Stokes flow. Computer Methods in Applied Mechanics Engineering 290, 496–523. doi:10.1016/j.cma.2015.03.014

Metivier, F., Gaudemer, Y., 1996. Mass transfer between eastern Tien Shan and adjacent basins (central Asia): constraints on regional tectonics and topography. Geophysical Journal International 128, 1–17.

Mezri, L., Le Pourhiet, L., Wolf, S., Burov, E., 2015. New parametric implementation of metamorphic reactions limited by water content, impact on exhumation along detachment faults. Lithos 236–237, 287–298. doi:10.1016/j.lithos.2015.08.021

Mikhailova, N., Mukambayev, A.S., Aristova, I.L., Kulikova, G., Ullah, S., Pilz, M., Bindi, D., 2015a. Central Asia earthquake catalogue from ancient time to 2009. Annals of geophysics 58, S0102. doi:10.4401/ag-6681

Mikhailova, N., Poleshko, N.N., Aristova, I.L., Mukambayev, A.S., Kulikova, G.O., 2015b. EMCA Central Asia Earthquake catalogue v1.0 (EMCA_seismocatv1.0). GFZ German Research Center for Geosciences. doi:http://doi.org/10.5880/GFZ.EWS.2015.001

Mikolaichuk, A., Kurenkov, K.E., Degtyarev, V., Rubetsov, V.I., 1997. Northern Tien Shan main stages of geodynamic evolution in the Late-Precambrian-Early Paleozoic. Geodynamics 6, 16–34.

Mikolaichuk, a. V., Apayarov, F.K., Buchroithner, M.F., Chernavskaja, Z.I., Skrinnik, L.I., Ghes, M.D., Neyevin, a. V., Charimov, T. a., 2008. Geological Map of Khan Tengri Massif. Geomap.Flameweb.Org.

Molnar, P., Tapponnier, P., 1975. Cenozoic Tectonics of Asia: Effects of a Continental Collision: Features of recent continental tectonics in Asia can be interpreted as results of the India-Eurasia collision. Science (New York, N.Y.) 189, 419–426. doi:10.1126/science.189.4201.419

Molnar, P., Tapponnier, P., 1981. A possible dependence of tectonic strength on the age of the crust in Asia. Earth and Planetary Science Letters 52, 107–114. doi:10.1016/0012-821X(81)90213-2

Nicholson, C., Sorlien, C.C., Atwater, T., Crowell, J.C., Luyendyk, B.P., 1994. Microplate capture, rotation of the western Transverse Ranges, and initiation of the San Andreas transform as a low-angle fault system. Geology 22, 491–495.

Nikolaev, V.A., 1933. About principal structure line of Tianshan. Proceedings of All-Russian Mineralogical Society 62, 347–354 (in Russian).

Osmonbetov, K.O., Knauf, V.I., Korolev, V.G., 1982. Stratified and intrusive formations of Kyrgyzstan, Illim Pres. ed. Frunze.

Patriat, P., Achache, J., 1984. India-Eurasia collision chronology has implications for crustal shortening and driving mechanisms of plates. Nature 311, 615–621.

Pili, E., Ricard, Y., Lardeaux, J., Sheppard, S.M.F., 1997. Lithospheric shear zones and mantle-crust connections. Tectonophysics 280, 15–29.

Qian, Q., Gao, J., Klemd, R., He, G., Song, B., Liu, D., Xu, R., 2009. Early Paleozoic tectonic evolution of the Chinese South Tianshan Orogen: Constraints from SHRIMP zircon U-Pb geochronology and geochemistry of basaltic and dioritic rocks from Xiate, NW China. International Journal of Earth Sciences 98, 551–569. doi:10.1007/s00531-007-0268-x

Rahl, J.M., Anderson, K.M., Brandon, M.T., Fassoulas, C., 2005. Raman spectroscopic carbonaceous material thermometry of low-grade metamorphic rocks: Calibration and application to tectonic exhumation in Crete, Greece. Earth and Planetary Science Letters 240, 339–354. doi:10.1016/j.epsl.2005.09.055

Ranalli, G., 2000. Rheology of the crust and its role in tectonic reactivation. Journal of Geodynamics 30, 3–15.

Ranalli, G., Murphy, D.E., 1987. Rheological stratification of the lithosphere. Tectonophysics 132, 281–295.

Rayleigh, Lord, 1916. LIX. On convection currents in a horizontal layer of fluid, when the higher temperature is on the under side. Philosophical Magazine Series 6 32, 529–546. doi:10.1080/14786441608635602

Renne, P.R., Basu, A.R., 1991. Rapid Eruption of the Siberian Traps Flood Basalts at the Permo-Triassic Boundary. Science 253, 176–179.

Roecker, S., 2001. Constraints on the crust and upper mantle of the Kyrgyz Tien Shan from the preliminary analysis of GHENGIS broad-band seismic data. Russian Geology and Geophysics 42, 1554–1565.

Rojas-Agramonte, Y., Herwartz, D., García-Casco, A., Kröner, A., Alexeiev, D. V., Klemd, R., Buhre, S., Barth, M., 2013. Early Palaeozoic deep subduction of continental crust in the Kyrgyz North Tianshan: Evidence from Lu-Hf garnet geochronology and petrology of mafic dikes. Contributions to Mineralogy and Petrology 166, 525–543. doi:10.1007/s00410-013-0889-y

Rolland, Y., Alexeiev, D. V., Kröner, A., Corsini, M., Loury, C., Monié, P., 2013. Late Palaeozoic to Mesozoic kinematic history of the Talas-Ferghana strike-slip fault (Kyrgyz West Tianshan) as revealed by 40Ar/39Ar dating of syn-kinematic white mica. Journal of Asian Earth Sciences 67–68, 76–92. doi:10.1016/j.jseaes.2013.02.012

Rolland, Y., Perincek, D., Kaymakci, N., Sosson, M., Barrier, E., Avagyan, A., 2012. Evidence for ~80-75Ma subduction jump during Anatolide-Tauride-Armenian block accretion and ~48Ma Arabia-Eurasia collision in Lesser Caucasus-East Anatolia. Journal of Geodynamics 56–57, 76–85. doi:10.1016/j.jog.2011.08.006

Rovetta, M.R., Blacic, J.D., Delaney, J.R., 1987. Microfracture and Crack Healing in Experimentally Deformed Peridotite. Journal of Geophysical Research 92, 902–910.

Rudnick, R.L., Fountain, D.M., 1995. Nature and composition of the continental crust: A lower crustal perspective. Reviews of Geophysics 33, 267–309.

Saliot, P., 1978. Le métamorphisme dans les Alpes françaises. Université Paris-Sud.

Saunders, A.D., England, R.W., Reichow, M.K., White, R. V, 2005. A mantle plume origin for the Siberian traps : uplift and extension in the West Siberian Basin , Russia. Lithos 79, 407–424. doi:10.1016/j.lithos.2004.09.010

Seltmann, R., Konopelko, D., Biske, G., Divaev, F., Sergeev, S., 2011. Hercynian post-collisional magmatism in the context of Paleozoic magmatic evolution of the Tien Shan orogenic belt. Journal of Asian Earth Sciences 42, 821–838. doi:10.1016/j.jseaes.2010.08.016

Şengör, a. M.C., Natal'in, B. a., Burtman, V.S., 1993. Evolution of the Altaid tectonic collage and Palaeozoic crustal growth in Eurasia. Nature 364, 299–307. doi:10.1038/364299a0

Sengör, C., 1984. The Cimmeride orogenic system and the tectonics of Eurasia. Geological Society of America Sepcial Paper 82.

Shea, W.T., Kronenberg, A.K., 1992. Rheology and Deformation Mechanisms of an Isotropic Mica Schist. Journal of Geophysical Research 97, 15,201-15,237. doi:92JB00620.0148-0227/92/92JB-00620

Simonov, V. a., Sakiev, K.S., Volkova, N.I., Stupakov, S.I., Travin, a. V., 2008. Conditions of formation of the Atbashi Ridge eclogites (South Tien Shan). Russian Geology and Geophysics 49, 803–815. doi:10.1016/j.rgg.2008.04.001

Sobel, E.R., Arnaud, N., 2000. Cretaceous – Paleogene basaltic rocks of the Tuyon basin , NW China and the Kyrgyz Tian Shan : the trace of a small plume. Lithos 50, 191–215.

Sobel, E.R., Chen, J., Heermance, R. V., 2006. Late Oligocene-Early Miocene initiation of shortening in the Southwestern Chinese Tian Shan: Implications for Neogene shortening rate variations. Earth and Planetary Science Letters 247, 70–81.

Sobel, E.R., Dumitru, T.A., 1997. Exhumation of the margins of the western Tarim basin during the Himalayan orogeny. Journal of Geophysical Research 102, 5043–5064.

Sternai, P., Avouac, J.P., Jolivet, L., Faccenna, C., Gerya, T., Becker, T.W., Menant, A., 2016. On the influence of the asthenospheric flow on the tectonics and topography at a collision-subduction transition zones: Comparison with the eastern Tibetan margin. Journal of Geodynamics 100, 184–197. doi:10.1016/j.jog.2016.02.009

Stüwe, K., White, L., Brown, R., 1994. The influence of eroding topography on steady-state isotherms. Application to fission track analysis. Earth and Planetary Science Letters 124, 63–74. doi:10.1016/0012-821X(94)00068-9

Su, W., Gao, J., Klemd, R., Li, J.-L., Zhang, X., Li, X.-H., Chen, N.-S., Zhang, L., 2010. U–Pb zircon geochronology of Tianshan eclogites in NW China: implication for the collision between the Yili and Tarim blocks of the southwestern Altaids. European Journal of Mineralogy 22, 473–478. doi:10.1127/0935-1221/2010/0022-2040

Tagiri, M., Yano, T., Bakirov, A., Nakajima, T., Uchiumi, S., 1995. Mineral parageneses and metamorphic P-T paths of ultrahigh-pressure eclogites from Kyrghyzstan Tien-Shan. The Island Arc 4, 280–292.

Tapponnier, P., Peltzer, G., Armijo, R., 1986. On the mechanics of the collision between India and Asia. Geological Society of London, Special publication 19, 115–157.

Tavarnelli, E., 1998. Tectonic evolution of the Northern Salinian Block, California, USA: Paleogene to Recent shortening in a transform fault-bounded continental fragment. Geological Society of London, Special publication 35, 107–118. doi:10/1144/GSL.SP.1998.135.01.07

Taylor, S.R., Mclennan, S.M., 1995. The geochemical evolution of the continental crust. Reviews of Geophysics 33, 241–265.

Thompson, S.C., Weldon, R.J., Rubin, C.M., Abdrakhmatov, K., Molnar, P., Berger, G.W., 2002. Late Quaternary slip rates across the central Tien Shan, Kyrgyzstan, Central Asia. Journal of Geophysical Research 107, 2203. doi:10.1029/2001LB000596

Tian, Z.L., Wei, C.J., 2013. Metamorphism of ultrahigh-pressure eclogites from the Kebuerte

Valley, South Tianshan, NW China: Phase equilibria and P-T path. Journal of Metamorphic Geology 31, 281–300. doi:10.1111/jmg.12021

Toussaint, G., Burov, E., Avouac, J.P., 2005. Tectonic evolution of a continental collision zone : A thermomechanical numerical model. Tectonics 23, 1–24. doi:10.1029/2003TC001604

Tucker, G.E., Slingerland, R., 1996. Predicting sediment flux from fold and thrust belts. Basin Research 8, 329–349. doi:10.1046/j.1365-2117.1996.00238.x

Turcotte, D.L., Schubert, G., 2014. Geodynamics, Second Edi. ed. Cambridge University Press, Cambridge.

Vacherat, A., Mouthereau, F., Pik, R., Bernet, M., Gautheron, C., Masini, E., Le Pourhiet, L., Tibari, B., Lahfid, A., 2014. Thermal imprint of rift-related processes in orogens as recorded in the Pyrenees. Earth and Planetary Science Letters 408, 296–306. doi:10.1016/j.epsl.2014.10.014

Van Wijk, J.W., 2005. Role of weak zone orientation in continental lithosphere extension. Geophysical Research Letters 32, 1–4. doi:10.1029/2004GL022192

Vanderhaeghe, O., 2012. The thermal-mechanical evolution of crustal orogenic belts at convergent plate boundaries: A reappraisal of the orogenic cycle. Journal of Geodynamics 56–57, 124–145. doi:10.1016/j.jog.2011.10.004

Vassallo, R., Jolivet, M., Ritz, J.F., Braucher, R., Larroque, C., Sue, C., Todbileg, M., Javkhlanbold, D., 2007. Uplift age and rates of the Gurvan Bogd system (Gobi-Altay) by apatite fission track analysis. Earth and Planetary Science Letters 259, 333–346. doi:10.1016/j.epsl.2007.04.047

Velasque, P.C.I., Ducasse, L., Muller, J., Olten, R.S.C., 1989. The influence of inherited extensional structures on the tectonic evolution of an intracratonic chain : the example of the Western Pyrenees and. Tectonophysics 162, 243–264.

Vergnolle, M., Calais, E., Dong, L., 2007. Dynamics of continental deformation in Asia. Journal of Geophysical Research: Solid Earth 112, 1–22. doi:10.1029/2006JB004807

Vinnik, L.P., Reigber, C., Aleshin, I.M., Kosarev, G.L., Kaban, M.K., Oreshin, S.I., Roecker, S.W., 2004. Receiver function tomography of the central Tien Shan. Earth and Planetary Science Letters 225, 131–146. doi:10.1016/j.epsl.2004.05.039

Vissers, R.L.M., Drury, M.R., Hoogerduijn Strating, E.H., Spiers, C.J., Van Der Wal, D., 1995. Mantle shear zones and their effect on lithosphere strength during continental breakup. Tectonophysics 249, 155–171.

von Tscharner, M., Schmalholz, S.M., Epard, J.L., 2016. 3-D numerical models of viscous flow applied to fold nappes and the Rawil depression in the Helvetic nappe system (western Switzerland). Journal of Structural Geology 86, 32–46. doi:10.1016/j.jsg.2016.02.007

Wagner, G.A., 1968. Fission track dating of apatites. Earth and Planetary Science Letters 4, 411–415. doi:10.1016/0012-821X(68)90072-1

Wang, B., Chen, Y., Zhan, S., Shu, L., Faure, M., Cluzel, D., Charvet, J., Laurent-charvet, S., 2007a. Primary Carboniferous and Permian paleomagnetic results from the Yili Block (NW China) and their implications on the geodynamic evolution of Chinese Tianshan Belt. Earth and Planetary Science Letters 263, 288–308. doi:10.1016/j.epsl.2007.08.037

Wang, B., Cluzel, D., Jahn, B., Shu, L., Chen, Y.A.N., Zhai, Y., Branquet, Y., Barbanson, L., Sizaret, S., 2014. Late Paleozoic Pre- and Syn-kinematic Plutons of the Kangguer-Huangshan Shear Zone; Inference on the Tectonic Evolution of the Eastern Chinese North Tianshan. American Journal of Science 314, 43–79. doi:10.2475/03.2014.00

Wang, B., Cluzel, D., Shu, L., Faure, M., Charvet, J., Chen, Y., Meffre, S., de Jong, K., 2009. Evolution of calc-alkaline to alkaline magmatism through Carboniferous convergence to Permian transcurrent tectonics, western Chinese Tianshan. International Journal of Earth Sciences 98, 1275–1298. doi:10.1007/s00531-008-0408-y

Wang, B., Faure, M., Shu, L., Cluzel, D., Charvet, J., De Jong, K., Chen, Y., 2008. Paleozoic tectonic evolution of the Yili Block, western Chinese Tianshan. Bulletin de la Societe Geologique de France 179, 483–490. doi:10.2113/gssgfbull.179.5.483

Wang, B., Faure, M., Shu, L., Jong, K. De, Charvet, J., Cluzel, D., Jahn, B., Chen, Y., Ruffet, G., The, S., January, N., Wang, B., Faure, M., Shu, L., Jong, K. De, Charvet, J., Cluzel, D., Jahn, B., Chen, Y., Ruffet, G., 2010. Structural and Geochronological Study of High - Pressure Metamorphic Rocks in the Kekesu Section (Northwestern China): Implications for the Late Paleozoic Tectonics of the Southern Tianshan Structural and Geochronological Study of High-Pressure Metamorp. Journal of Geology 118, 59–77. doi:10.1086/648531

Wang, B., Shu, L., Faure, M., Jahn, B.M., Cluzel, D., Charvet, J., Chung, S.L., Meffre, S., 2011. Paleozoic tectonics of the southern Chinese Tianshan: Insights from structural, chronological and geochemical studies of the Heiyingshan ophiolitic mélange (NW China). Tectonophysics 497, 85–104. doi:10.1016/j.tecto.2010.11.004

Wang, B., Shu, L.S., Cluzel, D., Faure, M., Charvet, J., 2007b. Geochemical constraints on Carboniferous volcanic rocks of the Yili Block (Xinjiang, NW China): Implication for the tectonic evolution of Western Tianshan. Journal of Asian Earth Sciences 29, 148–159. doi:10.1016/j.jseaes.2006.02.008

Wang, B., Zhai, Y., Shu, L., Liu, H., 2016. Diachronous evolution of back-arc oceanic basins in the South Chinese Tianshan : insights for Paleozoic accretionary tectonics of SW Central Asian Orogenic Belt. The Geological Society of America Bulletin.

Wang, Q., Shu, L., Charvet, J., Faure, M., Ma, H., Gao, J., Kroner, A., Xiao, W., Li, J., Windley, B., Chen, Y., Glen, R., Jian, P., Zhang, W., Seltmann, R., Wilde, S., Choulet, F., Wan, B., Quinn, C., Rojas-agramonte, Y., Shang, Q., Zhang, W., 2010. Understanding and study perspectives on tectonic evolution and crustal structure of the Paleozoic Chinese Tianshan. Episodes 242–247.

Wang, Q.M., Nishidai, T., Coward, M.P., 1992. The Tarim Basin, NW China: Formation and aspects of petroleum geology. Journal of Petroleum Geology 15, 5–34.

Wang, W., Qiao, X., Yang, S., Wang, D., 2016. Present-day velocity field and block kinematics of Tibetan Plateau from GPS measurements. Geophysical Journal International 1088–1102. doi:10.1093/gji/ggw445

Warren, C.J., Beaumont, C., Jamieson, R. a., 2008. Modelling tectonic styles and ultra-high pressure (UHP) rock exhumation during the transition from oceanic subduction to continental collision. Earth and Planetary Science Letters 267, 129–145. doi:10.1016/j.epsl.2007.11.025

Wei, X., Xu, Y., Feng, Y., Zhao, J., 2014. Plume-lithosphere interaction in the generation of the Tarim Large Igneous Province, NW China: Geochronological and geochemical constraints. American Journal of Science 314, 314–356. doi:10.2475/01.2014.09

Wessel, P., Smith, W.H.F., Scharroo, R., Luis, J.F., Wobbe, F., 2013. Generic Mapping Tools: Improved version released. EOS Trans. AGU 94, 409–410.

Whipple, K.X., 2009. The influence of climate on the tectonic evolution of mountain belts. Nature Geoscience 2, 730–730. doi:10.1038/ngeo638

Wilhem, C., Windley, B.F., Stampfli, G.M., 2012. The Altaids of Central Asia: A tectonic and evolutionary innovative review. Earth-Science Reviews 113, 303–341. doi:10.1016/j.earscirev.2012.04.001

Willett, S.D., 1999. Orogeny and orography: The effects of erosion on the structure of mountain belts. Journal of Geophysical Research 104, 28957. doi:10.1029/1999JB900248

Windley, B.F., Alexeiev, D.V., Xiao, W., Kröner, A., Badarch, G., 2007. Tectonic models for accretion of the Central Asian Orogenic Belt. Journal of the Geological Society, London 164, 31–47. doi:10.1144/0016-76492006-022

Windley, B.F., Allen, M.B., Zhang, C., Zhao, Z.Y., Wang, G.R., 1990. Paleozoic accretion and Cenozoic redeformation of the Chinese Tien Shan Range, central Asia. Geology 18, 128–131. doi:10.1130/0091-7613(1990)018<0128:PAACRO>2.3.CO;2

Xiao, W., Han, C., Liu, W., Wan, B., Zhang, J., Ao, S., Zhang, Z., Song, D., Tian, Z., Luo, J., 2014. How many sutures in the southern Central Asian Orogenic Belt: Insights from East Xinjiang-West Gansu (NW China)? Geoscience Frontiers 5, 525–536. doi:10.1016/j.gsf.2014.04.002

Xiao, W., Windley, B.F., Allen, M.B., Han, C., 2013. Paleozoic multiple accretionary and collisional tectonics of the Chinese Tianshan orogenic collage. Gondwana Research 23, 1316–1341. doi:10.1016/j.gr.2012.01.012

Xiao, W., Windley, B.F., Badarch, G., Sun, S., Li, J., Qin, K., Wang, Z., 2004. Paleozoic accretionary and convergent tectonics of the southern Altaids: implications for the growth of Central Asia. Journal of the Geological Society, London 161, 339–342.

Xiao, W.J., Windley, B.F., Huang, B.C., Han, C.M., Yuan, C., Chen, H.L., Sun, M., Sun, S., Li, J.L., 2009. End-Permian to mid-Triassic termination of the accretionary processes of the southern Altaids: Implications for the geodynamic evolution, Phanerozoic continental growth, and metallogeny of Central Asia. International Journal of Earth Sciences 98, 1189–1217. doi:10.1007/s00531-008-0407-z

Xu, Y., Wei, X., Luo, Z., Liu, H., Cao, J., 2014. Lithos The Early Permian Tarim Large Igneous Province : Main characteristics and a plume incubation model. Lithos 204, 20–35. doi:10.1016/j.lithos.2014.02.015

Yamato, P., Agard, P., Burov, E., Le Pourhiet, L., Jolivet, L., Tiberi, C., 2007. Burial and exhumation in a subduction wedge: Mutual constraints from thermomechanical modeling and natural P-T-t data (Schistes Lustrés, western Alps). Journal of Geophysical Research: Solid Earth 112, 1–28. doi:10.1029/2006JB004441

Yamato, P., Burov, E., Agard, P., Le Pourhiet, L., Jolivet, L., 2008. HP-UHP exhumation during slow continental subduction: Self-consistent thermodynamically and thermomechanically coupled model with application to the Western Alps. Earth and Planetary Science Letters 271, 63–74. doi:10.1016/j.epsl.2008.03.049

Yang, S., Li, Z., Chen, H., Santosh, M., Dong, C., Yu, X., 2007. Permian bimodal dyke of Tarim Basin , NW China : Geochemical characteristics and tectonic implications. Gondwana Research 12, 113–120. doi:10.1016/j.gr.2006.10.018

Yang, S.F., Chen, H.L., Li, Z., Li, Y., Yu, X., Li, D., Meng, L., 2013. early Permian Tarim Large Igneous Province in northwest China. Science China Earth Sciences 56, 2015–2026.

Yarmolyuk, V.V., Kuzmin, M.I., Ernst, R.E., 2014. Intraplate geodynamics and magmatism in the evolution of the Central Asian Orogenic Belt. Journal of Asian Earth Sciences 93, 158–179.

Ye, X.T., Zhang, C.L., Santosh, M., Zhang, J., Fan, X.K., Zhang, J.J., 2016. Growth and evolution of Precambrian continental crust in the southwestern Tarim terrane: New evidence from the ca. 1.4 Ga A-type granites and Paleoproterozoic intrusive complex. Precambrian Research 275, 18–34. doi:10.1016/j.precamres.2015.12.017

Yin, A., Craig, P., Harrison, T.M., Ryerson, F.J., Qian, X., Yang, G., 1998. Late Cenozoic tectonic evolution of the southern Chinese Tian Shan. Tectonics 17, 1–27.

Zhang, C.L., Zou, H.B., Santosh, M., Ye, X.T., Li, H.K., 2014. Is the Precambrian basement of the Tarim Craton in NW China composed of discrete terranes? Precambrian Research 254, 226–244. doi:10.1016/j.precamres.2014.08.006

Zhang, L., Zhang, J., Jin, Z., 2015. Metamorphic P-T-water conditions of the Yushugou granulites from the south-eastern Tanshan orogen: Implications for Palezoic accretionary orogeny. Gondwana Research. doi:10.1016/j.gr.2014.12.009

Zhang, L.F., Du, J.X., Shen, X.J., Lü, Z., Song, S.G., Wei, C.J., 2009. The timing of UHP-HP eclogitic rocks in Western Tianshan, NW China: the new SIMS U-Pb zircon dating, Lu/Hf and Sm/Nd isochron ages, in: 8th International Eclogite Conference.

Zhiwei, L., Roecker, S., Zhihai, L., Bin, W., Haitao, W., Schelochkov, G., Bragin, V., 2009. Tomographic image of the crust and upper mantle beneath the western Tien Shan from the MANAS broadband deployment: Possible evidence for lithospheric delamination. Tectonophysics 477, 49–57. doi:10.1016/j.tecto.2009.05.007

Zhong, L., Wang, B., Shu, L., Liu, H., Mu, L., Ma, Y., Zhai, Y., 2014. Structural overprints of early Paleozoic arc-related intrusive rocks in the Chinese Central Tianshan : implications for Paleozoic accretionary tectonics in SW Central Asian Orogenic Belts State Key Laboratory for Mineral Deposits Research , School of Eart. Journal of Asian Earth Sciences. doi:10.1016/j.jseaes.2014.12.003

Zhu, Y., Zhang, L., Gu, L., Guo, X., Zhou, J., 2005. The zircon SHRIMP chronology and trace element geochemistry of the Carboniferous volcanic rocks in western Tianshan Mountains. Chinese Science Bulletin 50, 2201–2212. doi:10.1007/BF03182672

Zubovich, A. V., Bobrovski, A., Mikolaichuk, A., Buchroithner, M.F., 2008. Quaternary removed geological map of the Khan Tengri Massif, 1:200 000. Kyrgyz-Russian Slavic university, International Science & Technology Center.

Zubovich, A. V., Wang, X.Q., Scherba, Y.G., Schelochkov, G.G., Reilinger, R., Reigber, C., Mosienko, O.I., Molnar, P., Michajljow, W., Makarov, V.I., Li, J., Kuzikov, S.I., Herring, T.A., Hamburger, M.W., Hager, B.H., Dang, Y.M., Bragin, V.D., Beisenbaev, R.T., 2010. GPS velocity field for the Tien Shan and surrounding regions. Tectonics 29, 1–23. doi:10.1029/2010TC002772